Study of the antihydrogen atom and ion production via charge exchange reaction on positronium

Barbara Maria Latacz

université PARIS-SACLAY

NNT : 2019SACLS266

Thèse de doctorat

Study of the antihydrogen atom and ion production via charge exchange reaction on positronium

Thèse de doctorat de l'Université Paris-Saclay
préparée à l'Université Paris-Sud au sein du Département de Physique des Particules, Irfu, CEA Saclay

École doctorale n°576 Particules, Hadrons, Énergie, Noyau, Instrumentation, Imagerie, Cosmos et Simulation (PHENIICS)
Spécialité de doctorat: Physique des particules

Thèse présentée et soutenue à Saclay, le 24 septembre 2019, par

MME BARBARA MARIA LATACZ

Composition du Jury :

M. Reza Ansari Professeur, Université Paris-Sud, Laboratoire de l'Accélérateur Linéaire (LAL)	Président
M. Alexandre Obertelli Professeur, Technische Universität Darmstadt, Department of Physics	Rapporteur
M. Svante Jonsell Professeur, Stockholm University, Department of Physics	Rapporteur
M. Daniel de Miranda Silveira Professeur, Universidade Federal de Rio de Janeiro, Institute of Physics	Examinateur
M. Patrice Pérez Ingénieur-chercheur, CEA, DRF, IRFU, Département de Physique des Particules	Directeur de thèse
M. Laszlo Liszkay Ingénieur-chercheur, CEA, DRF, IRFU, Département de Physique des Particules	Invité

Acknowledgments

I would like to express my special appreciation and thanks to my supervisor Patrice Pérez. You have made the preparation of this Ph.D. thesis an amazing experience. I would like to thank Pascal Debu, Laszlo Liszkay and Bruno Mansoulié for their enormous help. A special thanks to my Ph.D. committee Reza Ansari, Alexandre Obertelli, Svante Jonsell, and Daniel de Miranda Silveira for brilliant comments, suggestions and for letting my defense be an enjoyable moment.

Great thanks to the whole CEA Saclay group and the GBAR collaboration. Especially for good (actually mostly very bad) sense of humor! Thanks also to the whole AD and CERN community. The "AD spirit" I will miss the most.

At this point, I would like to thank the Polish Children's Fund for showing me an amazing world of science and believing in impossible.

A special thanks to my whole family. It is great to have so many people around me who are so warm, supportive and creative! Words cannot express how grateful I am to my parents for all of the sacrifices that you've made on my behalf. Greetings to my sisters for everything and especially for long movie evenings. I would also like to thank all of my friends who were cheering me up during the writing. I hope all our (safe) dreams will come true! In the end, I would like to express appreciation to my beloved partner Wojciech Rzadkowski who was always my greatest support in the darkest and brightest moments of last years. Dziękuję Ci ogromnie!

université PARIS-SACLAY | ÉCOLE DOCTORALE PHENIICS

Title: Study of the antihydrogen atom and ion production via charge exchange reaction on positronium

Keywords: Antiprotons, Antihydrogen, GBAR, Positron, Cross-sections, Simulation

Abstract: The main goal of the GBAR collaboration is to measure the Gravitational Behaviour of Antihydrogen at Rest. It is done by measuring the classical free fall of neutral antihydrogen, which is a direct test of the weak equivalence principle for antimatter.
The first step of the experiment is to produce the antihydrogen ion $\bar{H}^+$ and catch it in a Paul trap, where it can be cooled to μK temperature using ground state Raman sideband sympathetic cooling. The μK temperature corresponds to particle velocity in the order of 1 m/s. Once such velocity is reached, the antihydrogen ion can be neutralised and starts to fall. This allows reaching 1 % precision on the measurement of the gravitational acceleration g for antimatter with about 1500 events. Later, it would be possible to reach $10^{-5} - 10^{-6}$ precision by measuring the gravitational quantum states of cold antihydrogen.
However, in order to measure the free fall, firstly the antihydrogen ion has to be produced. It is formed in the charge exchange reactions between antiproton/antihydrogen and positronium:

$$Ps^* + \bar{p} \rightarrow \bar{H} + e^-$$
$$Ps^* + \bar{H} \rightarrow \bar{H}^+ + e^-.$$

The "*" next to an atom symbol indicates that it can be either in a ground state or in an excited state. An experimental study of the cross section measurement for these two reactions is described in the presented thesis.
The antihydrogen atom $\bar{H}$ and ion $\bar{H}^+$ production takes place in a cavity. The formation of one $\bar{H}^+$ ion in one beam crossing requires about 5×10^6 antiprotons/bunch and a few 10^{11} Ps/cm^{-3} positronium density inside the cavity, which is produced with a beam containing 5×10^{10} positrons per bunch. The production of such intense beams with required properties is a challenging task.
First, the development of the positron source is described. The GBAR positron source is based on a 9 MeV linear electron accelerator. The relatively low energy was chosen to avoid activation of the environment. The electron beam is incident on a tungsten target where positrons are created from Bremsstrahlung radiation (gammas) through the pair creation process. Some of the created positrons undergo a further diffusion in the tungsten moderator reducing their energy to about 3 eV. The particles are re-accelerated to about 53 eV energy and are adiabatically transported to the next stage of the experiment. Presently, the measured positron flux is at the level of $4.94 \pm 0.001(stat) \pm 0.030(sys) \times 10^7$ e$^+$/s, which is a few times higher than intensities reached with radioactive sources.
Then, the thesis features a short description of the antiproton/proton beam preparations, finalised with a chapter about the expected antihydrogen atom and ion production yield. After the reaction, antiproton, antihydrogen atom, and ion beams are guided to the detection system. It is made to allow for detection from 1 to a few thousand antihydrogen atoms, a single antihydrogen ion and all 5×10^6 antiprotons. It is especially challenging because antiproton annihilation creates a lot of secondary particles which may disturb measurements of single antihydrogen atoms and ions. The main part of the Thesis is the description of the expected background for the antihydrogen atom and ion detection. Additionally, the detection system allows measuring the cross sections for the symmetric reactions of a hydrogen atom and ion production through charge exchange between protons and positronium.
The $\bar{H}^+$ production part of the experiment was fully installed at CERN in 2018. The first tests with antiprotons from the ELENA decelerator were done. Currently, the experiment is being commissioned with positrons and protons, in order to perform the hydrogen atom and ion formation. The optimisation of the ion production with matter will help to be fully prepared for the next antiproton beam time in 2021.

Université Paris-Saclay
Espace Technologique / Immeuble Discovery
Route de l'Orme aux Merisiers RD 128 / 91190 Saint-Aubin, France

université PARIS-SACLAY | ÉCOLE DOCTORALE PHENIICS

Titre: Étude de la production d'atomes et d'ions d'antihydrogène par réaction d'échange de charge avec du positronium

Mots clés: Antiprotons, Antihydrogène, GBAR, Positon, Sections efficaces (physique nucléaire), Simulation

Résumé: Le but principal de la collaboration GBAR est de mesurer le comportement d'atomes d'antihydrogène sous l'effet de la gravité terrestre. Ceci est fait en mesurant la chute libre classique d'atomes d'antihydrogène, qui est un test direct du principe d'équivalence faible pour l'antimatière.
La première étape de l'expérience est de produire des ions d'antihydrogène $\bar{H}^+$ et de les amener dans un piège de Paul, où ils peuvent être refroidis à une température de l'ordre du μK en utilisant la technique du refroidissement sympathique avec des ions Be^+ eux-mêmes mis dans leur état fondamental par la technique Raman à bande latérale. Une température de l'ordre du μK correspond à une vitesse de la particule de l'ordre de 1 m/s. Une fois cette vitesse atteinte, l'ion antihydrogène peut être neutralisé et commence sa chute. Ceci permet une précision de 1 % sur la mesure de l'accélération gravitationnelle g pour l'antimatière avec environ 1500 événements.
Cependant, pour mesurer la chute libre, il faut d'abord produire l'ion antihydrogène. Celui-ci est formé dans les réactions d'échange de charge entre des antiprotons et des antihydrogènes avec du positronium:

$$Ps^* + \bar{p} \rightarrow \bar{H} + e^-$$

$$Ps^* + \bar{H} \rightarrow \bar{H}^+ + e^-.$$

Le symbole "*" associé à celui d'un atome indique que celui-ci peut se trouver soit à l'état fondamental, soit dans un état excité. Une étude expérimentale de la mesure de la section efficace de ces deux réactions est décrite dans cette thèse. La production de l'atome d'antihydrogène $\bar{H}$ ainsi que de l'ion $\bar{H}^+$ se passe à l'intérieur d'une cavité. La formation d'un ion $\bar{H}^+$ lors d'une interaction entre faisceaux requiert environ 5×10^6 antiprotons/paquet et quelques 10^{11} Ps/cm^{-3} de densité de positronium à l'intérieur d'une cavité. Celle-ci est produite par un faisceau contenant 5×10^{10} positrons par paquet. La production de faisceaux aussi intenses avec les propriétés requises est en soi un défi.
Le développement de la source de positrons de GBAR est décrite. Celle-ci est basée sur un accélérateur linéaire à électrons de 9 MeV. Le faisceau d'électrons est incident sur une cible de tungstène où les positrons sont créés par rayonnement de freinage (gammas) et création de paires. Une partie des positrons ainsi créés diffusent à nouveau dans un modérateur de tungstène en réduisant leur énergie à environ 3 eV. Ces particules sont re-accélérées à une énergie d'environ 53 eV. Aujourd'hui, le flux mesuré de positrons est au niveau de $4.94 \pm 0.001(stat) \pm 0.030(sys) \times 10^7$ e^+/s, soit quelque fois plus élevé que les intensités obtenues avec des sources radioactives.
Puis la thèse comporte une courte description des préparatifs pour les faisceaux d'antiprotons ou de protons, terminée par un chapitre sur le taux de production attendu d'atomes et d'ions d'antihydrogène. En aval de la réaction, les faisceaux d'antiprotons, d'atomes et d'ions d'antihydrogène sont guidés vers leur système de détection. Ceux-ci ont été conçus de façon à permettre la détection d'un à plusieurs milliers d'atomes d'antihydrogène, un seul ion antihydrogène et tous les 5×10^6 antiprotons. Ceci est particulièrement difficile parce que l'annihilation des antiprotons crée beaucoup de particules secondaires qui peuvent perturber la mesure d'un atome ou ion. La majeure partie de la thèse consiste en la description des bruits de fond attendus pour la détection des atomes et ions d'antihydrogène. De plus, le système de détection permet de mesurer les sections efficaces pour les réactions symétriques de production d'atomes et d'ions hydrogène par échange de charge entre protons et positronium.
La partie production d'ions $\bar{H}^+$ de l'expérience a été complètement installée au CERN en 2018. Les premiers tests avec des antiprotons provenant du décélérateur ELENA ont été effectués. Actuellement, l'expérience est testée avec des positrons et des protons, de façon à former des atomes et ions hydrogène. Une optimisation de la production de ces ions de matière aidera à se préparer pour la prochaine période de faisceau d'antiprotons en 2021.

Université Paris-Saclay
Espace Technologique / Immeuble Discovery
Route de l'Orme aux Merisiers RD 128 / 91190 Saint-Aubin, France

Résumé étendu en français

1 Recherche sur l'antimatière

En raison de la différence significative entre le nombre d'anti particules observé et prédit dans l'Univers, la recherche de différences entre la matière et l'antimatière est une partie essentielle de la physique fondamentale. Il est possible de le faire en utilisant des (anti)particules uniques ou en testant les propriétés de systèmes complexes, c'est-à-dire des atomes exotiques. Les atomes exotiques disponibles connus au niveau technique actuel sont :

- positronium Ps - l'état lié d'un électron et d'un positron [1] ;
- muonium Mu - l'état lié d'un antimuon et d'un électron [2] ;
- antiprotonic hélium $\bar{p}He^+$ - un atome composé d'un électron et d'un antiproton orbitant autour d'un noyau hélium [3];
- antihydrogen $\bar{H}$ - un atome fait d'un positron orbitant autour d'un noyau composé d'un antiproton [4].

Dans cette thèse, l'atome d'antihydrogène est discuté. Les tests de différences matière-antimatière avec l'antihydrogène froid peuvent donner la meilleure précision de tous les atomes exotiques, car ils peuvent être comparés aux mesures effectuées sur l'équivalent antihydrogène exact de la matière - l'hydrogène. De plus, l'antihydrogène est stable et l'hydrogène est le système complexe le plus connu au monde. La limite de précision pour certains tests est au niveau de 4 parties dans 10^{15} [5].

Actuellement, le test le plus précis de l'invariance CPT réalisée avec des atomes d'antihydrogène a été effectué en mesurant la transition 1S-2S par la collaboration ALPHA. La précision relative de l'invariance CPT est d'environ 2×10^{-12} [6].

1.1 Interaction gravitationnelle de l'antimatière

La théorie de la relativité générale est basée sur le principe d'équivalence faible (WEP), qui stipule que toutes les particules dans le même champ gravitationnel et au même point spatial-temps subissent la même accélération, indépendamment de leurs propriétés. Selon cette règle, l'interaction gravitationnelle de toute particule et de son antiparticule doit être la même. Cette affirmation n'a jamais été directement testée expérimentalement, principalement en raison de nombreuses difficultés techniques liées à la réalisation d'une véritable chute libre d'antimatière.

Une formulation équivalente du Principe d'Equivalence indique que les masses gravitationnelle et inertielle d'un objet sont égales. En principe, l'invariance CPT du modèle standard prédit la même masse inertielle pour la matière et l'antimatière, donc, si le WEP est correct, leur accélération gravitationnelle devrait être égale. Cependant, il n'est pas clair si le couplage entre l'antimatière et la gravitation est le même que pour la matière. Bien que non observées, il existe des théories qui prédisent soit une différence dans l'amplitude de l'interaction entre la matière et l'antimatière ou entre l'antimatière et l'antimatière, soit une répulsion gravitationnelle [7, 8, 9].

Aujourd'hui, trois expériences au CERN (GBAR [10], AEGIS [11], ALPHAg [12]), une au Paul Scherrer Institut (MAGE [13]) et une au UCL (D. Cassidy et al., [14]) visent la mesure des interactions gravitationnelles pour l'antimatière. Les premiers résultats des expériences du CERN sont attendus au printemps 2021.

2 L'expérience GBAR

Le principal de la collaboration GBAR est de mesurer le comportement d'atomes d'antihydrogène sous l'effet de la gravité terrestre. L'expérience est basée sur une idée de J. Walz and T. Hänsch [15], qui a été initiée par P. Pérez [16]. La description détaillée de l'expérience originale se trouve dans la proposition de GBAR [10].

L'idée principale de l'expérience est de mesurer la chute libre classique de l'antihydrogène neutre. C'est une mesure directe du principe d'équivalence faible de l'antimatière. La première étape de l'expérience consiste à produire un ion antihydrogène $\bar{\mathrm{H}}^+$ et à le capturer dans un piège Paul, où il peut être refroidi à une température de quelques μK en utilisant un refroidissement sympathique en bande latérale Raman à état fondamental. La température μK correspond à une vitesse des particules de l'ordre de 1 m/s. Une fois cette vitesse atteinte, l'ion antihydrogène peut être neutralisé et commence à tomber. Une chute de 10 cm de hauteur correspond à environ 0,14 s de temps de vol. Une chute libre aussi longue permet d'atteindre 37 % d'erreur sur la mesure de l'accélération gravitationnelle $\bar{g}$ pour l'antihydrogène après un seul événement. Avec cette méthode, l'objectif est d'atteindre une précision de 1 % avec environ 1500 événements [10].

Le deuxième objectif de l'expérience est d'atteindre une précision de $10^{-5} - 10^{-6}$ dans la mesure des états quantiques gravitationnels de l'antihydrogène froid [17, 18]. Cette méthode s'inspire d'une expérience similaire réalisée avec des neutrons froids [19].

La première partie de l'expérience GBAR est la production d'ions antihydrogènes. Ils sont produits dans les réactions suivantes :

$$Ps^* + \bar{p} \rightarrow \bar{\mathrm{H}}^* + e^- \tag{1}$$

$$Ps^* + \bar{\mathrm{H}} \rightarrow \bar{\mathrm{H}}^+ + e^-. \tag{2}$$

Le "$*$" à côté du symbole d'un atome indique qu'il peut être dans l'état fondamental ou dans un état excité. L'efficacité de production de $\bar{\mathrm{H}}^+$ dépend de la densité et de la température du nuage Ps, du niveau d'excitation de Ps et de $\bar{\mathrm{H}}$, de l'intensité et de l'énergie du faisceau antiproton. Tous ces paramètres doivent être optimisés en tenant compte non seulement de l'efficacité de la production mais aussi des contraintes techniques.

Le schéma général de la partie production d'ions antihydrogènes de l'expérience GBAR est illustré à la figure 1. La partie violette représente la préparation du faisceau de positrons de haute intensité pour la production de positronium. La partie verte décrit le faisceau d'antiprotons. La production de l'atome d'antihydrogène $\bar{\mathrm{H}}$ et de l'ion $\bar{\mathrm{H}}^+$ a lieu dans une cavité. En raison de l'énergie de positronium relativement faible par rapport à l'énergie antiprotonique, les produits de réaction les plus lourds (atomes et ions d'antihydrogène) combinés au faisceau $\bar{\mathrm{p}}$ sont transportés vers le séparateur électrostatique (Figure 1). Selon les estimations de la proposition de l'expérience [10], la production d'environ 0,3 ion antihydrogène nécessite 6×10^6 antiprotons

et 2×10^{10} positrons en une impulsion. Dans cette thèse, différentes intensités de faisceau sont considérées, ajustées aux conditions expérimentales mises à jour.

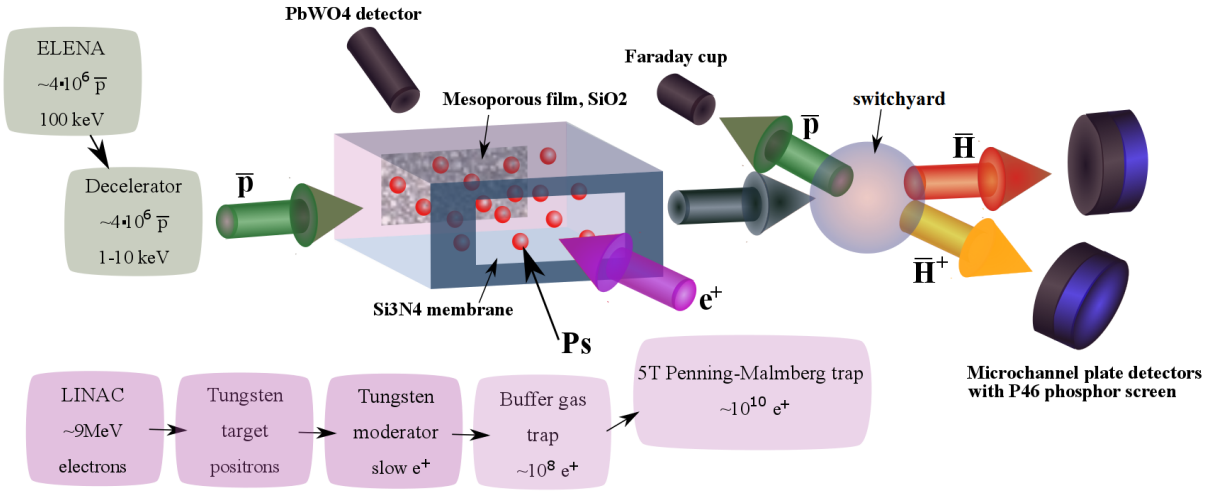

Figure 1: Le schéma général du dispositif de production d'ions antihydrogènes.

3 Présentation de l'esquisse de thèse

La thèse porte sur l'optimisation de la production et la détection des atomes et ions d'antihydrogène pour l'expérience GBAR. Pour ce faire, on étudie la façon de mesurer les sections efficaces. En outre, le chapitre 3 décrit la source de positrons lents de GBAR, dont la caractérisation et la maintenance étaient également la responsabilité de l'auteur de la thèse. Le chapitre 4 résume les calculs théoriques existants des valeurs de section transversale. Ils sont essentiels pour définir les exigences expérimentales minimales attendues, comme par exemple, le nombre minimum d'antiprotons et d'atomes de positronium. Ensuite, les paramètres à mesurer sont prédéfinis en examinant la méthode générale d'extraction des valeurs de section efficace dans le cadre de GBAR. Dans le chapitre 5, la cavité de réaction est présentée avec tous les détecteurs disponibles pour caractériser la procédure de mélange positronium - antiproton. Le taux prévu de production d'atomes et d'ions d'antihydrogène est calculé à l'aide de simulations. Comme on le montrera, on s'attend à ce que moins d'un ion antihydrogène se forme par paquet d'antiprotons. La détection d'un signal aussi faible nécessite un système de détection très bien conçu qui permettrait de minimiser tous les bruits de fond possibles. La principale source de bruit de fond qui pourrait gâcher l'expérience provient des annihilations d'antiprotons dans différentes parties de l'expérience. Afin d'introduire ce problème, le chapitre 6 contient une description générale de l'annihilation des antiprotons dans la matière. Le chapitre 7 décrit un transport d'antiprotons d'ELENA vers la décharge d'antiprotons. Il est axé sur le problème de la réduction des émissions de fond. Dans le dernier chapitre, l'antiproton, l'atome d'antihydrogène et le système de détection ionique sont décrits avec une estimation de fond attendue.

Voici un résumé des chapitres suivants :

Chapitre 3 Une étude de la source de positrons lents basée sur un accélérateur linéaire d'électrons. Il contient la préparation du faisceau de positrons et sa caractérisation.

Chapitre 4 Introduction à la mesure de section efficace. Il comprend une description des calculs théoriques disponibles et une description générale de la façon d'obtenir les valeurs de section efficace dans l'expérience.

Chapitre 5 Un résumé de la production prévue d'atomes d'antihydrogène et du taux de production d'ions dans des expériences spécifiques.

Chapitre 6 Une description du processus d'annihilation des antiprotons dans la matière. Ce résumé présente les problèmes possibles résultant des particules secondaires créées lors de la détection d'antiprotons, d'atomes d'antihydrogène ou d'ions.

Chapitre 7 Une description sommaire du transport des antiprotons jusqu'au niveau de la chambre de réaction et une motivation et une conception du système de transport des antiprotons, des atomes d'antihydrogène etdes anti ions après la chambre de réaction.

Chapitre 8 Une description du système de détection des antiprotons, des anti atomes et anti ions ainsi qu'une estimation des bruits de fond dans les conditions expérimentales choisies.

Chapitre 9 Un résumé de la thèse.

4 Conclusion

Le sujet principal de cette thèse est l'étude de la mesure de la section efficace de formation des atomes et ions d'antihydrogène. Pendant la durée du doctorat, l'ensemble du système de mesure de la section efficace, y compris la source de protons ou d'antiprotons, la source de positrons, le piégeage des positrons, la cavité de réaction avec le convertisseur au positronium et le système de détection ont été construits au CERN. Certaines parties du système ont été testées avec succès, ainsi qu' avec le premier faisceau antiproton dand GBAR. Avec le système conçu, on s'attend à ce qu'il atteigne même 20 % de précision sur la mesure des sections efficaces de formation d'antihydrogène.

Cette thèse porte sur la production d'antiprotons, d'atomes et d'ions d'antihydrogène et les problèmes de détection, ainsi que sur l'estimation des fonds. La conception du système a été optimisée pour réduire au minimum tous les bruits de fond possibles.

On s'attend à ce qu'il produise jusqu'à 3000 atomes d'antihydrogène avec 5×10^{10} positrons et 5×10^{6} antiprotons participant à la réaction. Cette mesure est presque sans bruit de fond. Dans le deuxième cas considéré, lorsque seulement 5×10^{8} positrons sont injectés dans la chambre de réaction, les mesures sont un peu plus difficiles. On s'attend à ce qu'il produise entre 3 et 30 atomes d'antihydrogène dans le schéma avec la cavité réactionnelle et entre 0,4 et 4 atomes d'antihydrogène dans le schéma avec la cible plate. Le contexte principal de ces tests provient de l'annihilation des antiprotons dans la chambre de réaction. Le rapport signal sur bruit de fond attendu se situe entre 0,1 % et 2 % dans le schéma de cavité et entre 2 % et 11 % dans le schéma cible plat. Ce rapport ne peut être amélioré qu'en diminuant la taille du faisceau d'antiprotons et son annihilation sur le collimateur devant la zone de réaction.

Le plus difficile est la détection des ions d'antihydrogène en raison du faible rapport signal sur bruit de fond. Le nombre prévu d'ions antihydrogènes détectés par impulsion pour une énergie de faisceau d'antiprotons de 10 keV est d'environ 0,2 et pour une énergie d'antiprotons de 6 keV est entre 0,4 et 0,8. Le bruit de fond correspondant est de 0,01 - 0,05 (10 keV) et

0,01 - 0,03 (6 keV) événements détectés. Dans le pire des cas, le rapport signal sur bruit de fond est d'environ 26 %. Cependant, la détection devrait encore être possible en raison de la différence d'amplitude des signaux provenant des atomes d'antihydrogène, des gammas et des neutrons. Les premiers tests très généraux de cette méthode semblent prometteurs. L'autre possibilité est de permuter les emplacements du système de détection des antiprotons avec ceux des ions antihydrogènes. Cela retarderait l'annihilation de l'antiproton, et la mesure des ions antihydrogène serait sans bruit de fond.

Une autre occasion a été d'étudier la source de positrons lents GBAR, qui est essentielle pour obtenir le faisceau de positrons à haut flux pour la formation du positronium. Le flux de positrons obtenu est de $N_{e^+/1s} = 4.94 \pm 0.001(stat) \pm 0.030(sys) \times 10^7$ e^+/s à 300 Hz fréquence de répétition linac. Il est au moins 5 fois plus élevé par rapport au flux maximum disponible avec une source Na^{22}.

Actuellement, le système est testé avec des protons pour effectuer la formation d'atomes d'hydrogène et d'ions. On pense que le système conçu peut permettre de produire des atomes d'hydrogène dans quelques mois.

5 References

[1] M. Deutsch. Three-quantum decay of positronium. *Physical Review*, 83(4):866, 1951.

[2] V. W. Hughes, D. W. McColm, K. Ziock, and R. Prepost. Formation of muonium and observation of its Larmor precession. In *A Festschrift In Honor Of Vernon W Hughes*, pages 208–210. World Scientific, 1992.

[3] M. Iwasaki et al. Discovery of antiproton trapping by long-lived metastable states in liquid helium. *Physical Review Letters*, 67(10):1246, 1991.

[4] G. Baur et al. Production of antihydrogen. *Physics Letters B*, 368(3):251–258, 1996.

[5] Ch. G. Parthey et al. Improved measurement of the hydrogen 1s–2s transition frequency. *Physical Review Letters*, 107(20):203001, 2011.

[6] M. Ahmadi et al. Characterization of the 1S–2S transition in antihydrogen. *Nature*, 557(7703):71, 2018.

[7] M. Kowitt. Gravitational repulsion and Dirac antimatter. *International Journal of Theoretical Physics*, 35(3):605–631, 1996.

[8] R. M. Santilli. A classical isodual theory of antimatter and its prediction of antigravity. *International Journal of Modern Physics A*, 14(14):2205–2238, 1999.

[9] M. Villata. CPT symmetry and antimatter gravity in general relativity. *Europhysics Letters*, 94(2):20001, 2011.

[10] P. Perez et al. Proposal to measure the Gravitational Behaviour of Antihydrogen at Rest GBAR. CERN-SPSC-2011-029; SPSC-P-342, 2011.

[11] G. Yu. Drobychev et al. Proposal for the AEGIS experiment at the CERN antiproton decelerator (Antimatter Experiment: Gravity, Interferometry, Spectroscopy). CERN-SPSC-2007-017; SPSC-P-334, (2007).

[12] J. S. Hangst, Addendum to the ALPHA Proposal. The ALPHA-g Apparatus. CERN-SPSC-2016-031; SPSC-P-325-ADD-1, 2016.

[13] A. Antognini, D. Kaplan, K. Kirch, A. Knecht, D. Mancini, J. Phillips, T. Phillips, R. Reasenberg, T. Roberts, and A. Soter. Studying antimatter gravity with muonium. *Atoms*, 6(2):17, 2018.

[14] D. B. Cassidy and S. D. Hogan. Atom control and gravity measurements using Rydberg positronium. In *International Journal of Modern Physics: Conference Series*, volume 30, page 1460259. World Scientific, 2014.

[15] J. Walz and T. W. Hänsch. A proposal to measure antimatter gravity using ultracold antihydrogen atoms. *General Relativity and Gravitation*, 36(3):561–570, 2004.

[16] P. Perez, A. Mohri, H. A. Torii, L. Liszkay, N. Kuroda, B. Mansoulié, J. M. Rey, and Y. Yamazaki. A new path to measure antimatter free fall. Technical report, 2007.

[17] A. Y. Voronin, P. Froelich, and V. V. Nesvizhevsky. Gravitational quantum states of Antihydrogen. *Physical Review A*, 83(3):032903, 2011.

[18] V. V. Nesvizhevsky, A. Y. Voronin, P.-P. Crépin, and S. Reynaud. Interference of several gravitational quantum states of antihydrogen in GBAR experiment. *Hyperfine Interactions*, 240(1):32, 2019.

[19] V. V. Nesvizhevsky et al. Quantum states of neutrons in the Earth's gravitational field. *Nature*, 415(6869):297, 2002.

Contents

List of Tables

List of Figures

Chapter 1

Introduction to antimatter physics

1.1 History

Research on the existence of substance with properties opposite to matter dates back to the 19th century when William Hicks proposed a new type of matter that would have negative gravity. The new idea was based on the vortex theory [1, 2], which attempted to explain gravity with only basic mechanical processes. Another theory, introduced by Karl Pearson at the end of the 19th century, describes two types of matter, as squirts and sinks of the flow of ether [3]. A bit later, in 1889, Arthur Schuster published his futuristic and philosophical paper "Potential matter. - A holiday Dream." [4], where the word *anti-matter* was used for the first time, as the name for something complementary which is a "leftover" from the matter production process. *Anti-matter* in this paper could create the same combined structures as standard matter, but would not be visible for us, as it is repelled by negative gravity. Even though the now known antimatter is defined differently than in the above mentioned theories, those three scientists should be remembered as visionaries of an idea which led to a new part of physics – antimatter physics.

1.1.1 The origin in modern physics

The modern understanding of antimatter starts in 1928 with the work of Paul Dirac about "The Quantum Theory of The Electron" [5]. The new description of the electron was supposed to explain the "duplexity" phenomena that the number of stationary states of an electron in an atom is twice the number predicted by existing theories.

The Dirac equation for an electron in an electromagnetic field with a scalar potential A_0 and vector potential $\mathbf{A}$ in the original form is:

$$\left[p_0 + \frac{e}{c}A_0 + \rho_1\left(\sigma, \mathbf{p} + \frac{e}{c}\mathbf{A}\right) + \rho_3 mc\right]\psi = 0,$$

where ψ is the four-component wave function, m is the mass of the electron, e is the charge of the electron, c is the speed of light, p_0 and $\mathbf{p}$ are the components of the electron momentum, $\sigma = (\sigma_1, \sigma_2, \sigma_3)$ and ρ_n are 4 by 4 Hermitian matrices which satisfy the following conditions $\alpha_i^2 = \rho_n^2 = \mathbf{I_4}$, $\alpha_i\alpha_j + \alpha_j\alpha_i = 0$ and $\rho_i\rho_j + \rho_j\rho_i = 0$ for $i \neq j$.
As described in the original paper, the Dirac equation *will have four times as many solutions as the non-relativity wave equation (...) Since half the solutions must be rejected as referring*

to the charge +e on the electron, the correct number will be left to account for duplexity phenomena [5].

The explanation of the duplexity problem, which nowadays is known as the electron spin problem, was a great success. It led Dirac to the Nobel Prize in 1933. However, the Dirac equation describes also two other unknown states with a positive charge, which even though primarily rejected, could have a deeper meaning. The possible explanation could be that there is a new particle, which has the same properties as the electron, but the opposite electric charge. The predicted particle was discovered in 1932 by Carl Anderson [6]. *The Positive Electron*, soon named the positron, was generated in the interaction of cosmic radiation with the material of a cloud chamber. By measuring the curvature of the particle track in a magnetic field, Anderson could prove that the observed particle had the same mass as that of the electron, but opposite sign, see Figure 1.1. Carl Anderson received the Nobel Prize for his discovery in 1936.

In summary, Dirac and Anderson for the first time in history presented the proper theory and experimental proof for the existence of an antiparticle. These discoveries established the ground for the future detailed studying of antimatter.

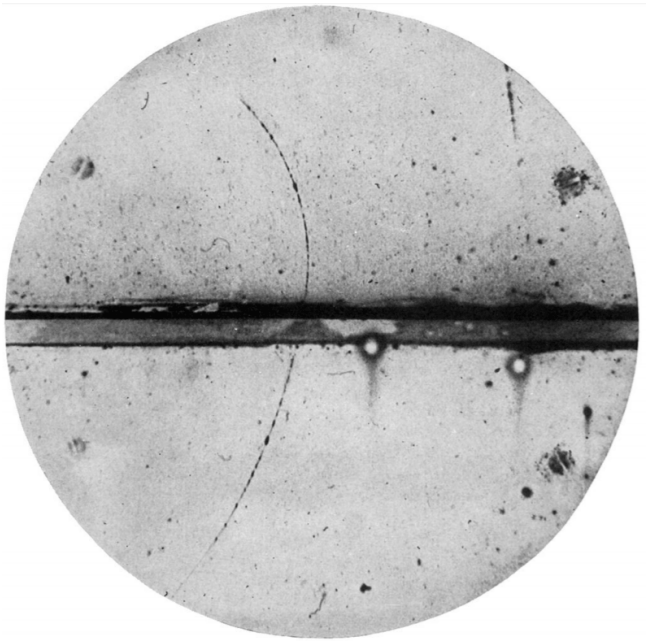

Figure 1.1: *A 63 million volt positron ($H_\rho = 2.1 \times 10^5$ gauss-cm) passing through a 6 mm lead plate and emerging as a 23 million volt positron ($H_\rho = 7.5 \times 10^4$ gauss-cm). The length of this latter path is at least ten times greater than the possible length of a proton path of this curvature.* Image and caption adapted from [6].

1.1.2 Motivation

Nowadays, antimatter is a part of the Standard Model [7, 8, 9, 10, 11, 12], in which every elementary particle has its symmetric counterpart (antiparticle) due to the charge conjugation symmetry. Particles and antiparticles are supposed to have the same properties as mass, but exactly opposite values of quantum numbers, like electric charge, magnetic moment or lepton and baryon numbers. Also, antiparticles and particles have to obey the same physical laws, which can be described using three fundamental symmetries: charge conjugation (C), parity

transformation (P) and time reversal (T). The application of any combination of these three symmetries on a physical process should result in the same observation.

Fundamental symmetries

In the first half of the 20th century, it was believed that each of C, P and T symmetries is individually conserved in nature. The first experimental disagreement with the theory was published in 1957, when Chien-Shiung Wu observed the violation of P symmetry in the weak interaction, by studying the β decay of Cobalt-60 [13]. One year later, M. Goldhaber observed that neutrinos are only left-handed, while antineutrinos are only right-handed [14]. According to charge conjugation symmetry, both helicities of massless neutrinos should occur in nature. As experiment shows exclusively only one type of helicity for matter or antimatter, this proves the "maximal violation" of charge conjugation C symmetry for charged currents in the weak interaction.

The mentioned β decay violates the parity symmetry, but it conserves all the combined symmetries. However, later in the history of physics also the combined CP symmetry violation was discovered. First in 1964 in the decay of K^0 mesons [15], later in the decay of B^0 mesons [16] and finally, only recently in the decay of D^0 mesons [17].

Even though individually C, P, and combined CP symmetries are violated, the CPT symmetry is still believed to be conserved. According to the theory, any model of a local quantum field theory which is Lorentz invariant and has a Hermitian Hamiltonian has to obey CPT symmetry. As the Standard Model is based on these assumptions, any experimental proof of CPT violation can strongly disturb our understanding of physics.

The search for CPT violation is an exciting topic and the studies of antimatter systems are also contributing to the field [18, 19].

Baryon asymmetry problem

According to the standard model of cosmology [20], the Universe was created in the so-called "Big Bang", in which pure energy converted into an equal amount of matter and antimatter. However, measurements show that the energy content of visible Universe is made of 5% of ordinary matter, 27% of dark matter and 68% of dark energy. This discrepancy between models and measurements, known as the baryon asymmetry problem [21, 22], is one of the greatest mysteries of modern physics.

A. Sakharov presented possible solutions in 1967 [21]. According to his work, the matter-antimatter asymmetry could be explained by simultaneously occuring three conditions:

- violation of baryon number;
- C and CP symmetry violation;
- lack of thermal equilibrium in the expanding Universe (or direct CPT violation).

The violation of baryon number is a requisite condition to produce the excess of baryons over antibaryons. The violation of C and CP symmetries ensures that if there is a process that produces more baryons than antibaryons, then there is a possibility that the symmetrical process does not counterbalance produced antibaryon yield. Finally, the lack of thermal equilibrium ensures that the CPT violation does not compensate the antibaryon formation.

The mentioned three requirements can be fulfilled by the Standard Model using the electroweak baryogenesis model [23, 24, 25, 26, 27]. However, the observed baryon assymetry is $Y_B = \frac{n_b - n_{\bar{b}}}{s} \approx 0.88 \times 10^{-10}$ [28], where $n_b(n_{\bar{b}})$ is the (anti)baryon density and s is the entropy density. It is commonly believed, that the minimal Standard Model underestimated the baryon assymetry by 10-12 orders of magnitude [29]. Thus, even though the possible solutions exist, they do not explain the whole matter-antimatter asymmetry. More study on antimatter properties is required to solve the baryon asymmetry problem.

Gravitational interaction of antimatter

The theory of general relativity is based on the Weak Equivalence Principle (WEP), which states that all particles in the same gravitational field and at the same spacetime point, undergo the same acceleration, independent of their properties. According to this rule, the gravitational interaction of any particle and its antiparticle should be the same. This statement has never been directly tested experimentally, mainly due to many technical difficulties with performing a real free fall of antimatter.

An equivalent formulation of the WEP states that the gravitational and inertial masses of an object are equal. In principle, the CPT-invariance of the Standard Model predicts the same inertial mass for matter and antimatter, thus, if the WEP is correct, their gravitational acceleration should be equal. However, it is not clear if the coupling between antimatter and gravitation is the same as for matter. Although unobserved, there exist theories which predict either a difference in the amplitude of the interaction between matter and antimatter or between antimatter and antimatter, or gravitational repulsion [30, 31, 32].

Nowadays, three experiments at CERN (GBAR [33], AEGIS [34], ALPHAg [35]), one in Paul Scherrer Institut (MAGE [36]) and one at UCL (D. Cassidy et al., [37]) aim to measure the gravitational interaction for antimatter. First results from experiments at CERN are expected in Spring 2021.

1.2 Antimatter research

Due to the significant difference between the observed and predicted number of antibaryons in the Universe, searching for differences between matter and antimatter is an essential part of fundamental physics. It is possible to do that using single (anti)particles or testing properties of complex systems, i.e., exotic atoms.

One of the greatest examples of an experiment which focuses on basic properties of single (anti)particles is the BASE experiment (the Baryon Antibaryon Symmetry Experiment [38]), which measures for example the charge-to-mass ratio $(q/m)_{\bar{p}}$ of antiprotons. Presently, the antiproton to proton charge-to-mass ratio is equal to $(q/m)_{\bar{p}}/(q/m)_p - 1 = 1(69) \times 10^{-12}$ [39]. The combined analysis of $(q/m)_{\bar{p}}/(q/m)_p$ measurements from BASE and TRAP [40] experiments gives $(q/m)_{\bar{p}}/(q/m)_p = 0.999\ 999\ 999\ 940(50)$, which is consistent with the CPT invariance within 1.2 standard errors [41]. Within the error bars, the results of the BASE experiment are in agreement with the Standard Model. However, it is not excluded, that a difference is present at higher precision.

The other possibility to study fundamental properties of antimatter is to use exotic atoms. The known available options at the current technical level are:

- positronium Ps - the bound state of an electron and a positron [42];

- muonium Mu - the bound state of an antimuon and an electron [43];
- antiprotonic helium $\bar{p}He^+$ - an atom composed of an electron and an antiproton orbiting around a helium nucleus [44];
- antihydrogen $\bar{H}$ - an atom made from a positron orbiting around a nucleus composed of one antiproton [45].

In this thesis, the antihydrogen atom is discussed. Tests of matter-antimatter differences with cold antihydrogen can give the best precision from all exotic atoms, because they can be compared to the measurements done on the exact antihydrogen equivalent in matter - hydrogen. Also, antihydrogen is stable and hydrogen is the best known complex system in the world. The precision limit for some tests is at the level of 4 parts in 10^{15} [46].

Currently, the most precise test of the CPT invariance performed with antihydrogen atoms was made by measuring the 1S-2S transition by the ALPHA collaboration. The relative precision of the CPT invariance is of around 2×10^{-12} [47].

1.2.1 Antihydrogen experiments

The first antihydrogen production was reported in 1995 by the PS210 collaboration [48]. This fixed target experiment used a 100 MeV antiproton beam from The Low Energy Antiproton Ring (LEAR) at CERN. After a few weeks of data taking, the production of 9 to 11 antihydrogen atoms was announced. Two years later, the E862 experiment at Fermilab confirmed the CERN result [49], by producing more than 100 antiatoms. These two collaborations opened the way for new ideas and experiments with antihydrogen.

Nowadays, 5 experiments attempt to perform measurements with antihydrogen:

- GBAR - Gravitational Behaviour of Anti-Hydrogen at Rest [33];
- ATRAP - the Cold antihydrogen for precise laser spectroscopy [50];
- ASACUSA - the Atomic Spectroscopy And Collisions Using Slow Antiprotons [51];
- ALPHA/ALPHAg - the Antihydrogen Laser PHysics Apparatus [52];
- AEGIS - the Antihydrogen Experiment: Gravity, Interferometry, Spectroscopy [34].

Three experiments, ALPHA, ASACUSA and ATRAP mastered the antihydrogen production and performed antihydrogen spectroscopy measurements. The direct competitors of the GBAR experiment in the measurement of WEP for antimatter are AEGIS and ALPHAg.

All five experiments are located at CERN and take advantage of the only existing low energy antiproton beam. CERN's two antiproton decelerators are the Antiproton Decelerator (AD) [53] and the Extra Low ENergy Antiproton ring (ELENA) [54, 55]. The AD provides antiprotons with 5.3 MeV energy. ELENA allows for further deceleration down to 100 keV. In the future, another antiproton center will be located in Darmstadt, Germany, where the Facility for Antiproton and Ion Research (FAIR) is being built [56].

1.2.2 Antihydrogen ion production

One of the goals of the GBAR experiment is to produce not only antihydrogen atoms but also antihydrogen ions consisting of one antiproton and two positrons. The primary motivation is that a charged ion can be easily stored and can be cooled even to μK temperatures, which is still not possible for neutral antihydrogen atoms. As a result, using these ions allows reaching a better precision than in other proposed experiments. GBAR is the only experiment which aims to produce antihydrogen ions. The thesis focuses on the antihydrogen atom and ion production study for the GBAR experiment.

Chapter 2

The GBAR experiment

2.1 Principle of the experiment

The main goal of the GBAR collaboration is to measure the **G**ravitational **B**ehaviour of **A**ntihydrogen at **R**est. The experiment is based on an idea of J. Walz and T. Hänsch [57], which was brought to life by P. Pérez [58]. The detailed description of the original experiment can be found in the GBAR proposal [33].

The main idea of the experiment is to measure the classical free fall of neutral antihydrogen. It is a direct measurement of the weak equivalence principle for antimatter. The first step of the experiment is to produce an antihydrogen ion $\bar{\mathrm{H}}^+$ and catch it in a Paul trap, where it can be cooled to μK temperature using ground state Raman sideband sympathetic cooling. The μK temperature corresponds to a particle velocity in the order of 1 m/s. Once such velocity is reached, the antihydrogen ion can be neutralised and starts to fall. Due to the low temperature, a fall from 10 cm height corresponds to about 0.14 s time of flight. Such a long free fall allows achieving 37 % error on the measurement of the gravitational acceleration $\bar{g}$ for antihydrogen after only one event. With this method, the aim is to reach 1 % precision with about 1500 events [33].

The second goal of the experiment is to reach $10^{-5} - 10^{-6}$ precision in the measurement of the gravitational quantum states of cold antihydrogen [59, 60]. This method is inspired by a similar experiment performed with cold neutrons [61].

2.2 Production of antihydrogen ions

The first part of the GBAR experiment is the production of antihydrogen ions. They are produced in the following reactions:

$$Ps^* + \bar{p} \rightarrow \bar{\mathrm{H}}^* + e^- \tag{2.1}$$

$$Ps^* + \bar{\mathrm{H}} \rightarrow \bar{\mathrm{H}}^+ + e^-. \tag{2.2}$$

The "$*$" next to an atom name indicates that it can be either in the ground state or in an excited state. The production efficiency of the $\bar{\mathrm{H}}^+$ depends on the density and temperature of the Ps cloud, the excitation level of Ps and $\bar{\mathrm{H}}$, and the intensity and energy of the antiproton

beam. All these parameters have to be optimised by taking into account not only the production efficiency but also the technical constraints.

The general scheme of the antihydrogen ion production part of the GBAR experiment is shown in Figure 2.1. The violet part represents the preparation of the high-intensity positron beam for positronium production. The green part describes the antiproton beam. The antihydrogen atom $\bar{H}$ and ion $\bar{H}^+$ production takes place in a cavity. Due to the relatively low positronium energy in comparison to the antiproton energy, the heaviest reaction products (antihydrogen atoms and ions) combined with the $\bar{p}$ beam are transported to the switchyard where they are separated in an electrostatic field (Figure 2.1). According to the estimations from the proposal of the experiment [33], the production of about 0.3 antihydrogen ions requires 6×10^6 antiprotons and 2×10^{10} positrons in one pulse. In this thesis, different beam intensities are considered, adjusted to the updated experimental conditions.

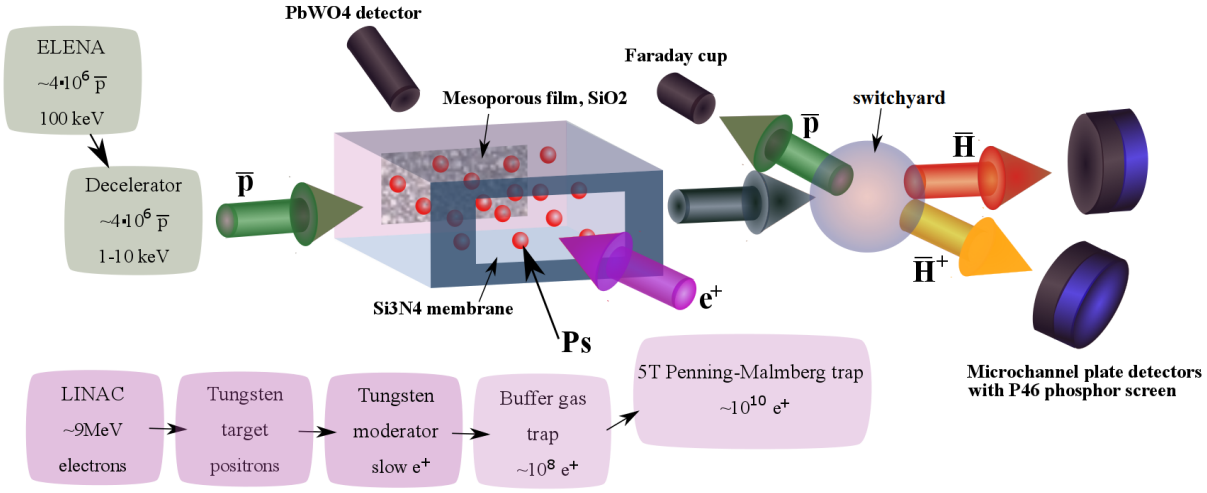

Figure 2.1: The general scheme of the antihydrogen ion production setup.

2.2.1 Antihydrogen atom and ion

An antihydrogen atom is a bound state of an antiproton and a positron. It is as stable as its matter counterpart - hydrogen. An antihydrogen atom annihilation is effectively an annihilation of an antiproton and a positron. The annihilation output consists of all antiproton annihilation products and two 511 keV gammas directed in opposite directions.

An antihydrogen ion is a three body system made from one antiproton and two positrons. Its small binding energy of 0.75 eV makes it very sensitive to any electrostatic field. Its annihilation products are the same as for the antihydrogen atom with the addition of two other 511 keV gammas. Both the antihydrogen atom and ion are relatively easy to detect even at low energies, as they release almost 1.9 GeV energy during the annihilation process.

2.2.2 ELENA and antiproton deceleration

The GBAR experiment receives an antiproton beam from the ELENA decelerator. The nominal beam properties are:

- beam intensity: 5×10^6 $\bar{p}$/pulse;

- beam energy: 100 ± 0.1 keV (standard deviation);
- pulse shape in time: Gaussian distribution with $\sigma_t \approx 50$ ns;
- beam emittance: 4π mm $\times$ mrad.

It is expected to reach the highest antihydrogen ion production for antiproton energies in the keV range [62, 63]. Thus the direct ELENA beam is too energetic for the GBAR experiment. To reach optimal antihydrogen ion production, a drift tube decelerator is added.

The GBAR decelerator is inspired by the heavy ion decelerator in ISOLDE [64, 65]. The working principle of a drift tube is shown in Figure 2.2. The antiprotons are decelerated by the electric field created by setting the tube at -99 kV. While the bunch reaches a local flat potential distribution inside the drift tube, the switch brings everything back to the ground, which prevents from reacceleration of antiprotons at the output of the decelerator. During the process, the electrostatic lenses before and after the drift tube focus the beam.

In the future, an antiproton trap will be added to the system to reach better beam parameters such as narrower energy distribution (smaller than $FWHM < 50$ eV) and shorter pulse length. The first parameter is crucial for the antihydrogen ion trapping efficiency in the Paul trap, see Section 2.3.1, while the shorter pulse length allows for better overlap between the positronium cloud and the antiproton beam, which results in higher antihydrogen ion production rate.

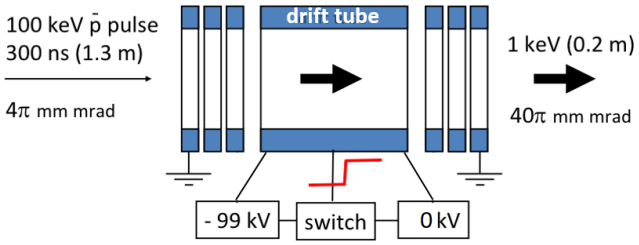

Figure 2.2: The principle of a drift tube operation. Figure taken from [65].

2.2.3 The slow positron source

The efficient production of antihydrogen atoms and ions requires a positron source with a beam intensity higher than 10^8 e^+/s. This intensity can be achieved only with the help of a nuclear reactor or an electron accelerator. The first option is not available at CERN, thus the GBAR experiment chose to use an electron linear accelerator (LINAC).

The GBAR electron accelerator is a compact device with 9 MeV beam energy. The relatively low energy was chosen to avoid activation of the environment with gamma radiation. The electron beam impinges on a tungsten target where positrons are created from Bremsstrahlung radiation (gammas) through the pair creation process. Some of the created positrons undergo a further diffusion in a tungsten moderator reducing their energy to about 3 eV. The particles are re-accelerated to about 53 eV energy and are adiabatically transported to the next stage of the experiment. Presently, the measured positron flux is at the level of 5×10^7 e^+/s.

2.2.4 Positron trapping

The goal of the GBAR experiment is to obtain more than 5×10^{10} e^+/pulse every 110 s. This bunch intensity has never been reached within such a short time. Presently, a two-stage trapping system is used.

The first device [66] is based on a Surko buffer gas trap. The main goal of this 40 mT magnetic field trap is to cool positrons and reduce their radial velocity [67, 68], so that they can be trapped for long time and even accumulated.

The GBAR buffer gas trap (BGT) is of the Penning-Malmberg type [69] in which cylindrical electrodes confine the beam axially while a magnetic field (maximum amplitude 80 mT) confines particles in the radial direction. The positrons are cooled through inelastic collisions with an appropriate buffer gas [70]. As the energy decreases, particles move towards a deeper potential well and further stage of the trap. In the end, they are trapped in the last stage where the beam energy spread after cooling is lower than a few tens of meV. The scheme of the GBAR buffer gas trap is shown in Figure 2.3.

The second device is another Penning-Malmberg trap with a high magnetic field of 5 T. In this trap, 5×10^{10} e^+ are going to be stored in the form of a non-neutral plasma. The study of this trap with electrons, performed by collaborators, has proven that possibility [71, 72]. Presently the positrons are cooled in the buffer gas trap. In the 5T, they can be further cooled by synchrotron radiation, but later the goal is to use an electron cooling technique [73]. At this time the measured positron flux after the trap is a few times 10^8 e^+/pulse.

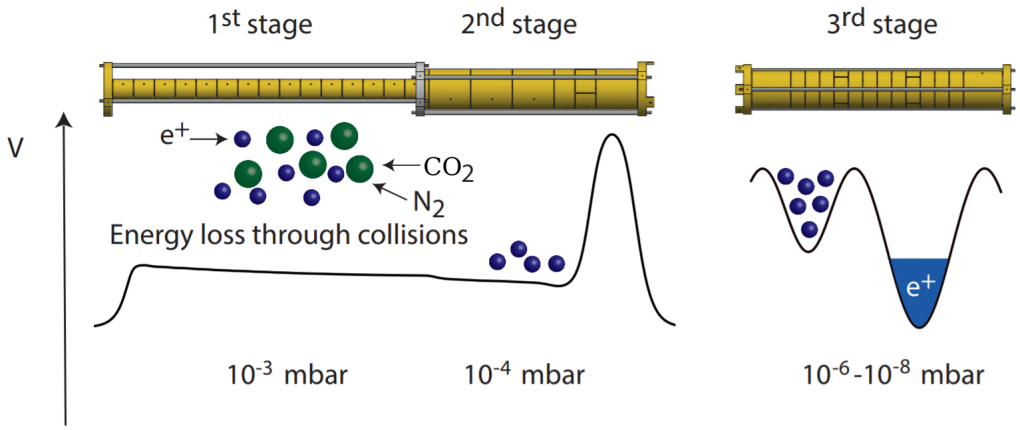

Figure 2.3: Illustration of an accumulation technique with a buffer gas trap. The positron beam comes from the left side of the picture. Positrons enter the trap and are cooled by inelastic collisions with a buffer gas (in this case nitrogen N_2) and cooling gas (CO_2). After a few collisions, they are trapped in the first stage and later in the second stage. Once they are cold enough they can be stored in the third stage where due to the low pressure the positron lifetime is much longer. Figure taken from [66].

2.2.5 Positronium formation and laser excitation

The production of the antihydrogen ion requires a cold (energy < 0.1 eV) dense positronium target. Cold positronium allows to keep it confined in a small cavity for a long time and decreases quenching probability from interactions with walls. It is produced by positron implantation in

a mesoporous silica target. This material allows to form Ps from a positron bound in a surface state in the material. The negative work function for positronium lets the Ps diffuse to the surface and create a Ps cloud inside the reaction cavity [74].

Positronium exists in two forms depending on the relative orientation of the electron and positron spins. The lifetime of the singlet state with antiparallel spins (para-positronium) is equal to 125 ps, which is too short to combine with antiprotons to produce antihydrogen atoms. However, the triplet state with parallel spins has a lifetime of 142 ns and can be used for ion production. The positron to ortho-positronium conversion efficiency for the mesoporous silica target is equal to 30 % [75, 76, 77]. The expected density of ortho-positronium for 5×10^{10} positrons incident on the target is equal to 7.5×10^{11} o-Ps/cm^3 density in the cavity volume $1\times\ 1\ \times\ 20$ mm^3.

According to calculations [78] the cross-sections for reactions 2.1 and 2.2 can be enhanced for excited states of o-Ps. This hypothesis will be tested for the 3D state of ortho-positronium.

2.2.6 Reaction chamber and detection system

The reaction takes place in a cavity of dimensions size $1\times\ 1\ \times\ 20$ mm^3. The largest dimension is along the direction of the antiproton beam. The size of the cavity is optimised for antihydrogen ion production. Notably, the length of the cavity is essential to allow for antihydrogen production and its interaction with o-Ps. The cavity must be located in a volume with low magnetic field in order to avoid quenching of the ortho-Ps state with spin component $S_z = 0$, which could decrease the total ortho-positronium cloud lifetime [79]. Additionally, a magnetic field perturbs the trajectories of the antiprotons, which is a significant problem at energies close to 1 keV.

After the reaction a beam composed of three species $\bar{\mathrm{p}}$, $\bar{\mathrm{H}}$ and $\bar{\mathrm{H}}^+$ is electrostatically separated into three different directions, whereupon each beam is guided to a dedicated detection system.

2.2.7 Lamb shift experiment

Just after the reaction chamber an additional experimental setup is added to the system, which aims at measuring the Lamb shift of the antihydrogen atom and determine the antiproton radius [80]. A scheme of the experiment is presented in Figure 2.4. First, the antihydrogen beam enters a microwave field region where antihydrogen 2S states are selected (HFS selector). Then, in the second microwave field region, the 2S to 2P transition is induced. The 2P state deexcite to the ground state within 1.6 ns, which is detected by the Lyman alpha detector. The measurement of the quenched fraction of antihydrogen atoms as a function of microwave frequency allows to determine the Lamb shift of antihydrogen atoms. It is then possible to determine the antiproton radius through the relation $\Delta E = \frac{1}{12}\alpha^4 m_r^3 r_{\bar{p}}^2$ with precision reaching 10%.

2.3 Antihydrogen ion cooling and free fall experiment

The second part of the experiment is designed to catch and cool the antihydrogen ion. Once it reaches neV energy, the extra positron is photodetached, and the neutral, cold antihydrogen

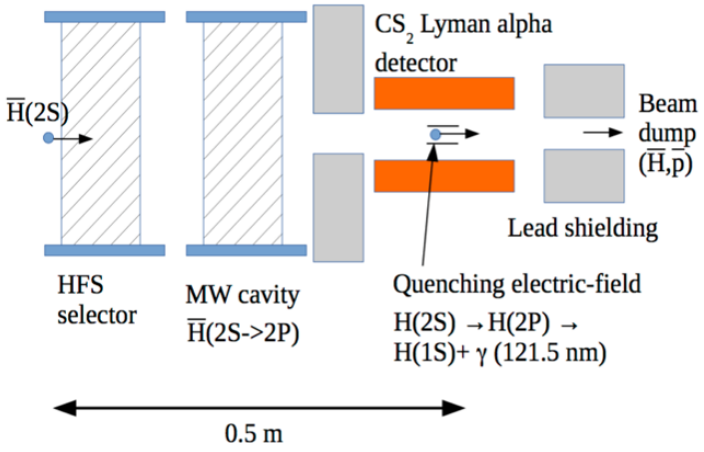

Figure 2.4: Scheme of the Lamb shift measurement. Figure taken from [80].

atom starts to fall. The scheme of the second stage of the GBAR experiment is shown in Figure 2.5.

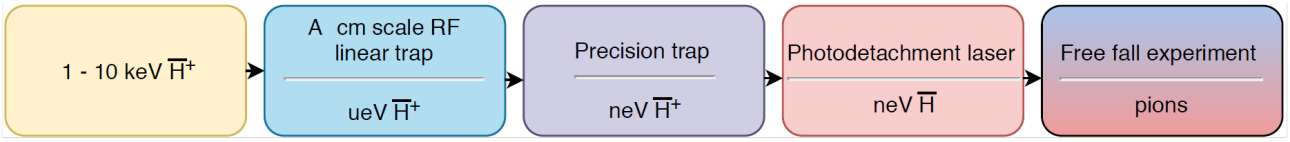

Figure 2.5: General scheme of the antihydrogen ion cooling and free fall experiment.

2.3.1 $\bar{H}^+$ capture and cooling

The first step of the ultracold $\bar{H}^+$ preparation is to catch it in a cm scale RF linear trap, see Figure 2.6. It is not possible to directly trap an ion of a few keV energy, this is why it is first decelerated in the electrostatic field of the RF linear trap, which is biased accordingly to the ion energy. Once the $\bar{H}^+$ energy is in the order of a few eV it can be trapped. The energy dispersion of the antihydrogen ion beam must be less than 20 eV to exceed 50% trapping efficiency. The energy spread of the anti ions is transferred from the antiproton beam. In ELENA this is of the order of 300 eV. Thus, an antiproton trap will be inserted just after the antiproton decelerator to reduce this energy dispersion and in the end, increase the antihydrogen ion trapping efficiency.

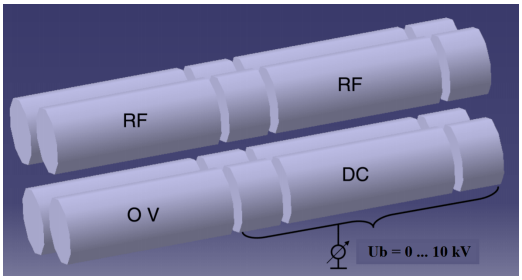

Figure 2.6: Quadrupole guide and biased linear RF Paul trap used to decelerate and trap $\bar{H}^+$. The central trap electrode length L is 30 mm. The trap can decelerate particles of energies between 0 and 10 keV. Figure taken from [81].

The antihydrogen ion does not have a transition allowing for direct laser cooling. In the first RF linear trap it will be cooled by interaction with a cloud of simultaneously trapped and laser-cooled beryllium ions Be^+. In this procedure, the final temperature is higher than the Doppler limit (e.g. 0.47 mK or 60 neV in the case of Be^+), but can go down to 5-100 mK range. It is reached within a few ms [82]. Once the antihydrogen ion is cold, it is injected into the precision RF trap where a single Be^+ ion is also trapped. In the precision trap the cold Be^+ and $\bar{H}^+$ ions are coupled harmonic oscillators on which ground state Raman sideband cooling can be performed [83]. This method allows for the reduction of vibrational energy levels. As a result, μK temperatures can be reached in less than 1 s. Both cooling methods were successfully tested by collaborators in dedicated traps with other ion species such as H_2^+ or Sr^+.

When the antihydrogen ion is cold, one of its two positrons can be photodetached by a 1.64 μm laser. This moment defines the start of the free fall measurement.

2.3.2 The free fall experiment

The final free fall experiment takes place in the so-called "free fall chamber", see Figure 2.7. It is a cylindrical chamber with at max 10^{-11} mbar pressure. The chamber is surrounded by detectors which measure the tracks of charged pions from the antihydrogen annihilation. They are able to reconstruct the antihydrogen annihilation vertex in four dimensions. Two types of detectors are used:

- tracker detectors - 50 cm by 50 cm MicroMegas chambers with a pion detection efficiency better than 96% per plane [84];
- 170 cm by 10 cm by 5cm Time of Flight Detectors built from scintillator bars. The time resolution of these detectors is better than 80 ps.

The first detector units were successfully tested with cosmic radiation and antiproton annihilations.

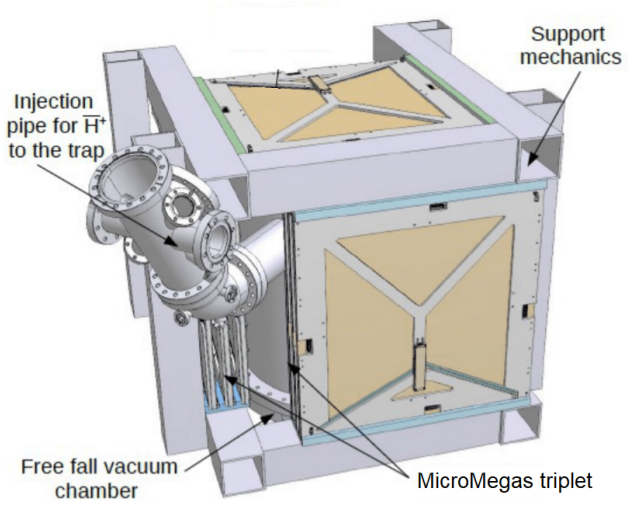

Figure 2.7: Sketch of the free fall chamber.

Measurement uncertainty

The classical measurement of the free fall requires information about the initial time t_0, position z_0, velocity in the direction perpendicular to the Earth surface v_{z0}, and final time t_1 and position z_1 of the particle's motion. With this information, the antihydrogen gravitational acceleration $\bar{g}$ can be calculated using:

$$z_1 - z_0 = \frac{1}{2}\bar{g}(t_1 - t_0)^2 + v_{z0}(t_1 - t_0).$$

The precision on $\bar{g}$ depends on the measurement precision of those 5 parameters. The initial parameters of the free fall are defined by the movement of the antihydrogen ion in the Paul Trap. In such a trap the initial position z_0 is known within a few μm. The precision on the start time t_0, defined by the photodetachment process, is better than 150 μs. The energy distribution is known within a few μeV precision. The final parameters of the free fall are defined by the position of the antihydrogen annihilation. As $\bar{\mathrm{H}}$ annihilates with the production of 2-4 charged pions of about 300 MeV energy, it is relatively easy to detect the annihilation point on the bottom plate with $\Delta z_1 < 100$ μm ($\Delta z_1 < 1$ mm on the side plates) and $\Delta t_1 < 100$ ps. The last parameter is v_{z0}. Its value is defined by the $\bar{\mathrm{H}}^+$ energy in the trap and the energy kick obtained during photodetachment. The uncertainty for these parameters sums to the initial velocity error equal to $\Delta V_{z0} = 0.3$ m/s. The overall uncertaintity is equal to 37 % for one measurement and 1 % after 1500 tests [33].

The second stage of the experiment would be to perform the measurement of the gravitational quantum states of cold antihydrogen [59]. This method can reach $10^{-5} - 10^{-6}$ precision. At that moment, there is only one other method which could allow to obtain equal measurement precision. It is using an interferometer and could be adapted for the ALPHA experiment [85].

2.4 Presentation of the thesis ouline

The thesis focuses on the optimisation of the production and detection of the antihydrogen atoms and ions for the GBAR experiment. This is done by studying how to measure the cross-sections. Additionally, Chapter 3 describes the GBAR slow positron source, which characterisation and maintenance was also a responsibility of the author of the thesis. In Chapter 4, the existing theoretical calculations of the cross-section values are summarised. They are essential in order to define the expected minimum experimental requirements, like for example, the minimum number of antiprotons and positronium atoms. Then, the parameters which have to be measured are predefined by looking at the general method of how to extract the cross-section values within the GBAR framework. In Chapter 5, the reaction cavity is introduced together with all detectors available to characterise the positronium - antiproton mixing procedure. The expected antihydrogen atom and ion production rate is calculated using simulations. As will be shown, less than one antihydrogen ion is expected to be formed per one antiproton bunch. The detection of such a small signal requires a very well designed detection system which would allow to minimise all possible backgrounds. The primary source of background which could spoil the experiment comes from the antiproton annihilations in different parts of the experiment. In order to introduce this problem, Chapter 6 contains a general description of the antiproton annihilation in matter. In Chapter 7, an antiproton transport from ELENA to the antiproton dump is described. It is focused on the background reduction problem. In the last Chapter,

the antiproton, antihydrogen atom, and ion detection system is described together with an expected background estimation.

Here is a summary of the following chapters:

Chapter 3 A study of the slow positron source based on an electron linear accelerator. It contains the preparation of the positron beam and its characterisation.

Chapter 4 An introduction to the cross-section measurement. It includes a description of available theoretical calculations and a general description of how to obtain the cross-section values from the experiment.

Chapter 5 A summary of the expected antihydrogen atom and ion production rate in dedicated experiments.

Chapter 6 A description of the antiproton annihilation process in matter. This summary introduces possible problems resulting from secondary particles created during the detection of antiprotons, antihydrogen atoms or ions.

Chapter 7 A summary description of the antiproton transport up to the reaction chamber level and a motivation and a design of the antiproton, antihydrogen atom and ion transport system after the reaction chamber.

Chapter 8 A description of the antiproton, antihydrogen atom and ion detection system together with an estimation of the background in chosen experimental conditions.

Chapter 9 A summary of the thesis.

Chapter 3

Slow positron source

3.1 Introduction

The positron is the lightest and the easiest antiparticle to produce. It does not occur naturally in stable systems thus it is very interesting from a scientific point of view. Moreover, it has applications in industry and medicine (for example positron-emission tomography - PET [86]). In nature, positrons are produced in the β^+ decay of proton-rich isotopes, $p \rightarrow n + e^+ + \nu_e$, and in the interaction of high energy γ rays with matter through the pair production process.

In antimatter physics, it is important to have a high-intensity stable positron beam. It can be achieved in three ways [87]. The most popular way is to use a radioactive source, for example ^{22}Na. Such sources are artificially produced with a maximum activity of few tens of mCi available commercially. They have a 2.6 years half-life. The beta particle occurs in 90% of all ^{22}Na decays with energy between 0 and 543 keV. Due to this wide energy distribution, the primary beam has to be moderated in order to obtain a monoenergetic beam. With sodium sources, it is possible to obtain up to $\approx 10^7$ e^+/s after moderation.

The most intense positron beams are obtained from the intense flux of neutrons and gammas at research nuclear reactors, reaching 10^9 e^+/s [88]. Incident neutrons hit a target made from for example cadmium, where 9 MeV gammas are produced in the neutron capture reaction, $^{113}Cd + n \rightarrow^{114} Cd + \gamma$. Photons reach a platinum or tungsten converter in order to induce the positron-electron pair creation. Either directly in the conversion target or in an additional moderator, the positrons undergo a moderation process in order to obtain a monoenergetic beam.

The third method is based on accelerators, for example an electron accelerator. Electrons hit a dense target and produce bremsstrahlung gammas, which may convert in an electron-positron pair in a dense target if their energy is greater than 1.022 MeV. An example of a source of that type is AIST in Japan, where it is possible to produce a moderated beam of $2 - 3 \times 10^7$ e^+/s [87].

3.2 GBAR slow positron source

The slow positron source for the GBAR experiment is a multi-stage device. Its general scheme is presented in Figure 3.1. The first part is an electron linac, which accelerates electrons to 9 MeV energy onto a tungsten target where positrons are created from Bremsstrahlung radiation (gammas) through the pair creation process. The cross-section for pair creation is proportional

to the logarithm of the gamma energy $\sigma_{pp} \sim ln(E_\gamma)$. Some of the produced positrons undergo a further diffusion in the tungsten moderator reducing their energy to about 3 eV at the emission from the material. The gammas previously created in the primary target interact with the tungsten moderator producing more slow positrons.

The created particles are adiabatically transported to the positron traps. A destructive beam diagnostics station is placed right upstream the traps in order to measure the beam properties.

The whole process of positron production is accompanied by a high-intensity gamma radiation, which, due to its low energy (below 10 MeV), does not activate the surrounding environment. This feature makes it a unique and relatively easy to handle device, although, it produces almost 16 MGy/year (1 year = 100 days of 24h work) radiation.

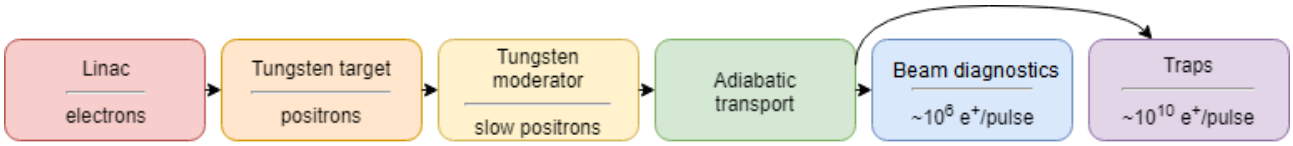

Figure 3.1: General scheme of the slow positron production line.

3.3 Electron linac

The production of positrons is based on a low energy, compact linear electron accelerator (*linac*) made by NCBJ (english *National Centre for Nuclear Research*), Poland. Its general scheme is presented in Figure 3.2 and the nominal working parameters are listed in Table 3.1.

The linac electron source is a triode gun. The electrons are guided by a 59 mT magnetic field to the standing wave bunching and accelerating structure. After acceleration, the linac produces a 9 MeV electron beam with 5.9×10^{12} particles per bunch within 2.85 μs at 300 Hz repetition frequency.

Parameter	**Value**
Energy	9 MeV
Number of e^-/bunch	5.9×10^{12}
Repetition frequency	300 Hz
Beam power	2.5 kW
Average current	0.28 mA
Peak current	330 mA
Pulse length	2.85 μs

Table 3.1: Electron linac nominal working parameters.

The measured characteristics of the electron beam are:

- the beam energy has a distribution with a mean energy $\mu_{Ee^-} = 9$ MeV and $FWHM_{Ee^-} = 0.5$ MeV, see Figure 3.3;
- the beam spot size in a plane perpendicular to the beam direction is $FWHM_x < 2.5$ mm, $FWHM_y < 2.5$ mm.

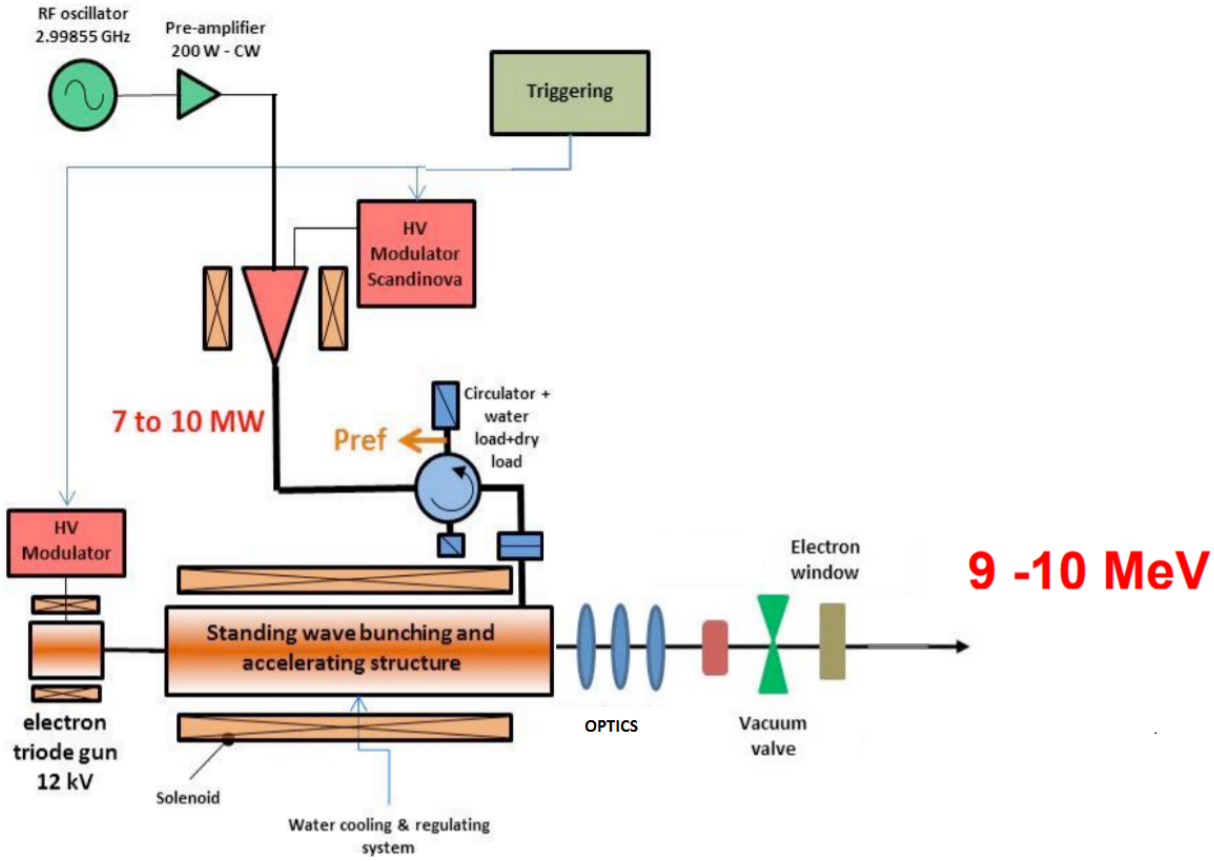

Figure 3.2: General scheme of the electron linac.

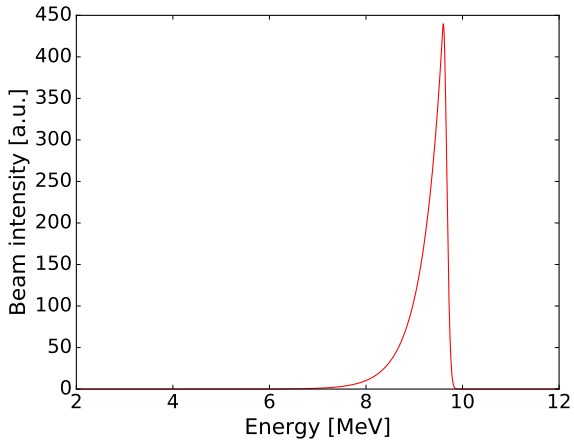

Figure 3.3: Measured energy distribution of the electron beam.

3.4 Positron production

The electron beam is incident on a water-cooled tungsten target where positrons are produced through Bremsstrahlung radiation and pair production. The positron beam has an energy distribution of up to a few MeV. It is moderated to a few eV energy using a tungsten mesh. In

order to perform a better transport, the slow positron beam can be accelerated to reach energy up to tens of electronvolts. The scheme of the system is presented in Figure 3.4.

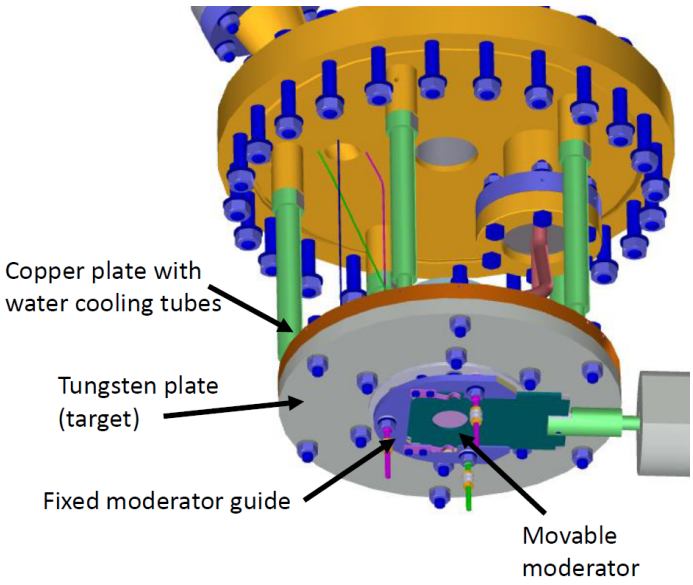

Figure 3.4: Scheme of the slow positron generator.

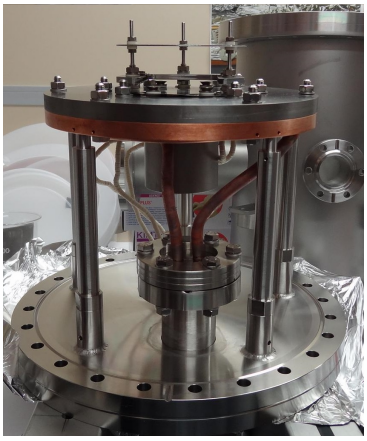

(a) Tungsten target together with the water cooling system.

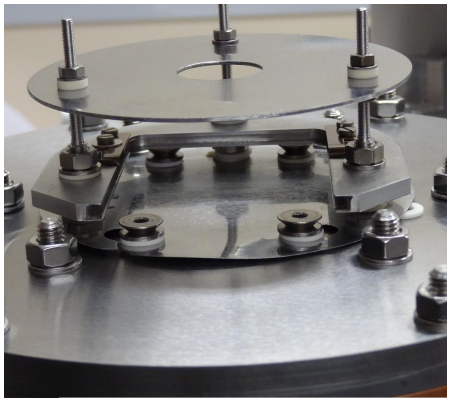

(b) Tungsten target with the support for the tungsten mesh and the accelerating electrode.

Figure 3.5: The slow positron generation system.

3.4.1 Tungsten target

The cross-section for electron-positron pair production for a given element is proportional to the square of the atomic number Z, $\sigma_{pp} \sim Z^2$. Thus, for positron production, elements like Ta, W and Pt are selected. In the present case tungsten was chosen due to its high melting point.

The target absorbs 1450 W of heat deposited by the electron beam, thus it is cooled by water through a copper plate attached to the tungsten target, see Figure 3.4 and Figure 3.5a. The copper plate is hollow in its center in order to allow electrons to hit directly the centre of the tungsten target, where the material is 1 mm thick. The selected thickness of the target

is a compromise between the positron production rate in the material, an efficient emission of positrons from the material and target cooling [89]. It was chosen based on the simulation described in Section 3.5.

The support for the moderator is placed at the back side of the target. Its construction allows for an easy replacement of the moderator. An annular electrode of 20 mm internal diameter is attached to the support in order to accelerate positrons. This electrode defines the maximum size of the beam.

3.4.2 Moderator

In order to produce a monoenergetic beam adequate for trapping from the fast positrons and gammas created in the target, solid state metal moderators with a negative positron work function Φ^+ or solid rare gases (for example neon) can be used [90]. The work function is equal to the minimum energy necessary to remove a positron from the material. It is equal to the value of chemical potential and the surface dipole potential. Due to the fact that positrons have an opposite charge to electrons, the surface dipole potential has a repulsive character. In some cases, it is larger than the chemical potential, and then the work function is negative.

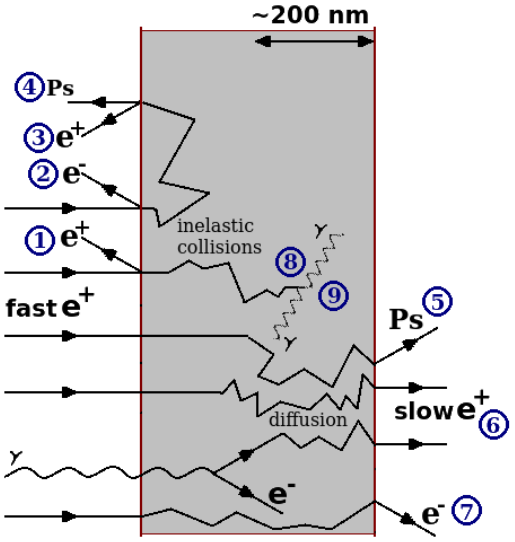

Figure 3.6: Positron interaction with matter. 1-2) Reflection or diffraction of positrons with secondary electron emission. 3-4) Emission of non thermalised positrons and positronium. 5-7) Emission of moderated positrons or thermally desorbed Ps after thermalisation and diffusion processes. Annihilation on the surface may produce Auger electrons and X-rays. 8-9) The thermalised positron can annihilate in the material, after being trapped in the material defects or from the delocalised state in the lattice. Figure adapted and changed from [91].

The interaction of positrons with matter is schematically shown in Figure 3.6. Some of the implanted positrons thermalise in the material within a few picoseconds and can diffuse to the surface of the material. The absolute value of the energy of such positrons corresponds to the value of Φ^+, which for tungsten is equal to $\Phi^+_W = -3$ eV [92]. The simulated energy distribution of positrons before the moderation on the tungsten mesh is presented in Figure 3.7. For such a wide energy distribution of the incident positrons, the moderation/transmission efficiency is smaller than 10^{-3}, which is a typical moderation efficiency for positrons originating from Na^{22}.

In order to keep a high efficiency, the surface of the moderator should be free of contamination. Additionally, to decrease the positron loss in defects of the material, the moderator can be annealed at a temperature usually between 1800-2500 C°.

The tungsten moderators are relatively easy to handle. They are produced as a foil or a mesh. According to the literature, mesh moderators give approximately 10 times more moderated positrons (e.g. [93]).

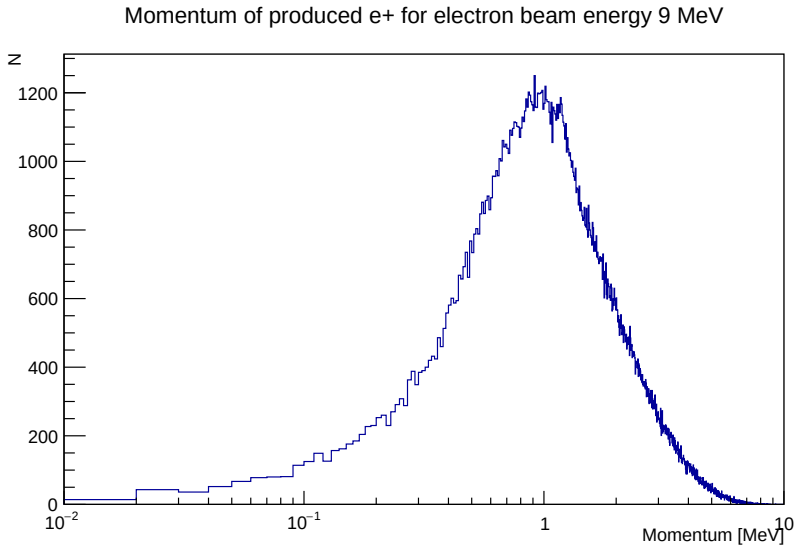

Figure 3.7: Simulated momentum spectrum of positrons produced by a 9 MeV electron beam in the tungsten target (before moderation).

The GBAR moderator is made of 12 layers of an annealed tungsten mesh with wires of 20 μm diameter. The mesh has 150 wires per inch. The number of meshes was optimised in a similar system (description in Section 3.5.4) with an electron beam of 4.3 MeV energy [94]. The moderator is joule heated with 900-1200 W for about 30 minutes with a maximum pressure better than 1×10^{-6} mbar. This process allows to prepare and clean the surface. Without it, the slow positron production rate would be close to zero. The size of the moderator is about 20 mm by 20 mm. In order to protect the surface from water pollution and oxidation, which can drastically change moderator properties, it has to be kept in vacuum. However, the moderators have been shortly exposed to air during transfer between the annealing chamber and the storage container, and the storage container and the electron target chamber. Examples of moderators are shown in Figure 3.8.

During the experiments, moderators made with 20 μm thick tungsten meshes were used. The original distance between the moderator and the target was 10 mm, Figure 3.8a. However, in order to increase the geometrical acceptance the mesh was moved to 2 mm from the target, Figure 3.8b. All presented measurements were performed using the second configuration.

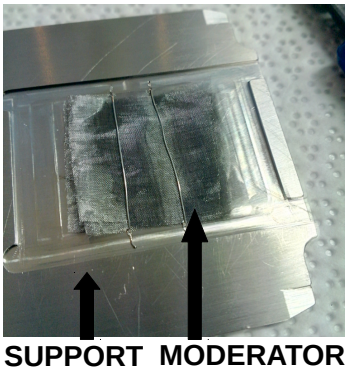

(a) Mesh 10 mm from the target.

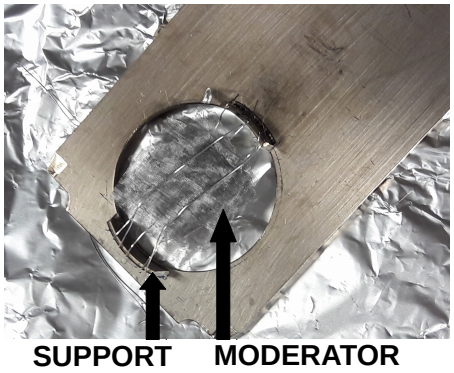

(b) Mesh 2 mm from the target.

Figure 3.8: Tungsten meshes used for the experiment.

3.5 Simulation of the production of positrons

The transmission efficiency $J(d)$ of the tungsten moderator with a thickness d can be described by the 1-dimensional diffusion model evaluated by A. Vehanen and J. Mäkinen [95]. The simplified model describes the diffusion process in an exponential form [93]. The transmission efficiency of a moderator in that model is equal to:

$$J(d) = Y_0 \int_0^d P_{1D}(z) \cdot e^{\frac{-(d-z)}{L_+}} dz$$

where

- $Y_0 = 0.33$ is the probability that the positron will be emitted from the tungsten surface as a slow positron [96];
- $L_+ = \sqrt{D_+ \cdot \tau_{e^+}} = 1350 = 0.135$ μm is the diffusion length [95]. D_+ is the material dependent diffusion coefficient and $\tau_{e^+} \approx 100$ ps is the positron lifetime;
- $P_{1D}(z)$ is the implantation profile of fast positrons.

This model assumes that positrons after thermalisation diffuse to the surface in the same z direction. It leads to an underestimation of the total interaction length between the positron and the moderator material, as the real positron diffusion is isotropic. The more realistic direction of the positron can be parametrised using a polar coordinate system with angles $\phi \in [0, 2\pi)$ and $\theta \in [0, \pi)$, see Figure 3.9. After the correction for isotropic positron diffusion the transmission efficiency is equal to [93] (after integration over ϕ):

$$J(d) = Y_0 \int_0^d P_{3D}(z) \left(\frac{1}{2} \int_0^{\pi/2} e^{\frac{-(d-z)}{L_+ \cos\theta}} \sin\theta d\theta \right) z^2 dz$$

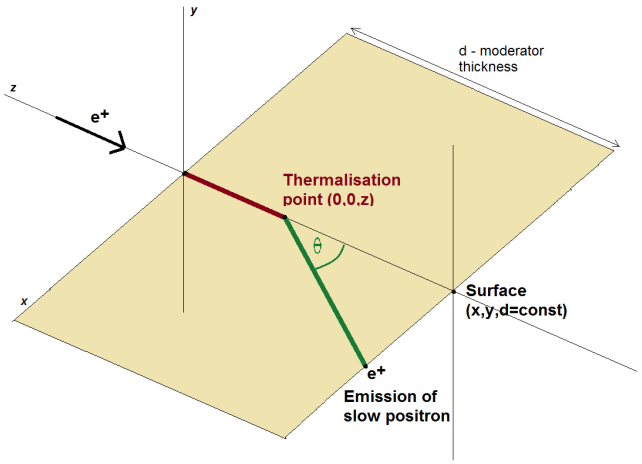

Figure 3.9: A simplified slow positron emission scheme from the moderator of thickness d.

In the presented simulation, the main source of particles is an electron linac. The implantation profile of slow positrons is simulated in Geant4. The simulation software keeps tracks of particles down to 10 eV energy, which is not far from the thermalisation point. Thus, the annihilation profile of positrons simulated in Geant4 can be used as a good approximation of the implantation profile. In all following simulations, the beam is propagating in the positive z-direction. The next step is to calculate the probability of transmission efficiency for each thermalised positron:

$$P_t = \frac{Y_0}{2} \int_0^{\pi/2} e^{\frac{-(d-z)}{L_+ \cos\theta}} \sin\theta d\theta$$

where d indicates the z-coordinate of the surface of the material and z is the z-coordinate of the thermalisation point.

The total number of moderated positrons is equal to:

$$N_{e^+} = \sum_i P_t^i$$

where

- P_t^i is the probability that a created thermalised positron with index i diffuses as a slow positron.

The overall slow positron production efficiency is equal to:

$$\eta_{e^+} = \frac{N_{e^+}}{N_{e^-}}$$

where N_{e^-} is the number of incident electrons.

The presented approximation is valid for the moderator in the form of a thin foil. According to the literature, mesh moderators give approximately 10 times higher number of moderated positrons (e.g. [93]) in measurements with ^{22}Na source. It is not clear if that factor is the same for an accelerator based positron sources, that is why it is not included in the simulation. It is recommended to test it experimentally.

Another effect which may change the number of slow positrons is the heating of the target and moderator. It is not included in the simulation, however, measurements show that the number of slow positrons decreases linearly with increasing temperature [97], which is caused by positron trapping in thermally induced defects, higher positronium formation rate and a variation with temperature of the positron diffusion length. The simulation is then valid for low temperatures, i.e. small linac repetition frequencies.

Additionally, the gamma radiation accompanying the positron production creates defects in the tungsten material. Effectively, the diffusion length L_+ of the irradiated tungsten is smaller than 0.135 μm as supposed in the simulation. Due to the lack of measurement, this effect is not included in the simulation. It is not sure if the value of 0.33 for Y_0 is correct since it depends strongly on the surface conditions.

3.5.1 Simulation of the slow positron production for the linac at CERN

The following parameters for the simulation of the slow positron production are used:

- Tungsten target:
    - 10 mm thick disk with radius 95 mm;
    - in the centre of the disk a cylinder of radius 2.5 mm and 9 mm length is emptied, leaving a 1 mm thick disk of the same radius as the effective target.
- Tungsten mesh:
    - moderator size 50 mm by 20 mm (the simulated moderator is larger than the one used in the experiment, but it does not change the result, as the positron beam is collimated after the emission);
    - the 12 layers of a 20 μm thick annealed tungsten mesh were replaced with a tungsten plate;
    - the distance between the target and the moderator is 2 mm;
    - after the moderator there is a 20 mm diameter collimator.
- Electron beam:
    - the beam energy has approximately a Gaussian distribution with $\mu_{Ee^-} = 9$ MeV, $\sigma_{Ee^-} = 0.2$ MeV;
    - the spatial distribution in the plane perpendicular to the positron beam is flat over a disk of radius 1 mm;
    - number of electrons: $N_e = 10^7$.

A simulated positron implantation profile is presented in Figure 3.10. The main target is placed between z=5 mm and z=15 mm. The 1 mm thick part of the target starts at z=14 mm. The moderator is placed at z=17 mm. The number of moderated positrons calculated using the model described earlier is equal to $N_{e^+\_(9MeV)} = 0.8$. The slow positron production efficiency is equal to $\eta_{(9MeV)} = N_{e^+\ (9MeV)}/N_e = 8 \times 10^{-8}$.

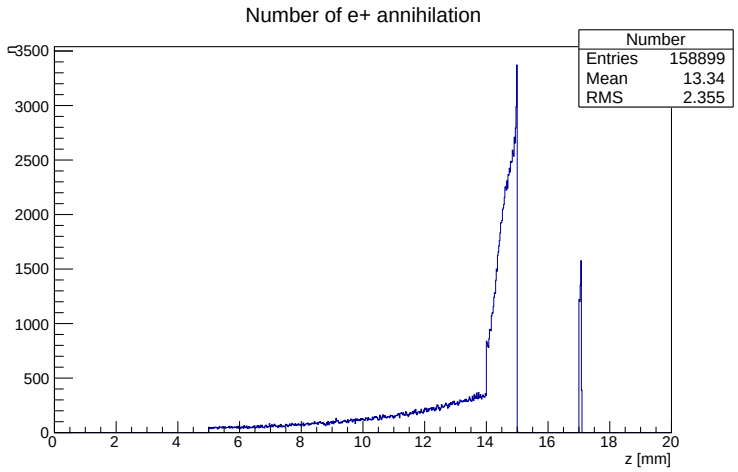

Figure 3.10: Number of positron annihilations as a function of the distance z. Simulation of the final system for 9 MeV electron beam energy.

3.5.2 Slow positron production simulation - target thickness

The thickness of the tungsten target is a compromise between the gamma and the positron production rate and an efficient moderation. In order to estimate the slow positron production as a function of the target thickness, the number of positron annihilations is calculated as a function of the distance z between the electron beam source and the annihilation point.

Simulation parameters:

- Target:
  - 20 mm by 50 mm square target, 6 mm thick (between $z = 4$ mm and $z = 10$ mm, it is an arbitrary number);
  - material: tungsten.
- Electron beam:
  - the beam energy has an approximately Gaussian distribution with $\mu_{Ee^-} = 9$ MeV, $\sigma_{Ee^-} = 0.2$ MeV;
  - the spatial distribution in the plane perpendicular to the positron beam is flat over a disk of radius 1 mm;
  - number of electrons: 10^6.

The results of the simulation are presented in Figure 3.11. Due to the very short diffusion length of positrons in tungsten, only positrons that thermalise within the last few hundreds of nanometers may leave the surface. Thus, the maximum of the positron implantation profile in the target defines its optimum thickness. In the present case, the positron annihilation (positron implantation profile) reaches its maximum for $z \approx 5$ mm, which corresponds to a 1 mm thick tungsten target.

A more detailed simulation to study the optimisation of the target thickness for the system at CERN is based on the geometry described in 3.5.1 In order to have a good statistical error the total number of positrons annihilating in the last 20 μm of the moderator is summed. This

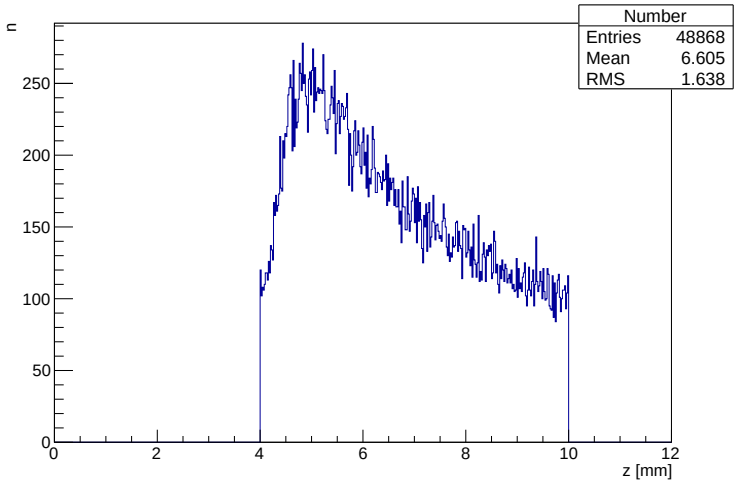

Figure 3.11: Number of positron annihilations as a function of the distance z - a positron implantation profile.

approximation does not give an absolute number of moderated slow positrons. Each simulation was performed with 10^7 electrons. The distance between the moderator and the target is fixed and the target thickness is varied between 0.6 and 1.2 mm. In Figure 3.12 the red points show the results for a 2 mm distance between the target and the moderator. The green points were obtained with 0.3 mm distance between the moderator and the target. Both curves show that the slow positron production saturates between 0.8 and 1.1 mm target thickness. The general shapes of both curves are very similar, however, the production of positrons is higher by 30 % in the second case. The change of the moderator position could largely increase the positron yield. The maximum positron production is achieved for 1 mm to 1.1 mm target thickness.

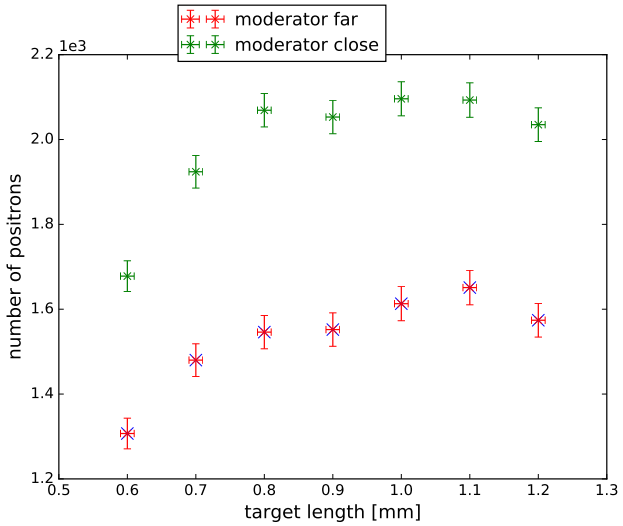

Figure 3.12: Number of annihilating positrons in the last 20 μm of the tungsten moderator as a function of the target thickness. The red/green points shows results for the 2/0.3 mm distance between the target and the moderator.

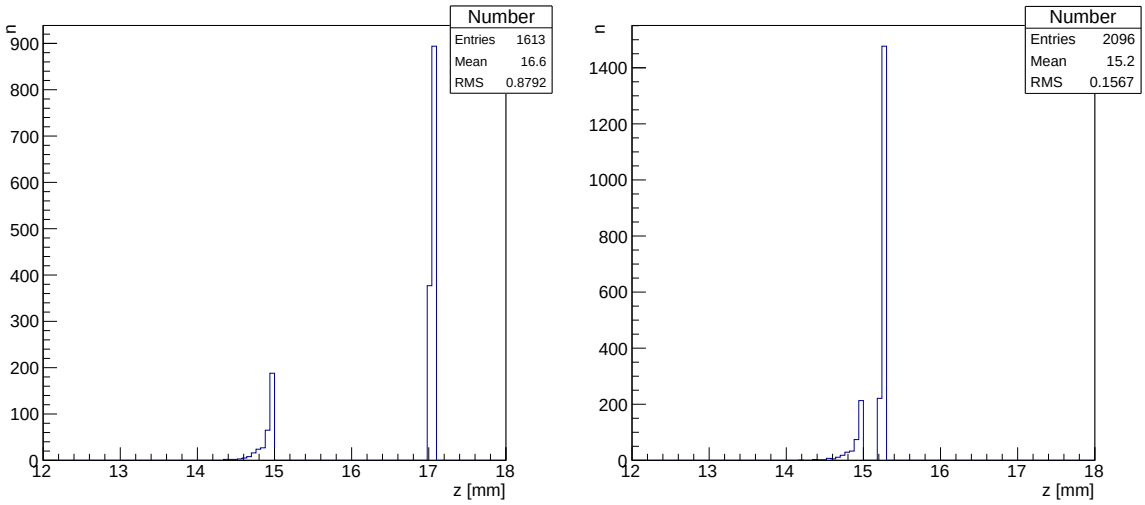

Figure 3.13: Distribution of the z-coordinate of the origin of positrons annihilating in last 20 μm of the moderator. The target is placed between 14 and 15 mm. Left: moderator placed 2 mm from the target, z=17 mm. Right: moderator placed 0.3 mm from the target, z=15.3 mm.

The distribution of the z-coordinate of the place of origin of the positrons annihilating in the last 20 μm of the moderator is shown in Figure 3.13. For both positions of the moderator, about 20 % of the selected positrons are created in the target and 80 % in the moderator. The 30 % difference in the slow positrons flux for two moderator positions is an effect of the angular distribution of gammas emitted from the target surface combined with the interaction path of positrons with the moderator.

3.5.3 Positron production rate as a function of electron energy

The simulation from Section 3.5.1 was repeated for different electron beam energies in the range from 1 MeV to 13 MeV. For all energies the same beam energy spread was used, $\sigma_{Ee^-} = 0.2$ MeV. The results are presented in Table 3.2 and in Figure 3.14. The number of produced slow positrons increases exponentially with the mean beam energy. In principle, the 10 MeV beam energy would increase the positron production rate by 20 %. At the moment it is not possible to increase the energy to 10 MeV due to safety reasons related to the activation of the surrounding environment.

electron beam energy	number of slow e^+	efficiency η
3 MeV	0.1	1×10^{-9}
5 MeV	2	2×10^{-8}
7 MeV	5	5×10^{-8}
9 MeV	8	8×10^{-8}
11 MeV	15	1.5×10^{-7}
13 MeV	18	1.8×10^{-7}

Table 3.2: Simulation of the CERN positron production system - number of positrons as a function of electron beam energy.

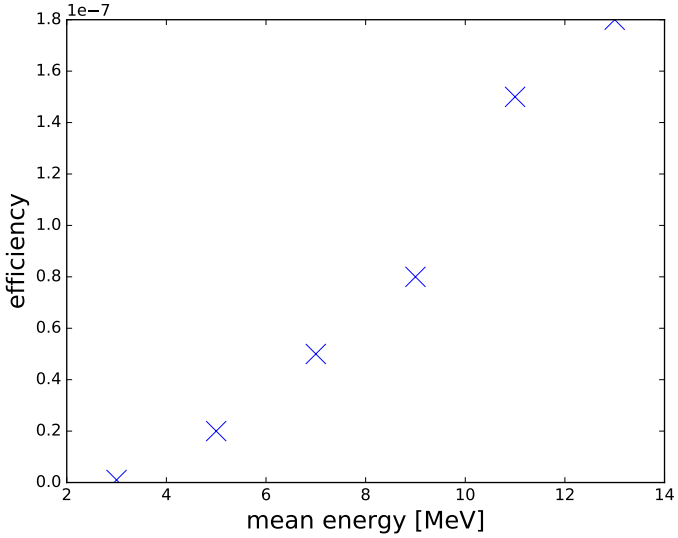

Figure 3.14: Simulation of the CERN positron production system - number of positrons as a function of electron beam energy.

3.5.4 Simulation of the slow positron production for the linac at CEA

The positron production was previously tested with an electron linac in CEA (fr. *Commissariat à l'énergie atomique et aux énergies alternatives*), Saclay. Electrons are incident on a 1 mm thick tungsten plate attached to a 5 mm thick cooling plate, which has a one inch diameter hole to let positrons go through. The moderator is attached to the other side of the plate on a metal grid. The conversion target, the cooling plate and the holder for the moderator are shown in Figure 3.15.

Figure 3.15: Photograph of the CEA positron production setup.

- Tungsten mesh:
    - moderator size 50 mm by 20 mm;
    - 12 layers of a 20 μm thick annealed tungsten mesh were replaced with a tungsten plate;
    - the distance between the target and moderator is 5 mm.
- Electron beam:

- the beam energy has approximately a Gaussian distribution with $\mu_{Ee^-} = 4.3$ MeV, $\sigma_{Ee^-} = 0.2$ MeV;
- the beam spatial distribution in XY plane is a disk with 1 mm radius;
- number of electrons: $N_e = 10^8$.

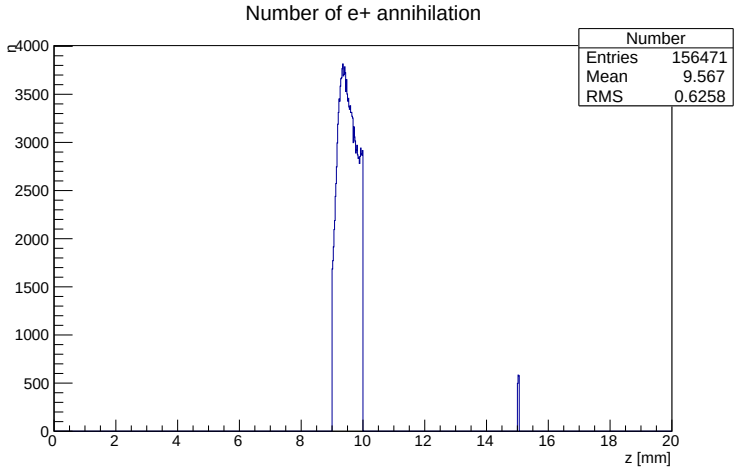

Figure 3.16: Simulation of the CEA positron production setup - results for 10^8 electrons.

The implantation profile for positrons is presented in Figure 3.16. The number of moderated positrons is equal to $N_{e^+\_(CEA,4.3MeV)} = 1.0$. The slow positron production efficiency is equal to $\eta_{(CEA,4.3MeV)} = N_{e^+\_(CEA,4.3MeV)}/N_e = 1.0 \times 10^{-8}$.

3.6 Adiabatic transport

Measurements of the slow positron flux were performed in order to characterise the performance of the systems and to compare it with the simulations presented above. It is not possible to measure the small positron signal close to the production target, which is inside the radiation shield (bunker of 1.2 m thickness with 30% of iron), because the electrons that have not produced positrons and the gammas are much more numerous and create an insurmountable background. The slow positrons are thus transported outside the bunker toward an analysis station.

The positron beam is transported from the moderator to the buffer gas trap using a magnetic field. The motion of particles is considered in two dimensions, parallel and perpendicular to the magnetic field. The parallel component does not depend on the magnitude of the magnetic field, while the perpendicular component is related to a cyclotron motion characterised by the cyclotron frequency $\Omega_c = qB/m$, where q/m is the particle charge over mass ratio and B is the magnetic field value. As a result, particles are propagating uniformly along the magnetic field and simultaneously circulate in the perpendicular plane. The radius of the cyclotron motion is equal to $r_c = v_\perp/\Omega_c$, where $v_\perp$ is the velocity perpendicular to the magnetic field.

In order to force the guiding center of the cyclotron motion of a particles to follow the magnetic field lines, the transport has to be adiabatic, i.e. the following inequalities have to be fulfilled [98]:

$$r_c \ll \left| \frac{B}{\nabla B} \right|, \tag{3.1}$$

$$\Omega_c \gg \left| \frac{\partial B}{\partial t} \frac{1}{B} \right|. \tag{3.2}$$

The positron beam in the GBAR experiment is transported adiabatically. In the 8 mT transport magnetic field the cyclotron frequency is $\Omega_c = 1.4$ GHz. Under an assumption that the energy related to the $v_\perp$ is $E_\perp = 1$ eV, the radius of the cyclotron motion is $r_c = 0.3$ mm. The change of the magnetic field in the system is smaller then 30 % over 10 cm, which gives the following relation for inequality 3.1, $r_c = 0.3$ mm $\ll 0.3$ m. The second inequality is also fulfilled. The time of flight of a 50 eV positron through a 10 cm long magnetic field interruption is equal to about 30 ns. This result in $\Omega_c = 1.4$ GHz $\gg 10^7$ Hz.

The scheme of the system is presented in Figure 3.17. The continuity of the transport field is assured by 8 guiding (POS:COIL), 8 deflecting (POS:DF) and 3 correction (POS:CF) coils. All currents in the guiding coils are optimised to have about 8 mT transport magnetic field and the highest beam intensity at the location of the diagnostics target. Additionally, it is possible to change the magnetic field in the primary target region using coils LIN:COIL-005 and LIN:COIL-006. This could be a useful feature in order to prevent the magnetic mirror effect at the entrance of the buffer gas trap. For most of the measurements, the magnetic field at the target position is equal to 9.7 mT. The magnetic field at the position of the energy analyser is equal to 5.2 mT.

The efficiency of the transport system between the electron linac and the diagnostics station is not known, as it is not possible to measure the positron current in the target area due to too high gamma radiation. That is why transport efficiency is included in the overall slow positron production efficiency.

The numbering of the deflectors is such that all odd numbers are horizontal (H) deflectors, and even numbers are vertical (V) deflectors. While looking along the positron beam, with increasing current, the beam should move from right to left or from top to bottom, assuming conventional positive polarity.

An important property of adiabatic transport is that it has two invariants. These are the orbital magnetic moment $\mu_p = \frac{E_\perp}{B}$ and the total energy $E_p = E_\perp + E_\parallel$ of a particle, where $E_\perp = 0.5mv_\perp^2$ and $E_\parallel = 0.5mv_\parallel^2$ is the kinetic energy corresponding to the velocity of a particle perpendicular $v_\perp$ or parallel $v_\parallel$ to the direction of the magnetic field. According to these equations, $E_\perp$ increases and $E_\parallel$ (later called parallel energy) decreases with an increasing magnetic field. Additionally, the position of the guiding center of a particle moves when the magnetic field changes. The relation between the radial position r of a particle in two different magnetic fields is equal to:

$$r_f = r_i \sqrt{\frac{B_i}{B_f}}. \tag{3.3}$$

This results in an increased beam size when propagating from a region with higher to lower magnetic field value.

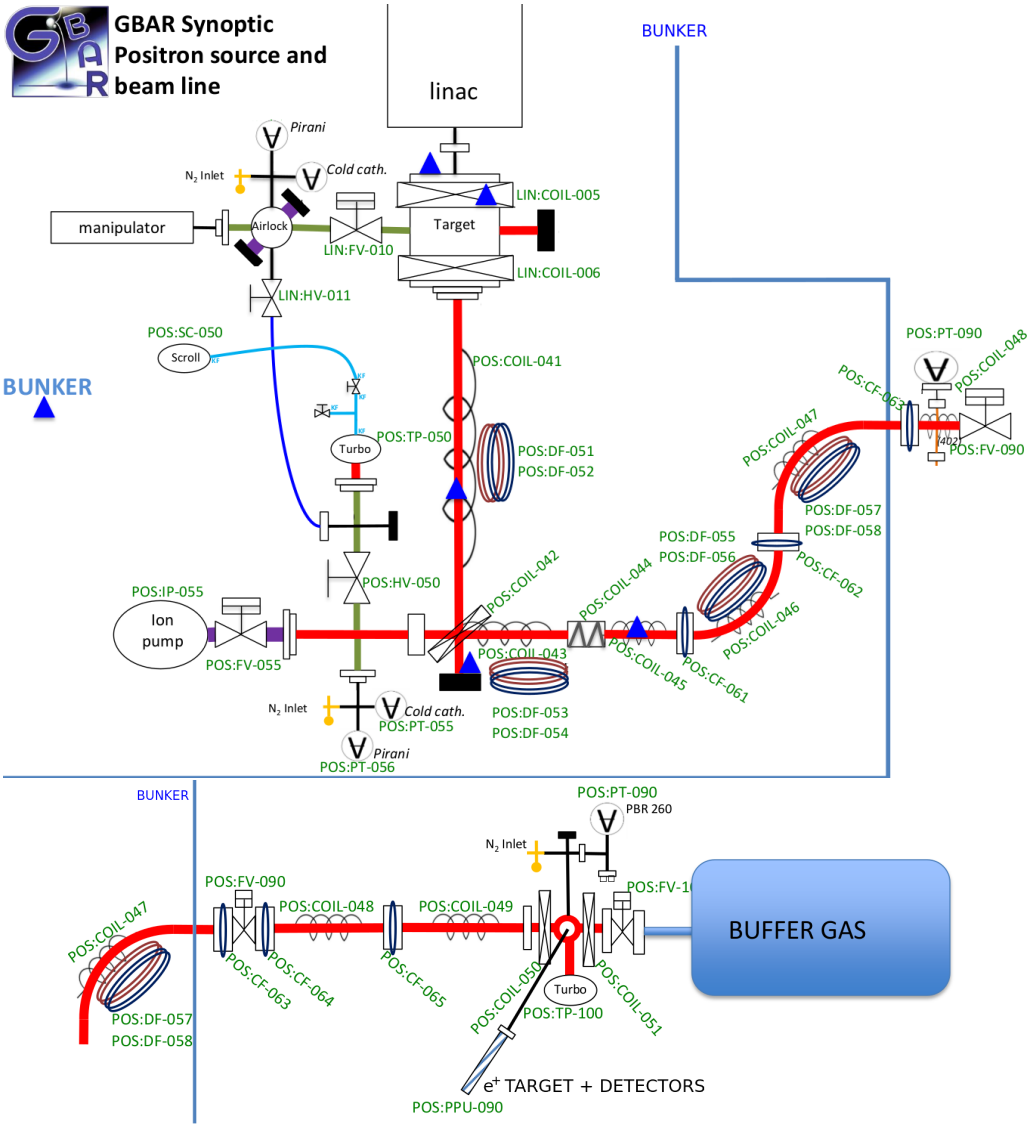

Figure 3.17: Scheme of the positron beam transport line.

3.7 Beam parameters

In this section the detectors used to measure the slow positrons are presented together with the results of the positron beam characterisation.

3.7.1 Detection system

The positron beam diagnostic station is placed downstream of the transport line, just in front of the buffer gas trap. It consists of an energy analyser and two gamma radiation detectors.

The energy analyser is presented in Figure 3.18. It is made of a stainless steel target with 3 molybdenum grids in front (the transparency of a grid is $\approx 96.5\%$), which allows to stop particles with energy lower than the potential barrier defined by the voltage on the analyser. The first grid seen by the beam is grounded and the other two are biased. Such architecture allows to minimise the effect of local inhomogeneities of the electric field that would focus a part

of the beam in an uncontrolled way. When positrons hit the target, they annihilate into two 511 keV photons, $e^- + e^+ \rightarrow \gamma + \gamma$, which are later registered by NaI and plastic scintillator detectors. The negative voltage on the target (currently used: -30 V) helps to collect all positrons. The setup allows to precisely determine the energy of the beam and estimate its size, using the fact that the internal diameter of the grid is equal to 1" (2.54 cm). The side length of the grid and the target is 40 mm. The calibration of NaI and plastic scintillator detectors is described in Appendix A.

Additionally, there is an MCP detector in the cross behind the energy analyser. It allows to determine easily the shape of the beam in two spatial and one time dimensions.

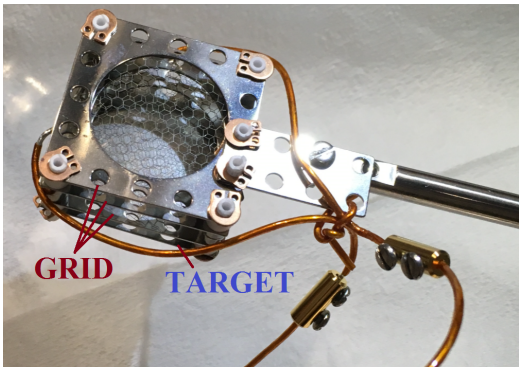

Figure 3.18: The energy analyser for the positron beam diagnostic station.

The second beam diagnostic station is situated after the buffer gas trap. Its main purpose is to characterise the positron beam after trapping, however, it can be used also as a straight-through beam diagnostic. The detection station consists of an MCP detector and a CsI scintillator which detects gamma radiation produced in positron annihilations. Additionally, the electrodes from the buffer gas trap can be used as an energy analyser. In this case, a few consecutive electrodes are biased with the same voltage. This creates the potential barrier which blocks all particles with energy lower than a certain value. It is possible to extract the energy distribution of the beam by varying the potential on the electrodes. The diameter of the electrodes used for this purpose is 16 mm.

3.7.2 Flux measurement and moderation efficiency.

One of the most important parameters for the GBAR experiment is the positron flux. The signal measured by the NaI detector is $V_{NaI} = -3.872 \pm 0.020(stat) \times 10^{-6}$ Vs (an average of 1043 measurements) for a 300 Hz linac repetition frequency. According to the calibration the number of slow positrons per pulse is equal to $N_{e^+} = 1.65 \pm 0.01(stat) \pm 0.18(sys) \times 10^5$ e^+/pulse (11 % error). The positron production per second is equal to $N_{e^+/1s} = 4.94 \pm 0.001(stat) \pm 0.030(sys) \times 10^7$ e^+/s. The presented data were collected after 12 hours of linac run, when the system reached stability (see next section). For 2.5 Hz linac repetition frequency, the number of positrons per pulse is equal to $N_{e^+} = 3.37 \pm 0.36(sys) \times 10^5$ e^+/pulse.

In Figure 3.19 the number of positrons produced per pulse and per second is shown as a function of the linac frequency. The positron flux per pulse decreases with the increasing linac frequency due to the heating of the moderator and gamma radiation (see next section).

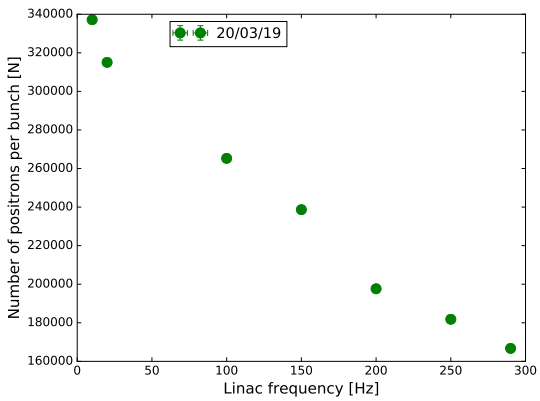

(a) Number of positrons per pulse.

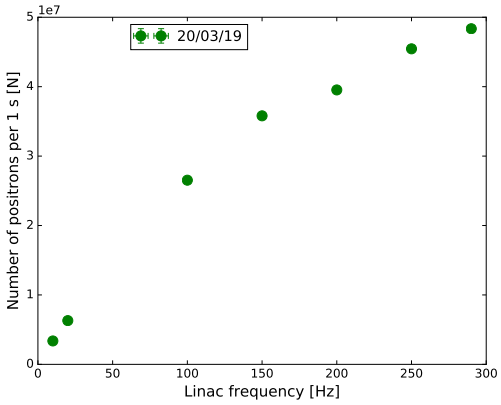

(b) Number of positrons per second.

Figure 3.19: Positron production. Error bars show the statistical error.

The effective slow positron production efficiency is about $\eta = N_{positrons}/N_{electrons} = 2.8 \times 10^{-8}$ for 300 Hz linac repetition frequency. The positron production efficiency at 10 Hz is $\eta_{10Hz} = 5.7 \times 10^{-8}$. The simulation result is $\eta_{10Hz}^{simulation} = 8 \times 10^{-8}$. The measured value has the same order of magnitude as the simulation.

Comparison to other positron sources based on electron linacs

The known positron production rates for existing sources based on electron linacs are summarised in Table 3.3. The GBAR linac reached a very good positron rate of 5×10^7 e^+/s at low electron beam energy, which is a very good achievement, comparable with already working devices.

Linac	**beam energy**	**current**	**Number of positrons**	η_{e^+}
Giessen (shut down)	35 MeV	160 mA	10^8 e^+/s	0.4×10^{-7}
Livermore (shut down)	100 MeV	400 mA	10^{10} e^+/s	16×10^{-7}
Oak Ridge	180 MeV	300 mA	10^8 e^+/s	0.53×10^{-7}
AIST, Japan	70 MeV	3 mA	2.5×10^7 e^+/s	13×10^{-7}
GBAR, CEA	4.3 MeV	140 mA	3×10^6 e^+/s	0.07×10^{-7}
GBAR, CERN	9 MeV	330 mA	5×10^7 e^+/s	0.28×10^{-7}

Table 3.3: Performance comparison between different positron sources based on the electron linacs.

3.7.3 Comparison between Saclay and CERN linacs

The results obtained for both linacs at CERN and CEA are summarised in Table 3.4.

parameter	CERN linac	CEA linac
Electron peak current	330 mA	150 mA
t_{impuls}	2.85 μs	2.5 μs
Electron energy	9 MeV	4.3 MeV
linac frequency	10 Hz	50 Hz
N_{e^-} per pulse	5.9×10^{12}	2.2×10^{12}
N_{e^+} per pulse	3.4×10^{5}	1.7×10^{4}
effective moderator thickness	0.0844 mm	0.0558 mm
efficiency	$\eta_{(CERN,9MeV)} = 5.7 \times 10^{-8}$	$\eta_{(CEA,4.3MeV)} = 0.8 \times 10^{-8}$
simulation	$\eta_{S(CERN,9MeV)} = 8 \times 10^{-8}$	$\eta_{S(CEA,4.3MeV)} = 1.0 \times 10^{-8}$

Table 3.4: Comparison of a performance of CEA and CERN linac.

In both cases the simulation gives a correct order of magnitude for the slow positron rate. The simulation slightly overestimates the number of moderated positrons. In the simulation, the moderator is a plate, while in the reality it is a mesh. In the literature, factors up to 10 are for the efficiency of the mesh with respect to that of a plate. This factor is not found globally in the yield here, but it is not known if it is not present because of the conditions (temperature, high gamma flux) or cancelled by other effects.

The ratio of efficiencies from the data is equal to $r = \eta_{(CERN,9MeV)}/\eta_{(CEA,4.3MeV)} = 7.1$. Close to this is the simulation result $r = \eta_{S(CERN,9MeV)}/\eta_{S(CEA,4.3MeV)} = 8$.

3.7.4 Beam flux stability

The positron flux is determined by the properties of the tungsten mesh, which may change in time. Generally, the efficiency of moderation can decrease due to three effects:

- surface contamination - decreases a probability of the diffusion of slow positrons from the moderator surface or changes the branching ratio of positron emission;
- heating - causing the following effects:
  - **a)** shorter positron diffusion length at higher temperatures caused by near-surface thermally-generated vacancies;
  - **b)** higher positronium production rate [97];
- radiation - increases the number of defects which trap positrons in the material.

In order to test the beam flux stability the idea is to measure the average of the detected signal during one second and repeat that measurement for a long time. Effectively, each measurement is an average value of maximum 45 pulses, limited by the oscilloscope speed.

The result of the beam stability measurement for the first moderator is presented in Figure 3.20. The measurement started just after switching on the linac with the brand new moderator. At the beginning, the number of positrons decreases approximately exponentially with time toward a stable value. The estimated time constant of the process of reaching the equilibrium state is approximately 3 hours. It means that after 24 hours, the system should reach its stability.

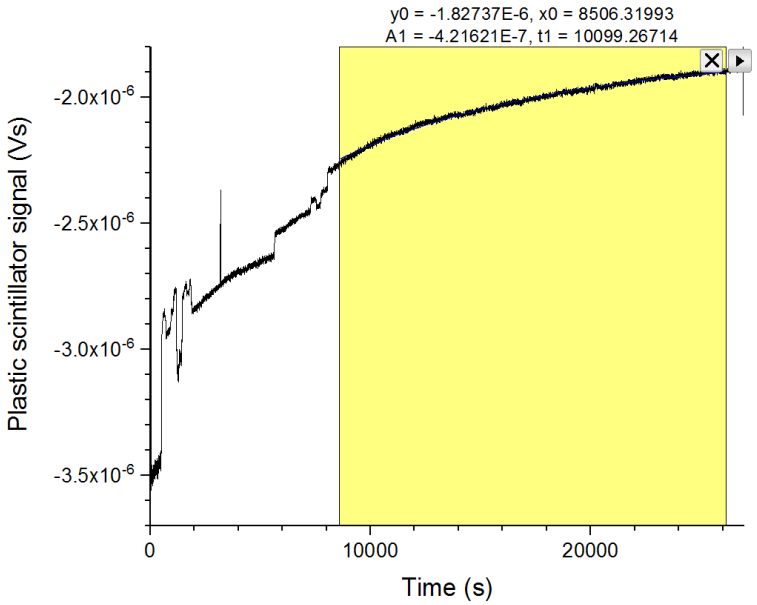

Figure 3.20: Positron beam flux measurement as a function of time for the first usage of the moderator. The visible steps are due to a change of the linac frequency. At the beginning, the linac was running at 2.5 Hz, later at 50 Hz, 75 Hz and finally at 100 Hz for most of the duration of the measurement. Note that the sign of the signal pulse is negative.

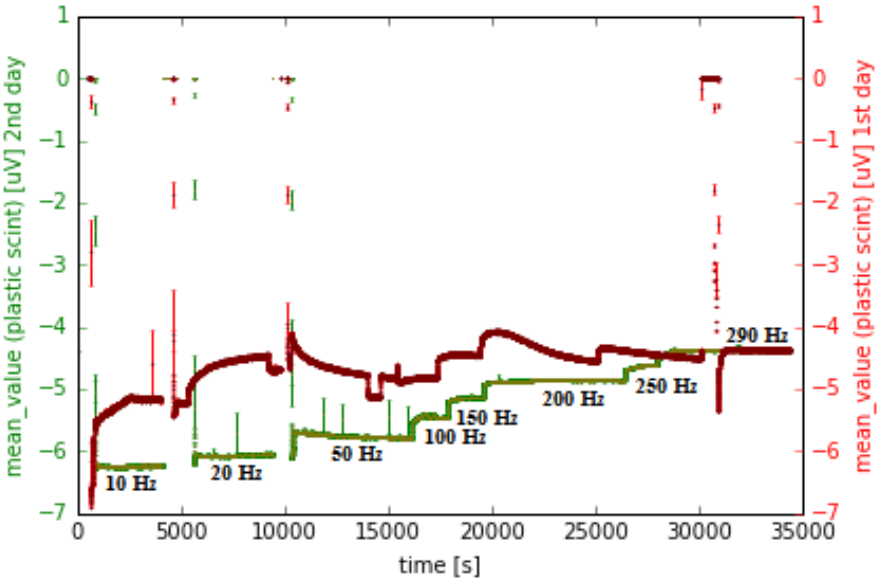

Figure 3.21: Measurement of the positron flux for different linac frequencies. The red (right scale) curve shows measurements during the first day of the run with a new moderator. The green curve (left) represents the same measurements performed during the second day.

In order to test the initial behavior of the moderator in a gamma radiation environment an additional test was performed. The linac frequency was increasing slowly and the beam flux at every step was observed. Figure 3.21 presents the data. The red (resp. green) curve represents the data collected during the first (resp. second) day of the run. There is a large difference

between the two days, however, the beam intensity at 290 Hz is the same in both cases. The difference can be explained by a few effects: cleaning of the surface, annealing or long lasting defects production. More study is required to understand the observed and unexpected behavior of the moderator during the first run.

The number of positrons decreases with the increasing linac repetition frequency due to heating and radiation effects [97], see Section 3.5.

3.7.5 Electron background

Together with positrons the system produces electrons. Some of them can also be transported, depending on the beam line design, and thus can be injected in the buffer gas trap. In order to prevent this, it is important to characterise the electron part of the beam.

The intensity of the electron beam can be checked directly by measuring the electric signal in the target of the energy analyser. According to the performed tests, the number of electrons strongly exceeds the number of positrons. Also, about half of the electron beam has an energy higher than 100 eV. It is recommended to repel the electron beam before it enters the buffer gas trap, so it would not disturb the trapping process.

Electron repeller

In order to block electrons before the buffer gas trap, an electron repeller was added to the system. An image of the device is shown in Figure 3.22. It is an electrode with a grid of about 90% transparency, which can be biased to repel electrons.

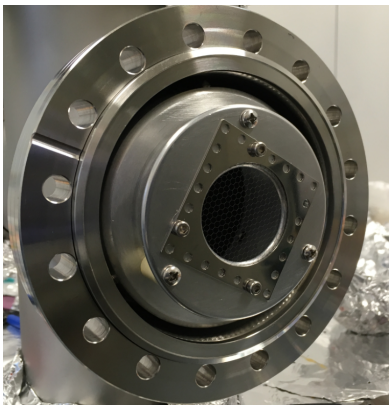

Figure 3.22: Photograph of the electron repeller.

Electron - positron beam on the MCP detector

In order to measure the size of the electron and positron beams, a micro-channel plate (MCP) detector was used. The magnetic field in the MCP region is equal to 20 mT, which is about 2.2 times higher than in the moderator area. In Figure 3.23a the electron-positron beam is shown. An image was taken with a voltage on the electron repeller $V_r = 2$ kV. Figure 3.23b is the difference between an image with the positron-electron beam and an image with only the electron beam (created by switching off the moderator voltage). The difference corresponds to the positron beam. To complement this observation, the electric signal on the MCP is shown in Figure 3.24. The blue curve (*0 V on the moderator*) is the electron beam signal. The red curve

(*50 V on the moderator*) is the signal for the electron-positron beam. The yellow curve is the difference between electron and electron-positron beam signals. The shape of the yellow curve is exactly the same as the shape of the signal on the plastic scintillator.

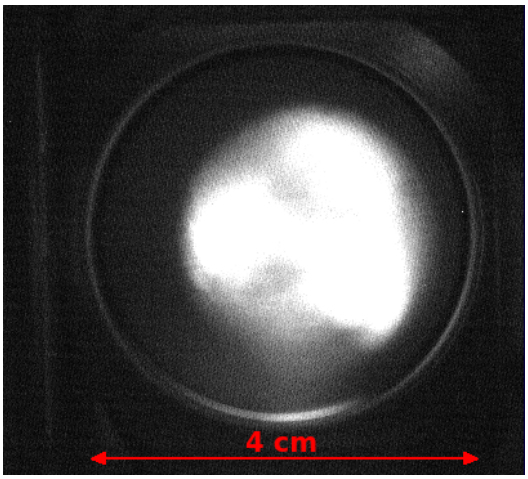

(a) The electron-positron beam. Average of 10 photographs.

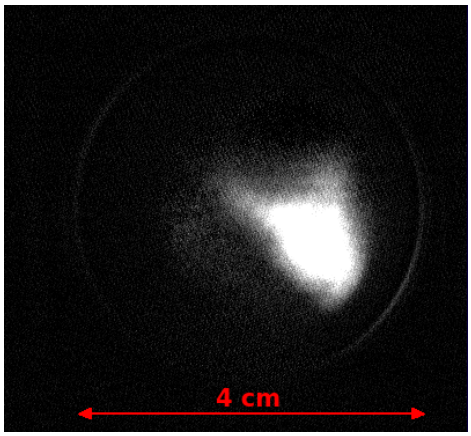

(b) The difference between the electron-positron beam and electron beam, i.e. the positron beam. Average of 10 photographs.

Figure 3.23: Images of the positron-electron beam on the MCP detector. Voltage on the electron repeller $V_r = 2$ kV.

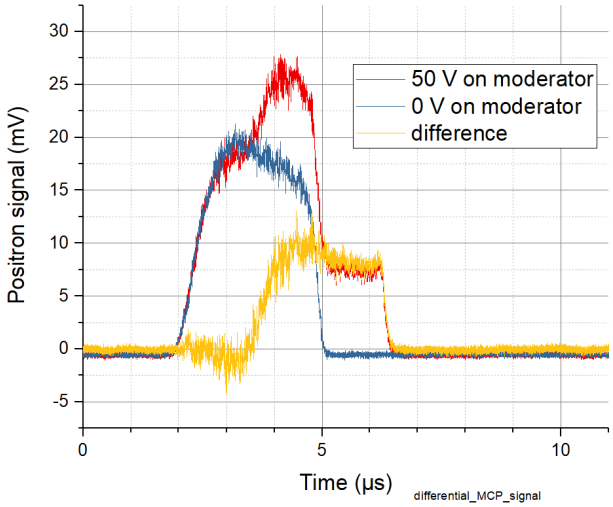

Figure 3.24: The electric signal from the MCP detector for the electron beam (blue) and the positron-electron beam (red). The yellow curve is the difference between the red and blue curves. It represents the pure positron beam.

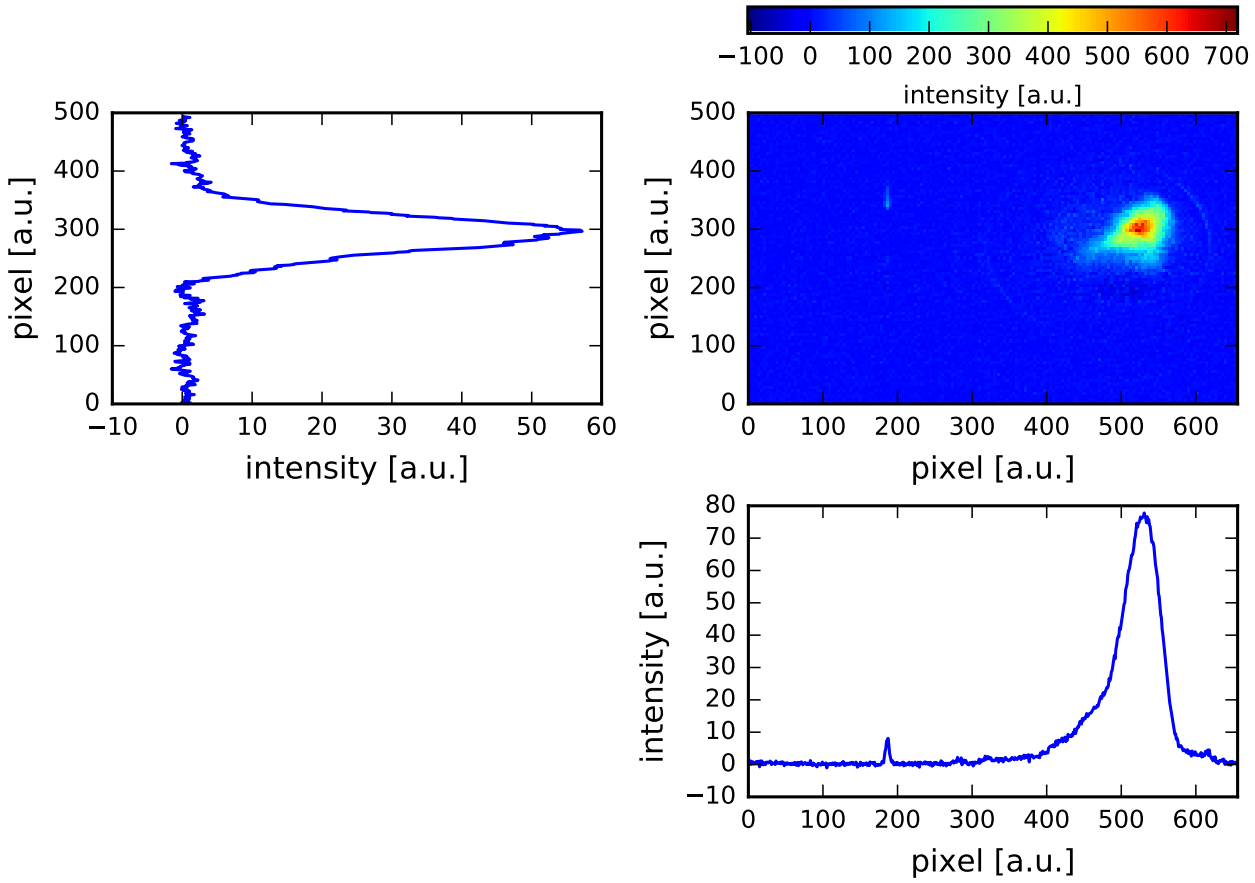

Figure 3.25: The positron beam on the MCP detector (from subtraction) together with an image projection on x and y axes. 7.5 pixels correspond to 1 mm.

3.7.6 Beam size

The size of the positron beam can be estimated from Figure 3.23b. The projection of the image intensity on the x and y axes is presented in Figure 3.25. The expected positron current that reaches the MCP detector is of the order of a few μA. In this range of current the MCP response is not linear, thus it is not possible to measure the details of the beam spatial distribution. It is not possible to correctly estimate the systematic error in this measurement, it is thus omitted.

The radius of the MCP detector is 20 mm. The estimated beam full width at 90 % maximum in x and y direction is equal to $FW90M_x = 17.5$ mm and $FW90M_y = 20$ mm. The size of the beam is overestimated, as the MCP response is not linear at that beam intensity. The magnetic field at the measurement location is equal to 20 mT.

The main diagnostics station for the positron beam flux is called the energy analyser which is situated upstream the buffer gas trap (see Section 3.7.1). The beam size in the target area of the energy analyser can be estimated from the measurement performed with the MCP detector. According to equation 3.3, the relation between the beam size on the MCP detector and the target is equal to:

$$FW90M_{x\_target} = FW90M_x \sqrt{\frac{B_{MCP}}{B_{target}}} = 17.5 \text{ mm} \cdot \sqrt{\frac{20.0 \text{ mT}}{5.2 \text{ mT}}} \approx 34 \text{ mm},$$

$$FW90M_{y\_target} = FW90M_y \sqrt{\frac{B_{MCP}}{B_{target}}} = 20 \text{ mm} \cdot \sqrt{\frac{20.0 \text{ mT}}{5.2 \text{ mT}}} \approx 39 \text{ mm},$$

where $FW90M_{x\_target}$ ($FW90M_{y\_target}$) is the FWHM of the beam in the target position, $FW90M_x$ ($FW90M_y$) is the FW90M of the beam on the MCP detector, B_{MCP} is the magnetic field value in the MCP area and B_{target} is the magnetic field value in the target area. The magnetic field values were calculated using simple solenoid models. Their precision is not known, however, it was estimated that a change of the beam size of 1 mm (which gives about 1 % difference on calibration) requires a 20 % change in the magnetic field value. Such a big error is not expected, thus the magnetic field error is omitted as insignificant.

The beam size in the moderator area is estimated to be $FW90M_{x\_target} = 25$ mm and $FW90M_{y\_target} = 29$ mm. It is larger than the inner diameter of the collimator in front of the moderator (20 mm). First, the beam size is overestimated, due to unknown MCP behavior. Also, the beam size could be enlarged during the transport, which would indicate some inhomogeneities in adiabatic transport.

3.7.7 Beam position on the target of the energy analyser

The energy analyser (see Section 3.7.1) is made from the target of the energy analyser and three 2.54 cm diameter grids. The grids are located in the 40 mm by 40 mm metal frame. To check if the beam is centered on the target, a scan of the beam intensity for different currents in the last two deflecting coils located before the target was performed. In the measurement, the positron beam energy was set at 50 eV. Each measured value is an average of 5-7 single measurements using the plastic scintillator detector.

In Figure 3.26 (left) the data for a scan of the horizontal beam position obtained by varying the current in the coil POS:DF-057 are presented. The blue points (dots) are obtained for a voltage on the grid of the energy analyser $V_g = 0$ V, so that the whole beam could reach the target. By changing the current in the coil, the beam position moves in the horizontal direction. The beam intensity changes, as a different percentage of the beam annihilates on the target. The minimum signal intensity corresponds to the central position of the positron beam on the target. Two local minimq for $I_{D57} = -2.1$ A and $I_{D57} = 4.1$ A indicate the annihilation on the metal frame of the grids of the energy analyser.

The yellow points (stars) were measured for a grid voltage $V_g = 70$ V, for which most of the centred beam is reflected before the target. In the position where previously was the global minimum, now there is a maximum. In principle, if the beam size is smaller than the grid diameter, the whole centered beam is reflected. In this case, the beam size is larger than 25.4 mm, thus a part of the beam annihilates on the frame supporting the grid. The minimum of the blue curve together with the local maximum of the yellow curve is for $I_{D57} = 1$ A. For this value of the current the beam is in the center of the target. The local minima related to the metal frame of the grid are in the same position. Both measurements for $V_g = 0$ V and $V_g = 70$ V are in good agreement showing minima or maxima in the corresponding beam positions.

In Figure 3.26 (right) the data for a vertical scan obtained by varying the current in the coil POS:DF-058 are presented. Blue dots and yellow stars represent the measurements done for grid voltages $V_g = 0$ V and $V_g = 70$ V. The minimum of the blue curve is for $I_{D58} = 1.4$ A and a local maximum of the yellow curve is for $I_{D58} = 0.7$ A. The position difference between these two extrema is caused by the change in the distance of the annihilation point with respect to

the position of the plastic scintillator. The center of the target is around $I_{D58} = 1$ A. Again, the local minima indicate the positron beam annihilation on the metal frame of the grids of the energy analyser.

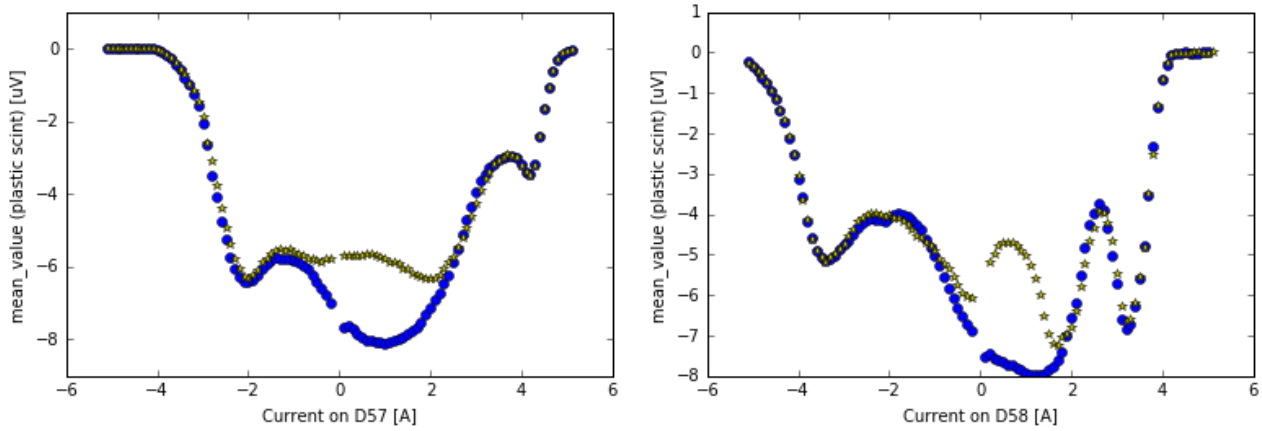

Figure 3.26: Beam intensity measured by the plastic scintillator as a function of the current in the deflecting coil POS:DF-057 (left image) and POS:DF-058 (right image). Blue/yellow points (dots/stars) are the results obtained for grid voltage $V_g = 0$ V/$V_g = 70$ V.

3.7.8 "Parallel energy" distribution measurement

Moderated slow positrons have an absolute energy equal to the moderator work function Φ^+. Positrons are emitted perpendicularly to the material surface. They are then accelerated with a constant voltage V_{acc}. If the moderator is a flat plate, then the absolute value of the mean positron energy is equal to $(V_{mod} - V_{acc}) \cdot q + \mid \Phi^+ \mid$, where q is the positron charge and V_{mod} is the voltage on the moderator. In a more realistic description the shape of the moderator has to be included. For a mesh structure which has wires with a circular cross-section, positrons are emitted in all directions. It means that the total energy distribution for a tungsten moderator should fit within about 4 eV interval, with maximum energy equal to $(V_{mod} - V_{acc}) \cdot q + 3$ eV [99]. The parallel energy distribution is different from the total energy distribution, but has the same maximum value. The mean value for both distributions is somewhere between $(V_{mod} - V_{acc})$ and $(V_{mod} - V_{acc}) \cdot q + 3$ eV, depending on the moderator structure and external magnetic field lines. It is not equal to $(V_{mod} - V_{acc})$, because not all positrons emitted in the direction of the tungsten target can be collected.

The total positron energy E_p can not change in a magnetic transport. While the ratio between the parallel and perpendicular velocities strongly depends on the magnetic field. The parallel energy $E_{\parallel\_i}$ in the position with magnetic field value B_i is related to the parallel energy in the position with magnetic field B_f by the relation

$$\frac{E_p - E_{\parallel\_i}}{B_i} = \frac{E_p - E_{\parallel\_f}}{B_f},$$

which is equivalent to

$$E_{\parallel\_i} = E_p - \frac{B_i}{B_f}(E_p - E_{\parallel\_f}). \tag{3.4}$$

Under the assumption that the beam energy has a Gaussian distribution, the standard deviation is equal to

$$\sigma_i = \left| \frac{B_i}{B_f} \right| \cdot \sigma_f. \tag{3.5}$$

The energy dispersion of the positron beam should be as narrow as possible in order to increase the trapping efficiency.

The "parallel energy" distribution measurement with the buffer gas trap electrodes

The energy distribution of the positron beam for a given accelerating voltage V_{acc} is obtained from the measurement of the beam flux as a function of the voltage on six consecutive buffer gas trap electrodes $V_{electrodes}$. The biased electrodes create a potential barrier which blocks positrons with energy smaller than $e \cdot V_{electrodes}$, where e is the value of the electric charge of positrons. The curve obtained for $V_{acc} = 0$ V and $V_{mod} = 50$ V is shown in Figure 3.27. As expected, the maximum beam energy is equal to about 53 eV. The positron flux is measured with a CsI detector.

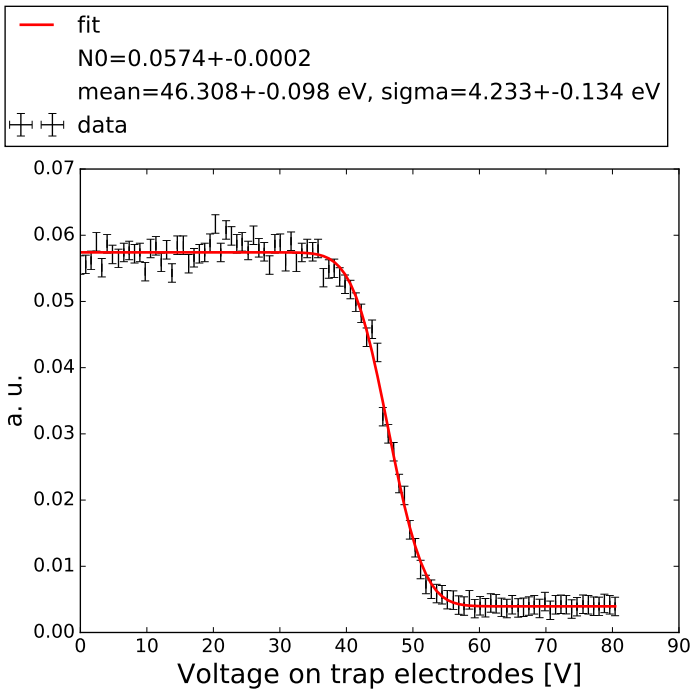

Figure 3.27: Measurement of the beam flux as a function of the voltage on six consecutive buffer gas trap electrodes for the moderator voltage $V_{mod} = 50$ V. The red line is a fitted error function.

Under the assumption that the energy of the beam follows a Gaussian distribution, the collected data can be fitted with an error function, from which the mean energy and the standard deviation of the distribution can be extracted. In presented case E= 46.3 ± 0.1 eV and ΔE= 4.2 ± 0.1 eV. The measurement was performed in a 60.0 mT magnetic field. The measurement points include the statistical error and a correction related to the calibration of voltages on electrodes.

In principle, using equations 3.4 and 3.5 it is possible to extrapolate the mean value and sigma parameter of the energy distribution to the original moderator position (9.7 mT). However, obtaining the value of the mean energy requires information about the total energy E_p, which is not measured in the experiment. The standard deviation can be extrapolated without this information and is equal to

$$\sigma_{mod} = \frac{9.7 \text{ mT}}{60 \text{ mT}} \cdot 4.2 \text{ eV} = 0.7 \text{ eV},$$

$$FWHM_{mod} = 2.35 \cdot \sigma_{mod} = 1.6 \text{ eV}.$$

This result is in agreement with the expected energy spread. Usually, experiments which moderate positrons use a neon moderator. The original moderator invented by A. P. Mills and E. M. Gullikson had an energy spread equal to $FWHM_{Neon} = 0.58$ eV [100]. The commonly used moderator has a different shape than the original one in order to increase the moderation efficiency. The typically used neon moderators have an energy dispersion equal to $FWHM_{Neon} = 2.0$ eV [101]. The energy spread obtained in our system is similar to the one of commonly used neon moderators, which is a very good result.

"Parallel energy" distribution measurement with the buffer gas trap electrodes - different accelerating voltage

The energy distribution measurement was repeated for six different values of the accelerating voltage $V_{mod} \in \{20, 30, 40, 50, 60, 70\}$ [V], see Figure 3.28. This time, the first three electrodes of the buffer gas trap were used. All measured curves have a similar shape and the same zero value for fully blocked beam. The initial beam intensity is smaller for low energy beams, which agrees with expectations, as the beam transport was optimised for 50 eV beam energy. The parameters of the energy distributions, extracted from a Gaussian fit, are summarised in Table 3.5. The energy spread for beam energies above 40 eV is the same. It means that indeed the designed transport system is adiabatic.

V_{acc} [V]	mean [eV]	σ [eV]	$\approx$ FWHM [eV]
20	16.7 ± 0.4	6.0 ± 0.6	14.1
30	25.7 ± 0.1	4.9 ± 0.2	11.5
40	36.2 ± 0.4	4.2 ± 0.6	9.9
50	45.9 ± 0.1	4.3 ± 0.1	10.1
60	56.1 ± 0.1	4.3 ± 0.2	9.9
70	66.3 ± 0.1	4.2 ± 0.2	9.9

Table 3.5: Parameters of the positron beam energy distribution measured insite the buffer gas trap for different accelerating voltages V_{acc}.

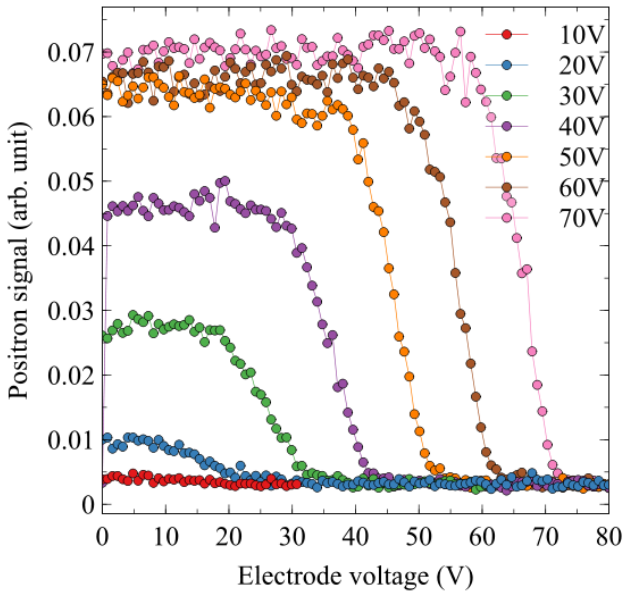

Figure 3.28: Measurements of the beam flux as a function of the voltage on three consecutive buffer gas trap electrodes for different accelerating voltages.

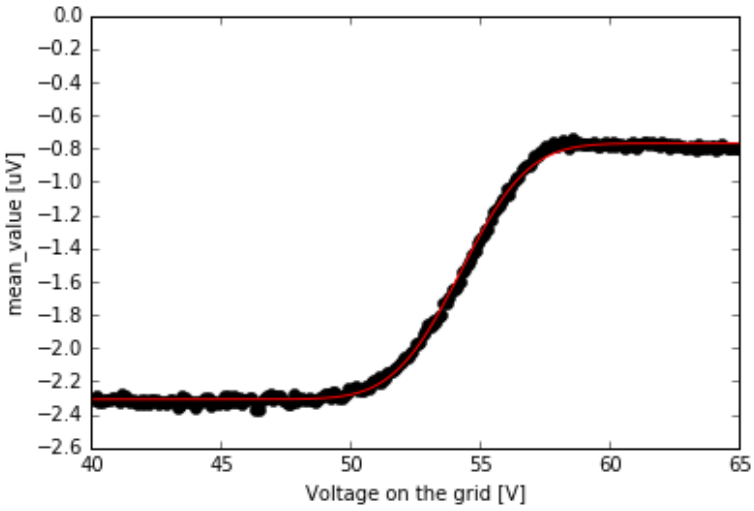

Figure 3.29: Measurement of the beam flux as a function of the voltage on the energy analyser grid for a voltage on the moderator $V_{mod} = 50$ V. The data collected with the plastic scientillator. Red line is a fitted error function.

"Parallel energy" distribution measurement with the energy analyser

The second method to measure the energy and the energy spread of the positron beam is to use the energy analyser described earlier in the text. An energy distribution of the positron beam for a given voltage on the moderator V_{mod} is obtained from the measurement of the beam flux as a function of the voltage on the energy analyser grid. An exemplary result for $V_{mod} = 50$ V is shown in Figure 3.29. Under an assumption that the energy of the beam follows a Gaussian

distribution, the data can be fitted with an error function, from which the mean energy and the standard deviation of the distribution can be extracted - E= 53.2 eV and ΔE= 1.6 eV. The value of the magnetic field in the energy analyser area is equal to 5.2 mT. Results disagree with predictions. The mean value is higher than expected maximum energy and the energy spread is too high. The possible explanation for that behavior is that the grid mesh is too coarse. A finer grid is being prepared.

3.8 Summary

The slow positron source for the GBAR experiment at CERN was successfully developed. It provides 5×10^7 e^+/s at 300 Hz linac repetition frequency. It has an excellent energy dispersion equal to $FWHM = 1.6$ eV, which is comparable to the typical performance of beams from radioactive sources. The beam quality allows for efficient positron trapping in the buffer gas trap and later in the high field magnetic trap.

However, in order to obtain the planned 3×10^8 e^+/s further developments are required. For instance, a new moderator with a wire diameter of 10 um may increase the slow positron flux by up to a factor two. Additionally, moving the moderator closer to the target can also increase the beam flux by 30 %. The overall expected slow positron beam intensity should not be far from the nominal value.

Chapter 4

The antihydrogen atom and ion production cross-sections by charge exchange reactions on positronium

In this Chapter the existing theoretical calculations of the cross-section values are summarised. They are important to determine the minimum experimental requirements. Then, the parameters which have to be measured are predefined by looking at the general method of how to extract the cross-section values within the GBAR framework.

4.1 Motivation

The GBAR experiment requires the production of antihydrogen ions $\bar{\mathrm{H}}^+$. It is done via charge exchange reactions between antiproton or antihydrogen and positronium:

$$\bar{\mathrm{p}} + \mathrm{Ps}(n_p, l_p, m_p) \rightarrow \bar{\mathrm{H}}(n_h, l_h, m_h) + e^- \tag{4.1}$$

$$\bar{\mathrm{H}}(n_h, l_h, m_h) + \mathrm{Ps}(n_p, l_p, m_p) \rightarrow \bar{\mathrm{H}}^+ + e^-. \tag{4.2}$$

where (n, l, m) are principal, azimuthal and magnetic quantum numbers.

The optimisation of the antihydrogen ion production rate is crucial for the experiment, as it defines the minimum time required to obtain a defined statistical precision of the final free fall experiment. One of the key aspects of this optimisation is the knowledge of the cross-sections for reactions 4.1 and 4.2. This allows to choose the best antiproton incident energies, positronium excited states or correctly adjust the cavity size. The theoretical calculations provide values for these cross-sections, but sometimes with large discrepancies.

Currently, there are no measurements of the cross-sections for reactions 4.1 and 4.2. However, there are three measurements of the total hydrogen formation cross-section from a ground state positronium $\mathrm{p} + \mathrm{Ps}(1s) \rightarrow \mathrm{H} + e^+$ at proton impact energies 11.3, 13.3, and 15.8 keV. The measurements were done by J. P. Merrison et al. [63]. In this thesis, a first study about the cross-section measurement for the production of antihydrogen atoms and ions is described.

4.2 Cross-section calculations

There are several theoretical models that calculate the cross-section for reactions 4.1 and 4.2. They are valid at different energy ranges. The energies available in the GBAR experiment are in the so-called intermediate region, between 1 eV and 10 eV center of mass energy, which corresponds to 1 keV - 10 keV antiproton beam energy in the GBAR laboratory frame.

Generally, calculations can be made either directly for reactions 4.1 and 4.2 or their charge-conjugated and time-reversed form:

$$e^+ + \mathrm{H}(n_h, l_h, m_h) \rightarrow \mathrm{Ps}(n_p, l_p, m_p) + \mathrm{p} \tag{4.3}$$

$$e^+ + \mathrm{H}^- \rightarrow \mathrm{Ps}(n_p, l_p, m_p) + \mathrm{H}(n_h, l_h, m_h). \tag{4.4}$$

where (n, l, m) are principal, azimuthal and magnetic quantum numbers describing the state of the atoms. Depending on the model, calculations may be more straightforward in one or the other direction, but they can always be brought back to the needed form using assumptions like microreversibility. In the following Section, a short summary of the available calculations for both reaction pairs are described.

This Section is based on several doctoral dissertations by P. Comini [102], M. Valdes [103] and I. Abdurakhmanov [104]. The most detailed calculations for the required cross-sections are performed by P. Froelich et al. However, currently only part of them is published [105]. Atomic units are used ($m_e = e = \hbar = k_e = 1$, $1\pi a_0^2 \approx 0.88 \times 10^{-16}$ cm^2).

4.2.1 $\bar{\mathrm{H}}$ production

The $\bar{\mathrm{H}}$ production process is a three body charge exchange reaction between an electron, a positron and an antiproton. The required minimum kinetic energy in the center of mass is equal to (1 a.u. $\approx$ 27.2 eV):

$$T_{CM} = \frac{1}{4n_p^2} - \frac{1}{2n_h^2}.$$

If $T_{CM} \geq 0$ there are no restrictions for the reaction. The positronium energy is set experimentally with an average equal to 50 meV, and thus, if needed, the whole missing kinetic energy must come from the antiproton. The energy in the centre of mass T_{CM} is in the order of the kinetic energy of positronium, i.e. maximum a few electronvolts. In the laboratory frame, when positronium is almost at rest, the energy is $T_{lab\_\bar{p}} = \frac{m_{Ps}+m_{\bar{p}}}{m_{Ps}} \cdot T_{CM}$, where m_{Ps} and $m_{\bar{p}}$ are the masses of Ps and $\bar{p}$ respectively. Its value is related to the antiproton energy and is between a few hundred eV and a few keV. The production of antihydrogen in the $n_h = 1$ state does not have any threshold. The threshold values for different positronium and antihydrogen states are summarised in Table 4.1.

Of all the available methods used to calculate the cross-sections of reaction 4.1, three main groups are presented here:

- Faddeev-Merkuriev method;
- close-coupling approximation;
- perturbation method.

n_p	n_h	T_{CM} **[eV]**	$T_{lab\_\bar{p}}$ **[keV]**
1	1	0	0
	2	3.4	3.1
	3	5.3	4.9
2	1, 2	0	0
	3	0.19	0.17
3	1, 2, 3, 4	0	0

Table 4.1: Selected threshold values for reaction 4.1 for different positronium and antihydrogen states. T_{CM} is the threshold value in the centre of mass frame and $T_{lab\_\bar{p}}$ is the corresponding threshold for antiproton energy in the laboratory frame.

While each of them has its limitations and many sub-methods, only a summary of calculations useful for the GBAR experiment are presented here.

Faddeev-Merkuriev method

The direct cross-section calculations require solving the Faddeev-Merkuriev equations. In 1960s L. D. Faddeev introduced his equations in order to solve nonrelativistic quantum three particle scattering problems for short range potentials [106]. It was expanded later by S. Merkuriev to treat also a long range Coulomb interaction [107], which fits the problem of the antihydrogen atom formation. The crucial element of this method is to represent a 3-body interaction as a sum over all combinations of a 2-body system plus one free particle, described with Jacobi coordinates. As the Coulomb interaction has an infinite range it is not possible to directly treat one particle as "free". The Coulomb potential has to be split into a short-range and a long-range potential using a cutoff function defined by S. Merkuriev [107].

Calculations using the Faddeev-Merkuriev equations for reaction 4.1 were performed by M. Valdes et al. [108, 103]. A numerical method of solving the Faddeev-Merkuriev equations with the Lagrange-mesh method was used, as analytical calculations are not possible. In principle, this type of calculations is valid for every energy. However, with increasing energy the number of possible reaction channels increases and calculations become more complex. Nevertheless, in the energy range studied in [108, 103], the calculations are considered to be complete.

Even though this is a very good method to calculate the cross-sections, it is very challenging due to its complexity. This is why not all interesting positronium and antihydrogen atom states were considered. In the mentioned paper [108], the total cross-sections are calculated for $\bar{\mathrm{p}} + \mathrm{Ps}(1s) \rightarrow \bar{\mathrm{H}}(1s, 2s, 2p) + e^-$ and $\bar{\mathrm{p}} + \mathrm{Ps}(2s, 2p) \rightarrow \bar{\mathrm{H}}(1s, 2s, 2p) + e^-$. The calculated cross-sections give an excellent basis for evaluating other existing approximations.

Close-coupling approximation

The close-coupling method is similar to the Faddeev-Merkuriev method, but in this case, the total wave function is expanded using the target-state wave functions. The precision of this method depends on the expansion method, on the number of considered channels and all included approximations.

The most recent calculations for reaction 4.1 using the CC approach are done using the

two-center convergent close-coupling (CCC) method. They were performed by Kadyrov et. al. [109, 110]. In the collision of an antiproton with positronium, the antiproton can either scatter leaving the target intact or excited, or form a bound state with the active positron and create the antihydrogen atom. Therefore, this problem has to be treated as having two centers - one related to the target and one to a possible formed final state. This consideration of the dependence between two centers gives the method its name [104].

The calculations presented in [109, 110] were performed for six Ps states, from Ps($1s$) to Ps($3d$), and 10 $\bar{\mathrm{H}}$ states, from $\bar{\mathrm{H}}(1s)$ to $\bar{\mathrm{H}}(4f)$. The comparison between the Faddeev-Merkuriev and CCC results for chosen channels at low energy is presented by Valdes et. al. in [108], an exemplary comparison is shown in Figure 4.1. The CCC results are in good agreement with the direct calculations, which allows thinking that calculations of the total and partial cross-sections for the sum of many states and higher energies are also correct.

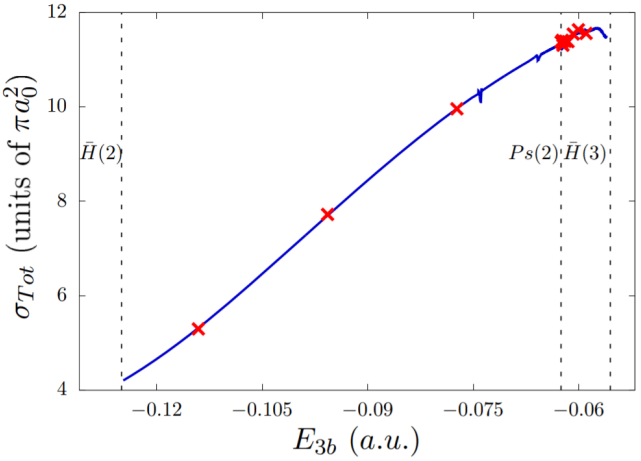

Figure 4.1: Total cross-section of the reaction $\bar{\mathrm{p}} + \mathrm{Ps}(n_p = 1) \rightarrow \bar{\mathrm{H}}(n_h = 1, 2) + e^-$. The blue line are calculations made with Faddeev-Merkuriev method [108] and red crosses are CCC calculations [110]. The E_{3b} is the centre of mass energy of a three-body system, which is available in the reaction. Figure taken from [108].

Perturbation methods

Perturbation methods are based on the assumption that the wavefunction for the scattering system can be expanded in rapidly convergent series. It is possible to use the Born approximation with initial and final states as plane waves. However, the usage of plane waves for reaction 4.1 in the energy range between 1 keV and 10 keV may not be sufficient. There is a possibility that potential from a charged antiproton may distort the positronium, even though it is neutral. Models using second-order of the Born approximation in which initial or final state is a distorted wave are commonly marked with a shortcut DW - Distorted Wave. Perturbation methods are usually valid when the scattering potential is relatively small in comparison to the incident energy. That is why it is applicable at energies a few times higher than the reaction threshold. Even though these methods are not precise at the energies interesting for the GBAR experiment, the availability of the analytic formulas allows making relatively easy calculations for many antihydrogen and positronium excited states.

Calculations using the CDW-FS method and the Coulomb-Born approximation (CBA) are described in the papers of P. Comini and P-A. Hervieux [111, 112]. In the first model Coulomb

wave functions are used to describe the projectile and outgoing product particles. In the CBA model the Coulomb wave function are used for incoming particles and plane waves are used for outgoing particles. The cross-sections were calculated for six Ps states, from Ps($1s$) to Ps($3d$), and thirteen $\bar{\mathrm{H}}$ states, from $\bar{\mathrm{H}}(1s)$ to $\bar{\mathrm{H}}(5h)$, or even $\bar{\mathrm{H}}(5d)$ for Ps($1s$).

For all Ps states, the production of excited $\bar{\mathrm{H}}$ dominates over the almost negligible $\bar{\mathrm{H}}(1s)$ formation. The only exception is for a ground state Ps below the 3.1 keV energy threshold, where only the $\bar{\mathrm{H}}(1s)$ state is produced. The ground state antihydrogen is important for the production of the antihydrogen ion (see next Section). Its suppressed production is an essential information for the GBAR collaboration, as the length of the reaction cavity has to be adjusted in a way to allow the antihydrogen atom to de-excite and produce an antihydrogen ion [102]. The largest ground state antihydrogen formation cross-section is obtained with a ground state positronium. The cross-section calculations for CDW–FS and CBA models and ground state positronium are shown in Figure 4.2.

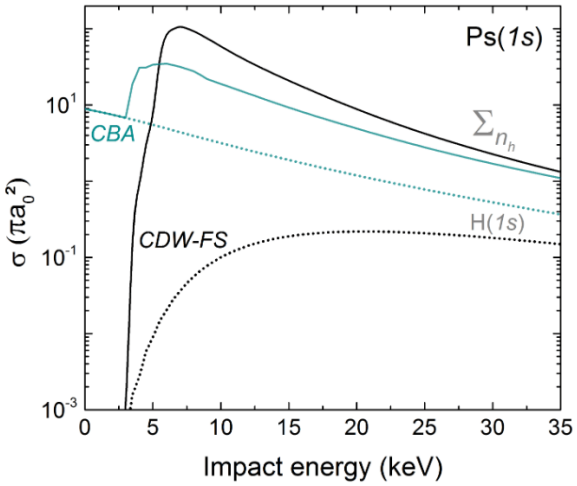

Figure 4.2: CDW–FS (black) and CBA (teal) $\bar{\mathrm{H}}$ production cross-sections for ground state positronium. The dotted lines correspond to the formation of ground state antihydrogen and the solid lines are the summed cross-sections up to H(4f). Impact energy is the energy of the antiproton beam in the laboratory frame calculated for the configuration of the GBAR experiment. Figure taken from [102].

Comparison between different models and with measurements

Currently, there are no direct measurements of the cross-sections for reaction 4.1. The only existing measurements were performed for the charge conjugate reaction of hydrogen production from a ground state positronium $\mathrm{p} + \mathrm{Ps}(1s) \rightarrow \mathrm{H} + e^+$ at proton impact energies 11.3 keV, 13.3 keV, and 15.8 keV. The measurements were done by J. P. Merrison et al. [63]. It is expected that the hydrogen and antihydrogen formation cross-sections are equal. Measurements of the total cross-section for the CT symmetric reaction 4.3 for the hydrogen ground state can be found in [113, 114].

Presented close-coupling CCC and CBA calculations give different cross-section values, which are in relatively good agreement with J. P. Merrison measurements, see Figure 4.3. Below 10 keV energy, it is believed that CCC and Faddeev-Merkuriev methods give the most correct results, however, the aforementioned perturbation models could be also used to ex-

trapolate relative values of antihydrogen production cross-sections for different Ps states. All methods conclude that the formation of higher antihydrogen states is promoted for excited Ps states.

In this thesis, the CBA model [111, 112] and the CCC model [110] are going to be used to estimate the antihydrogen atom production rate. Deducing from the data depicted in Figure 4.3, the largest antihydrogen atom production rate is between 6 keV and 10 keV antiproton beam energy.

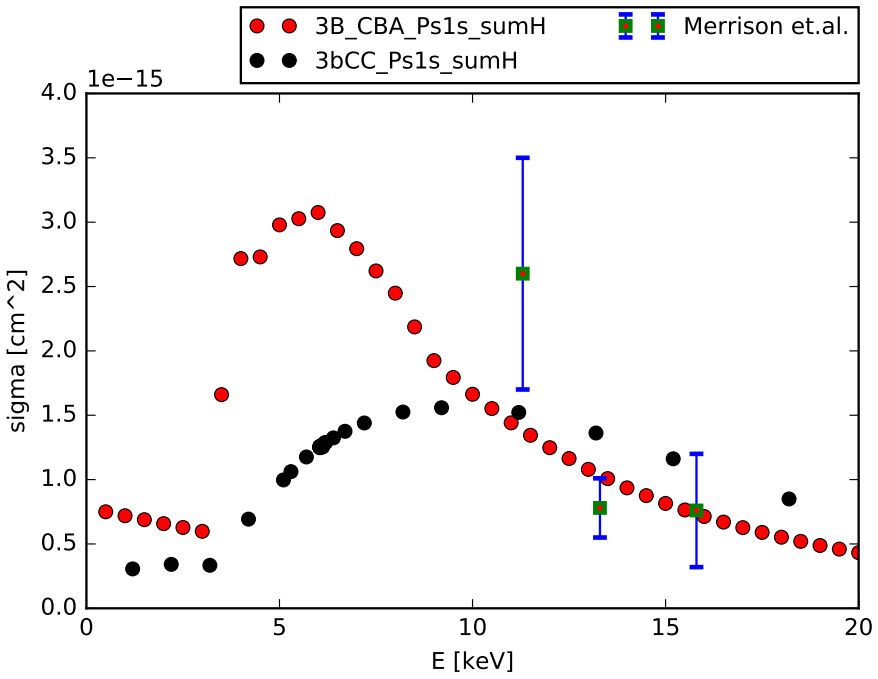

Figure 4.3: Total cross-sections for antihydrogen formation from a ground state positronium as a function of antiproton energy in the laboratory frame of the GBAR experiment. Calculations 3B_CBA_Ps1s_sumH are for the CBA model [111, 112] and points 3bCC_Ps1s_sumH are for the CCC model [110]. Calculations for a ground state positronium Ps($1s$) are compared with the measurement performed by J. P. Merrison et al. [63].

4.2.2 $\bar{H}^+$ cross-section calculations

The antihydrogen ion $\bar{H}^+$ formation according to reaction 4.2 is a four-body charge exchange reaction. The threshold for the production of an antihydrogen ion in the centre of mass is equal to:

$$T_{CM} = \frac{1}{4n_p^2} + \frac{1}{2n_h^2} - 0.5277 a.u.,$$

where 0.5277 a.u. is the binding energy of $\bar{H}^+$ [115]. In accordance with the reaction 4.1, the Ps kinetic energy is equal to 50 meV. However, it is neglected in calculations as it is very small in comparison to the antiproton energy. The total missing kinetic energy must come from antihydrogen atom. The threshold in the laboratory frame for the production of an antihydrogen ion from ground states of Ps and $\bar{H}$ is equal to $T_{\bar{H}(1s)} = 5.553$ keV. For excited states of Ps

and ground state $\bar{H}$ the thresholds are below 1 keV, see Table 4.2. There is no threshold for reactions with any excited state of antihydrogen.

n_p	n_h	T_{CM} **[eV]**	$T_{lab\_\bar{H}}$ **[keV]**
1	1	6.1	5.6
	2, 3	0	0
2	1	0.95	0.87
	2, 3	0	0
3	1	0.002	0.002
	2, 3	0	0

Table 4.2: Selected threshold values for reaction 4.2 for different positronium and antihydrogen states. T_{CM} is the threshold value in the centre of mass frame and $T_{lab\_\bar{H}}$ is the corresponding threshold for antihydrogen energy in the laboratory frame.

Comparison between different models

There is a shortage of calculations regarding reaction 4.2 in particular for excited states of positronium. Their summary for the ground states of Ps and $\bar{H}$ is shown in Figure 4.4. In this Figure the possible spread of cross-section values is visible. There are large discrepancies between the different predictions, mainly due to the complexity in the 4-body reaction treatment and the lack of exact analytical formulae for the hydrogen ion wave functions. In Figure 4.4, symbols PrCBA/PsCBA stands for CBA calculations of J. C. Straton and R. J. Drachman [116] for the *prior* and *post* form respectively. The Fock-Tani calculations are PsCDO and PsCDIO [116]. The close-coupling calculations are $2CH^d$ of P. Biswas [117] and CC^d [118] of J. E. Blackwood. CC^r stands for coupled pseudo-states computations of M. T. McAlinden [119]. $CMEA^d$ is for the Coulomb modified eikonal approximation model of S. Roy and C. Sinha [120].

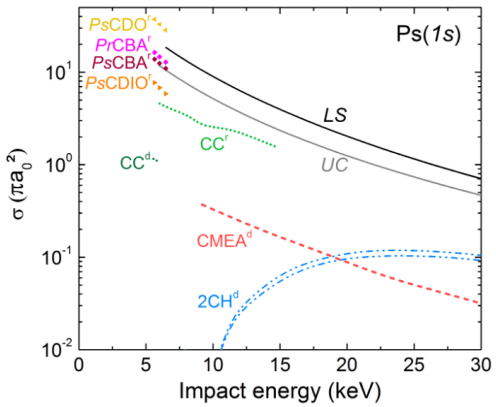

Figure 4.4: Comparison between different models of $\bar{H}^+$ formation cross-sections from ground state $\bar{H}$ and ground state Ps as a function of antiproton impact energy in the laboratory frame. Abbreviations on the picture: PsCDO/PrCBA/PsCBA/PsCDIO [116], $2CH^d$ [117], CC^d [118], CC^r [119], $CMEA^d$ [120], LS/UC [111]. Figure adapted from [102].

The most comprehensive calculations were performed by P. Comini and P-A. Hervieux using CDW-FS model [111, 112]. They calculated cross-sections using the CT conjugated reaction 4.4 for a wide range of states, from Ps($1s$) to Ps($3d$), and from H($1s$) to H($4f$). Two different initial forms of wave functions were used: uncorrelated Chandrasekhar (UC symbol) and Le Sech (LS symbol) wave functions. Even though the perturbation method is not completely valid at the energy range below 10 keV, performed calculations give an insight into the antihydrogen ion formation rate at different excited states of the incident particles.

According to CDW-FS calculations for excited Ps states, the antihydrogen ion production from antihydrogen states $n_h \geq 2$ is insignificant at energies below 10 keV. For the ground state positronium the largest contribution comes from $1S$, $2S$ and $2P$ antihydrogen states. Also, the cross-section for antihydrogen atom in the ground state goes up when approaching the reaction threshold, a feature particularly strong for Ps excited states. A detailed study of Ps excited states shows that the cross-section for excited Ps states (for instance Ps($3d$)) around 1 keV antihydrogen energy can be two orders of magnitude higher than the maximum of the cross-section for Ps($1s$) (obtained at the threshold). This is a key information, as it can significantly increase the antihydrogen ion production. However, this calculations have been recently revised following the discovery of an error in the computing code. The new results suggest lower cross-sections for the positronium excited states. The corrected results are going to be published soon [121].

Recently a preliminary results for a new calculations using an Faddeev-Merkuriev method for antihydrogen ion were published by P. Froelich et al. [105], but only for the S-wave. The published data shows cross-section values in the order of a few a.u., which is an order of magnitude lower than the cross-sections from CDW-FS calculations. The more comprehensive calculations are expected to be published soon.

Both calculation of P. Comini and P-A. Hervieux, and of P. Froelich et al. are of great importance especially from the experimental point of view. They help to guide the experiment in a correct direction. In this thesis, CDW-FS model for LS wave functions is used to estimate the antihydrogen ion production rate [111, 112].

4.3 Cross-section measurements

In this Section, a general method to extract the cross-section values of the antihydrogen atom and ion formation is discussed.

The scheme of the cross-section measurement setup is shown in Figure 4.5. As described earlier in Section 2.2, the antihydrogen atoms and ions formation take place in a cavity filled with the ortho-positronium cloud. Ortho-positronium has about 50 meV energy and a decay time equal to 142 ns. While the oPs is produced, a 1 keV to 10 keV antiproton beam with 300 ns pulse length passes through the cavity initiating the antihydrogen atom and ion formation. Due to a large difference in momentum between oPs and $\bar{p}$, produced antihydrogen atoms and ions follow the antiproton beam to the switchyard, where they are electrostatically separated. Then, all particles are guided to the dedicated detection system. The measurement of the cross-section for antihydrogen atom and ion production requires detailed knowledge about the properties of all beams. However, it is not always possible to extract all required information.

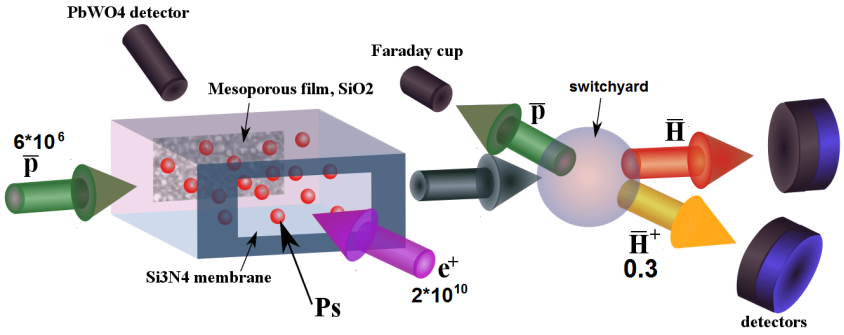

Figure 4.5: Scheme of the cross-section measurement setup.

In the thesis, the term "total cross-section" refers to the sum of all resulting states for a given initial state. For example, the total cross-section $\sigma(oPs(1s), \bar{p})$ for antihydrogen production from oPs in the $(1s)$ state and antiproton is the sum of cross-sections for all the produced antihydrogen states.

4.3.1 Reaction 4.1 with a ground state Ps

The number of antihydrogen atoms produced at a given centre of mass energy can be written as:

$$N^0_{\bar{H}} = d_{oPs(1s)} \cdot N_{\bar{p}} \cdot L \cdot \sigma(oPs(1s), \bar{p})$$

where:

- $d_{oPs(1s)}$ - ground state ortho-positronium density (later called positronium density);
- $N_{\bar{p}}$ - number of antiprotons;
- L - length of the cavity or interaction region;
- $\sigma(oPs(1s), \bar{p})$ - the total cross-section for Ps$(1s)$.

This method assumes a complete overlap in time and space between the antiproton beam and the Ps target. However, the density of the positronium cloud changes in time and space due to Ps lifetime and finte Ps velocity. Also the antiproton beam has both time and spatial distributions. The above formula must then be changed to:

$$N_{\bar{H}} = \sigma(oPs(1s), \bar{p}) \cdot f^{(t,z,y,x)}_{oPs(1s)} \tag{4.5}$$

where $f^{(t,z,y,x)}_{oPs(1s)}$ describes the antiproton - positronium interaction

$$f^{(t,z,y,x)}_{oPs(1s)} = \int_{-\infty}^{\infty} \int_{z_0}^{z_1} \int_{y_0}^{y_1} \int_{x_0}^{x_1} d_{oPs(1s)}(t,z,y,x) \cdot N_{\bar{p}}(t,z,y,x) dx dy dz \cdot v_{\bar{p}} dt, \tag{4.6}$$

and:

- $d_{oPs(1s)}(t,z,y,x)$ - ground state orto positronium density distribution (measured);
- $v_{\bar{p}}$ - antiproton velocity (measured);

- $N_{\bar{p}}(t, z, y, x)$ - antiproton distribution (measured);
- x_0/x_1, y_0/y_1, z_0/z_1 - the cavity or interaction region borders in x/y/z dimension (simulated).

Then, the total cross-section for antihydrogen formation with a ground state positronium is equal to:

$$\sigma^t(oPs(1s), \bar{p}) = \frac{N_{\bar{H}}}{f_{oPs(1s)}^{(t,z,y,x)}}. \tag{4.7}$$

The better is the estimation of $f_{oPs(1s)}^{(t,z,y,x)}$ and $N_{\bar{H}}$, the more precise value of the cross-section is obtained. However, an experimental estimation of the $f_{oPs(1s)}^{(t,z,y,x)}$ can be challenging, as it requires a detailed knowledge about the antiproton beam profile and ortho-positronium density distribution inside the cavity.

The expected uncertainty of the measurement of the antiproton distribution $N_{\bar{p}}(t, z, y, x)$ is at the level of 10 %. The precision is limited by the unknown branching ratios for the secondary particle production in antiproton annihilation [122]. The expected precision of $d_{oPs(1s)}(t, z, y, x)$ measurement should be similar to the precision of the positron flux measurement, which was measured to be about 10 %, see Appendix A. Then, the error of $f_{oPs(1s)}^{(t,z,y,x)}$ is minimum at 14 % level.

The accuracy of the measurement of the number of the antihydrogen atoms is limited by the uncertainty of the calibration of the MCP detector and the number of antihydrogen atoms hitting the detector. The calibration methods are described in Chapter 8. They are limited by the antiproton flux measurement accuracy which is about 10 %. In the final experiment, it is expected to detect between 150 (for 1 keV $\bar{p}$ energy) to 900 (10 keV $\bar{p}$ energy, see Chapter 5) antihydrogen atoms per pulse. The statistical error of that measurement is between 8 % to 3 %. The overall error of the antihydrogen atom detection should be between 13 % (1 keV) and 10 % (10 keV).

The achievable error for the cross-section measurement is in the order of 20 %.

4.3.2 Correction due to the energy distribution

The above equations assume that both positronium and antiproton bunches are monoenergetic. This is not experimentally achievable, that is why an effect of the beam energy distribution has to be studied.

The positronium energy is defined as a Maxwell-Boltzmann distribution with a mean value of 50 meV. In comparison to the antiproton beam energy, it has a negligible effect on the total energy of the collision. The antiproton beam energy is expected to have a Gaussian-shaped distribution with FWHM equal to 100 eV.

The cross-sections for the production of antihydrogen atoms and ions are calculated for given antiproton energy. Their values for the interaction of ground state positronium with antiprotons for two models, one from close-coupling family [110] and perturbation family [112] are shown in Figure 4.3. In order to estimate the effect of the antiproton beam energy distribution on the measurement, the weighted arithmetic mean of the cross-section values for realistic antiproton energies is calculated. The cross-section values were multiplied by a normalised antiproton beam energy distribution with FWHM equal to 100 eV. The cross-section values for intermediate

energies were interpolated between the available values. If this effective mean energy is equal to the mean initial beam energy, then the tested beam energy distribution does not have an effect on the cross-section measurement. Within 0.3 % there is no difference between the initial and the effective mean energy of the beam. This result is below the precision of the mean antiproton beam energy measurement, which means that the dependence of the cross-section mesurement on the energy distribution of the antiproton beam can be neglected.

Summary

The proposed method allows to extract the cross-sections $\sigma(oPs(1s), \bar{p})$, by measuring the ortho-positronium density and antiproton beam distributions together with the number of produced antihydrogen atoms. All these parameters can be measured using a designed detection system, which will be discussed later in the text.

4.3.3 Reaction 4.1 with mixed Ps states

According to calculations (for example [111, 112]), some positronium excited states can increase the antihydrogen atom/ion production even by two orders of magnitude. One of the possibilities is to use the oPs($3d$) state with 31 ns lifetime, or oPs($2p$) with 3.2 ns lifetime. In those cases, the cross-section measurements are more complicated.

Two positronium states

In the following Section two Ps states are considered. One in the ground state for which $\sigma(oPs(1s), \bar{p})$ is known (measured in the previous measurement). The other state is denoted by oPs(i). Then, the following system of linear equations can be written:

$$
\begin{aligned}
N_{\bar{H}} &= N_{\bar{H}\_oPs(1s)} + N_{\bar{H}\_oPs(i)} \\
\sigma(oPs(1s), \bar{p}) &= \frac{N_{\bar{H}\_oPs(1s)}}{f_{oPs(1s)}} \\
\sigma(oPs(i), \bar{p}) &= \frac{N_{\bar{H}\_oPs(i)}}{f_{oPs(i)}}
\end{aligned}
$$

where:

- $f_{oPs(j)}$ - describes the $\bar{p}$ - oPs(j) interaction;
- $N_{\bar{H}}$ - ia a total number of antihydrogen atoms;
- $N_{\bar{H}\_oPs(j)}$ - is a number of antihydrogen atoms formed from oPs(j) state.

Out of 7 parameters, three are not measured with the designed detection system: $N_{\bar{H}\_oPs(1s)}$, $N_{\bar{H}\_oPs(i)}$ and $\sigma(oPs(i), \bar{p})$. As there are three unknowns and three equations, this system is solvable and the total cross-section for antihydrogen atom formation with an excited positronium oPs(i) is equal to:

$$
\sigma(oPs(i), \bar{p}) = \frac{N_{\bar{H}} - \sigma(oPs(1s), \bar{p}) \cdot f_{oPs(1s)}}{f_{oPs(i)}}. \tag{4.8}
$$

The minimum precision of that measurement is about 20 %, which follows the precision of the cross-section measurement with only $1s$ positronium state.

More than two positronium states

The method described in the earlier paragraph can be extended to many positronium states. Then the cross-section for antihydrogen formation with an excited positronium state Ps(j) is equal to:

$$\sigma(oPs(j), \bar{p}) = \frac{N_{\bar{H}} - \sum_{n \neq j} \sigma(oPs(n), \bar{p}) \cdot f_{oPs(n)}}{f_{oPs(j)}}, \tag{4.9}$$

where $\sum_{n \neq j}$ means the sum over all included positronium states despite oPs(j). It is assumed that all $\sigma(oPs(n), \bar{p})$ are known.

The more complicated case, when three or more Ps states are included, but only $\sigma(oPs(1s), \bar{p})$ is known would require a simultaneous measurements of densities for different positronium excited states. At the moment it is not clear if it is possible to measure it within the setup of the GBAR experiment.

4.3.4 Reaction 4.2 with a ground state Ps

The number of antihydrogen ions produced at a given centre of mass energy can be written as:

$$N^{+}_{\bar{H}} = \sum_{k} \left(\int_{-\infty}^{\infty} \int_{z_0}^{z_1} \int_{y_0}^{y_1} \int_{x_0}^{x_1} d_{oPs(1s)}(t, z, y, x) \cdot N_{\bar{H}(k)}(t, z, y, x) \cdot \sigma^{t}(oPs(1s), \bar{\mathrm{H}}(k)) dx dy dz \cdot v_{\bar{\mathrm{H}}} dt \right), \tag{4.10}$$

where:

- $d_{oPs(1s)}(t, z, y, x)$ - density distribution of the ground state positronium (measured);
- x_0/x_1, y_0/y_1, z_0/z_1 - the cavity or interaction region borders in x/y/z dimension (simulated);
- $v_{\bar{\mathrm{H}}}$ - antihydrogen velocity (measured);
- $N_{\bar{H}(k)}(t, z, y, x)$ - distribution of antihydrogen atoms in state k (unknown);
- $\sigma^{0}(oPs(1s), \bar{\mathrm{H}}(k))$ - total antihydrogen ion formation cross-section for oPs($1s$) and $\bar{\mathrm{H}}(k)$ states (unknown);
- $\sum_{k}$ - sum over all antihydrogen states. The number of states is equal to $N_{\bar{H}\_st}$.

Simultaneously the number of $\bar{\mathrm{H}}$ is measured and is equal to:

$$N_{\bar{H}} = \sum_{k} \left(\int_{-\infty}^{\infty} \int_{z_0}^{z_1} \int_{y_0}^{y_1} \int_{x_0}^{x_1} N_{\bar{H}(k)}(t, z, y, x) dx dy dz dt \right).$$

This method has $2 \cdot N_{\bar{H}\_st} - 1$ uknown parameters. The presented experimental method, in which antihydrogen atoms and ions are produced at the same time in the same cavity, does not

allow to measure the antihydrogen ion formation cross-section directly. It is due to unknown distributions of antihydrogen atom states. However, according to theoretical calculations, the most significant contribution to the antihydrogen ion formation comes from three antihydrogen states $1s$, $2s$ and $2p$. This decreases the number of free parameters. Additionally, there is a possibility to extract the $N_{\bar{H}(2s)}$ in the Lyman alpha measurement [123], which could eliminate one free parameter.

4.3.5 Reaction 4.2 with mixed Ps states

In this Section, N_{Ps} number of positronium excited states is considered. The number of formed produced antihydrogen ions is equal to:

$$N^{+}_{\bar{H}} = \sum_{i}\sum_{k}\left(\int_{-\infty}^{\infty}\int_{z_0}^{z_1}\int_{y_0;x_0}^{y_1,x_1} d_{oPs(i)}(t,z,y,x)\cdot N_{\bar{H}(k)}(t,z,y,x)\cdot\sigma^{t}(oPs(i),\bar{\mathrm{H}}(k))dxdydz\cdot v_{\bar{\mathrm{H}}}dt\right), \tag{4.11}$$

where:

- $d_{oPs(i)}(t,z,y,x)$ - oPs(i) state density (measured);
- $v_{\bar{\mathrm{H}}}$ - antihydrogen velocity (measured);
- $N_{\bar{H}(k)}(t,z,y,x)$ - number of antihydrogen atoms in state k (unknown);
- $\sigma^{0}(oPs(i),\bar{\mathrm{H}}(k))$ - total antihydrogen ion formation cross-section for Ps(i) and $\bar{\mathrm{H}}(k)$ states (unknown);
- $\sum_i$ - sum over all considered positronium states;
- $\sum_k$ - sum over all available in the beam antihydrogen states. The total number of states is equal to $N_{\bar{H}\_st}$.

The measured number of $\bar{\mathrm{H}}$ is equal to:

$$N_{\bar{H}} = \sum_{k}\left(\int_{-\infty}^{\infty}\int_{z_0}^{z_1}\int_{y_0}^{y_1}\int_{x_0}^{x_1} N_{\bar{H}(k)}(t,z,y,x)dxdydzdt\right).$$

It is assumed that the antihydrogen beam flux does not change during the reaction, as only few antihydrogen ions can be produced during one beam crossing for given beam parameters. This model has $N_{\bar{H}\_st}\cdot N_{Ps} + N_{Ps} + N_{\bar{H}\_st} - 1$ uknown parameters.

However, according to theoretical calculation, the excited positronium states interact almost only with a ground state antihydrogen atom. Including that assumption in the model, the number of free parameters decreases to $2\cdot N_{Ps} + 2\cdot N_{\bar{H}\_st} - 2$.

4.3.6 Possible improvement of the cross-section measurements for reaction 4.2

Generally, the cross-section measurements of antihydrogen ion production are very challenging. An easier solution would be to measure these cross-sections with a direct antihydrogen beam in

a ground state. In principle, the first reaction provides an antihydrogen beam that after some time deexcites fully to the ground state. This beam could be used to measure the reaction 4.2 with only one antihydrogen atom state, but it would require making a second equally dense positronium target within a very short time. At the current stage of the experiment, it is not technically available. Another possibility is to perform symmetric measurements of the hydrogen ion formation with a hydrogen beam. This solution is recommended to be considered during future upgrades of the apparatus.

4.4 Summary

Some of the key parameters for the GBAR experiment are the cross-section values for the antihydrogen atom and ion production. They are necessary as they allow to optimise the antihydrogen ion production. A few theoretical calculations are available. However, there is a lack of measurements, which could settle which model is correct in the energy region relevant to the GBAR experiment.

Within the GBAR experiment infrastructure, it is possible to perform the antihydrogen atoms and ions formation for different positronium excited states. The basic tests with a ground state positronium require measurements of:

- $d_{oPs(1s)}(t, z, y, x)$ - ground state positronium density distribution;
- $v_{\bar{p}}$ - antiproton velocity;
- $N_{\bar{p}}(t, z, y, x)$ - antiproton beam distribution;
- $N_{\bar{H}}$ - number of produced antihydrogen atoms;
- $N_{\bar{H}^+}$ - number of antihydrogen ions.

The energy distribution of the antiproton beam should be also measured in order to support the hypothesis about the independence of the cross-section value from antiproton beam energy distribution.

The tests with excited positronium states require additional measurements of the densities of the excited Ps states distributions $d_{oPs(i)}(t, z, y, x)$ and antihydrogen atom distributions $N_{\bar{H}(k)}(t, z, y, x)$. Any additional test of antihydrogen states population would be of great importance. However, it is not planned at that stage of the experiment.

The measurement of antihydrogen atom formation cross-sections can be performed entirely experimentally, while the extraction of antihydrogen ion cross-section from the data would require some theoretical assumptions.

Chapter 5

Positronium cloud - antiproton beam interaction

In this chapter, the antiproton - positronium interaction region is described. Also, the number of antiatoms that may be produced is estimated. It is done for given assumptions on the incident antiproton and positron beams and different geometries of the positronium target using a developed Monte-Carlo simulation in Python programming language.

5.1 Geometries of the interaction region

The process of antihydrogen atom and ion formation requires mixing of an antiproton beam with a positronium cloud. In GBAR, the final antihydrogen ion production will take place in a reaction cavity to confine the positronium cloud. Its detailed design can be found in [102]. A general scheme of the cavity is presented in Figure 5.1. It has the shape of a tube with a square cross-section of 2 mm × 2mm and 20 mm length. In the future, the cross-section will be decreased to 1 mm by 1 mm to increase the Ps cloud density. However, focusing of antiproton and positron beams to that size is a very challenging task. The four walls of the tube are made of different materials.

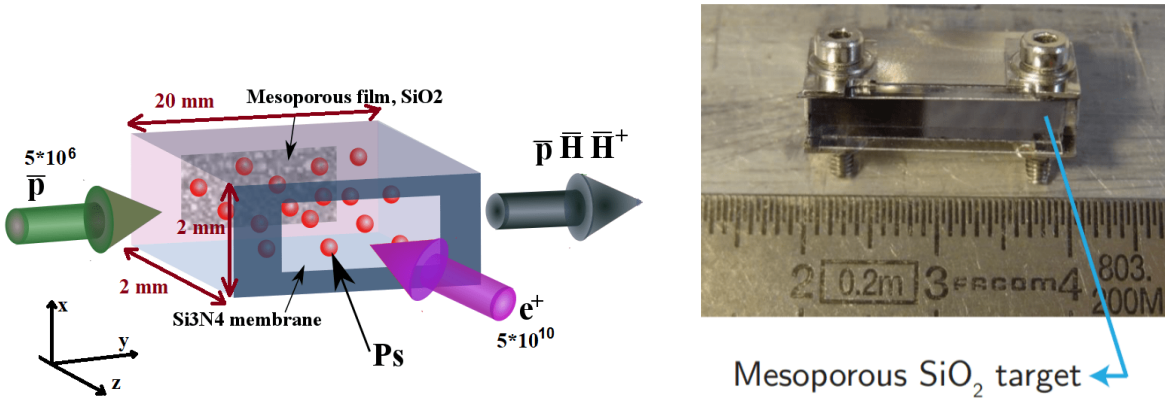

Figure 5.1: Reaction cavity where the positronium cloud interacts with the antiproton beam. Left: scheme. Right: photograph.

The antiproton beam enters the cavity from a 2 mm × 2 mm side. The antiproton entrance and exit walls are empty. The positron beam comes from a side through a 2 mm by 10 mm window made from 30 nm thick Si_3N_4. The positrons then reach the opposite wall made of a 1.6 μm mesoporous silica layer deposited on a 500 μm thick silica plate. They convert inside this layer into o-Ps which is re-emitted into the tube.This construction allows positrons to go through and at the same time confine the positronium cloud. The support for the window is made from 200 μm thick silicon. The top of the cavity is made from a fused silica plate with high transparency for the lasers that are used to excite positronium. The bottom wall consists of an aluminum mirror which is supposed to reflect the laser light. The mirror is coated with a 100 nm thick silica layer to allow for 100 % positronium reflection. A photograph of a reaction cavity is shown in Figure 5.1. In front of the cavity, a collimator will be added to block a possible antiproton beam halo (see Section 6.2.1).

When ELENA comes in operation there will be a learning period during which it is expected that the antiproton beam will not be focused onto this 2 mm × 2 mm cavity. To be able to produce antihydrogen even with the imperfect beam, another interaction scheme has been developed, in which the positron beam is incident on a flat mesoporous silica target. There are no walls to keep Ps from flying, so the positronium cloud is slowly expanding. The antiproton beam is guided to this cloud through a collimator placed just in front of the target, see Figure 5.2. The collimator is very important as it increases the beam quality. It stops the antiproton beam halo which does not participate in the reaction.

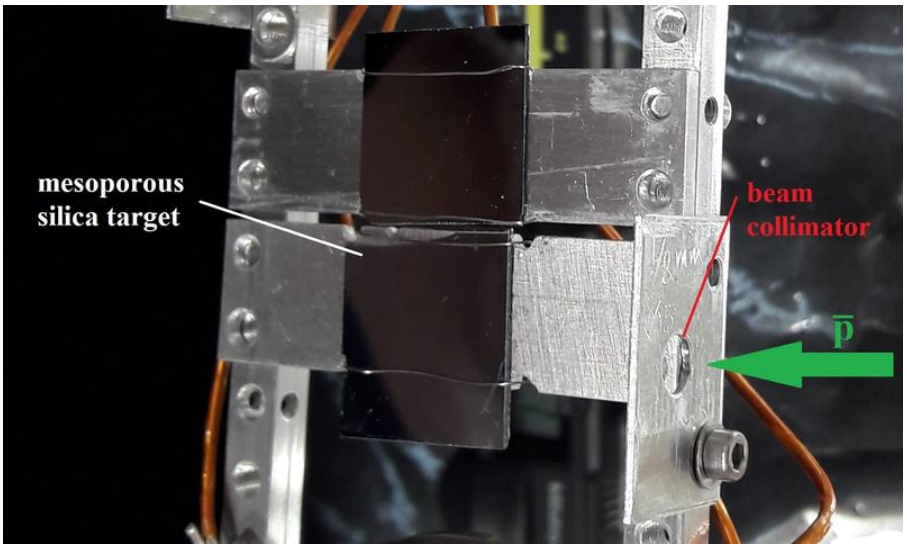

Figure 5.2: Photograph of a flat mesoporous silica target with an antiproton beam collimator.

5.2 Positronium production

The slow positron beam used for positronium formation is prepared with the electron linac and the two Penning Malmberg traps. Once the high intensity beam is produced, it is transported to the reaction chamber where conversion from positron to positronium takes place. The main difficulty related to this process is that the beam has to be transported from a high magnetic field to a region with almost no magnetic field. This requires a complicated focusing system as well as a shielding for the magnetic field. The beam energy has to be increased to 3 keV to obtain

the optimum positron implantation depth (193 nm), which allows creating cold positronium. Cold positronium is essential to keep Ps within the reaction cavity.

Positronium for the GBAR experiment is produced by positron implantation on a mesoporous silica target as already developed and tested by collaborators [75, 76, 77]. The target which is going to be used in the final experiment is a mesoporous film prepared via a sol-gel process. Its ortho-positronium emission yield is 30 % with an energy of 48 ± 5 meV [124].

There are three detectors which are used to characterise the positron beam in the reaction chamber. One of them is an MCP detector, which allows to precisely determine the position and time distribution of the positron pulse. It is crucial, as the beam has to be guided through the 2 mm $\times$ 10 mm window. The second detector is a plastic scintillator, which is used to cross-check the time distribution of the beam.

The primary detector used for the positronium density measurement is a $PbWO_4$ crystal situated 10 cm from the reaction cavity. This detector has a short signal time width of 10 ns. It can work at a relatively low gain of 10^3, which allows detecting the annihilation of the expected 10^{10} Ps. This detector could also be used to determine the positron beam flux. A positronium density measurement method is described in more detail in [66].

5.2.1 Positronium formation simulation

The positronium formation process is studied using a Python simulation developed for this thesis. It is a Monte-Carlo simulation which generates positronium atoms as individual objects of the Ps class. The propagation of each atom is tracked every constant interval of time.
The following positronium beam characteristic is used:

- Ortho-positronium formation - 30 % of the positron beam;
- Cosine angular distribution of Ps emission and reflection from the cavity walls. In principle, these distributions are not known because they strongly depend on the material surface. It is expected, that these distributions are either isotropic or cosine. According to the experience of our and other groups working with the same positronium converters, the cosine distributions are expected. These parameters are going to be tested with a dedicated experiment.
- Maxwell-Boltzmann energy distribution with 50 meV mean.
- Time between the implantation of the positron beam and the positronium emission - 10 ns [125].

Positronium formation for a reaction cavity

In this case positronium is produced at the back side of the 2 mm by 2 mm by 20 mm cavity. The parameters of the incident positron beam used in the simulations are:

- The positron bunch has a Gaussian time distribution with 30 ns standard deviation.
- The spatial distribution in the plane perpendicular to the beam is Gaussian with standard deviations of 0.3 mm in the x direction and 2 mm in the y direction, i.e. along the antiproton beam. The size of the beam is truncated by the Si_3N_4 window.

- The number of positrons is $N_{e^+} = 5 \times 10^{10}$ e^+/pulse.

The positronium distribution is simulated in all 4 dimensions. The number of Ps participating in the reaction does not include Ps escaping the cavity, which is equal to up to 3 % during the first 100 ns of the positronium formation. The positronium density as a function of time is shown in Figure 5.3a.

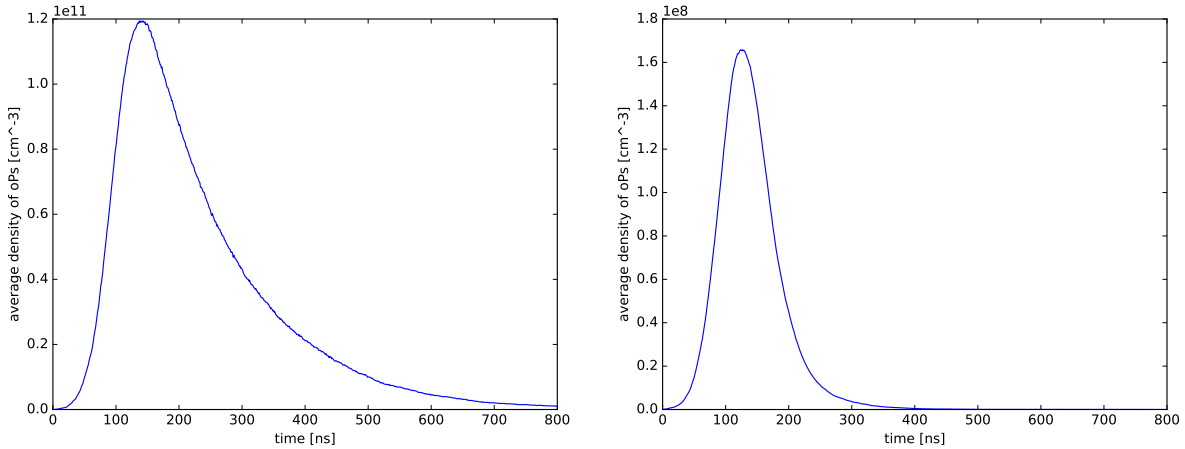

(a) Number of incident positrons: 5×10^{10}. (b) Number of incident positrons: 5×10^{8}.

Figure 5.3: Positronium density as a function of time for a) a 2 mm × 2 mm × 20 mm cavity, b) a flat positronium converter.

Positronium formation for a flat positronium converter

In that case the positron beam is incident on a flat mesoporous silica target.
The parameters of the incident positron beam used in the simulation are:

- The positron bunch has a Gaussian time distribution with 30 ns standard deviation.
- The spatial distribution in the plane perpendicular to the beam is Gaussian with standard deviations of 1 mm in the x direction and 3 mm in the y direction, i.e. along the antiproton beam.
- The number of positrons is $N_{e^+} = 5 \times 10^{8}$ e^+/pulse.

Additionally, there is a 5 mm diameter collimator in front of the positronium - antiproton interaction region. Taking into account these assumptions the positronium - antiproton interaction region is considered to be $6 \cdot \sigma_y = 18$ mm long tube with radius equal to 2.5 mm, see Figure 5.4.

Comparison

The use of the cavity allows confining positronium inside the antiproton-positronium interaction region. The 90 % of the beam fits within 450 ns time interval. In the flat target case, the 90 % of the beam fits only within 200 ns. This largely decreases the antiproton-positronium interaction time and affects the antihydrogen atom and ion production rate, which is discussed in the next Sections.

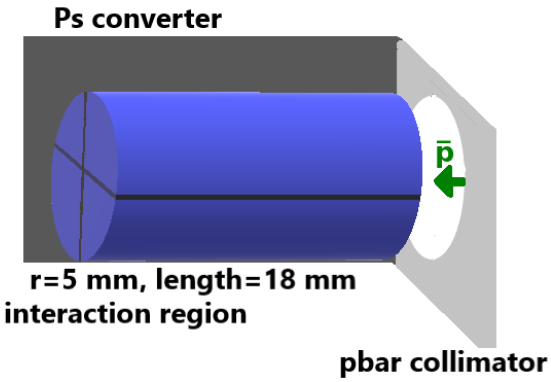

Figure 5.4: Scheme of the positronium - antiproton interaction region with a flat positronium converter.

5.3 Antiproton beam

The antiproton beam comes originally from ELENA. It is guided and focused into the interaction region using a designed system described in the next Chapter. Its characteristics at the reaction chamber level is measured using two detectors. The first is an MCP detector with a fast P46 phosphor screen. It allows seeing the beam spot size. The second detector is a plastic scintillator, which is sensitive to the secondary particles emitted in the antiproton annihilation process. It is used to measure the time distribution and to estimate the antiproton beam flux.

The following parameters of the antiproton beam are used in the estimation of the antihydrogen production rate:

- constant energy between 1 keV and 10 keV.
- number of particles: 5×10^6 antiprotons/pulse or 4×10^6 antiprotons/pulse (20 % of the beam annihilates on the collimator), depending on the case;
- time distribution - Gaussian distribution with $\sigma_t = 50$ ns; the time shape is inherited from the ELENA beam; the delay with respect to the positron timing is adjusted to obtain the highest antihydrogen production rate;
- distribution in the plane perpendicular to the antiproton beam direction

  cavity - two dimentional Gaussian distribution with $\sigma_x = \sigma_y = 0.3$ mm;

  flat target - two dimentional Gaussian distribution with $\sigma_x = \sigma_y = 0.8$ mm.

The antiproton beam distribution in space and time is simulated using similar simulation like the one prepared for positronium formation. The advantage of this simulation technique is that it allows for easy modification of any beam parameter and if needed, it includes interactions with other objects in the simulation.

5.4 Estimation of the antihydrogen production rate

The production of antihydrogen atoms from ground state positronium is considered. In this estimation, the interaction between the positronium cloud and the antiproton beam in four dimensions is considered.

To estimate the antihydrogen formation rate, the interaction region is divided into small cells of size 0.2 mm × 0.2 mm × 0.2 mm. The number of particles in each cell is registered every 0.2 [mm]/$v_{\bar{p}}$ [mm/ns] ns, where $v_{\bar{p}}$ is the velocity of antiprotons. Under these assumptions, the number of antihydrogen atoms formed in one cell is equal to:

$$N_{\bar{H}}^{cell}(x, y, z, t) = d_{oPs(1s)} \cdot N_{\bar{p}} \cdot L \cdot \sigma(oPs(1s), \bar{p})$$

where:

- $d_{oPs(1s)}$ - ground state ortho-positronium density in a cell;
- $N_{\bar{p}}$ - number of antiprotons in a cell;
- L - 0.2 mm;
- $\sigma(oPs(1s), \bar{p})$ - the total cross-section for antihydrogen formation from Ps($1s$).

The total number of produced antihydrogen atoms is equal to the sum of $N_{\bar{H}}^{cell}(x, y, z, t)$ over all cells and all time steps.

Two following theoretical models for the total antihydrogen formation cross-section are used:

- 3bCC Ps1s sumH - close-coupling model from 2016 [110];
- 3B CBA Ps1s sumH - perturbation model from 2014 [112].

5.4.1 Experimental conditions

In this thesis three different interaction models are considered:

Case A. The interaction between the antiprotons and the positrons takes place inside a cavity of size 2 mm by 2 mm by 20 mm

A.1. with 5×10^{10} incident positrons and 5×10^{6} antiprotons. This model describes the nominal parameters of the GBAR experiment. It is crucial, as this is the case in which the antihydrogen ion can be produced. It assumes no antiproton beam losses.

A.2. with 5×10^{8} incident positrons and 4×10^{6} antiprotons. It is assumed that 20 % of the beam annihilates before reaching the cavity. This is a more realistic model which suits the first antihydrogen production tests with the cavity. It can be also directly compared with a model B.

Case B. The interaction between the antiprotons and the positrons takes place inside a cavity in front of a flat positronium conversion target with 5×10^{8} incident positrons and 4×10^{6} antiprotons. 20 % of the beam annihilates before reaching the interaction region. This case describes the first antiydrogen production test.

5.4.2 Case A.

The resulting antihydrogen production rates for different cross-section values are summarised in Table 5.1, Figure 5.5, for Case A.1. and Table 5.2 for Case A.2. In case A.1. between 350 to 3000 antihydrogen atoms are produced within one pulse. In case A.2. only between 3 to 25 antihydrogen atoms are expected.

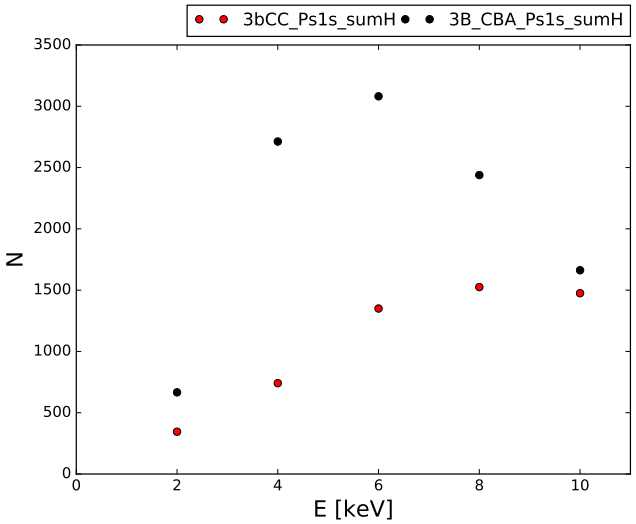

Figure 5.5: Number of antihydrogen atoms produced in Case A.1. calculated for antiproton energies between 2 keV and 10 keV.

$\bar{p}$ energy	3bCC Ps1s sumH	3B CBA Ps1s sumH
2 keV	345	666
4 keV	741	2710
6 keV	1350	3080
8 keV	1530	2440
10 keV	1480	1660

Table 5.1: Number of antihydrogen atoms produced in Case A.1. calculated for antiproton energies between 2 keV and 10 keV.

$\bar{p}$ energy	3bCC Ps1s sumH	3B CBA Ps1s sumH
2 keV	2.8	5.3
4 keV	5.9	21.7
6 keV	10.8	24.7
8 keV	12.2	19.5
10 keV	11.8	13.3

Table 5.2: Number of antihydrogen atoms produced in Case A.2. calculated for antiproton energies between 2 keV and 10 keV.

Antihydrogen ion production

The number of produced antihydrogen ions can be estimated using a simple model:

$$N_{\bar{H}^+} = d_{oPs(1s)} \cdot L \cdot N_{\bar{H}(1s)} \cdot \sigma^0(oPs(1s), \bar{\mathrm{H}}(1s)) + d_{oPs(1s)} \cdot L \cdot N_{\bar{H}(2s)} \cdot \sigma^0(oPs(1s), \bar{\mathrm{H}}(2s)) \quad (5.1)$$

where:

- $d_{oPs(1s)}$ - ground state Ps density in the cavity, constant in all four dimensions;
- L - length of the cavity;
- $N_{\bar{H}(1s)} = 0.3 \cdot N_{\bar{\mathrm{H}}}$ - number of antihydrogen atoms in the ground state. According to calculations it should be about 30 % of the total antihydrogen atom beam. This ratio depends not only on cross-section values but also on the cavity length. In order to estimate the amount of antihydrogen atom the models presented in the previous sections are used.
- $N_{\bar{H}(2s)} = 0.6 \cdot N_{\bar{\mathrm{H}}}$ - number of antihydrogen atoms in the 2s state.
- $\sigma^0(oPs(1s), \bar{\mathrm{H}}(1s))$ - the total antihydrogen ion formation cross-section for Ps($1s$) and $\bar{\mathrm{H}}(1s)$ states. In this case only the *CDW-FS Ps1s* model is used [111, 112]. Ion formation from the $1s$ and $2s$ states of the antihydrogen atoms dominates over the ion formation from the other antihydrogen atom states, justifying their neglect.

The results of the estimation are summarised in Table 5.3. When only the antihydrogen atom in the ground state is included, the optimal energy range narrows between 5.5 keV and 10 keV. Between 4 keV and 5.5 keV antihydrogen energy, the production of the ion from the 2s antihydrogen state dominates. Below 4 keV antiproton energy only the ground state antihydrogen is produced, thus the antihydrogen ion formation is not possible.

$\bar{\mathrm{H}}$ **model**	**CDW-FS Ps1s**	**CDW-FS Ps1s**
$\bar{p}$ **energy**	**3bCC Ps1s sumH**	**3B CBA Ps1s sumH**
4 keV	0.09	0.3
6 keV	0.4	0.8
8 keV	0.3	0.4
10 keV	0.2	0.2

Table 5.3: Estimation of the number of antihydrogen ions formed in Case A.1. calculated for antiproton energies between 4 keV and 10 keV

5.4.3 Case B.

Results for the production rate of antihydrogen for different cross-section values are summarised in Table 5.4, Figure 5.6. The expected number of antihydrogen atoms is between 0.4 and 3.9.

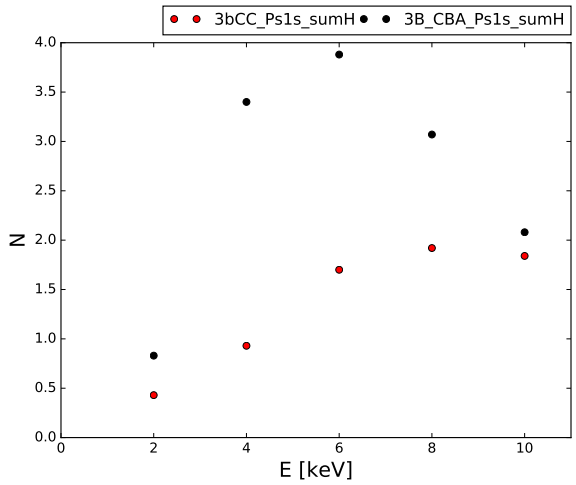

Figure 5.6: Number of antihydrogen atoms produced in Case B calculated for antiproton energies between 2 keV and 10 keV.

$\bar{p}$ **energy**	**3bCC Ps1s sumH**	**3B CBA Ps1s sumH**
2 keV	0.4	0.8
4 keV	0.9	3.4
6 keV	1.7	3.9
8 keV	1.9	3.1
10 keV	1.8	2.1

Table 5.4: Number of antihydrogen atoms produced in Case B calculated for antiproton energies between 2 keV and 10 keV.

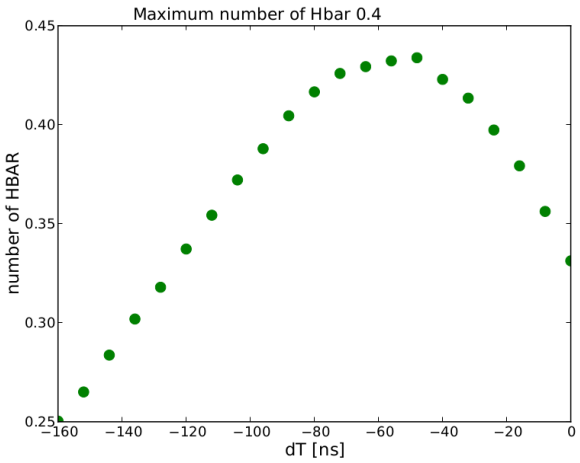

Figure 5.7: Antihydrogen atom production yield as a function of the time difference between the antiproton and positron bunches for case B. The 3bCC_Ps1s_sumH model for 2 keV antiproton energy is used.

5.4.4 Optimisation of the time delay between the antiproton beam and the positron beam

The relative beam timings between the antiproton beam and the positron beam should be optimised in order to obtain the highest antihydrogen production rate. This can be simulated by varying the difference between the mean values of the two bunch time distributions. The optimum delay of the antiproton beam with respect to the positrons is -50 ns for all cases, A.1., A.2. and B, see an exemplary Figure 5.7.

5.5 Summary

The antiproton - positronium mixing scheme developed by the GBAR collaboration allows producing more than a few hundred antihydrogen atoms and about 0.3 antihydrogen ions using the ground state positronium. A simplified scheme with an open reaction target is also proposed. It can be used to perform first antihydrogen atom formation. It is easier to perform the experiment with this configuration as it does not require very accurate beam focusing. In this case, it is expected to get a few antihydrogen atoms per pulse. The expected low production rate for antihydrogen atoms in cases B. and A.2. and antihydrogen ion in case A.1. requires a detailed study of the detection possibilities.

Chapter 6

Study of the annihilation of antiprotons

6.1 Introduction

The variety of processes occuring during the interaction of an antiproton with a nucleus was discussed for the first time by H-P. Duerr and E. Teller in 1956 [126]. The purpose of this Chapter is to describe the interaction of a low energy antiproton ($E < 10$ keV) with matter in order to understand the phenomena occurring during the detection of antiprotons, antihydrogen atoms and ions. The description of $\bar{p}$ annihilation is focused on the production of secondary particles in the realistic conditions of the GBAR experiment. A correctly understood annihilation background allows to minimise systematic errors in the measurements of antiproton, antihydrogen atom and ion fluxes.

In this Chapter, it is assumed that antiprotons are created in vacuum and propagate in the positive z-axis direction with a given energy and after a certain time hit a target made of a defined material. When an antiproton hits the target it may undergo elastic or inelastic scattering. If it is elastically scattered it annihilates somewhere else in the system. If the antiproton goes inside the target, it loses its energy. The energy loss of an ion in matter is described by the stopping power S. The electric and nuclear stopping powers in different materials are described in [127]. The penetration depth of 10 keV antiprotons in silicon is about 1500 nm), which is about 1.6 times larger than for 10 keV protons ($\approx$ 900 nm). For antiproton energies lower than tens of eV, which is usually below the excitation and ionisation energy of an atom in the target material, the antiproton kicks out one electron from an atom and binds with the created ion [128]. Then, the bound antiproton cascades to lower energy levels of the created exotic nucleus. This process is accompanied by X-ray and Auger electrons emission. After typically a few ps, the antiproton is in the range of the strong interaction and annihilates either on a proton or a neutron. The only known long lived exotic atoms with an antiproton are the antiprotonic helium and protonium. The first one has been thoroughly studied by the collaborations working with the LEAR accelerator and nowadays by the ASACUSA experiment [129, 130]. The protonium was produced and detected by ATHENA collaboration [131].

6.1.1 Annihilation channels

The main annihilation channels of antiprotons on neutrons and protons are shown in Table 6.1, [132, 133]. On average, in one $\bar{p}p$ annihilation $N_{anni-p} = 1.5\pi^+ + 1.5\pi^- + 1.9\pi^0$ are produced. An annihilation on a neutron gives $N_{anni-n} = 1.1\pi^+ + 2.1\pi^- + \pi^0$.

$\bar{p}p$	
Channel	**BR**
$2\pi^0$	0.0693 ± 0.0043 [134]
$n\pi^0$ $(n \geq 1)$	$4.1^{+0.2}_{-0.6}$ [135, 136, 137]
$\pi^- + \pi^+$	0.307 ± 0.013 [134]
$\pi^- + \pi^+ + \pi^0$	5.82 ± 0.43 [138]
$\pi^- + \pi^+ + 2\pi^0$	9.3 ± 3.0 [135, 136, 137]
$\pi^- + \pi^+ + 3\pi^0$	23.3 ± 3.0 [135, 136, 137]
$\pi^- + \pi^+ + 4\pi^0$	2.8 ± 0.7 [135, 136, 137]
$2\pi^- + 2\pi^+$	6.9 ± 0.6 [135, 136, 137]
$2\pi^- + 2\pi^+ + \pi^0$	19.6 ± 0.7 [135, 136, 137]
$2\pi^- + 2\pi^+ + 2\pi^0$	16.6 ± 1 [135, 136, 137]
$2\pi^- + 2\pi^+ + 3\pi^0$	4.2 ± 1 [135, 136, 137]
$3\pi^- + 3\pi^+$	2.1 ± 0.25 [135, 136, 137]
$3\pi^- + 3\pi^+ + \pi^0$	1.85 ± 0.15 [135, 136, 137]
$3\pi^- + 3\pi^+ + n\pi^0$ $(n \geq 2)$	0.3 ± 0.1 [137]
$K^+ + K^-$	0.099 ± 0.005 [134]
$K^+ + K^- + K^0$	0.237 ± 0.016 [139]
$K^+ + K^- + \pi^0$	0.237 ± 0.015 [140]
$K^\pm + K^0 + \pi^\mp$	0.46 ± 0.07 [139]
$K^\pm + K^0 + \pi^\mp + \pi^0$	0.47 ± 0.06 [140]
$\bar{p}n$	
Channel	**BR**
$\pi^- + n\pi^0$ $(n \geq 1)$	16.4 ± 0.5 [137, 141]
$2\pi^- + \pi^+ + n\pi^0$ $(n \geq 0)$	59.7 ± 1.2 [137, 141]
$3\pi^- + 2\pi^+ + n\pi^0$ $(n \geq 1)$	23.4 ± 0.7 [137, 141]
$4\pi^- + 3\pi^+ + n\pi^0$ $(n \geq 1)$	0.39 ± 0.07 [137, 141]

Table 6.1: Antiproton annihilation on proton and neutron. Table adapted from [133]. More channels including decays with η mesons are available in [142].

The following description concerns a situation when a single antiproton annihilates on a free proton or a neutron. It is possible to imitate these conditions by using for example hydrogen as a target material [134]. However, in the case of the GBAR experiment, antiprotons annihilate on a target and detectors made from elements with a mass number $A > 1$. Annihilation inside the nucleus leads to the excitation of the nucleus and causes additional interactions of annihilation products with both the nucleus and the surrounding atoms.

Additionally, a part of the antiprotons annihilates in flight [143], i.e. when the antiproton momentum contributes to the secondary particles momenta. In 2012 it was detected for the first time for low energy $E = 130$ keV antiprotons [144]. The main mechanism of annihilation is the same as for stopped antiprotons, thus it will not be discussed in detail.

6.2 Antiproton annihilation simulation

In order to study the antiproton annihilation products a simplified simulation was performed with 10^4 antiprotons in a form of a mono-energetic beam with 10 keV energy. It is propagating in the z direction from a point-like source towards a target located at $z = 1817$ mm. In order to keep the discusion consistent with the experiment, the following target elements are considered: carbon in the form of graphite (Z=6, A=12), iron (Z=26, A=56), gold (Z=79, A=297) and lead (Z=82, A=207). The first two elements are light, with relative equilibrium between their number of neutrons and protons. The other two are heavier, but with Z smaller than 92. A graphite cup is one of the internal components of the Faraday Cup used for the measurement of the antiproton flux. Gold is sometimes used as a front coating of the MCP detector. Iron is the main ingredient of stainless steel, which is used for antiproton flux detectors. Lead is the main ingredient of lead glass, from which an MCP is made. Additionally two types of targets composed of several materials are considered: stainless steel and lead glass.

The simulated scheme represents the GBAR antihydrogen ion production system together with detectors. It consists of the reaction chamber, antiproton, anihydrogen atoms and ions transport lines, and concrete walls and floor. It is described in detail in the following Chapters. In the present Section it is used as an example setup, which allows to study antiproton annihilation in realistic conditions.

The simulation was implemented in the framework of the Geant4 software. The interaction of antiprotons with nuclei is described with the FTF (Fritiof) model and precompound nuclear de-excitation model of Geant4 [145]. An experiment has proven [146] the inconsistency between the FTF model and data, however the model is now largely improved [145]. Another model, CHIPS, described in the paper [146] is not supported by Geant4 anymore, and is not considered. The name of the corresponding library is: $QGSP\_BERT\_EMX$. The goal of this Section is to describe the simulation results and compare them with simple naive models.

Composition of materials

In the simulation, the target thickness is 1 mm. A few target materials are used: lead glass, stainless steel, graphite, iron, gold, lead. All vacuum pipes and flanges are made from stainless steel. The wall and the floor are made from 50 cm thick concrete. The following materials compositions in fraction of mass are used:

Lead glass (MCP detector material):

- 15.7% oxygen; 8% silicon; 0.8% titanium; 0.3% arsenic; 75.2% lead.

Stainless steel:

- 74% iron; 18% chromium; 8% nickel.

Concrete:

- 1% hydrogen; 0.1% carbon; 52.9% oxygen; 1.6% sodium; 0.2% magnesium; 3.4% aluminium; 33.7% silicon; 1.3% potassium; 4.4% calcium; 1.4% iron.

6.2.1 Antiproton elastic scattering

Elastic scattering of antiprotons is very important from a background estimation point of view. When antiprotons are elastically backscattered, they annihilate on different parts of the system, even up to few meters away from the target. Considering that antiproton velocities are smaller than 1.3 m/μs, annihilations of backscattered antiprotons may create a background delayed in time.

The cross-section for antiproton elastic scattering at the surface of the material is equal to $\sigma_{total}^{elast} = \sigma_{EM}^{elast} + \sigma_{had}^{elast}$, where σ_{EM}^{elast} is the electromagnetic elastic scattering amplitude and σ_{had}^{elast} is the hadronic elastic scattering amplitude. The hadronic interaction is well described by the extended Glauber model of the antiproton-nucleus interaction [147, 148]. The electromagnetic part is dominant at energies below 10 keV and can be approximately estimated using Rutherford scattering.

The Rutherford formula for the elastic scattering of charged particles in the Coulomb interaction is

$$\frac{d\sigma}{d\Omega} = \left(\frac{Z_1 Z_2 \alpha \hbar c}{4 E_{k1} sin^2(\theta/2)} \right)^2$$

where Z_1 is the charge of the incident particle with kinetic energy E_{k1} [MeV], Z_2 is the mean charge of the target nuclei, $\alpha = 1/137$ is the fine structure constant, $\hbar c = 197$ MeV $\cdot$ fm, and θ is the scattering angle.

The backscattering cross-section is equal to $\int_{\pi/2}^{\pi} \frac{d\sigma}{d\Omega}$. An example target is a plate made from lead glass. For this material the mean nuclear charge is $Z_2 = 64$ and the average particle density is 1.2×10^{22} cm^{-3}. The calculated cross-section for backscattering of 10 keV antiprotons on lead glass is equal to 1.1×10^{-19} cm^2. Considering that the penetration depth of antiprotons in lead is about 10 times smaller than in silicon ($\approx$ 150 nm), then the probability for elastic backscattering of an antiproton on lead glass is equal to about 20 %.

This information is very important, as very often a target made from lead glass or iron is used to detect the antiproton flux. The correction on the antiproton flux of the order of 20 % is significant and has to be included in the measurement, unless the measurement technique demands that antiprotons annihilate within the detector. Also, backscattered antiprotons annihilate on unknown parts of the experiment which creates an extra, delayed background. Finally, the MCP detector is going to be used for antihydrogen ions detection, and here the elastic scattering correction should be also included.

Simulation - Faraday Cup

The elastically scattered antiprotons can annihilate very far away from the target, when there is space to fly backwards. As antiprotons used in the experiment are relatively slow (more than 0.7 μs per meter), this can induce an unwanted, delayed background for other measurements. We must then force the antiprotons to annihilate as close to the target as possible. This could be done for example by using a Faraday Cup.

In this case a cylindrical Faraday Cup is used. The drawing is presented in Figure 6.1. It is 5 cm long and has a 1 cm diameter input window. The percentage of 10 keV antiprotons annihilating inside the cup is equal to 99.9 %, thus this is a recommended solution for the antiproton flux measurement.

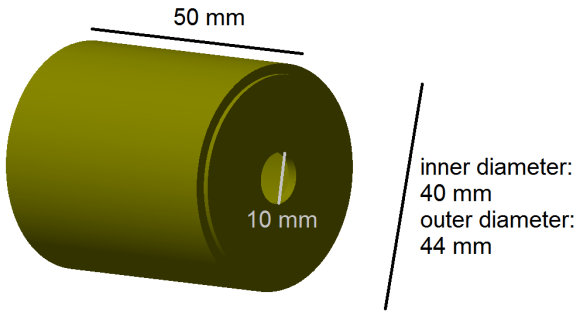

Figure 6.1: Drawing of a stainless steel Faraday Cup used as an antiproton flux detector.

6.2.2 Particle emission induced by an antiproton annihilating in a nucleus

The background estimation requires a knowledge about the secondary particles production in an antiproton annihilation process. For antiproton incident energies in the 1 to 10 keV range, when the annihilation occurs with one of the nucleons inside a nucleus, the annihilation takes place in the outer part of the nucleus, where the nuclear density is equal to about 10 % of the central density [149]. It releases 1.88 GeV energy. On average 5 pions are produced with a mean energy of about 230 MeV, and reaching 1 GeV. About 25 % of the created pions interact with the nucleus before escaping and start an intranuclear cascade. These pion-nucleus interactions have a short range and have a large energy transfer. Pions can either be scattered or absorbed. Also the Δ resonance or additional pions can be produced. The large energy can lead to kick out of protons, neutrons, deuterons, tritons, Δ particles or even light nuclei, like helium [150]. After emission of many particles, the residual nucleus is left in an excited state, which leads to evaporation of other particles such as neutrons and protons.

The modelling of antiproton annihilation in a nucleus requires a good description of the intranuclear cascade, the particle emission, and the distribution of residual nuclei. The light particle emission induced by stopped antiprotons for different targets was thoroughly studied with the LEAR accelerator, for example in [151, 152].

Simulation

According to the Geant4 simulation the following particles are produced in an antiproton annihilation: photons, pions (plus, minus, zero), neutrons, protons, eta, kaons and light nuclei. The energy distributions of these particles (except light nuclei that immediately stop in the considered detectors) for the stainless steel target and 10 keV antiproton energy are shown in Figure 6.2. Pions, eta and kaons are direct products of the antiproton annihilation. Neutrons, protons and light nuclei are produced from the cascade or evaporadion when the nucleus reaches its equilibrium state.

The simulated number of neutrons, protons, photons, eta (all states) and kaons (all states) per annihilation for different targets are presented in Table 6.2. Even though there are measurements of neutron and proton production in antiproton annihilations [152, 151], they are all performed at higher energies. It is thus not possible to say whether the absolute numbers are correct or not. The production of eta mesons and kaons is similar for all targets. Both particles have wide energy distributions.

target material	n	p	γ	eta	kaons
graphite	0.79 ± 0.01	0.77 ± 0.01	9.70 ± 0.03	0.30 ± 0.01	0.026 ± 0.002
iron	1.48 ± 0.01	0.59 ± 0.01	16.00 ± 0.04	0.31 ± 0.01	0.027 ± 0.002
gold	2.34 ± 0.02	0.21 ± 0.01	16.62 ± 0.04	0.29 ± 0.01	0.028 ± 0.001
lead	3.08 ± 0.02	0.125 ± 0.004	21.83 ± 0.05	0.29 ± 0.01	0.030 ± 0.002
stainless steel	1.48 ± 0.01	0.59 ± 0.01	16.02 ± 0.04	0.30 ± 0.01	0.027 ± 0.002
lead glass	2.63 ± 0.02	0.30 ± 0.01	20.35 ± 0.05	0.29 ± 0.01	0.028 ± 0.002

Table 6.2: Neutron/proton/γ/η/kaons production yield per antiproton annihilation on different target materials. The antiproton energy is equal to 10 keV. The simulation is performed for 10000 antiprotons.

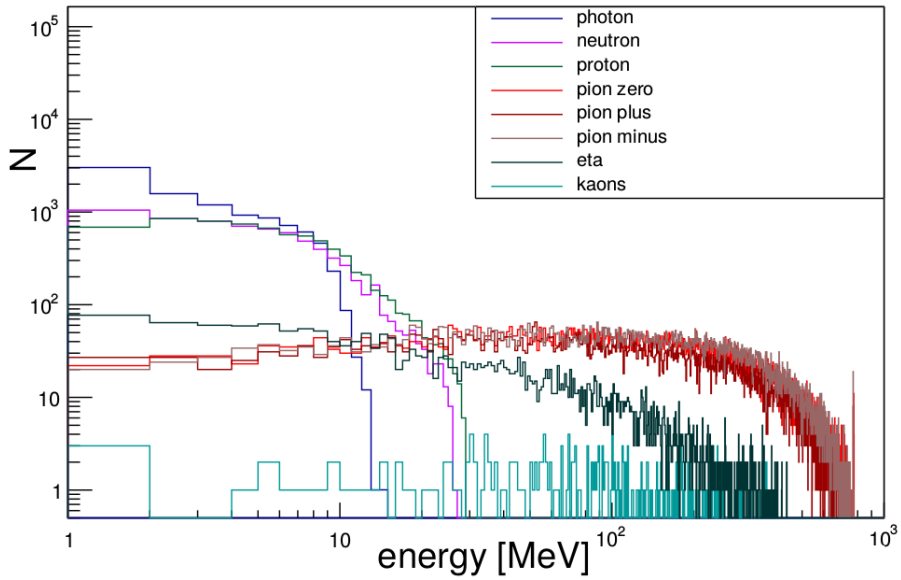

Figure 6.2: Energy distribution of the main annihilation products for an incident antiproton energy of 10 keV and a stainless steel target.

6.2.3 Number of pions produced in the annihilation

Introduction

The number of pions produced in the antiproton annihilation depends on the $\bar{p}$ absorption cross-section on a proton or a neutron inside a nucleus (Z,A). At low $\bar{p}$ energies the ratio between the $\bar{p}$ absorption on neutrons and protons $R_{n/p} = \sigma_n/\sigma_p \sim N/Z$, where N is the number of neutrons and Z is the number of protons inside the nucleus. For lighter nuclei, a similar number of antiprotons annihilate on protons and neutrons, and for heavier nuclei, more antiprotons annihilate on neutrons.

In the GBAR experiment, antiprotons are incident on targets containing mostly carbon (A=12) and iron (A=56). The corresponding R values are R=1 for carbon and R=1.15 for iron. The average number of charged pions produced in the annihilation of an antiproton with a nucleus (Z, N) can be estimated using:

$$N_{av} = \frac{Z}{Z+N} \cdot (1.5\pi^+ + 1.5\pi^-) + \frac{N}{Z+N} \cdot (1.1\pi^+ + 2.1\pi^-). \tag{6.1}$$

The result for iron and carbon is about $1.3\pi^+ + 1.8\pi^-$. The errors of the estimation are omitted due to too many unknowns. According to this estimation there should be no difference in the pion production in the annihilation of antiprotons on carbon or iron targets. However, it has to be remembered that the observed number of pions is not necessarily the same, because a part of the pions interact within the nucleus [151].

Simulation

The number of pions per antiproton annihilation on different targets was tested. It is the number of pions created directly from the annihilation. Results are summarised in Table 6.3 and show, as expected, a larger production of negative than positive pions. Also, there is a slightly increasing production of π^- and decreasing number of π^+ for increasing target atomic number. The measured pion multiplicities for carbon are $M_{\pi^-} = 1.58 \pm 0.07$, $M_{\pi^+} = 1.33 \pm 0.08$ and $M_{\pi^0} = 1.15 \pm 0.3$ [153]. The comparison to the simulation results shows a large discrepancy with the neutral pion multiplicity.

Generally, the total pion production multiplicity is between 4 and 5, which is in agreement with measurements and estimations [154]. The absolute numbers are not accurate enough to fully rely on the simulation, as was also proven by other collaborations [146]. However, the simulation can still be used as a guidance for the estimation of backgrounds. In this context, the π^0, with lifetime being equal to 8.4×10^{-17} s, decays quasi immediately into 2 photons (98.8 %) or an electron-positron pair (1.2 %). Thus only the decay products are observed in the detectors. Charged pions have a lifetime equal to 2.6×10^{-8} s. Due to this long lifetime and their high energy, they can travel few tens of meters before decaying. The main decay channels are $\pi^+ \to \mu^+ + \nu_\mu / \pi^- \to \mu + \bar{\nu_\mu}$ (99.9877 %) and $\pi^+ \to e^+ + \nu_e / \pi^- \to e + \bar{\nu_e}$ (0.0123 %).

target material	π^0	π^+	π^-	sum
graphite	1.55 ± 0.01	1.21 ± 0.01	1.71 ± 0.01	4.47
iron	1.54 ± 0.01	1.18 ± 0.01	1.74 ± 0.01	4.46
gold	1.54 ± 0.01	1.17 ± 0.01	1.78 ± 0.01	4.49
lead	1.54 ± 0.01	1.13 ± 0.01	1.79 ± 0.01	4.46
stainless steel	1.52 ± 0.01	1.19 ± 0.01	1.74 ± 0.01	4.45
lead glass	1.54 ± 0.01	1.15 ± 0.01	1.78 ± 0.01	4.47

Table 6.3: Pion production rate per antiproton annihilation with different target materials (simulation). The antiproton energy is equal to 10 keV. Errors are statistical.

6.3 Secondary particles production

The antiproton beam from ELENA has about 5×10^6 $\bar{\text{p}}$/bunch. Their annihilation creates a lot of energetic particles, which interact with parts of the vacuum equipment, supports, walls and floor. This causes the production of additional secondary particles. In this section the overall production of particles in the antiproton annihilation is discussed.

6.3.1 Simulation

In this Section the same simulation setup is being used but with 3.24×10^7 antiprotons originating from a pointlike source. The particles reaching a virtual detector located behind the stainless steel annihilation target are considered. In order to avoid elastic scattering, the target is in the form of a Faraday Cup (see Section 6.2.1) which has its back side situated at $z = 1817$ mm. The virtual detector is placed at $z = 2126.9$ mm. The geometrical acceptance for the virtual detector is equal to $A_{virtual} = 0.06$.

Rate of secondary particles production

Figure 6.3 shows the primary annihilation products reaching the virtual detector as a function of the energy. There are only photons, charged pions, kaons, neutrons and protons. In Figures 6.4 - 6.9 the same distributions are shown together with distributions for all particles reaching the detector. In this case high energy photons are coming from π^0 decay. Some of them are also the result of pion inelastic scattering, neutron inelastic scattering, neutron capture, Compton and Rayleigh scattering. The number of detected kaons does not change, as they are not produced in any secondary particle interaction. The number of charged pions is slightly increased by η decay. Neutrons are more energetic due to pion inelastic scattering, which also increases the overall neutron production yield. Additionally, there are positrons formed in photon conversion, muon decay, π^0 and kaon decay. Electrons are coming from gamma conversion, muon decay, π^0 and kaon decay, Compton scattering, photoelectric effect and ionisation processes. The detected protons are produced in pion/neutron intelastic scattering. Muons are coming from pion decay.

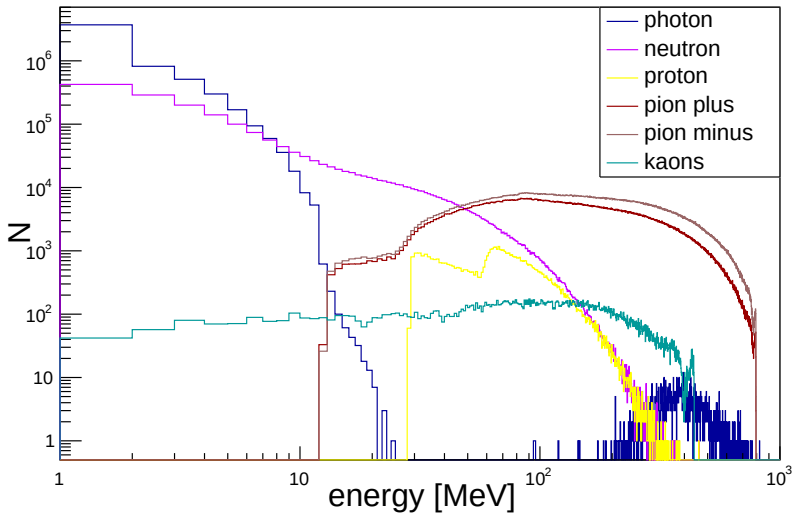

Figure 6.3: Energy distribution of the primary annihilation products reaching the virtual detector.

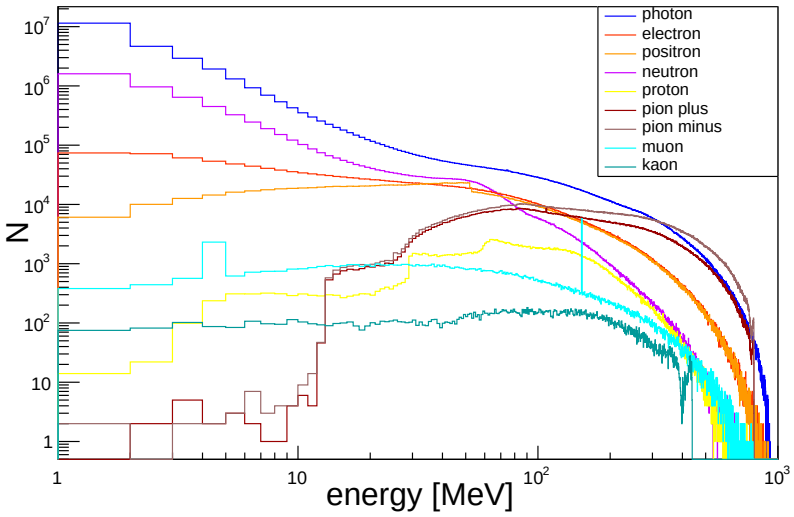

Figure 6.4: Energy distribution of all particles reaching the virtual detector.

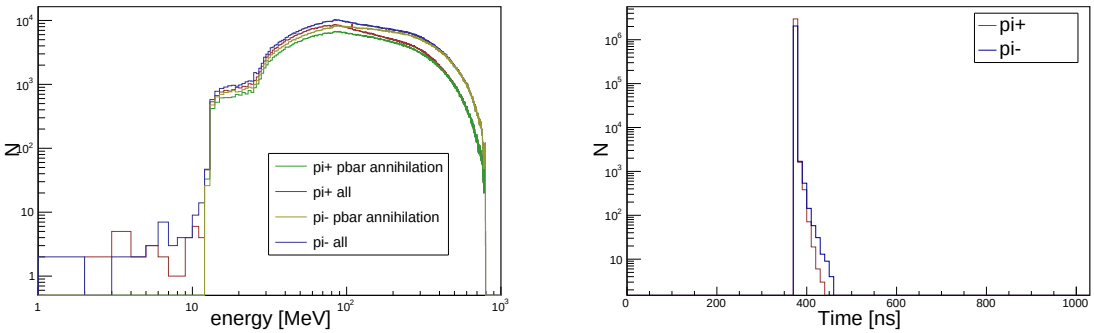

Figure 6.5: The left Figure shows the energy distribution of charged pions reaching the virtual detector. Two data sets are considered - particles coming directly from the annihilation or all particles. The right Figure is the distribution of the detection time of all particles.

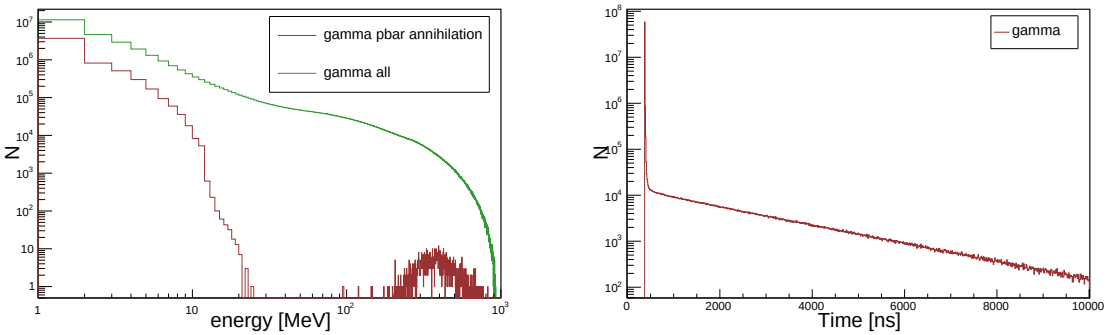

Figure 6.6: The same as Figure 6.5, for photons.

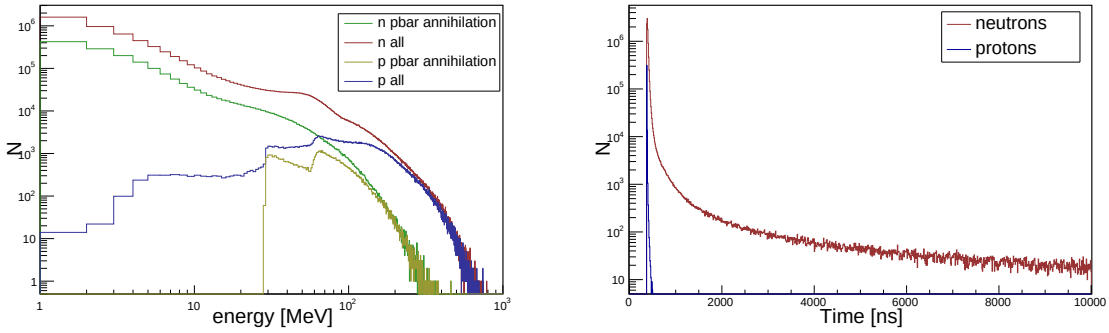

Figure 6.7: The same as Figure 6.5, for neutrons and protons.

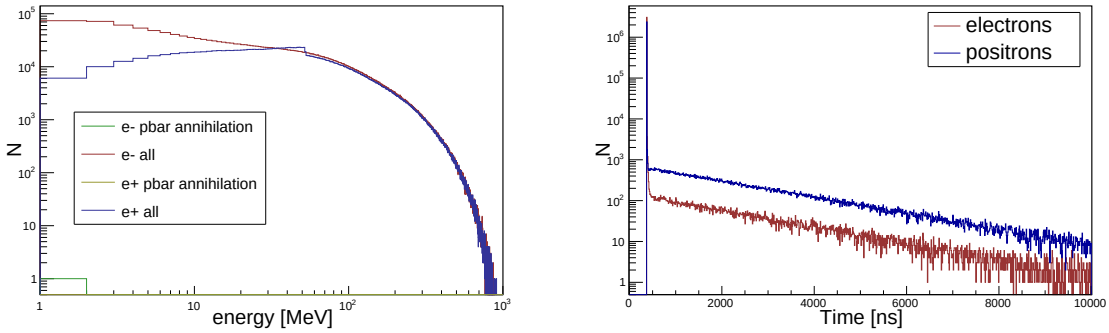

Figure 6.8: The same as Figure 6.5, for electrons and positrons.

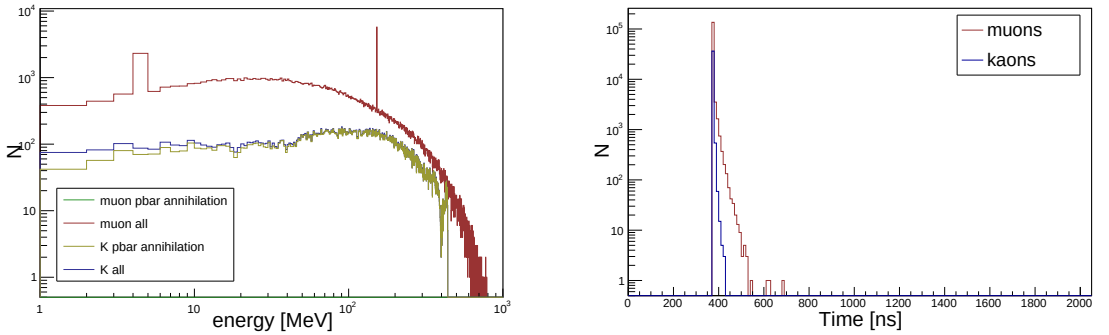

Figure 6.9: The same as Figure 6.5, for muons and kaons.

Time of secondary particles production

The arrival time distribution for all particles is shown in Figure 6.10 and the arrival time distributions of individual species of particles are presented in Figures 6.5 - 6.9. Most particles reach the detector just after the antiproton annihilation. However, there is a clear delayed background, which even about 5 μs after the antiproton annihilation is at the level of 10^{-5} particles per antiproton annihilation. The delayed background consists of neutrons, photons, electrons and positrons. The neutron and a part of the photon background comes from neutron interactions with surrounding materials, which has a time constant in the ms range. In order

to correctly simulate this background it is important to include walls and floor made from concrete. Some electrons and positrons come from gamma conversion. However, the main part of the electron, positron background comes from pion/muon decay $\pi^- \rightarrow \mu^- + \bar{\nu}$ and later $\mu^- \rightarrow e^- + \bar{\nu} + \nu$. The half life time of the muon in the second reaction is equal to 2.2 μs. The asymmetry in electron-positron production in delayed background is caused by the asymmetry in charged-muon production, which is an effect of the nuclear capture of negative pions. The lifetime of the negative pions in the system is about four times shorter than the pion lifetime in vacuum. Also, the process of nuclear capture does not produce muons, like in a standard pion decay [155], so the number of negative muons is smaller than the number of positive muons.

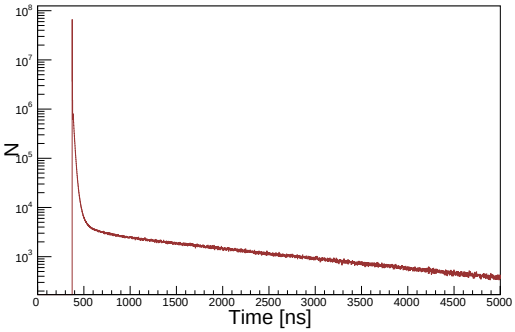

Figure 6.10: Arrival time of all particles to the virtual detector.

Energy of secondary particles in the delayed background

The energy distribution of secondary particles detected between 1 μs and 3 μs after the antiproton annihilation is shown in Figure 6.11. The mean kinetic energy of neutrons is equal to 1.6 MeV, electrons - 10.5 MeV, positrons - 38 MeV and photons - 2.5 MeV.

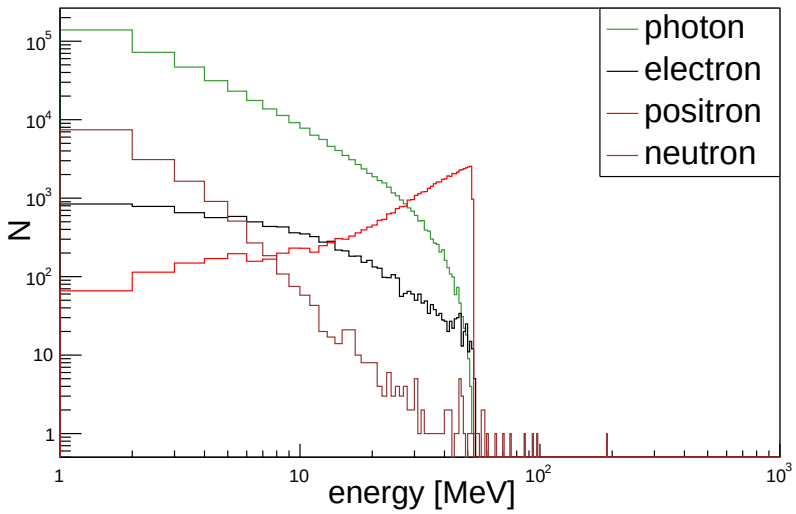

Figure 6.11: Energy distribution of all particles reaching the virtual detector within a time window 1 μs to 3 μs after the antiproton annihilation.

Expected detection efficiencies on the MCP detector

In the next Chapter, it will be shown that the antihydrogen atom and ion detection system is designed in a way to be sensitive only to the delayed background coming from antiproton annihilation. The main detectors used for antihydrogen atom and ion detection are MCPs. It is essential to know what is the expected detection efficiency of the MCP detector for particles at energies similar to the ones produced in the delayed background.

The detection efficiency of the MCP detector depends on the type and energy of the particle. The following detection efficiencies are going to be used later in the text:

- charged pions - (6.0 ± 1.3) %; it was measured for 172–345 MeV pions [156];
- muons - 6 % ; there are no data, however it is expected to have the same value as for charged pions;
- electrons - (5.8 ± 0.5) %; it was measured for 17.5–300 MeV electrons [156];
- positrons - 6 % ; there are no data; it is expected that the detection efficiency is equal to the charged pions detection efficiency;
- neutrons - 0.14 % - 0.64 %; it was measured for 2.5 MeV to 14 MeV neutrons [157];
- photons - 0.26 %; estimation for 511 keV gammas described in Appendix B; other measurements show (0.388 ± 0.251) % [158] and (0.21 ± 0.14) % [159] for a similar energy. The mean photon energy coming from antiproton annihilation is higher, and then the expected detection efficiency is smaller. However, this value depends on the angle between the momentum of the incident photon and the MCP. The efficiency increases with increasing angle. That is why a 0.26 % value is going to be used, as a decent estimation.

6.4 Summary

The annihilation of antiprotons in matter is a complex subject. The main annihilation processes are included in the commonly used simulation libraries. However, it is essential to remember that all available models do not provide absolute production rates for secondary particles.

The Geant4 simulation was studied in order to understand the possible effects of antiproton annihilation on the detection system. The most significant output of these studies is that the antiproton annihilation produces a lot of secondary particles, not only pions, and that there is a time delayed background, which can spoil the antihydrogen atom and ion detection. In the next Chapter, this knowledge is going to be used to describe the design of the detection system.

Chapter 7

(Anti)proton, antihydrogen atom and ion beams transport

In this Chapter a system to transport antiproton, antihydrogen atom and ion beams is described. It is crucial as it defines the possible sources of backgrounds.

7.1 Introduction

Antiproton beam is one of the two ingredients required to produce antihydrogen atoms and ions. The antiproton beam has to be decelerated to the energy between 1 and 10 keV and focused inside the 2 by 2 mm cavity. It is done with a specially designed system, whose general scheme is presented in Figure 7.1 (see thesis of Audric Husson [65]). The antiproton beam comes from the ELENA decelerator. It is slowed by a drift tube decelerator and guided to the reaction chamber using electrostatic lenses and a quadrupole triplet. The experiment also developed a proton source. The proton beam can be used to commission different parts of the experiment or to produce hydrogen atoms and ions in the charge exchange reactions on positronium.

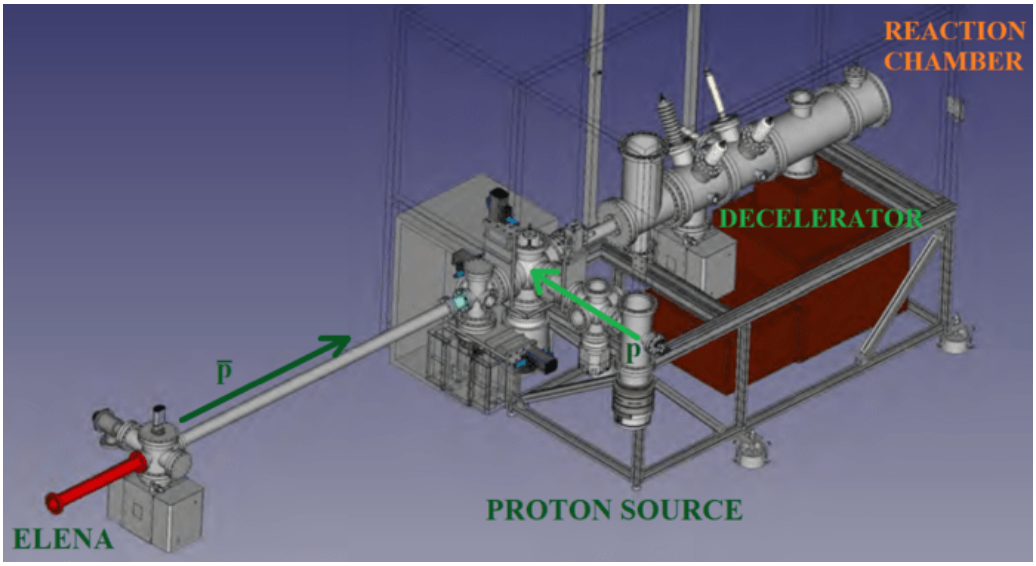

Figure 7.1: General drawing of the antiproton/proton beam lines before the reaction chamber. Figure modified from [65].

The production of (anti)hydrogen atoms and ions takes place in the reaction tube at the centre of the reaction chamber. After the reaction, all three beams, i.e. (anti)protons, (anti)hydrogen atoms and (anti)hydrogen ions, are mixed and have very similar emittance. However, for the free fall experiment a pure antihydrogen ion beam is needed. Also the cross-section measurements require the precise detection of the beam intensities. For these reasons, the beams have to be separated and led to appropriate detection systems.

In order to separate the beams an electrostatic switchyard has been designed. It allows neutral particles to go straight, while particles with positive and negative charge are led to opposite directions at an angle of 30/-30 degrees to the original direction, see Figure 7.2. After the switchyard the beams are led into the straight tubes to appropriate detection systems or to the free fall chamber in the case of the antihydrogen ion. In the present Chapter the detailed design of the transport system after the reaction chamber is presented.

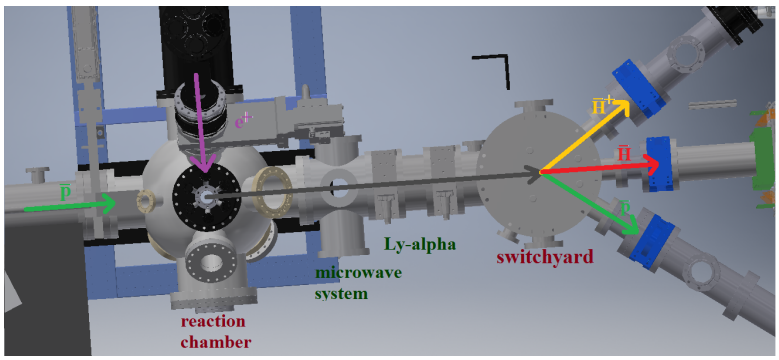

Figure 7.2: Realistic scheme of the reaction chamber and switchyard.

AD and ELENA decelerators

The antiproton beam for the GBAR experiment is provided by the CERN antiproton facility. First, the beam is prepared in the Antiproton Decelerator (AD), which cools antiprotons with electrons and the method of stochastic cooling to 5.5 MeV energy. Every 109.2 seconds, the beam is sent to the second deceleration stage, the Extra Low ENergy Antiproton ring (ELENA). Using the electron cooling technique supported by simultaneous magnetic field ramping [55], ELENA reaches 100 keV antiproton energy.

The nominal beam properties are:

- beam intensity: 5×10^6 $\bar{\text{p}}$/pulse;
- beam energy: 100 ± 0.1 keV (FWHM);
- pulse length: 300 ns (90% of the beam);
- beam emittance: 4π mm $\times$ mrad.

At the end of the first antiproton run in 2018, ELENA reached the 4.3×10^6 $\bar{\text{p}}$/pulse beam intensity with the nominal energy and pulse length. ELENA is the only source of low energy antiprotons in the world. It is also equipped with an H^- source, which allows to test the decelerator and its connections to experiments independently from the general CERN beam time schedule. The largest advantage of performing tests with a hydrogen beam is a much higher repetition rate, which is equal to 1 pulse every 5 s.

7.2 Decelerator and focusing system

The beam from ELENA is decelerated in the GBAR area with a specially designed decelerator, whose detailed description can be found in [65]. It can slow particles to any energy between 100 keV and 1 keV. A scheme of the decelerator together with other beam optics is shown in Figure 7.3.

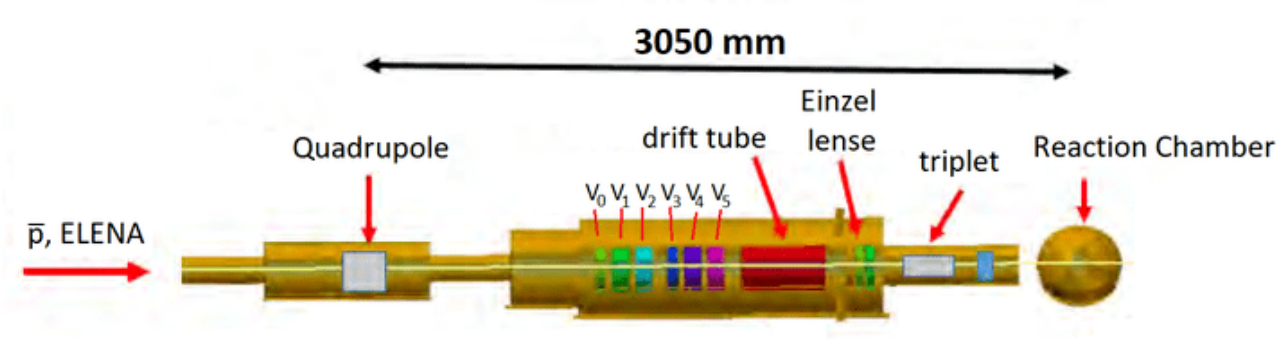

Figure 7.3: Scheme of the deceleration and focusing system for the antiproton beam. Figure modified from [65].

In principle, the focusing system consisting of Einzel lenses and a triplet of quadrupoles should allow to focus the antiproton beam into the 2 by 2 mm cavity. However, this statement has still to be experimentally proven.

In the future, an antiproton trap will be added to the system to reach better beam parameters. The most important for the experiment is to reduce the energy distribution and the pulse length of the original antiproton beam.

7.2.1 Proton line

The GBAR experiment developed its own proton source, which is connected to the system through a quadrupole bender before the decelerator, see Figure 7.1. The proton beam can be used both to test the beam transport and measure the hydrogen atom and ion production. The original proton line and source designed for the experiment in CEA did not fulfill the requirements of the experiment, mainly due to a too low proton beam intensity, see Appendix C. The system was upgraded with an Electron Cyclotron Resonance source (ECR) (Polygon Physics, model TES35).

Proton source

During tests in CEA, a Penning-type ion source was used. Its general scheme is shown in Figure 7.4. First, the discharge chamber is filled with a neutral gas, in this case hydrogen H_2. Then, a DC voltage typically between 500 - 5000 V is applied between an anode and a cathode. The induced voltage makes ionising electrons to oscillate between electrodes, which increases the efficiency of the discharge by increasing the electrons path length. The addition of a magnetic field B causes the gyration of electrons around the magnetic field lines with a Larmor radius equal to

$$r_L = \frac{m}{|q|}\frac{v_\perp}{B}$$

where $v_\perp$ is the velocity of the electron perpendicular to the magnetic field, m and q is the mass and the charge of an electron. The Larmor radius is typically adjusted for electrons to be in the order of a few millimeters (in our case 2 mm). The overall combination of electrostatic and magnetic fields traps electrons inside the discharge chamber and forces them to constantly interact with the neutral gas upholding the discharge in much smaller pressure than it would be possible otherwise [160].

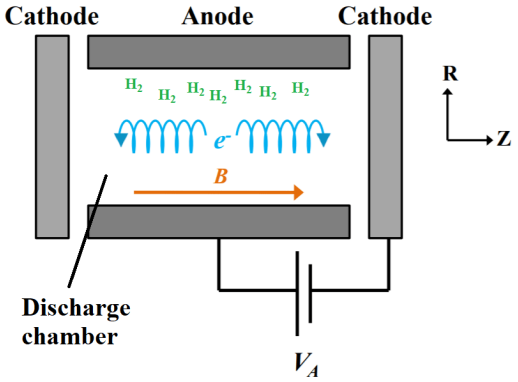

Figure 7.4: Proof of principle scheme of a Penning-type proton source. The presented geometry is cylindrically symmetric about the central axis. Figure adapted with modifications from [160].

Accelerated electrons interact with the neutral hydrogen in the chamber forcing its ionisation. This causes two effects. First, the ejected electrons are also trapped in the chamber and help to uphold the discharge reaction. Second, hydrogen ions are produced through one of the following processes [161]:

ionisation process	**required electron energy [eV]**
$e^- + \mathrm{H}_2 \rightarrow e^- + \mathrm{H} + \mathrm{H}$	8.8
$e^- + \mathrm{H} \rightarrow e^- + e^- + \mathrm{H}^+$	13.6
$e^- + \mathrm{H}_2 \rightarrow e^- + e^- + \mathrm{H}_2^+$	15.4
$e^- + \mathrm{H}_2 \rightarrow e^- + e^- + \mathrm{H} + \mathrm{H}^+$	18
$e^- + \mathrm{H}_2 \rightarrow e^- + e^- + e^- + \mathrm{H}^+ + \mathrm{H}^+$	46

The cross-section values for these processes are summarised in Figure 7.5. At the beginning of the ionisation process electrons have about 1000 eV energy, which drops with every collision. The cross-section for the formation of molecular hydrogen ions is one order of magnitude higher than for the production of atomic hydrogen ions. The beam produced in a typical Penning source thus consists of up to 10 % of atomic ions, and about 90 % of molecular ions. These ions have a much larger Larmor radius than electrons, thus they are not trapped in the source, but guided to electrodes. By making a hole in one of the electrodes and correctly adjusting an electric field, it is possible to guide the ions away from the discharge chamber and produce an ion beam. Generally, Penning-type sources have a relatively short life time due to ion sputtering on electrodes, which causes damage and changes properties of the source.

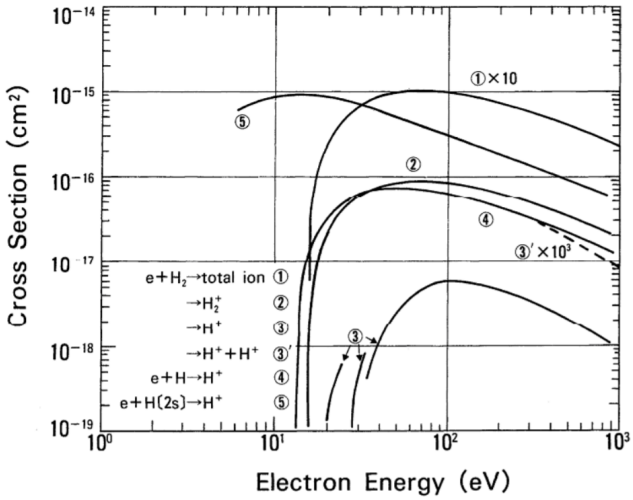

Figure 7.5: Cross-section values for hydrogen ionisation processes as a function of incident electron energy. Figure adapted from [162].

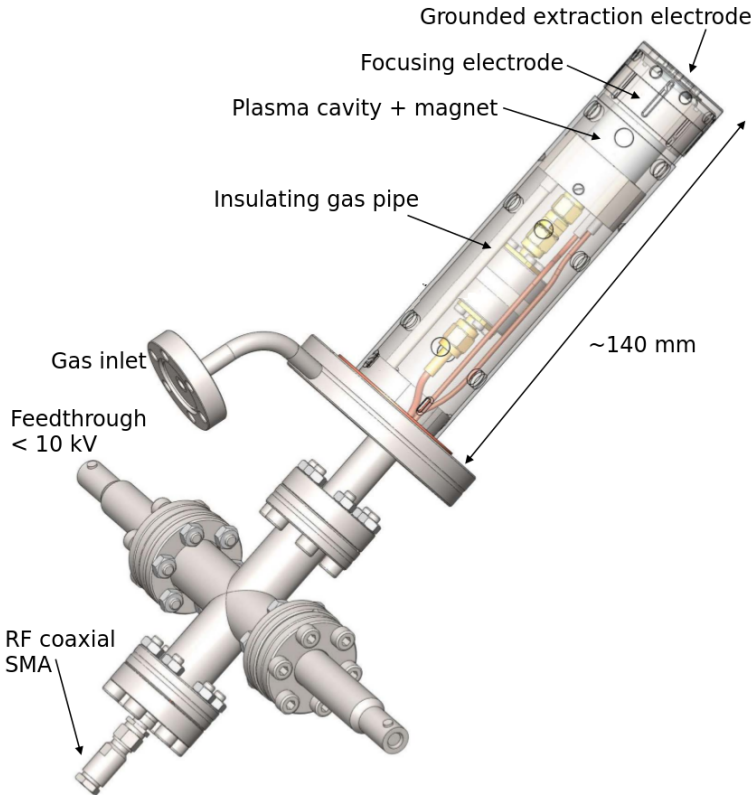

Figure 7.6: Scheme of the ECR (2.45 GHz) proton source from Polygon Physics.

A more solid solution is to use an Electron Cyclotron Resonance source (ECR), see scheme in Figure 7.6. In this case, the electric field required to accelerate electrons is generated by a 2.45 GHz radio-frequency wave in resonance with the cyclotron frequency of the electron cloud. In the GBAR source, the electric field is generated by variation of the magnetic field in a solenoid-shaped antenna. The electric lines of this source do not guide ions to any conductor,

thus the damage caused by sputtering effect is minimised [163]. The presented source is much more compact than the Penning-type source.

Proton beam guiding system

The beam created from the source is focused using Einzel lenses. It is connected to the antiproton line using an electrostatic quadrupole bender placed before the decelerator, see Figure 7.1. In that configuration, the whole antiproton focusing and steering system of the GBAR experiment can be tested.

The GBAR proton beam consists of three types of ions H^+ (5 %), H_2^+ (58 %) and H_3^+ (37 %). The protons are separated from other ions using a Wien filter [164], which applies magnetic and electrostatic fields in the plane perpendicular to the beam direction. By adjusting the fields, it is possible to select particles only with a well-defined mass and deflect others. However, after the device, the FWHM of the energy distribution of the beam increases from less than 1 eV to about 120 eV. This distribution is wider than for the antiproton beam, thus requires different transport parameters. Currently, the proton source can provide a continuous proton beam with 1.5 μA current. It is enough to produce 300 ns long proton pulses with 3×10^6 protons.

7.2.2 The first beam in the GBAR area

Hydrogen ion beam

A connection between ELENA and GBAR experiment was set up in Spring 2018. The first beam sent by ELENA to GBAR experiment was the H^- beam. In order to detect it, an MCP detector was placed after the reaction chamber. The front of the MCP is biased by 1100 V and the phosphor screen is biased by -1000 V. The diameter of the MCP is 40 mm. An image of the first hydrogen minus beam received by the GBAR experiment is shown in Figure 7.7. The beam has a rectangular shape, due to the 12 mm wide vertical slit of the quadruple bender situated 262 cm earlier. The prepared detection system was used by the ELENA collaboration to test the GBAR-ELENA connection with H^- beam.

The possibility of using the H^- beam from ELENA is invaluable because it allows testing the ELENA - GBAR connection independently from the CERN beam schedule.

Antiproton beam

In the summer and autumn of 2018 , the first tests of the deceleration system were performed. Unfortunately, due to a bad ELENA beam quality, it was not possible to fully commission the antiproton decelerator. Details about these tests can be read in the Ph.D. dissertation of A. Husson [65].

7.3 Beam correction at the reaction chamber level

The antihydrogen detection must to be possible even with imperfect beam quality. A 5 mm diameter collimator was added before the cavity area, see Figure 7.8, to annihilate parts of the beam which would not participate in the antihydrogen production, due to small positronium cloud size, but could create a background for the detection. In this way, the effective beam

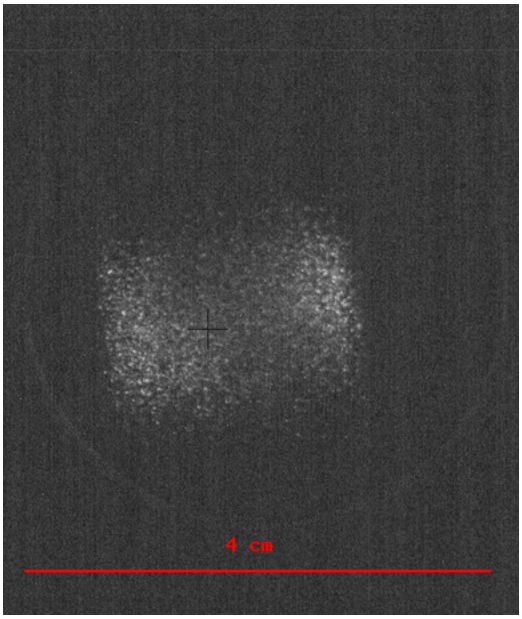

Figure 7.7: An MCP image of the first H^- beam from the ELENA decelerator in the GBAR experiment. The MCP detector is situated at the back of the reaction chamber.

has a much better quality and can go through the rest of the system without annihilating on different parts of the experiment in an uncontrolled way.

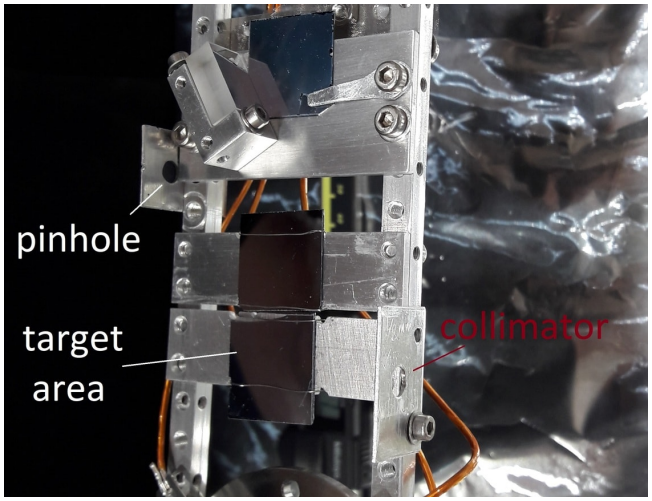

Figure 7.8: Target holder prepared for the antihydrogen formation in reaction with positronium.

Upgraded antiproton beam collimator

For the future tests with antiprotons it is proposed to use a collimator with a cylindrical shape, see Figure 7.9. It is a cylindrical box with a large hole in a front plate (radius 7.5 mm) and a smaller hole in the back plate (radius 2.5 mm). Its total length and radius are equal to 20 mm. This device works like a collimator, as a part of the beam is stopped by the smaller radius of the hole in the back side of the cup. The stopped part of the 10 keV beam has about 20 % probability to be elastically back-scattered and annihilate on different parts of equipment. In

order to avoid this, the cylindrical collimator forces antiprotons to annihilate within a few tens of ns. The final diameters of holes have to be adjusted to the size of the available beam.

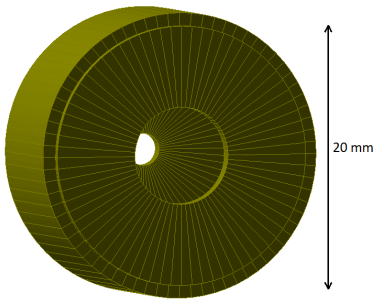

Figure 7.9: Scheme of the recommended cylindrical collimator in front of the reaction cavity.

In order to evaluate the device a Geant4 simulation was performed. The antiproton beam has a uniform distribution in the plane perpendicular to the beam direction. Its radius is 7 mm. Histograms of the z-coordinate of the antiproton annihilation vertex are shown in Figure 7.10. The left histogram presents data for a flat collimator identical to the back side of the cylindrical collimator. The back-scattered antiprotons annihilate until the end of the simulation world. The right histogram shows results for the cylindrical collimator. Most antiprotons annihilate inside the collimator, between z=0 mm and z=20 mm. According to the simulation, the proposed geometry allows to block 90 % of the backscattered beam. This result is of a great importance for the beam diagnostic and Lamb shift measurements, as it blocks a large part of the delayed background coming from back-scattered antiproton annihilations.

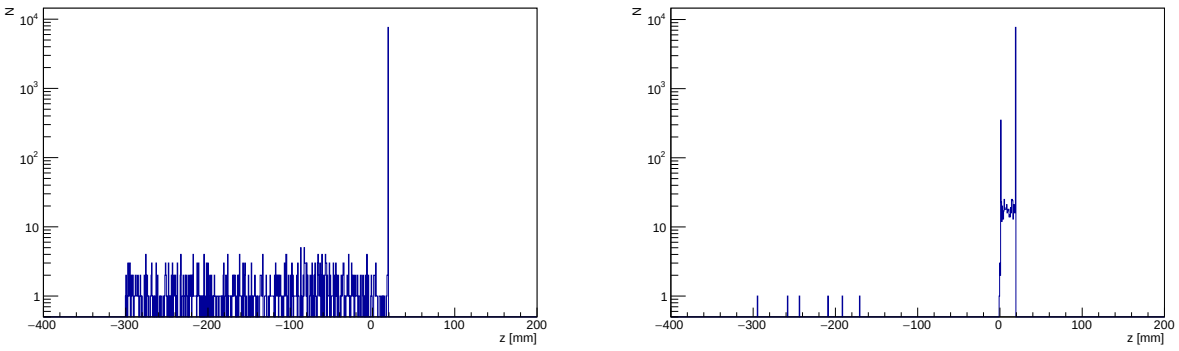

Figure 7.10: Histograms of the z-coordinate of the antiproton annihilation vertex. The left histogram presents results for a flat collimator. The right histogram shows data for a cylindrical collimator. The back side of the cylindrical collimator is situated between z=19 mm and z=20 mm. The front side of the cylindrical collimator is placed at z=0 mm.

Pinhole for low intensity antiproton beam production

A beam of single antiprotons could be used to test the detection system. In order to produce it, a collimator with 100 μm diameter is added, see Figure 7.8. According to estimations, it is possible to obtain a beam with only a few antiprotons per pulse with this device. This feature was used to perform the first test of the detection system with antiprotons, see Section 8.5.3.

7.4 Antiproton, antihydrogen atom and ion transport system after the reaction chamber

The production of (anti)hydrogen atoms and ions takes place in the reaction chamber. After the reaction, the three beams are combined, and thus, have to be separated and guided to their proper detection system. In order to optimise the precision of the measurements of the cross-sections, the design of the beam transport must aim at minimising the possible sources of systematic errors.

7.4.1 Possible limitations resulting from the background analysis

In order to produce hydrogen or antihydrogen ions, the (anti)proton intensity must be of the order of 5×10^6 antiprotons per pulse. This will produce a few thousand atoms but only a few ions. In the design of the transport and detection system for the three beams it is important to keep in mind, that during one measurement cycle beam intensities differing by seven orders of magnitude have to be detected. The details about the detection system and systematic errors are presented in Chapter 8. However, some basic constraints coming from the background analysis are also included in this Section as they are crucial for a full understanding of the transport system.

The hydrogen/antihydrogen detector is an MCP equipped with a fast P46 phosphor screen. The image from the detector is collected using a CCD camera with an exposure time of 1 μs. This means that the minimum detection time for antihydrogen is 1 μs. A very similar detector is used for the antihydrogen ion. MCP detectors are sensitive to many kinds of particles, including neutrals. In order to detect antiprotons a Faraday cup is used. This detector is fast, thus the main limit for the detection time comes from the beam length, which is expected to be about 300 ns.

The main sources of systematic errors for the flux measurements of the three beams are:

A) positron beam annihilation in the reaction tube, which creates 511 keV γ immediately after annihilation;

B) ortho-positronium decay to 511 keV γ's with decay time $\tau_{oPs} = 142$ ns, also in the reaction tube;

C) antiproton, antihydrogen atom or ion annihilations in case of antimatter reactions;

D) beam losses during transport.

Backgrounds A and B originate from the centre of the reaction chamber. The 511 keV gammas have a range of 1.25 cm in 316L stainless steel, which with 1.5 mm thick walls of tubes and chambers, gives them a high probability to reach any detector in the zone. The background originating from antiproton or antiatom annihilation mostly consists of pions, muons, electrons, positrons, neutrons and photons. The number of secondary particles produced in one antiproton annihilation depends strongly on the environment, but can reach few tens of particles per annihilation.

In order to minimise the influence of the secondary particles on the MCP detectors two methods can be used:

- add detector shielding;
- add time separation between different annihilations and detections.

These two methods will be discussed in the following sections in the context of antimatter detection. The proton, hydrogen atom, and ion detection are less complicated due to the lack of backgrounds coming from antiproton annihilation, thus the system designed for antimatter can be directly used for matter.

7.5 Neutral beam line

The antihydrogen beam originates from the centre of the reaction chamber. The only known possibility to steer the neutral beams is to use a magnetic field guiding. However, that would require a magnetic field gradient of at least a few orders of magnitude T/m, which is technically not available. That is why the antihydrogen beam propagates straight from the reaction chamber and its parameters are defined at its origin. The design of this line should be focused on three main matters: minimising beam losses and background, and maximising beam flux detection.

7.5.1 Beam line design

A scheme of the antihydrogen line from the reaction chamber to the detection of the neutral beam is shown in Figure 7.11. The total length of the antihydrogen beam line from the centre of the reaction chamber to the MCP detector is $d_{RCh\_\bar{H}MCP} = 201.6$ cm. This is the smallest possible distance resulting from the technical constraints. It is the sum of the following distances: 24 cm - cut radius of the reaction chamber, 7.0 cm - a CF160 output tube from the reaction chamber, 2.2 cm - a zero length reducer from CF160 to CF100, 9.0 cm - CF100 bellow, 2.2 cm - a zero length reducer from CF160 to CF100, 7.5 cm - CF160 valve, 25.0 cm - microwave setup, 7.5 cm - CF160 valve, 14.0 cm - Lyman alpha setup, 7.5 cm - CF160 valve, 8.0 cm - entrance tube of the switchyard, 15.0 - radius of the switchyard, 72.7 - distance from the middle of the switchyard to the MCP detector. The neutral beam is propagating freely in the system, which is why there is no mesh in its path and all the collimators have a diameter larger than 40 mm.

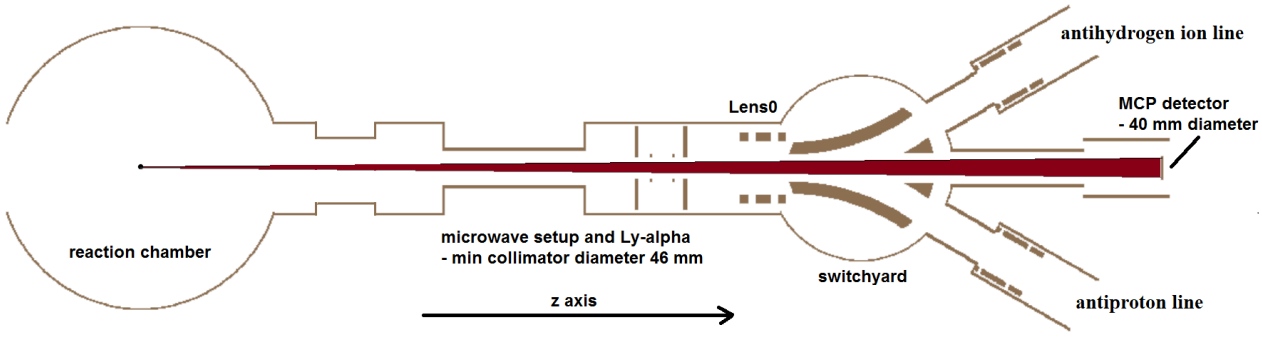

Figure 7.11: General scheme of the antihydrogen atom line.

Beam angular dispersion

Antihydrogen atoms are detected on the MCP detector with 40 mm diameter. In order to detect the whole beam, the direction of the beam momentum has to be perfectly aligned with the z

axis of the system. Also, the best half angle of the beam momentum distribution is when the antihydrogen beam uniformly covers the whole surface of the MCP detector. If the antihydrogen beam is too much focused, it may saturate the channels in the MCP detector and the obtained signal will not be linearly proportional to the number of incident atoms. The half angle is equal to:

$$\alpha_{max\_MCP} = arctan\left(\frac{20 \text{ mm}}{2016 \text{ mm}}\right) = 10 \text{ mrad}.$$

The maximum half angle resulting from the cavity size (20 mm by 1 mm by 1 mm) is equal to:

$$\alpha_{max\_cavity} = arctan\left(\frac{0.5 \text{ mm}}{10 \text{ mm}}\right) = 50 \text{ mrad}.$$

The maximum beam angular distribution is 5 times larger than the optimum. The antiproton beam will have to be correctly focused in order to allow the detection of the whole antihydrogen beam. It is also not really possible to increase the distance between the reaction chamber and the MCP, because then the antiproton beam would have to be much better focused, which may be technically challenging.

Background

The largest possible background comes from antiproton/positron/Ps annihilations in the reaction chamber. When the antihydrogen detection window overlaps in time with the positron, positronium and antiproton annihilation, then the measurement of antihydrogen atoms is not possible due to the detection of too many secondary particles. However, in this case the minimum time distance between antihydrogen formation and detection is equal to:

$$\Delta t_{\bar{\text{H}}\_min} = d_{RCh\_\bar{\text{H}}MCP}/v_{10keV\bar{\text{p}}} = 1.4 \ \mu\text{s}$$

where $v_{10keV\bar{\text{p}}} = 1.37 \times 10^6$ m/s is the velocity of 10 keV antiprotons and $d_{RCh\_\bar{\text{H}}MCP} = 201.6$ cm is the distance between the reaction chamber and $\bar{\text{H}}$MCP detector. As will be shown in the next Chapter this is enough to suppress most of the background originating from the reaction chamber.

Summary

The antihydrogen atom detection is placed 201.6 cm from the reaction chamber. Its position is good for the experiment, thus the positions of the antiproton and antihydrogen ion detection systems should be adjusted in a way that the antihydrogen detection system does not have to be moved.

7.6 Antiproton line

The antiproton flux has to be measured in order to extract the antihydrogen formation cross-section. It is expected to contain 5×10^6 $\bar{\text{p}}$/pulse. The annihilation of so many antiprotons creates about 2.5×10^7 pions and many more other particles. Such an intense particle flux can prevent any measurement of the numbers of antihydrogen atoms or ions. At the end of the antiproton line, it is foreseen to install antiproton flux detectors and a shielding, whose function will be to protect personnel and also to reduce the amount of particles produced in

the annihilation of these antiprotons that may induce background in the other detectors. The position and the design of the antiproton dump must then be carefully established.

In the following sections two methods of minimising the background coming from the antiproton annihilations are considered:

- detector shielding;
- time separation between different annihilations and detections.

7.6.1 Antiproton dump shielding

In order to test whether shielding can decrease significantly the number of secondary particles coming from the antiproton dump, a simulation in Geant4 was performed. The number of annihilating antiprotons is 10^6.

The studied geometry is presented in Figure 7.12. The antiproton dump is situated at the end of a stainless steel pipe. A box-shaped shielding is placed around the dump. In order to test the number of particles coming through the shielding, a 20 x 20 cm virtual detector is placed 1 m from the annihilation point. The floor and wall are added to simulate the environment correctly.

The number of particles reaching the virtual detector is calculated for four different shielding materials: concrete, iron, lead and paraffin. Also, three thicknesses of the shielding walls are considered: 10 cm, 20 cm and 50 cm.

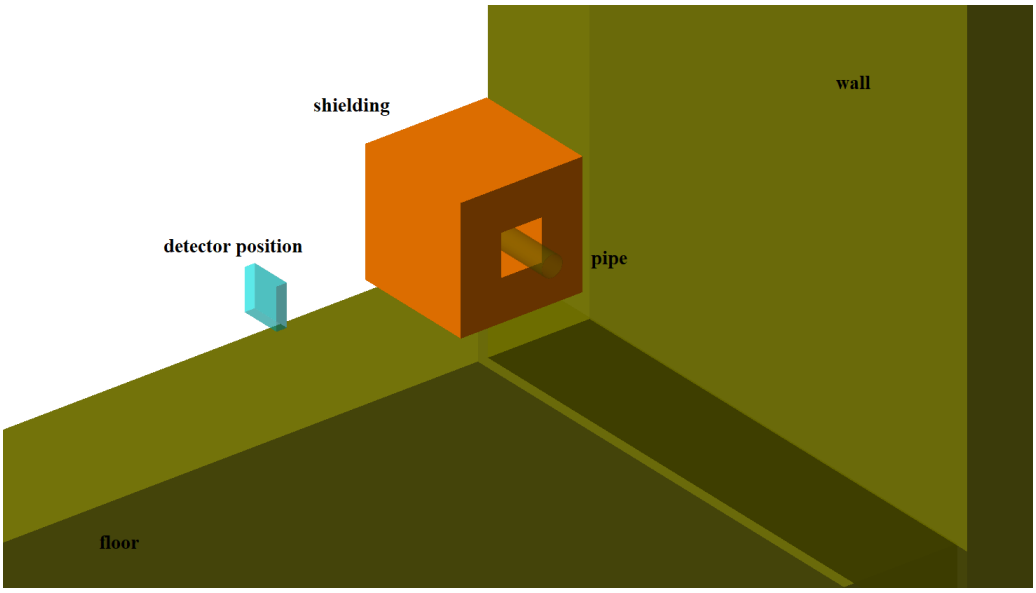

Figure 7.12: Scheme of the antiproton dump geometry with 10 cm thick walls of the shielding.

No shielding

The number of different types of particles produced in antiproton annihilation that reach the virtual detector is summarised in Table 7.1. The number of particles reaching the detector 1 μs after the annihilation time is shown in Table 7.2. As expected, the delayed background is dominated by positrons, neutrons and photons. The most troublesome particles as a background are charged particles (electrons, positrons, pions, muons, protons), as their detection efficiency

is expected to be higher than 5 % (see Section 6.3.1). Also, the amplitude of the signal produced by charged particles in the MCP detector can be similar to the antihydrogen atom signal. This is not the case for a gamma or neutron detection, see Appendix B. The signal coming from neutral particles should be easier to discriminate and its detection efficiency is expected to be smaller than 1 %.

Particle	**N of particles**	**MCP detection eff**	**N of detected particles**
pions $\pi^{+/-}$	6917 ± 83	6 %	415
neutrons	6935 ± 83	$0.14 - 0.64$ %	10 - 44
electrons	2419 ± 49	5.8 %	140
positrons	2138 ± 46	6 %	124
muons	660 ± 26	6 %	40
photons	53906 ± 232	0.26 %	140
protons	267 ± 16	55 %	147
sum	73242 ± 271		1016 - 1050

Table 7.1: List of particles reaching the virtual detector without any shielding. The MCP detection efficiency and corresponding number of detected particles is also given per particle type.

Particle	**N of particles**	**MCP detection eff**	**N of detected particles**
neutrons	361 ± 19	$0.14 - 0.64$ %	0.5 - 2.3
electrons	40 ± 6	5.8 %	2.3
positrons	208 ± 14	6 %	12
photons	1072 ± 33	0.26 %	3
sum	1681 ± 41		18 - 20

Table 7.2: List of particles reaching the virtual detector 1 μs after the annihilation time. Case without any shielding. The MCP detection efficiency and corresponding number of detected particles is also given per particle type.

Concrete shielding

The numbers of particles reaching the virtual detector for a concrete shielding are summarised in Table 7.3. The comparison between the 10 cm and 20 cm thick shielding shows, that the overall number of produced particles increases for thicker shielding due to a larger production of neutrons and photons. The 50 cm thick shielding quite efficiently stops charged secondary particles. The numbers of particles reaching the virtual detector 1 μs after the annihilation time of antiprotons are presented in Table 7.4. The 50 cm thick concrete shielding has a significant influence on that background. The number of neutrons and photons is higher than for the case with no shielding, but the number of electrons and positrons is strongly suppressed.

Particle	N (10 cm)	N (20 cm)	N (50 cm)
pions $\pi^{+/-}$	4546 ± 67	2949 ± 54	750 ± 27
neutrons	15091 ± 123	15916 ± 126	9021 ± 95
electrons	5265 ± 73	5184 ± 72	2158 ± 47
positrons	3542 ± 60	3121 ± 56	1087 ± 33
muons	357 ± 19	250 ± 16	60 ± 8
photons	111940 ± 335	133097 ± 365	78715 ± 281
protons	350 ± 19	268 ± 16	92 ± 10
sum	141091 ± 376	160785 ± 401	91883 ± 303

Table 7.3: List of particles reaching the virtual detector with a concrete shielding - 10 cm, 20 cm or 50 cm thick.

Particle	N (10 cm)	N (20 cm)	N (50 cm)
neutrons	1599 ± 40	2057 ± 45	997 ± 32
electrons	41 ± 6	44 ± 7	18 ± 4
positrons	134 ± 12	79 ± 9	19 ± 4
photons	3993 ± 63	3460 ± 58	1240 ± 35
sum	5767 ± 76	5640 ± 75	2274 ± 48

Table 7.4: List of particles reaching the virtual detector 1 μs after the antiproton annihilation time. Case with a concrete shielding - 10 cm, 20 cm or 50 cm thick.

Particle	N (10 cm)	N (20 cm)	N (50 cm)
pions $\pi^{+/-}$	2080 ± 46	617 ± 25	2 ± 1.4
neutrons	45665 ± 214	63372 ± 252	36385 ± 191
electrons	1966 ± 44	293 ± 17	17 ± 4
positrons	1180 ± 34	136 ± 12	1 ± 1
muons	180 ± 13	52 ± 7	0
photons	126051 ± 355	31238 ± 177	3360 ± 58
protons	192 ± 14	60 ± 8	2 ± 1.4
sum	177314 ± 421	95768 ± 309	39767 ± 199

Table 7.5: List of particles reaching the virtual detector with an iron shielding - 10 cm, 20 cm or 50 cm thick.

Iron shielding

The numbers of particles reaching the virtual detector for an iron shielding are summarised in Tables 7.5 and 7.6. The iron shielding has a larger influence on the particles like pions, muons, electrons, and positrons, which are completely stopped with the 50 cm shielding. The gamma background is also suppressed. However, the shielding largely increases neutron production.

Particle	N (10 cm)	N (20 cm)	N (50 cm)
neutrons	2863 ± 54	9290 ± 96	14631 ± 121
electrons	14 ± 4	3 ± 2	5 ± 2
positrons	29 ± 5	9 ± 3	0
photons	1524 ± 39	652 ± 26	800 ± 28
sum	4430 ± 67	9954 ± 100	15436 ± 124

Table 7.6: List of particles reaching the virtual detector 1 μs after the antiproton annihilation time. Case with an iron shielding - 10 cm, 20 cm or 50 cm thick.

Lead shielding

The total numbers of particles reaching the virtual detector for lead shielding are summarised in Tables 7.7 and 7.8. The lead shielding blocks the charged particles as well as an iron shielding. However, it blows the number of secondary neutrons.

Particle	N (10 cm)	N (20 cm)
pions $\pi^{+/-}$	2015 ± 45	456 ± 21
neutrons	107713 ± 328	170018 ± 412
electrons	96 ± 10	31 ± 6
positrons	60 ± 8	10 ± 3
muons	150 ± 12	45 ± 7
photons	20548 ± 143	4473 ± 67
protons	142 ± 12	33 ± 6
sum	130724 ± 362	175066 ± 418

Table 7.7: List of particles reaching the virtual detector with a lead shielding - 10 cm or 20 cm thick.

Particle	N (10 cm)	N (20 cm)
neutrons	5387 ± 73	15964 ± 126
electrons	11 ± 3	4 ± 2
positrons	30 ± 6	7 ± 3
photons	647 ± 25	379 ± 20
sum	6075 ± 78	16354 ± 128

Table 7.8: List of particles reaching the virtual detector 1 μs after the annihilation time. Case with a lead shielding - 10 cm or 20 cm thick.

Iron and paraffin shielding

All considered shielding materials stop charged particles, but increases the number of secondary neutrons. To stop them, the best is to use paraffine.

In this case, a 20 cm thick iron shielding is surrounded by a 20 cm thick paraffine box. The results are summarised in Table 7.9. The effect of that shielding is similar to the one of 50 cm concrete shielding. In this case, the number of neutrons is strongly suppressed, but the number of gammas is larger.

	all	1 μs later
Particle	**N**	**N**
pions $\pi^{+/-}$	356 ± 19	
neutrons	3672 ± 61	118 ± 11
electrons	303 ± 17	24 ± 5
positrons	59 ± 8	12 ± 3
muons	25 ± 5	
photons	28511 ± 169	2769 ± 53
protons	87 ± 9	
sum	33013 ± 182	2923 ± 54

Table 7.9: List of particles reaching the virtual detector with a 20 cm thick iron shielding surrounded by a 20 cm thick paraffine layer. The left column shows results for all particles. The right column contain the results for particles reaching the virtual detector 1 μs after the annihilation time.

Summary

The total number of secondary particles reaching the virtual detector is too high for antihydrogen atom or ion detection for all considered shielding options. If the antihydrogen detection takes place at the same time as the antiproton annihilation, close to the annihilation point, the expected number of detected background events would be at the level of a few tens to a few hundred events. Thus, the only option for antihydrogen atom and ion detection is to delay the detection with respect to the antiproton annihilation.

In the case of a delayed detection, it is worth to consider adding a shielding. The absolute number of secondary particles is higher with then without shielding. However, the shielding blocks electrons and positrons which may have the same signal shape as incoming antihydrogen atoms. It is expected that the neutron and photon signal is easier to discriminate, see Appendix B. There are three options worth considering. The first it to use a 10 cm thick iron shielding. It stops very well positrons, electrons, and photons and does not increase too much the number of neutrons. The second option would be to use the 10 cm iron shielding and add a concrete block of at least 50 cm thickness. The third option is to use a combined iron - paraffine shielding.

These options will be considered in Chapter 8 for the estimation of the background.

Now, the second option for the rejection of background will be considered, i.e., by delaying the antiproton annihilation in time with respect to the detection of the antihydrogen atom or ion.

7.7 Time separation between different detection stations

In order to minimise the background of the antihydrogen atom and ion detection, their annihilation may be separated in time. The antiprotons, antihydrogen atoms and ions have an energy between 1-10 keV, which corresponds to the velocity in the range between 1 m/2.3 μs and 1 m/0.73 μs. The separation of different annihilations in time should be optimised for the fastest, 10 keV particles, but should also take into account that the beam transport difficulties increase with decreasing energy.

The scheme of the proposed system is presented in Figure 7.13. In this proposal, the antiproton, antihydrogen atom and ion beams are transported a few meters away from the switchyard. This allows to separate the different annihilation points by at least 1 μs time. This delay of 1 μs was chosen, as it is the minimum exposure time of the detection system (CCD camera exposure time). Also, such delay allows to eliminate the fast components of the antiproton annihilation background. In principle it would be possible to extend the proposed lines even further away, however, it would not change significantly the slow neutron background, which has a time constant in the order of ms. Moreover, the GBAR experimental area is too small to accommodate a larger system.

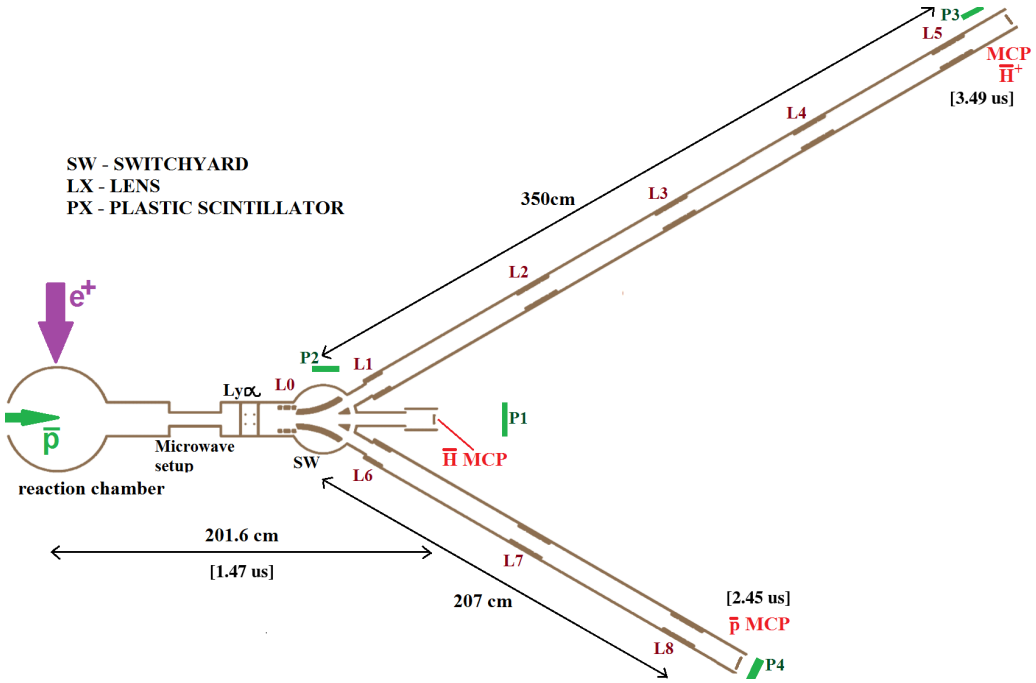

Figure 7.13: Scheme of the transport and detection system of antiproton, antihydrogen atom and ion beams.

7.7.1 Antiproton/antihydrogen ion transport line

The antiproton line is 2.07 m long, and the antihydrogen ion line is 3.5 m long. A beam-loss free transport system to the detectors was designed. The first component is a switchyard designed by A. Husson [65]. Then, there are two straight lines with electrostatic lenses used to focus the beam during the transport.

Switchyard

The switchyard is an electrostatic bender consisting of four electrodes and grounded gates at the entrance and outputs, see Figure 7.14. Two long electrodes are curved along the required antiprotons and antihydrogen ions paths. The system is designed in a way to let the neutral particles go straight to the detection system placed outside the switchyard.

In the switchyard, an electrostatic field gradient is applied in the y-plane, perpendicular to the beam direction. If the beam is not parallel, its size in the y-dimension increases after the switchyard. Also, particles with energy higher than the mean energy $< E >$ are going to deviate less than particles with energy smaller than $< E >$. The switchyard enlarge the beam size according to its energy spread.

The basic switchyard design was proven to work for antiproton energies between 1 keV and 10 keV. However, according to SIMION simulations, at energies lower than 4 keV, the beam after the switchyard has a too large angular distribution and thus only after few tens of centimeters hits the vacuum pipes. In order to decrease the beam spread, electrostatic lenses were added before and after the switchyard. The proposed focusing system is also beneficial when the beam quality is not as good as expected.

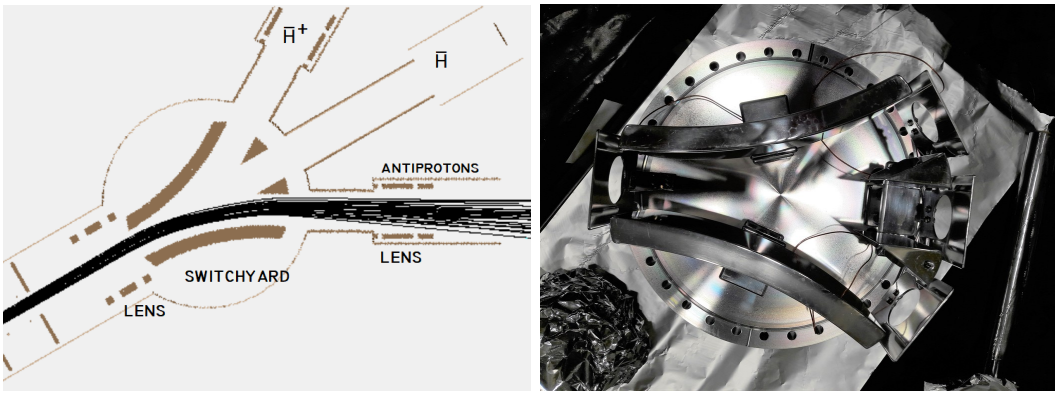

Figure 7.14: Scheme and photograph of the switchyard.

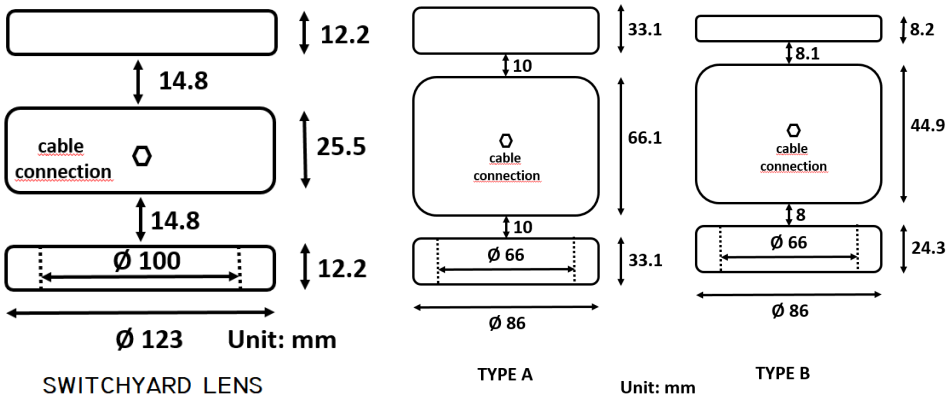

Figure 7.15: Left: Scheme of the lens before the switchyard. Right: The two types of focusing lenses used for antiproton and antihydrogen ion transport.

Focusing lenses

The focusing lens before the switchyard had to fit within an 8 cm long, DN160 pipe. Its design is presented in Figure 7.15.

In order to focus and transport antiprotons and antihydrogen ions the transport lines were designed. The main ingredients of these lines are electrostatic Einzel lenses. Two types of focusing Einzel lenses were prepared, see Figure 7.15, in order to fit into the different mechanical parts. The inner diameter of the lens is equal to 86 mm, which is about 2 times larger than the expected beam size to avoid focusing aberrations.

7.7.2 Antiproton line

The scheme of the antiproton line is shown in Figure 7.16. The first lens of type B is situated as close to the switchyard as possible. It is necessary in order to refocus the beam before it hits the walls. The next lens is placed in the middle between the first lens and the antiproton detector. The simulation performed in SIMION shows that the beam after the switchyard can be successfully refocused and fit inside the Faraday Cup detector. According to the SIMION simulation performed in an ideal case, the antiproton beam line has 100 % transport efficiency at antiproton energies between 1 keV and 10 keV.

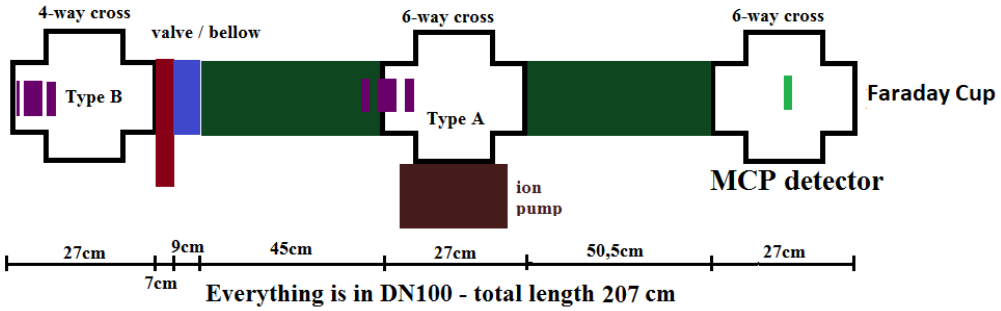

Figure 7.16: Scheme of the antiproton beam line.

7.7.3 Pumping system for antiproton line

The antiproton transport requires a pressure at least in the order of 10^{-10} mbar. In order to reach this value, an ion pump with 300 l/s pumping speed was placed in the middle cross of the antiproton line. The choice of the pump is supported by two arguments:

- calculations including outgasing and the system conductance show that 150 l/s is a proper pumping speed;
- in the other parts of the experiment 300 l/s pumps are being used, thus in case of failure it could be temporarily exchanged with an other pump.

7.7.4 Antihydrogen ion line

The general scheme of the antihydrogen ion line is presented in Figure 7.17. Again, the first lens is situated as close as possible to the switchyard output. The other lenses are uniformly

distributed along the line. According to the SIMION simulation performed in an ideal case, the system has 100 % transport efficiency.

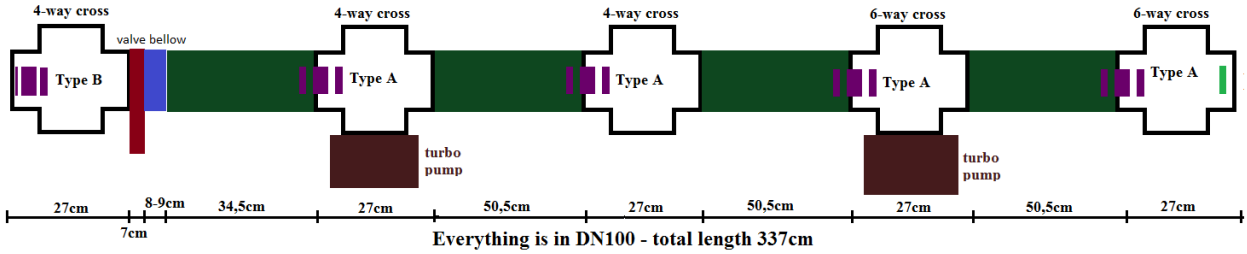

Figure 7.17: The scheme of the antihydrogen ion line after the switchyard.

7.7.5 Pumping system for antihydrogen ion line

The antihydrogen ion line is almost two times longer than the antiproton line. Thus it requires two pumping stations in the second and the fourth crosses, see Figure 8.13. In this case it is not possible to use ion pumps, because the emitted ions could create a background for the single antihydrogen ion measurement. Turbo pumps with a pumping speed in the order of 350 l/s are recommended.

7.8 Temporary antiproton line

In the summer of 2018 the first GBAR antiproton run took place. A temporary antiproton line was built, see Figure 7.18. It is longer than the original design (see Section 7.7.2) in order to delay the annihilation of the antiprotons. This relaxes some constraints on the parameter of the experiment. In standard experimental conditions it is not possible to use an extended beam line, because the delayed antiproton annihilation creates a higher background for antihydrogen ion detectors.

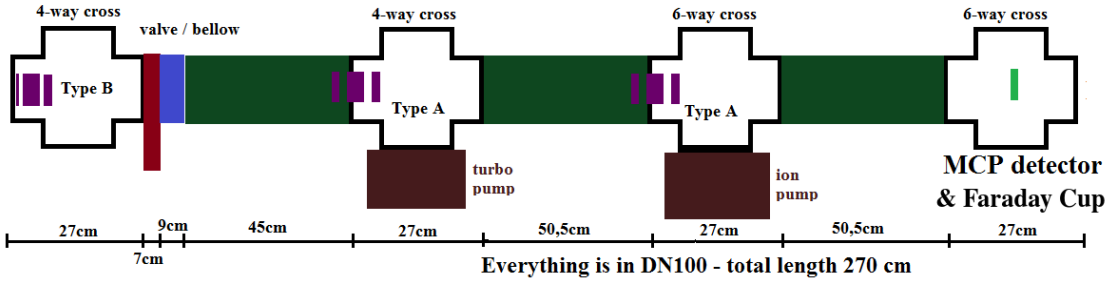

Figure 7.18: Scheme of the temporary antiproton beam line after the switchyard.

At the end of the temporary line a Faraday Cup and an MCP detector were placed. This detector has a stainless steel cover. The inside of the cup is made from graphite to decrease the number of emitted secondary electrons. The entrance to the detector has a 10 mm diameter and is covered with a grid which can be used as an energy analyser, see Figure 7.19.

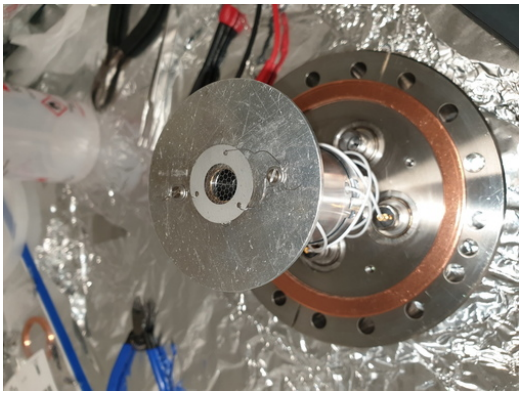

Figure 7.19: Photograph of the Faraday Cup used for the detection of the antiproton and proton beams flux.

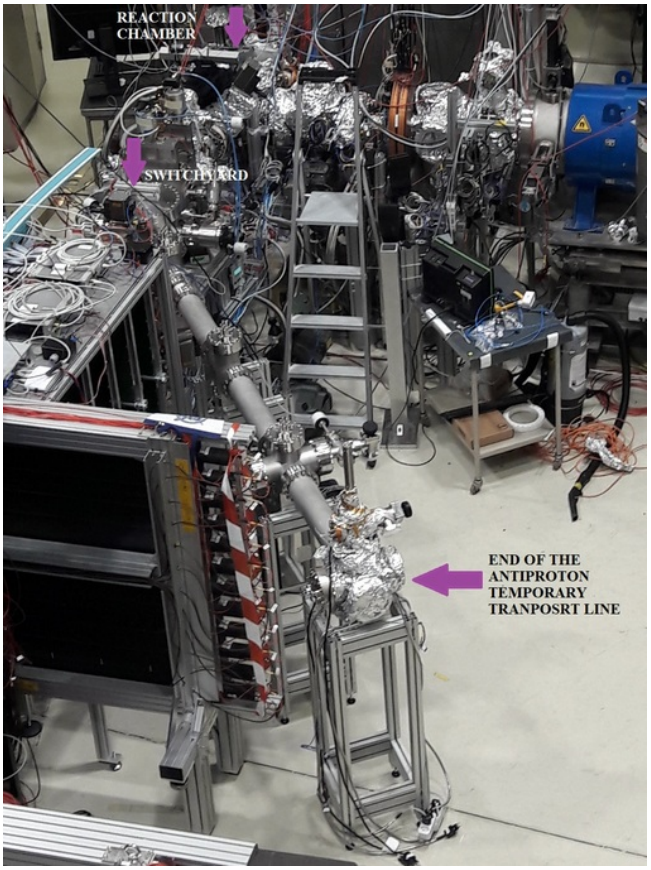

Figure 7.20: Photograph of the temporary antiproton beam line after the switchyard.

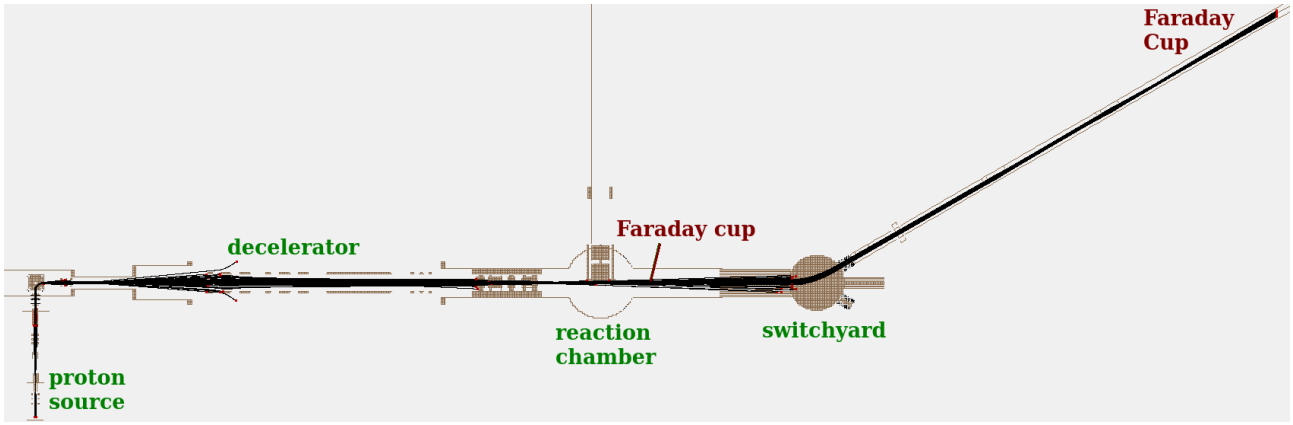

Figure 7.21: Scheme of the proton beam transport from the proton source up to the end of the transport line. Screenshot from the SIMION.

7.8.1 Performance

A photograph of the setup is shown in Figure 7.20. A pressure level of 10^{-10} mbar was achieved. Recently, the first tests with the H_3^+ beam were performed. The measured transmission efficiency from the reaction chamber till the Faraday Cup at the end of the temporary antiproton line was 90 %. It should be noted that the tests were carried out with a not fully optimized beam, which allows to believe that further optimisations will allow for 100 % beam transmission.

The procedure of the optimisation of the beam transport is based on the SIMION simulation developed by the collaboration. It describes the ion transport from the ELENA decelerator or the proton source up to the free-fall chamber. The full simulation setup starting from the proton source is shown in Figure 7.21. Parameters of the steering elements are first obtained from the simulation and they are compared to the experiment. Then, the simulation is corrected if any differences were found and understood. This iterative procedure gives now a good agreement between the simulation and experiment.

7.9 Summary

The system of (anti)proton beam preparation was successfully developed together with the transport system for (anti)protons, (anti)hydrogen atoms and ions after the reaction chamber. The scheme was optimised to minimise the backgrounds and beam losses. The first tests of deceleration with 100 keV antiprotons were performed during the summer of 2018.

The ideal simulations of the transport system after the reaction chamber show 100 % transport efficiency. Now, the whole transport system is being tested and optimised in a realistic conditions with the proton beam.

The tests with the proton beam helps to understand the developed system. However, the beam tunning with antiprotons may be different than for protons, as the initial parameters of the beam are disparate and there is a magnetic field coming from the positron traps.

Chapter 8

$\bar{H}$ and $\bar{H}^+$ detection system and background estimation

8.1 Detection system

The antihydrogen atom and ion cross-section measurement requires a precise detection of the antiproton, antihydrogen and antihydrogen ion beam intensities. The detection system has been designed in a way to increase the detection efficiency and minimise the background and systematic errors.

The scheme of the detection and transport system is shown in Figure 8.1. The antiproton-positronium reaction takes place at the centre of the reaction chamber. The created beams propagate along the antiproton beam direction. They are separated at the switchyard level, from where they are guided to their proper detection systems.

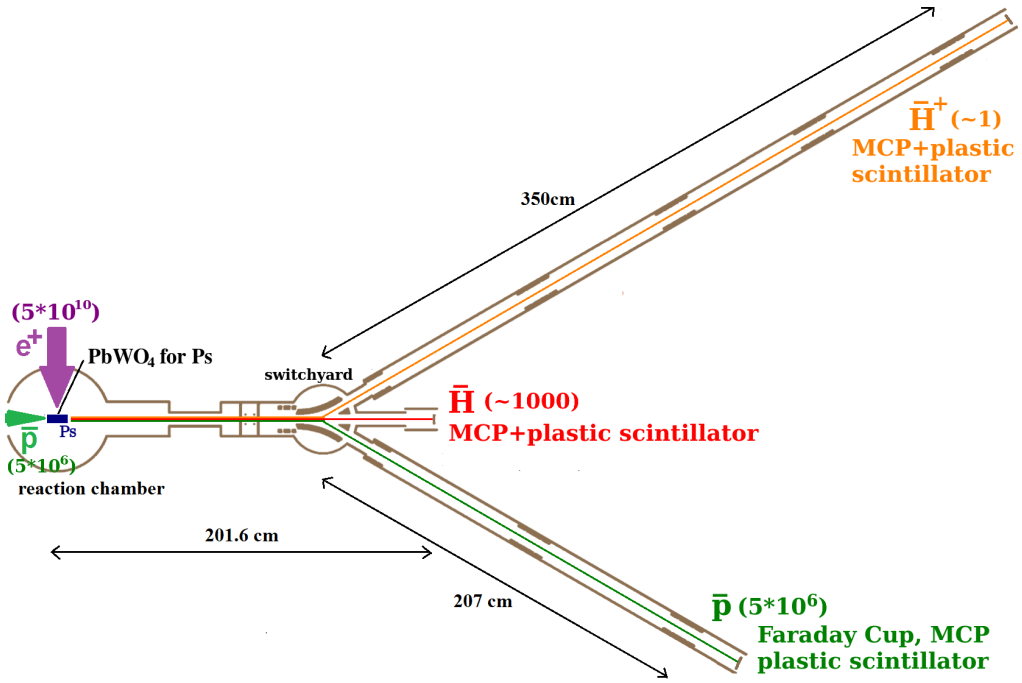

Figure 8.1: Antiproton, antihydrogen and antihydrogen ion detection scheme together with the transport system.

The first version of the control system for the cross-section measurements was developed and is described in Appendix D.

8.1.1 Antihydrogen atom detection system

In order to measure the amount of antihydrogen atoms an MCP/CCD detector is developed. When a particle hits the MCP detector then it works like an electron multiplier. Electrons then hit a phosphor screen, whose light is collected by a 14bit CCD camera. The pictures taken by the camera are analysed using a software written in C++/ROOT and Python programming languages. The whole setup is presented in Figures 8.2 and 8.3. The electric signal from the back side of the MCP detector is collected. The MCP detector has been chosen due to its expected very high antihydrogen detection efficiency and the possibility to measure from one to few thousand particles with the same setup [165, 166, 167].

Next to the MCP there is a fast plastic scintillator detector, which is sensitive to almost all antihydrogen annihilation products. It is used for beam diagnostics.

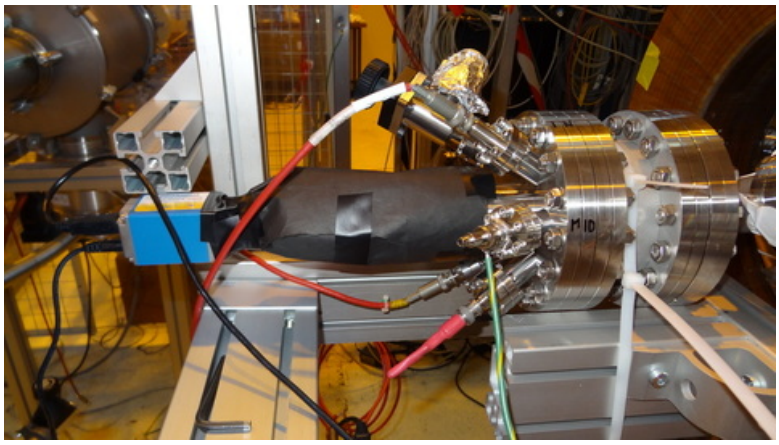

Figure 8.2: Photograph of the MCP/CCD detector. The MCP together with the phosphor screen is placed in the vacuum chamber (right side of the picture). In order to protect the CCD camera from external light the black plastic cover is used.

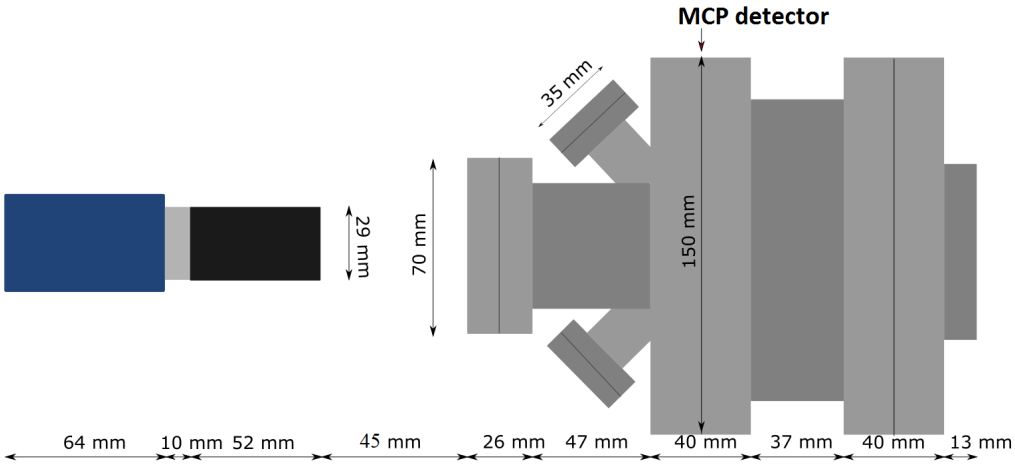

Figure 8.3: Scheme of the CCD/MCP detector.

Antihydrogen MCP detector

The MCP detector is made from two Microchannel Plates in a Chevron configuration and a P46 phosphor screen. The front side of the MCP is gold plated to allow for fast switching on the detector. All three plates are mounted in a stainless steel frame. In front of the MCP there are two electrodes (later called grid) that are supposed to repel incoming charged particles. In principle, the system is designed to minimise the presence of any charged particles, so both electrodes should not be necessary. A photograph of the detector is presented in Figure 8.4a. Its center is placed 72.7 cm from the centre of the switchyard.

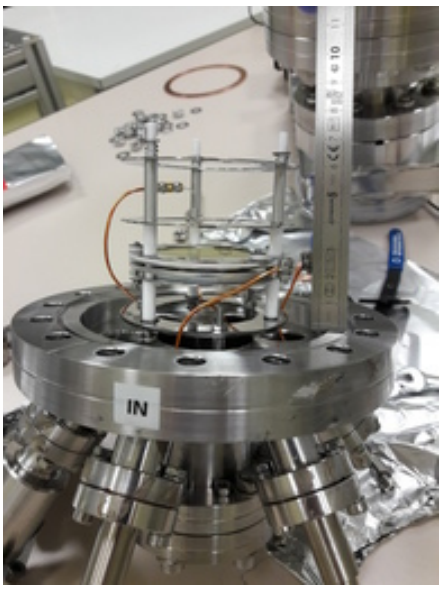

(a) The MCP detector.

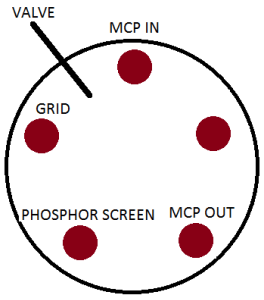

(b) The MCP detector electrical connections. A perspective towards the upcoming beam.

Figure 8.4: The MCP detector for antihydrogen atom detection.

The most important informations from the manufacturer about the MCP are:

- diameter: 40 mm (minimum);
- center-to-center spacing: 12 μm;
- pore size diameter: 10 μm;
- bias angle: $8° \pm 1°$;
- open area ratio: 55% minimum;
- electron Gain at 2400 Volts: 1.7×10^7;
- dark count: 0.4 (cts/sec/cm^2) maximum.

The detector has 4 high voltage connectors, see Figure 8.4b. The following voltages should be used for single antihydrogen atom detection:

- MCP in $-2kV$;

- MCP out GND;
- phosphor screen $+2kV$;
- grid $+2kV$ - can be adapted according to ion background.

The most important information about the fast P46 phosphor screen:

- 90% - 10% decay times of around 100 to 300 ns;
- maximum power per 1cm^2 - 1W.

A more detailed description of the behavior of the MCP detector and camera properties is given in Appendix B. Some results from the proton tests are described in Appendix C. In both appendices, a different MCP detector is used than the one used in this Chapter, as the original detector broke during the transport.

Plastic scintillator

The second device used for antihydrogen detection is a 55 mm thick plastic scintillator with a light guide and an XP2020 photomultiplier tube. Its front side is 11.8 cm by 13 cm. The centre of this detector is placed 297.5 mm from the center of the MCP detector. The working voltage of the detector's photomultiplier is -1800 V.

8.1.2 Antihydrogen ion detection system

The antihydrogen ion detector is an MCP detector identical to that of the antihydrogen atom detector. Here, there is no grid in front of the MCP and the front side of the detector is grounded as the electrostatic field generated by the grid and the MCP could ionise the antihydrogen ion. However, if there is no possibility to determine the detection efficiency for antihydrogen ions, but the one for the atoms is known, it is possible to neutralise the ion via a voltage on a grid placed just in front of the MCP surface. The detection problem then turns back to that for the atoms, plus determining the neutralisation efficiency.

8.2 Systematic errors

The measurements of the antihydrogen atom and ion beam intensities have the following systematic errors:

A beam losses due to:

- A1 inadequate transport, for example too large beam emittance, incorrect focusing and steering. This background should be eliminated with the designed transport system.
- A2 interaction of antihydrogen atom and ion with residual gas (mainly hydrogen), see Section 8.2.1.

B detection method:

- B1 antihydrogen detection efficiency of the MCP for a given antihydrogen energy, see Section 8.3.

B2 elastic back-scattering of antihydrogen atoms and ions at the MCP surface, it can be included in the definition of the detection efficiency.

B3 dark noise of the MCP detector and natural background, see Section 8.4.1.

B4 gamma background from positron annihilation, see Section 8.4.2.

B5 gamma background from positronium annihilation, see Section 8.4.3.

B6 background from antiproton annihilation in the reaction chamber, see Section 8.4.5, and in the antiproton dump, see Section 8.4.6.

B7 background from antiproton, antihydrogen atom and ion annihilation on the residual gas, see Section 8.2.1.

B8 data analysis error. This error is not discussed in detail in this thesis, since it strongly depends on the data set and the analysis algorithm.

B9 only for antihydrogen ion: background from antihydrogen annihilation, see Section 8.4.7.

The total number of produced antihydrogen atoms/ions can be extracted from the detector signal using the following equation:

$$N_{\bar{\mathrm{H}}} = \frac{N_{\bar{\mathrm{H}}0} - N_{background}}{\eta_{analysis} \cdot \eta_{detection} \cdot R_{residual-gas}} \tag{8.1}$$

where

$N_{\bar{\mathbf{H}}0}$ - number of events extracted from the MCP/CCD image analysis;

$N_{background}$ - number of background events measured separately;

$\eta_{analysis}$ - data analysis efficiency;

$\eta_{detection}$ - antihydrogen atom/ion detection efficiency;

$R_{residual-gas}$ - percentage of antihydrogen atoms not lost due to interactions with residual gas.

The number of background events is:

$$N_{background} = N_{B3} + N_{B4} + N_{B5} + N_{B6} + N_{B7} + (N_{B9}) \tag{8.2}$$

where N_{B9} is counted only for the antihydrogen ion detection.

8.2.1 Interactions of antiprotons, antihydrogen atoms and ions with residual gas

The goal for the pressure value in the system is 10^{-10} mbar. At that level the main component of the residual gas is molecular hydrogen. The expected hydrogen density in the system is $n_{H_2} = 2.5 \times 10^6$ cm^{-3}. The antiproton, antihydrogen atom and ion beams may interact with hydrogen to either create an additional background or cause beam losses and bias the flux measurements.

The number of interactions is:

$$N_{interactions} = N_{particles} \cdot n_{H_2} \cdot L \cdot \sigma, \tag{8.3}$$

where

- $N_{particles}$ - number of particles in the beam;
- n_{H_2} - density of hydrogen molecules in the residual gas;
- L - length of the interaction region;
- σ - cross-section for the interaction between the particles in the beam and the residual gas.

Antiproton scattering

A summary of antiproton interactions with different gases is presented in [168]. The total cross-section for the interaction of antiprotons with molecular hydrogen is calculated to be in the range $(10-20)\times10^{-16}$ cm^2 [169]. This gives only up to 10 lost antiprotons during the transport over 4 m. This effect is below the uncertainty of the antiproton beam flux measurement. Also, the loss of 10 antiprotons can not create a significant background for the antihydrogen atom/ion measurement due to the small geometrical acceptances of detectors.

The total ionisation cross-section for antiproton interaction with H_2 is equal to about 1.5×10^{-16} cm^2 at 10 keV antiproton energy. This gives a negligible effect for the measurement of the total antiproton beam intensity, however, it could be a source of a background for other measurements, as ions can be guided together with other beams. The ionisation process of the molecular hydrogen creates two potential backgrounds for antihydrogen ion production - formation of H^+ and H_2^+. The cross-section values at 13 keV antiproton initial energy are $\sigma_{H^+} = (0.26\pm0.03)\times10^{-16}$ cm^2 and $\sigma_{H_2^+} = (1.04\pm0.1)\times10^{-16}$ cm^2 [170]. According to [169] the cross-section values are equal or smaller in the energy range between 1 and 10 keV. The expected number of ions formed for 5×10^6 antiprotons transported over a 2 m distance (up to the switchyard level) is $N_{H^+} = 0.065$ and $N_{H_2^+} = 0.26$. These numbers may seem significant, however the ions are produced in an inelastic process, so most of them will not follow the beam. Additionally, the difference in velocity results in more than 1 μs delay between the detection of the antihydrogen and H_2^+ ions, under the assumption that the detector is at 3.5 m distance from the switchyard. The time delay is larger than the detection window, thus H_2^+ will not be detected.

Antihydrogen scattering

According to calculations from [171, 172], the total cross-section for antihydrogen loss on molecular hydrogen is in the order of a few 10^{-16} cm^2. The expected maximum cross-section value is for 8.16 keV energy and is equal to $(4.0\pm0.2)\times10^{-16}$ cm^2. The transport length for antihydrogen is about 200 cm. With up to 2000 antihydrogen atoms in the beam and an overestimated total cross-section of 10^{-15} cm^2, the number of lost antihydrogen atoms is smaller than 10^{-3}. This effect is thus negligible for the current system.

Antihydrogen ion scattering

There are no calculations for the interaction of antihydrogen ions with molecular hydrogen. The total cross-section value in the energy range between 1 keV and 10 keV can be approximated with a simple geometrical elastic cross-section. The total elastic cross-section for the collision of two hard spheres with radii r_1 and r_2 is equal to $\sigma = \pi(r_1+r_2)^2$. The Van der Waals radius

of an antihydrogen ion is equal to the radius of the hydrogen anion $r_1 = 154$ pm. The kinetic radius of the hydrogen molecule is $r_2 = 145$ pm. Then, the cross-section is $\sigma = 28.1 \times 10^{-16}$ cm^2.

It is expected to produce maximum 1 antihydrogen ion which has to be transported over 500 cm. The probability for its interaction with hydrogen gas is smaller than 10^{-6}. No beam loses due to the interaction with residual gas are expected.

8.3 Detection efficiency of the MCP detector for antihydrogen atoms and ions

The hydrogen detection efficiency of the MCP has been thoroughly studied by a few groups around the world. The expected maximum absolute detection efficiency for matter particles is equal to the ratio of the open area of the micro channels to the surface of the whole MCP. Its value depends on the MCP model and is usually equal to about $50 - 60\%$. The relative detection efficiency of the MCP is equal to the measured detection efficiency divided by the maximum absolute detection efficiency.

According to the published data [166, 167, 165] it is expected to have 100% relative detection efficiency for hydrogen atoms with kinetic energies above 1 keV. Example results are shown in Figure 8.5, where the dashed line represents the maximum absolute detection efficiency. The probability to eject an electron from the wall of the MCP should be the same for hydrogen atoms and ions, due to the secondary electron emission process dependent on the kinec energy of the incident particle [173]. It is correct to assume that the relative detection efficiency for the hydorgen ion is also equal to 100% for kinetic energies higher than 1 keV. The measurements presented in [165] show that the detection efficiency of hydrogen atoms and ions are decreasing for energies below 1 keV, see Figure 8.6.

It is assumed that the antihydrogen detection efficiency should be at least equal to the detection efficiency of hydrogen due to the similar properties and that the secondary particles produced in the annihilation may leave an additional signal in the MCP detector. In order to check that hypothesis it is recommended to perform a detection efficiency measurement of the MCP for single protons and antiprotons.

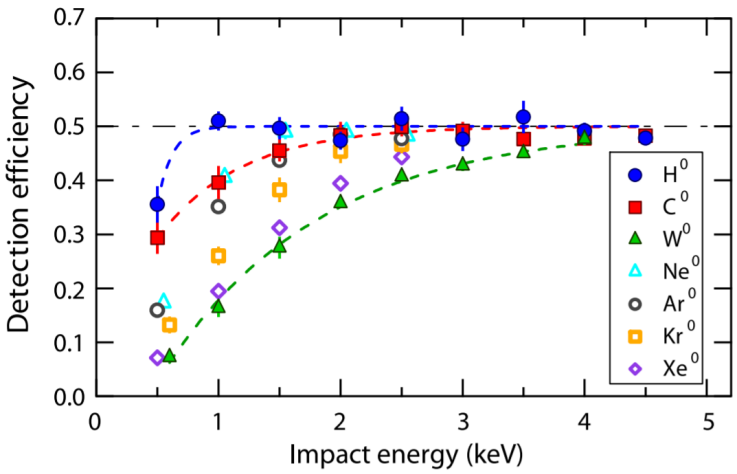

Figure 8.5: Absolute detection efficiencies for H, C, and W as a function of impact energies. Figure adapted from [166].

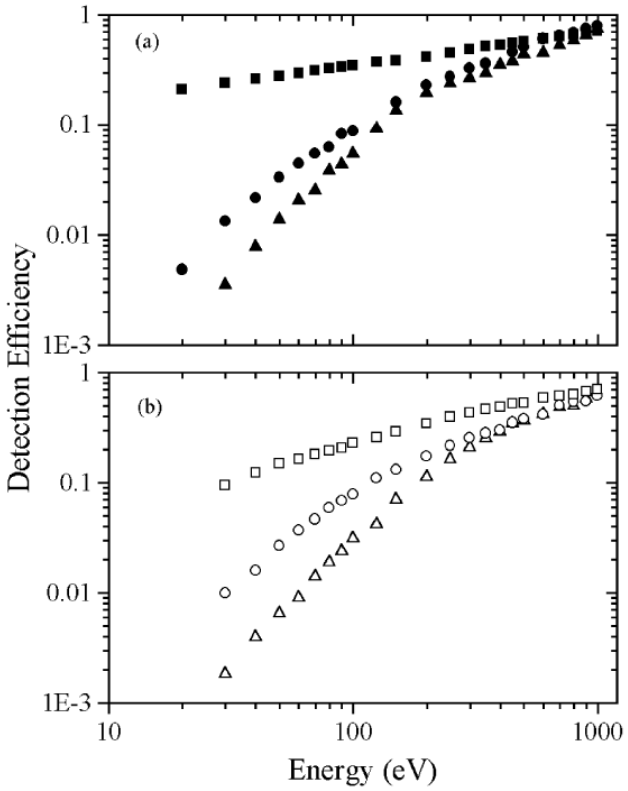

Figure 8.6: (a) Relative detection efficiencies for H^- (black square), H (black circle) and H^+ (black triangle) as a function of impact energy. (b) Efficiencies for D^- (empty square), D (empty circle) and D^+(empty triangle). Figure adapted from [165].

8.3.1 Proposals to measure the MCP detection efficiency

There are three ideas to measure the MCP detection efficiency for protons, antiprotons, hydrogen or antihydrogen which can be adapted to the GBAR experimental setup:

Idea 1 protons and antiprotons - using a low intensity beam produced with a 100 μm pinhole;

Idea 2 hydrogen and antihydrogen - cross calibration with the setup used in the Lamb shift experiment;

Idea 3 hydrogen - with a low intensity hydrogen beam produced from protons interactions with the residual gas.

8.3.2 Proton and antiproton detection efficiency - idea 1

At the centre of the reaction chamber a 100 μm pinhole is installed. It allows to decrease the beam intensity to few tens of particles per pulse. By measuring the initial beam profile it is possible to estimate how many particles are left after collimation. The precision of that measurement is limited by the precision of the measurement of the antiproton beam profile, which is expected to be at the level of 10 %. The transport efficiency of the single particle beam is equal to the transport efficiency of the full beam, i.e. 100 %. This low intensity beam can be

used to test detectors and measure the proton and antiproton detection efficiency. This method allows to easily compare the MCP detection efficiency for matter and antimatter.

8.3.3 Hydrogen and antihydrogen detection efficiency - idea 2

The MCP detector can be cross-calibrated with another detector which has a known hydrogen/ antihydrogen detection efficiency. For that purpose, the detection system from the Lamb shift measurement (Section 2.2.6) can be used. The Lamb shift system can estimate the H(2s) beam population by measuring the Lyman alpha transition. In this case, atoms can be measured on the MCP in coincidence with the Lamb shift detector. The main constraints on these experiments are that the beam has to have very low intensity and the Lyman alpha detectors have to be well-calibrated. A proper calibration for 121.5 nm photon of used MCP detectors with a special CsI coating is a challenging task and an experiment on its own.

8.3.4 Hydrogen detection efficiency - idea 3

The measurement of the MCP detection efficiency for 1-10 keV hydrogen atoms requires a low intensity hydrogen beam. It is possible to produce it using a charge exchange process between protons and molecular hydrogen from the residual gas. A scheme of the detection system and hydrogen beam production is shown in Figure 8.7. When the proton beam propagates through the system a part of it interacts with the residual gas and produces a hydrogen beam.

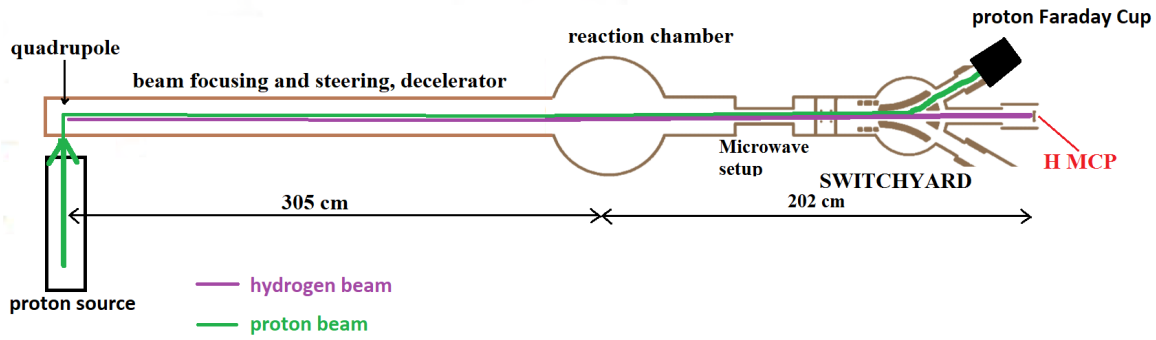

Figure 8.7: Scheme of a hydrogen beam production setup and the detection system.

Low intensity hydrogen beam

A typical composition of the residual gas in an ultra high vacuum (UHV) environment is shown in Figure 8.8. The dominant ingredient is H_2 gas. All other gasses are present with a pressure at least one order of magnitude lower.

The main interaction channels between the protons and the residual gas are elastic scattering and charge exchange reactions. The second one leads to the production of neutral hydrogen atoms

$$p + H_2 \rightarrow H + H_2^+. \tag{8.4}$$

A study of this process is presented in [175]. The cross-section values for different proton incident energies are summarised in Table 8.1. An important property of the charge exchange reaction is that the momentum of the produced hydrogen is equal to the momentum of the incident

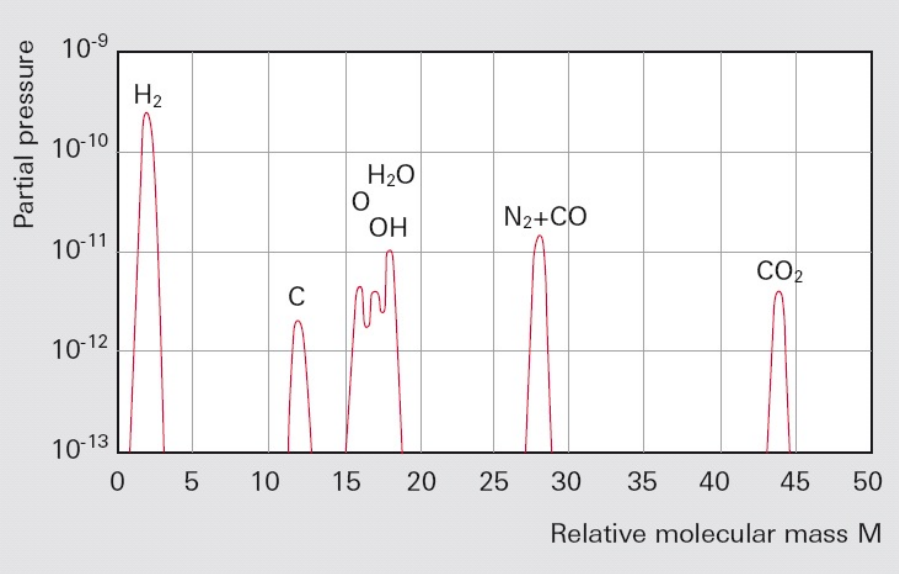

Figure 8.8: Typical residual gas spectrum of a vessel evacuated by a turbomolecular pump. Figure adapted from [174].

protons. It allows to create a hydrogen beam with known emittance, which can be deduced by measuring the properties of the proton beam. This reaction allows to produce a low intensity hydrogen beam with a known intensity.

proton energy [keV]	$\sigma(p, \mathbf{H}_2)$ **[cm^2]**
6	8.8×10^{-16}
7	8.9×10^{-16}
8	8.9×10^{-16}
9	8.9×10^{-16}
10	8.8×10^{-16}

Table 8.1: Cross-section values for reaction 8.4 for different proton incident energies. The error for every value is within ±5 % [175].

Hydrogen beam intensity

The number of produced hydrogen atoms is equal to

$$N_{\mathrm{H}} = N_p \cdot n_{H_2} \cdot L \cdot \sigma(p, \mathrm{H}_2), \tag{8.5}$$

where

- N_p - number of protons in a pulse;
- n_{H_2} - density of hydrogen molecules in the residual gas;
- L - length of the interaction region;
- $\sigma(p, \mathrm{H}_2)$ - cross-section for reaction 8.4.

Proton beam characteristics

The present proton gun produces a continuous proton beam of 1.5 μA intensity. In order to obtain a better detector resolution it is better to use a pulsed beam (no shadow from previously detected particles on an image). For 500 ns bunch length the number of protons in the beam is equal to $N_p = 5 \times 10^6$.

The idea is to create a parallel beam which propagates from the quadrupole bender to the switchyard, see Figure 8.7. The proton beam is then deflected and guided to the Faraday Cup where its intensity can be measured. The neutral hydrogen beam goes straight to the MCP detector. Using a focusing and steering system available in the experiment, it should be possible to create a 1 cm wide parallel proton beam. This problem requires more detailed study and tests. Additionally, it is possible to simulate the eventual hydrogen beam emittance based on the proton beam behavior along the beam transport.

Density of hydrogen molecules

The density n_{H_2} of hydrogen molecules can be estimated from the pressure measurement using

$$p = n_{H_2} \cdot k \cdot T, \tag{8.6}$$

where p is the pressure in the system, k is the Boltzman constant and $T = 293$ K is the gas temperature.

The main error on the density comes from the measurement of pressure. The hydrogen molecules density for 10^{-8} mbar gas pressure is 2.5×10^8 cm^{-3}.

Length of the interaction region

The length of the interaction region where the protons interact with the residual gas is equal to 409 cm. This distance is measured from the quadrupole bender to the centre of the switchyard.

Number of hydrogen atoms in the beam

According to equation 8.5 the number of hydrogen atoms produced by a 10 keV proton bunch at 10^{-8} mbar pressure is equal to about 440 atoms/bunch.

Changing the pressure value in the system allows to obtain different hydrogen beam intensities starting from only a few particles for 10^{-10} mbar pressure to even few thousand particles for 10^{-7} mbar pressure. This is an important feature which can be used to perform detailed study of the MCP detector properties.

The real number of hydrogen atoms that reach the MCP detector is:

$$N_{\mathrm{H}_{MCP}} = N_{\mathrm{H}} \cdot R_{elastic} \cdot R_{residual-gas} \cdot A_{MCP} \tag{8.7}$$

where

$N_{\mathbf{H}}$ - estimated number of hydrogen atoms in the beam based on equation 8.5;

A_{MCP} - detector acceptance;

$R_{elastic}$ - percentage of hydrogen atoms that do not elastically back-scatter from the MCP surface;

$R_{residual-gas}$ - percentage of hydrogen atoms not lost in interactions with the residual gas.

Hydrogen detection efficiency of the MCP detector

The total number of antihydrogen atoms can be extracted from the detector signal using the following equation:

$$\eta_{detection} = \frac{N_{\mathrm{H0}} - N_{background}}{N_{\mathrm{H}_{MCP}} \cdot \eta_{analysis}} \tag{8.8}$$

where

$\eta_{detection}$ - hydrogen atom detection efficiency;

$N_{\mathbf{H0}}$ - number of events extracted from MCP/CCD image analysis;

$N_{background}$ - number of events from the background measured separately. The only background comes from cosmic radiation and dark noise of a detector, which is measured to be smaller than 2×10^{-5} events per image.;

$\eta_{analysis}$ - data analysis efficiency;

$N_{\mathbf{H}_{MCP}}$ - number of hydrogen atoms reaching the MCP detector.

8.4 Background estimation

The following Section describes the estimation of possible backgrounds that may occur during the antihydrogen atom and ion detection. Estimations are based on both simulations and measurements performed by either the GBAR collaboration or other groups.

8.4.1 Environmental background

According to the measurement described in Appendix B, the probability of detection of a natural background event or dark noise is $p_D = 2.2 \pm 0.83 \times 10^{-5}$ for 1 μs measurement duration. This measurement was performed for the antihydrogen detector. This value should be similar for the antihydrogen ion MCP.

8.4.2 Positron annihilation background

The whole positron pulse will have a maximum length of 100 ns. About 70 % of the particles should annihilate into two 511 keV gammas on the target cavity. Considering the fact, that the antihydrogen measurement is delayed in time by at least 1.29 μs in case of 10 keV antiprotons, it is expected to have zero background coming from positron annihilation. The same argument can be used for antihydrogen ion detector. In order to cross-check that hypothesis Geant4 simulation was performed.

In the reaction chamber, 70 % of the interactions of expected 5×10^{10} positrons produce two 511 keV gammas. This number stands for direct positron annihilation (50 %), backscattered positron annihilation (10 %) and para-positronium annihilation (10 %, τ = 125 ps). The positron beam has a Gaussian distribution in time with σ_t = 30 ns. The spatial distribution can be omitted, as the acceptances of the antihydrogen atom and ion MCPs are equal to $A_{\bar{\mathrm{H}}MCP} = 3.23 \times 10^{-5}$ and $A_{\bar{\mathrm{H}}^+MCP} = 5.1 \times 10^{-6}$. As expected, due to the time difference between gamma production and detection time, the gamma background is equal to 0.

8.4.3 Positronium annihilation background

Positronium annihilates into 3 gammas with energy between 0 to 511 keV. The range of these photons in stainless steel is smaller than 3 cm. Between the reaction chamber and antihydrogen atom MCP there is a lot of vacuum equipment, thus the antihydrogen MCP is able to detect only photons produced directly in front of it in the reaction cavity. All of them have incident momentum perpendicular to the detector surface. Estimated numbers of photons reaching the antihydrogen atom MCP are summarised in Table 8.2 and Table 8.3. The number of detected photons is always smaller than 1, as the gamma detection efficiency for 511 keV energy is equal to 0.26 %. In case of antihydrogen ion detector, the estimated positronium annihilation background is summarised in Table 8.4. The effect of material between the reaction chamber and the detector is not included, but even without it, the background is negligible.

$\bar{H}$ energy	velocity	t_{meas} [μs]	expected N of γ	Detected N of γ
2 keV	1 m/1.6μs	3.2	$< 6 \times 10^{-5}$	0
6 keV	1 m/0.94μs	1.8	1.3	0.003
10 keV	1 m/0.73μs	1.4	21	0.05

Table 8.2: Case A.1. Expected number of detected photons on the antihydrogen atom MCP coming from positronium annihilation. The time t_{meas} is counted from the beginning of the positronium production.

$\bar{H}$ energy	velocity	t_{meas} [μs]	expected N of γ	Detected N of γ
2 keV	1 m/1.6μs	3.2	0	0
6 keV	1 m/0.94μs	1.8	0.01	$< 3 \times 10^{-5}$
10 keV	1 m/0.73μs	1.4	0.2	0.001

Table 8.3: Case A.2./B. Expected number of detected photons on the antihydrogen atom MCP coming from positronium annihilation. The time t_{meas} is counted from the beginning of the positronium production.

$\bar{H}$ energy	Time of flight	t_{meas}	expected N of γ
2 keV	1 m/1.6μs	7.6	$< 10^{-17}$
6 keV	1 m/0.94μs	4.5	$< 10^{-8}$
10 keV	1 m/0.73μs	3.5	$< 10^{-5}$

Table 8.4: Case A.1. Expected number of detected photons on the antihydrogen ion MCP coming from positronium annihilation. The time t_{meas} is counted from the beginning of the positronium production.

8.4.4 Antiproton annihilation simulation setup

The antiproton/antihydrogen annihilation background estimation is done using a Geant4 simulation. It is using the same scheme as the one presented in Chapter 6, see Figure 8.9. The

reaction chamber, switchyard and three beam transport lines are included in the simulation together with the concrete wall and floor. It is important to add the floor and walls to the simulation, as a slow neutron background is originating mostly from them. The antiproton detector is a Faraday Cup in order to minimise the delayed background caused by elastic scattering. Also an antiproton beam collimator in the reaction chamber has a cylindrical shape.

Detectors in the simulation:

- a Faraday Cup for antiproton detection, 210 cm from the switchyard centre;
- an MCP for antihydrogen detection, 73 cm from the switchyard centre;
- an MCP for antihydrogen ion detection, 350 cm from the switchyard centre.

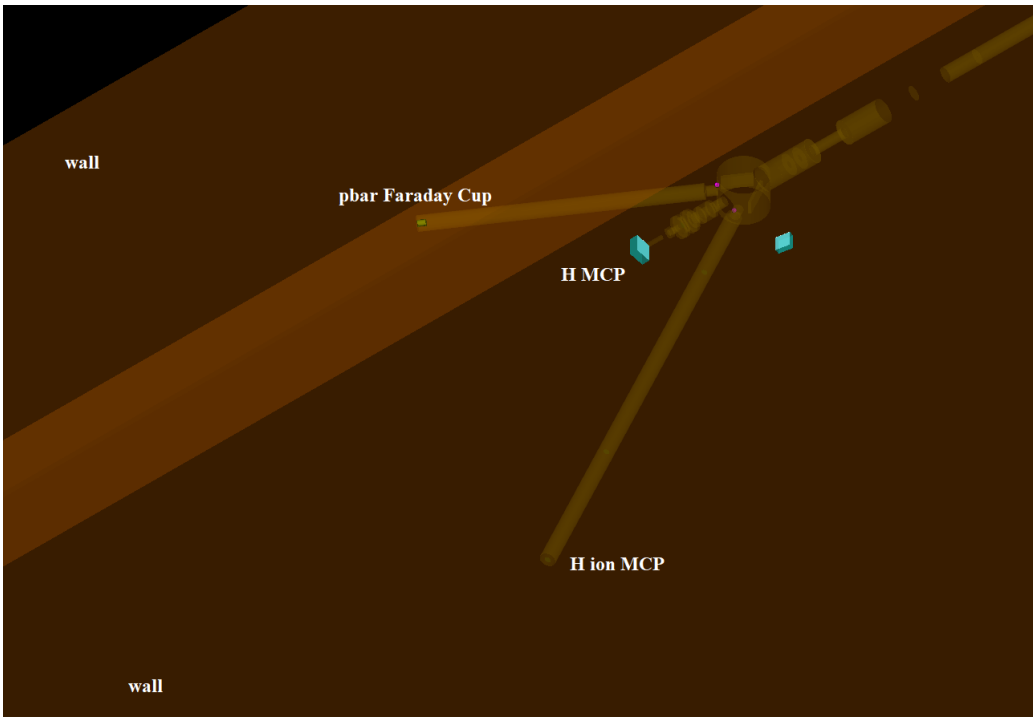

Figure 8.9: Scheme of the antiproton/antihydrogen annihilation simulation. There are 3 main detectors - a Faraday Cup and two MCP detectors.

8.4.5 Antiproton beam annihilation in the reaction chamber

In considered models A.2. and B 20 % of the antiproton beam annihilates in the reaction chamber. This produces a background for antihydrogen atom detection. It is studied using the simulation with 1×10^8 antiprotons with a uniform distribution in time over 300 ns. Antiprotons annihilate in the reaction chamber on the flat collimator. The results are scaled to 1×10^6 antiprotons.

Antihydrogen atom MCP

The results of the simulations for cases A.2 and B are summarised in Table 8.6. Among the particles reaching the detector the biggest part are neutrons and photons, however, due to the

expected low detection efficiency, they do not contribute significantly to the background. The largest signal comes from positrons. The detection windows of antihydrogen atoms for different beam energies are summarised in Table 8.5. The time $t = 0$ corresponds to the beginning of the positronium production.

$\bar{p}$ **energy [keV]**	**detection window [μs]**
10	1.4 - 2.5
6	1.8 - 2.8
2	3.2 - 4.2

Table 8.5: Antihydrogen atom detection window for different antiproton energies.

	detection efficiency	**N 10 keV**	**N det**	**N 6 keV**	**N det**
n	0.14% - 0.64%	1.89 ± 0.14	$0.0026 - 0.0121$	1.42 ± 0.12	$0.0020 - 0.0091$
e^-	5.8%	0.051 ± 0.023	0.0030	0.051 ± 0.023	0.0030
e^+	5.8%	0.540 ± 0.074	0.0313	0.469 ± 0.069	0.0272
γ	0.26%	5.72 ± 0.24	0.0149	4.82 ± 0.22	0.0125
sum		8.20 ± 0.29	$0.052 - 0.061$	6.76 ± 0.26	$0.045 - 0.052$

	detection efficiency	**N 2 keV**	**N det**
n	0.14% - 0.64%	0.663 ± 0.082	$0.0009 - 0.0042$
e^-	5.8%	0.051 ± 0.023	0.0030
e^+	5.8%	0.143 ± 0.038	0.0082
γ	0.26%	2.56 ± 0.16	0.0067
sum		3.41 ± 0.19	$0.019 - 0.022$

Table 8.6: Case A.2./B. Expected number of particles produced from antiproton annihilation in the reaction chamber, which can be detected by the antihydrogen atom MCP. Simulation performed for 10 keV, 6 keV and 2 keV beam energy.

Antihydrogen ion MCP

In considered models antihydrogen ions can be produced in a significant rate only in case A.1. This model assumes that there is no antiproton annihilation in the reaction chamber. However, for the future reference, that possibility is also considered. The results of the simulation for 1×10^6 antiprotons annihilating in the reaction chamber are summarised in Table 8.8. The effect of antiproton annihilation in the reaction chamber is negligible. The detection windows of antihydrogen ions for different beam energies are summarised in Table 8.7. The time $t = 0$ corresponds to the beginning of the positronium production.

$\bar{p}$ **energy [keV]**	**detection window [μs]**
10	3.5 - 4.5
6	4.5 - 5.5
2	7.6 - 8.6

Table 8.7: Antihydrogen ion detection window for different antiproton energies. The time $t = 0$ corresponds to the moment when antiprotons reach the interaction region.

	detection efficiency	**N 10 keV**	**N det**	**N 6 keV**	**N det**
n	0.14% - 0.64%	0.112 ± 0.034	$0.0002 - 0.0007$	0.183 ± 0.043	$0.0003 - 0.0012$
e^-	5.8%	0.010 ± 0.010	0.0006	–	–
e^+	5.8%	0.051 ± 0.023	0.0030	0.020 ± 0.014	0.0012
γ	0.26%	0.500 ± 0.071	0.0013	0.316 ± 0.057	0.0008
sum		0.673 ± 0.083	$0.005 - 0.006$	0.520 ± 0.073	$0.002 - 0.003$

	detection efficiency	**N 2 keV**	**N det**
n	0.14% - 0.64%	0.082 ± 0.029	$0.0001 - 0.0005$
e^-	5.8%	–	–
e^+	5.8%	0.010 ± 0.010	$0.0006 - 0.0061$
γ	0.26%	0.102 ± 0.032	0.0003
sum		0.194 ± 0.044	$0.001 - 0.007$

Table 8.8: Case A.2./B. Expected number of particles produced from antiproton annihilation in the reaction chamber, which can be detected by the antihydrogen ion MCP. Simulation performed for 10 keV, 6 keV and 2 keV beam energy.

8.4.6 Annihilation of the antiproton beam in the dump

The antiproton annihilation in the dump affects only the detection of antihydrogen ions, as antihydrogen atoms are detected at least 1 μs earlier. The annihilation of 10^8 antiprotons inside a Faraday Cup is simulated. Results are normalised to 5×10^6 antiprotons. The detection windows of antihydrogen ions for different beam energies are presented in Table 8.9. The time $t = 0$ corresponds to the moment when antiprotons reach the Faraday Cup at the end of antiproton beam line. Results of the simulation for case A.1. are summarised in Table 8.10. Like for antihydrogen detection, the largest effective background comes from positrons.

$\bar{p}$ energy [keV]	detection window [μs]
2	1.04 - 2.04
6	1.34 - 2.34
10	2.28 - 3.28

Table 8.9: Antihydrogen ion detection window for different antiproton energies. The time $t = 0$ corresponds to the moment when antiprotons reach the Faraday Cup.

	detection efficiency	N 10 keV	N det	N 6 keV	N det
n	0.14% - 0.64%	17.82 ± 0.95	$0.025 - 0.114$	12.85 ± 0.80	$0.018 - 0.082$
e^-	5.8%	0.50 ± 0.16	0.029	0.55 ± 0.17	0.032
e^+	5.8%	2.61 ± 0.36	0.151	2.41 ± 0.35	0.140
γ	0.26%	30.5 ± 1.2	0.079	27.5 ± 1.2	0.072
sum		51.4 ± 1.6	$0.285 - 0.373$	43.3 ± 1.5	$0.261 - 0.326$

	detection efficiency	N 2 keV	N det
n	0.14% - 0.64%	6.17 ± 0.56	$0.009 - 0.040$
e^-	5.8%	0.40 ± 0.14	0.023
e^+	5.8%	1.10 ± 0.24	0.064
γ	0.26%	15.61 ± 0.89	0.041
sum		23.3 ± 1.1	$0.137 - 0.168$

Table 8.10: Case A.1 Expected number of particles produced from antiproton annihilations in the dump, which can be detected by the antihydrogen ion MCP. Simulation performed for 10 keV, 6 keV and 2 keV beam energy.

Annihilation of antiprotons in the dump shielded with 10 cm thick iron

In the following paragraph the antiproton dump is surrounded by the 10 cm thick iron shield described in Section 7.6.1. Results of the simulation for case A.1. are summarised in Table 8.11. The number of detected electrons, positrons and photons is smaller than in the previous case. However, the number of neutron is doubled. The sum of expected backgrounds is two times smaller than in the case when the antiproton dump is not shielded.

	detection efficiency	**N 10 keV**	**N det**	**N 6 keV**	**N det**
n	0.14% - 0.64%	114.3 ± 2.4	$0.16 - 0.73$	70.7 ± 1.9	$0.099 - 0.45$
e^-	5.8%	0.053 ± 0.053	0.0031	0	0
e^+	5.8%	0.37 ± 0.14	$0.021 - 0.22$	0.42 ± 0.15	$0.024 - 0.25$
γ	0.26%	11.54 ± 0.78	0.03	9.43 ± 0.70	0.025
sum		126.3 ± 2.6	$0.21 - 0.99$	80.5 ± 2.1	$0.15 - 0.73$

	detection efficiency	**N 2 keV**	**N det**
n	0.14% - 0.64%	29.4 ± 1.2	$0.041 - 0.188$
e^-	5.8%	0.053 ± 0.053	0.003
e^+	5.8%	0.32 ± 0.13	$0.018 - 0.19$
γ	0.26%	6.59 ± 0.59	0.017
sum		36.4 ± 1.4	$0.080 - 0.40$

Table 8.11: Case A.1 Expected number of particles produced from antiproton annihilations in the dump, which can be detected by the antihydrogen ion MCP. The antiproton dump is shielded with 10 cm thick iron box. Simulation performed for 10 keV, 6 keV and 2 keV beam energy.

Annihilation of antiprotons in the dump shielded with 10 cm thick iron and a 60 cm thick concrete block

In the following paragraph, the antiproton dump is surrounded by the 10 cm thick iron shield. Additionally, two 2 m × 60 cm × 80 cm concrete blocks are placed on both sides of the antihydrogen ion detector. The results are summarised in Table 8.12. In this case, the background consists of only neutrons and photons.

	detection efficiency	**N 10 keV**	**N det**	**N 6 keV**	**N det**
n	0.14% - 0.64%	28.0 ± 2.8	$0.039 - 0.179$	20.9 ± 2.4	$0.029 - 0.134$
γ	0.26%	2.82 ± 0.89	0.007	5.6 ± 1.3	0.015
sum		30.8 ± 2.9	$0.046 - 0.186$	26.6 ± 2.7	$0.044 - 0.148$

	detection efficiency	**N 2 keV**	**N det**
n	0.14% - 0.64%	12.4 ± 1.9	$0.017 - 0.080$
γ	0.26%	1.41 ± 0.63	0.004
sum		13.8 ± 2.0	$0.021 - 0.083$

Table 8.12: Case A.1 Expected number of particles produced from antiproton annihilations in the dump, which can be detected by the antihydrogen ion MCP. The antiproton dump is shielded with 10 cm thick iron box. The antihydrogen ion detector is shielded with two 60 cm thick concrete blocks. Simulation performed for 10 keV, 6 keV and 2 keV beam energy.

Annihilation of antiprotons in the dump shielded with 20 cm thick iron and 20 cm thick parrafine, and a 60 cm thick concrete block

This case is very similar to the previous situation, but in this case, the iron shield is 20 cm thick and is surrounded by 20 cm thick paraffine layer. This construction should stop the remaining neutron background. The results are summarised in Table 8.13. In this case, the background consists only of neutrons and protons and is almost completely suppressed. The mean energy of the remaining neutrons is almost 10 MeV and the mean energy of photons is 200 keV, which allows to use mentioned detection efficiencies. This is the recommended shielding solution for the final experiment.

	detection efficiency	**N 10 keV**	**N det**	**N 6 keV**	**N det**
n	0.14% - 0.64%	8 ± 2	$0.01 - 0.05$	4.5 ± 1.5	$0.006 - 0.029$
γ	0.26%	1 ± 0.7	0.003	0.5 ± 0.5	0.001
sum		9 ± 2	$0.013 - 0.053$	5 ± 1.6	$0.007 - 0.030$

	detection efficiency	**N 2 keV**	**N det**
n	0.14% - 0.64%	2 ± 1	$0.003 - 0.013$
γ	0.26%	0	0
sum		2 ± 1	$0.003 - 0.013$

Table 8.13: Case A.1 Expected number of particles produced from antiproton annihilations in the dump, which can be detected by the antihydrogen ion MCP. The antiproton dump is shielded with 20 cm thick iron box and 20 cm paraffine layer. The antihydrogen ion detector is shielded with two 60 cm thick concrete blocks. Simulation performed for 10 keV, 6 keV, and 2 keV beam energy.

8.4.7 Antihydrogen beam annihilation

The annihilation of antihydrogen atoms on the MCP can be a potential background for the detection of antihydrogen ions. The acceptance of the antihydrogen ion MCP is equal to 1×10^{-5} and the number of annihilating antihydrogen atoms reaches 3000 antiatoms, from which each produces at least 5 particles. It could give a potential background at the level of 0.2 events per pulse. However, the antihydrogen ion detection starts at least 1.7 μs after the last antihydrogen atom annihilation. According to the simulations, this time difference decreases the background to a level smaller than 10^{-4} events per pulse.

8.4.8 Summary - antihydrogen atom detection

The summary of the expected signal and background for the detection of antihydrogen atoms is presented in Table 8.14 for case A.1., Table 8.15 for case A.2. and Table 8.16 for case B. The number of antihydrogen atoms is multiplied by the expected 55 % detection efficiency. According to estimations, expriments with antihydrogen formation in the reaction cavity are feasible. The measurements with the flat target (Case B.) are more challenging due to the low expected signal and background coming from the antiproton annihilations in the reaction chamber. However, the measurement is still possible.

Background	10 keV beam	6 keV beam	2 keV beam
cosmic radiation/ dark noise	$< 2 \times 10^{-5}$	$< 2 \times 10^{-5}$	$< 2 \times 10^{-5}$
γ from e^+	0	0	0
γ from Ps	0.05	0.003	0
$\bar{p}$/H interactions	0	0	0
sum	0.05	0.003	0
3bCC Ps1s sumH	810	740	190
3B CBA Ps1s sumH	910	1690	370

Table 8.14: Case A.1 List of expected backgrounds for antihydrogen atom detection. The number of antihydrogen atoms was multiplied by the expected 55 % detection efficiency.

Background	10 keV beam	6 keV beam	2 keV beam
cosmic radiation/ dark noise	$< 2 \times 10^{-5}$	$< 2 \times 10^{-5}$	$< 2 \times 10^{-5}$
γ from e^+	0	0	0
γ from Ps	0.001	$< 3 \times 10^{-5}$	0
$\bar{p}$ in the RCh (20 %)	0.052-0.061	0.045 - 0.052	0.019-0.022
$\bar{p}$/H interactions	0	0	0
sum	0.052-0.061	0.045 - 0.052	0.019-0.022
3bCC Ps1s sumH	6.5	5.9	1.5
3B CBA Ps1s sumH	7.3	13.6	2.9

Table 8.15: Case A.2 List of expected backgrounds for antihydrogen detection. The number of antihydrogen atoms was multiplied by the expected 55 % detection efficiency.

Background	10 keV beam	6 keV beam	2 keV beam
cosmic radiation/ dark noise	$< 2 \times 10^{-5}$	$< 2 \times 10^{-5}$	$< 2 \times 10^{-5}$
γ from e^+	-	-	-
γ from Ps	0.001	$< 3 \times 10^{-5}$	0
$\bar{p}$ in the RCh (20 %)	0.052-0.061	0.045 - 0.052	0.019-0.022
$\bar{p}/\bar{\mathrm{H}}$ interactions	0	0	0
sum	0.052-0.061	0.045 - 0.052	0.019-0.022
3bCC Ps1s sumH	1.0	0.9	0.2
3B CBA Ps1s sumH	1.2	2.1	0.4

Table 8.16: Case B. List of expected backgrounds for antihydrogen detection. The number of antihydrogen atoms was multiplied by the expected 55 % detection efficiency.

8.4.9 Summary - antihydrogen ion background estimation

The summary of the expected signal and background for an antihydrogen ion detection in case A.1. is presented in Table 8.17. The main contribution to the background comes from antiproton annihilations in the beam dump. When not shielded, the estimated background exceeds or is equal to the expected antihydrogen ion signal, which makes the experiment impossible. However, the combined iron-paraffine-concrete shielding decreases the background by more than 95 %. The main ingredients of the shielded background are neutrons and photons, which have a low detection efficiency and leave a very small signal in the MCP detector, see Appendix B. That is why it should be possible to discriminate them by adding an extra cut on the signal amplitude.

Background	10 keV beam	6 keV beam	2 keV beam
cosmic radiation/ dark noise	$< 2 \times 10^{-5}$	$< 2 \times 10^{-5}$	$< 2 \times 10^{-5}$
γ from e^+	0	0	0
γ from Ps	$< 10^{-5}$	0	0
$\bar{p}$ in the dump (100 %)	$0.285 - 0.373$	$0.261 - 0.326$	$0.137 - 0.168$
$\bar{\mathrm{H}}$ on the MCP	$< 10^{-4}$	$< 10^{-4}$	$< 10^{-4}$
sum	$0.285 - 0.373$	$0.261 - 0.326$	$0.137 - 0.168$
$\bar{p}$ in the dump, shielded	$0.013 - 0.053$	$0.007 - 0.030$	$0.003 - 0.013$
signal	0.2	0.4-0.8	-

Table 8.17: Case A.1 List of expected backgrounds for antihydrogen ion MCP detector. The number of antihydrogen atoms was multiplied by the expected 55 % detection efficiency.

This estimation assumes the 100 % antiproton beam transport efficiency. If this would not be the case, then the background would be smaller, as antiproton would annihilate earlier. Generally, an easy option to decrease the antiproton background is to annihilate the antiproton beam just after the reaction chamber. This does not allow for the cross-section measurement, but allows to eliminate the background.

Another idea is to use a more sophisticated detection system consisting of an MCP detector as an annihilation target and a few MicroMegas detectors surrounding the MCP. MicroMegas

detectors can be used to reconstruct the antihydrogen ion annihilation vertex from the detected charged pions. Also, the MicroMegas detectors are very well known in the GBAR experiment as they are used for the final free fall experiment. The second option is to switch antiproton and antihydrogen ion lines and detectors. In this case, the antiprotons annihilate after the antihydrogen ions, which makes the measurement of the antihydrogen ions background free. However, the reversed detection scheme can not be used as the diagnostics station for antihydrogen ion in front of the free fall chamber. The last improvement can be done by delaying the antiproton annihilation by reflecting them electrostatically to the reaction chamber.

8.4.10 Summary - hydrogen atom and ion background estimation

Within the GBAR framework is possible to perform symmetric tests with a hydrogen production thorough reactions

$$\mathrm{p} + \mathrm{Ps}(n_p, l_p, m_p) \rightarrow \mathrm{H}(n_h, l_h, m_h) + e^+ \tag{8.9}$$

$$\mathrm{H}(n_h, l_h, m_h) + \mathrm{Ps}(n_p, l_p, m_p) \rightarrow \mathrm{H}^- + e^+. \tag{8.10}$$

The mixing procedure of protons and positronium is the same as for antiprotons and positronium, including expected identical cross-sections values. Additionally, the Faraday Cup can be used as a detector for the proton flux, and MCP detectors are designed for hydrogen detection. The only difference between the two cases is in the expected background.

The main differences are the following:

- there is no antiproton annihilation background;
- the interaction of protons with a residual gas leads to the production of a neutral hydrogen background through the charge exchange reaction, see Section 8.3.4.

The neutral background is essential for hydrogen atom detection. At 10^{-10} mbar pressure the expected number of produced hydrogen atoms over 2 m distance (from the lens in front of the reaction chamber to the middle of the switchyard) is 2.2 atoms for 5×10^6 protons in the beam and 1.8 atoms for 4×10^6 protons in the beam. It is not a significant background for the final GBAR configuration when a few thousands of hydrogen atoms are going to be produced. However, in case of hydrogen production with a flat target (case B), this is a significant background. To decrease it, it is recommended to bend the proton beam just after the reaction chamber. That decreases the proton-residual gas interaction region to 1 m and reduces by half the expected background. A summary of the expected backgrounds is presented in Table 8.18.

There is a possibility that also other gasses are present in the system, like for example N_2. Generally, the cross-sections for proton charge exchange reaction in collisions with multi-electron atoms are in the same order of magnitude, smaller than 10^{-15} cm^2 [176], in considered energy range. Thus the number of background events should not vary much with the composition of the residual gas in the system.

Background	10 keV beam	6 keV beam	2 keV beam
cosmic radiation/ dark noise	$< 2 \times 10^{-5}$	$< 2 \times 10^{-5}$	$< 2 \times 10^{-5}$
γ from e^+	0	0	0
γ from Ps	0.001	$< 3 \times 10^{-5}$	0
H from interaction with residual gas (1 m)	0.5	0.5	0.5
sum	0.5	0.5	0.5
3bCC Ps1s sumH	1.0	0.9	0.2
3B CBA Ps1s sumH	1.2	2.1	0.4

Table 8.18: Case B. for hydrogen atom formation. List of expected backgrounds for hydrogen MCP detector. The number of hydrogen atoms was multiplied by expected 55 % detection efficiency.

The hydrogen ion detection in much simpler. The expected cosmic radiation, dark noise, and gamma backgrounds and smaller than $< 2 \times 10^{-5}$. In given conditions, there is no interaction of proton beam with residual gas which could lead to the production of H^-. Also, the beam loses are negligible. This makes the hydrogen ion detection on the MCP background free.

8.5 First tests of antihydrogen detectors with antiprotons

In Summer 2018 the GBAR experiment received its first antiproton beam from the ELENA decelerator. Both groups worked hard on the ELENA - GBAR connection. Due to many technical difficulties, it was not fully commissioned, however, still, some tests of the detection system were performed.

For the 2018 antiproton beam time the switchyard, the antihydrogen atom line, and the temporary antiproton line were installed. The description of the long antiproton line can be found in Section 7.8. To increase the probability of the antihydrogen detection, the detectors prepared for the free fall experiments were placed near the antihydrogen atom MCP detector, see Figure 8.10. The following detectors were prepared:

- MCP detector placed at the end of antihydrogen line;
- 3 plastic scintillators situated after the antihydrogen MCP, near the switchyard and next to the antiproton MCP;
- 5 times 10 cm by 10 cm MicroMegas detectors brought from ETH surrounding the antihydrogen MCP;
- 16 times 50 cm by 50 cm MicroMegas brought from CEA Saclay, placed behind the antihydrogen MCP;
- 2 plates of time of flight detectors made from plastic scintillators brought from Seul University, situated behind the big MicroMegas detectors.

That multi-detector system was supposed to detect the first antihydrogen atom production in the GBAR experiment.

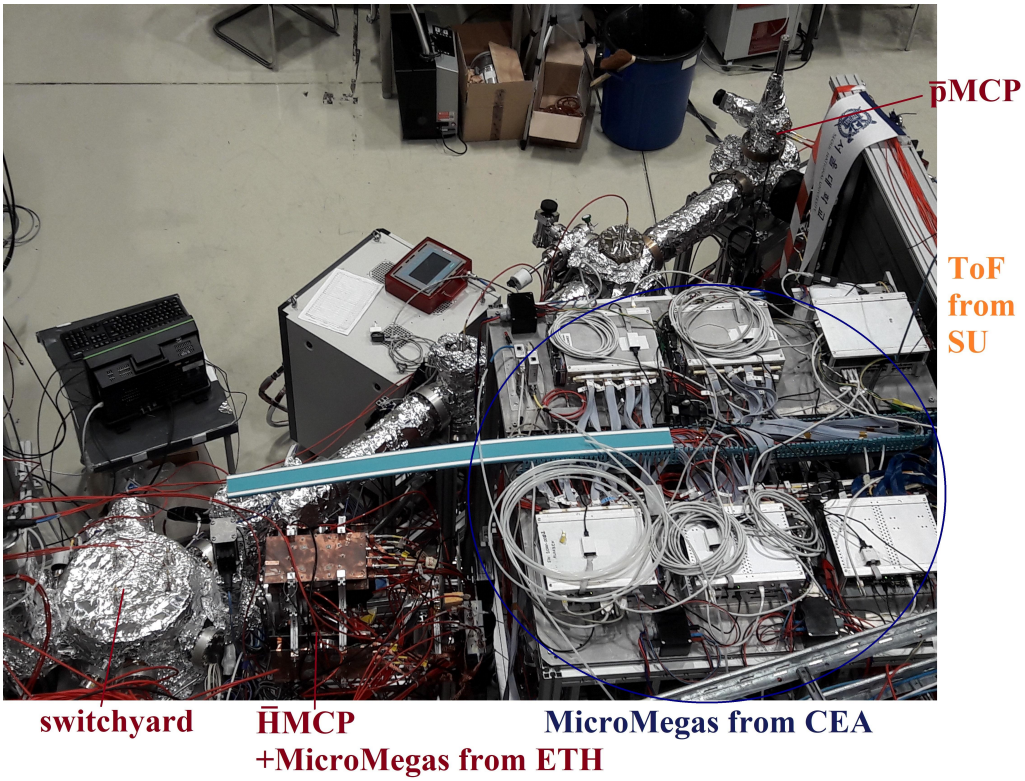

Figure 8.10: Scheme of the antihydrogen ion line after the switchyard.

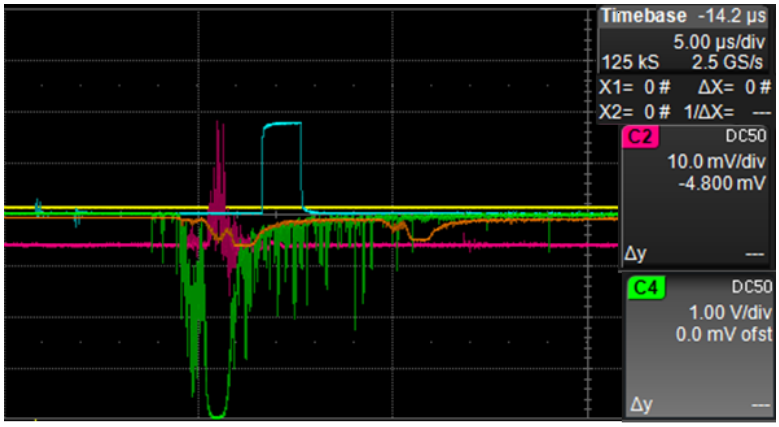

Figure 8.11: A screenshot from the oscilloscope. Three curves are corresponding to the following detectors: the plastic scintillator signal (green), the CCD camera detection window (light blue) and the antihydrogen MCP electric signal (pink).

8.5.1 Annihilation of the antiproton beam in the reaction chamber - background test

A test of possible background coming from antiproton annihilation in the reaction chamber was performed. For this, the full 100 keV antiproton beam with an intensity of about 10^6 antiprotons per pulse was annihilating on the MCP detector inside the reaction chamber. By

looking at the signal on the plastic scintillator detector, it was possible to set the MCP trigger on the expected antihydrogen detection window for 10 keV antiprotons. Figure 8.11 shows the plastic scintillator signal (green), the CCD camera detection window (light blue) and the antihydrogen MCP electric signal (pink). An exemplary image from the MCP/CCD detector is shown in Figure 8.12. Generally, the MCP detector always detected maximum 1 event. The order of magnitude agrees with expectations. This is only a qualitative result, as there was no full control over the beam parameters. The valve just in front of the detector was closed, so no antiprotons were detected.

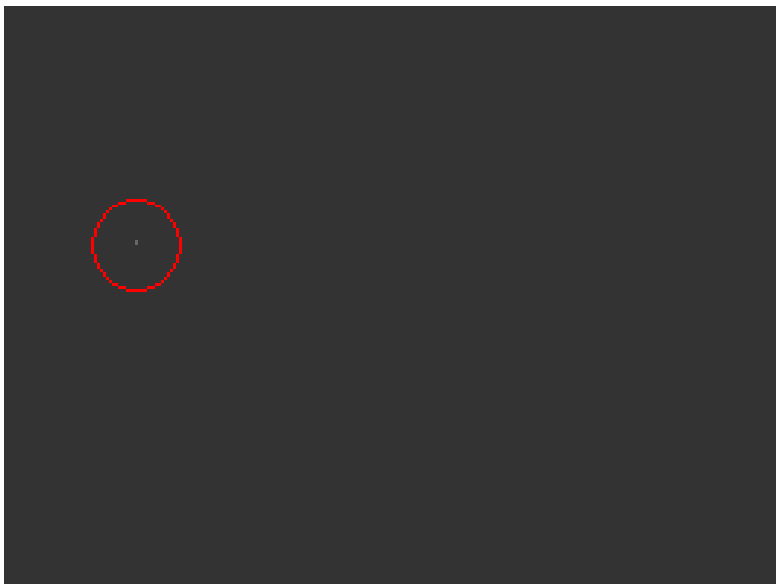

Figure 8.12: An exemplary result of the measured background produced from the antiproton annihilation in the reaction chamber. Picture was modified in order to clearly show the result.

8.5.2 Detection of particles produced in antiproton annihilation

The antihydrogen MCP detector was tested with a particle flux coming from the antiproton annihilation in the reaction chamber. To detect only the secondary particles, the valve in front of the detector was closed. Each event can be characterised with a few parameters. Three of them are x and y position of the center of the event and the flux of the event, which is an average density of the peak intensity. The x and y distributions of positions of the events are shown in Figure 8.13. Both distributions have the expected shape related to the circular form of the MCP detector. The peak flux distribution is shown in Figure 8.14. The measured distribution has a shape with the bump. This allows believing that pions, muons, electrons and positrons were part of the secondary particles flux. This is because the probability of the secondary electron emission from the surface of the MCP is higher for charged particles like electrons than for neutral particles like neutrons, see Appendix B. For a higher number of emitted secondary particles, the MCP channel can saturate and create a characteristic value of the amplitude of the signal for a given energy and type of particle. The mixture of different particle types and energies create a broadened bump. Obtained histograms are just a qualitative result, which requires more systematic experimental study.

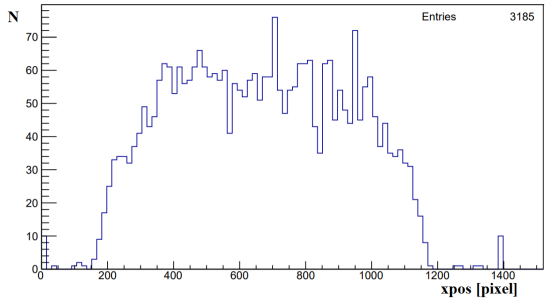

(a) x distribution

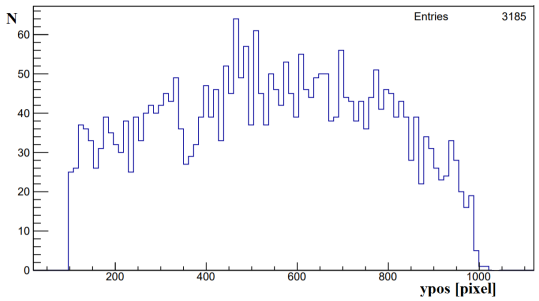

(b) y distribution

Figure 8.13: Position distributions of detected secondary particles produced in an antiproton beam annihilation in the reaction chamber. The antihydrogen MCP nominal working parameters were used.

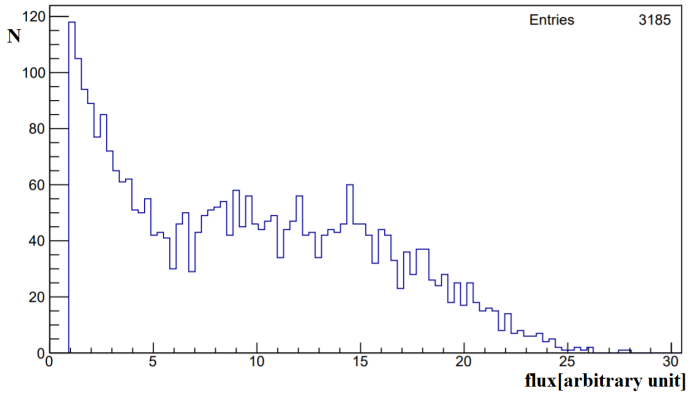

Figure 8.14: Flux distribution of detected secondary particles produced in an antiproton beam annihilation in the reaction chamber. The antihydrogen MCP nominal working parameters were used.

8.5.3 Beam of single 10 keV antiprotons

During the last shift, it was possible to perform tests of a detection system with a single 10 keV antiproton beam. To do it, the 100 keV beam from ELENA was partially decelerated to 10 keV. Due to technical difficulties, it was not possible to fully decelerate the beam. Signals from two plastic scintillators and MCP are shown in Figure 8.15. The signal between two blue lines corresponds to the 10 keV antiproton beam. The antiproton beam was sent on the 100 μm diameter collimator to decrease its intensity.

An exemplary image from the MCP/CCD detector is shown in Figure 8.16. This is a signal from 10 keV antiproton annihilations and secondary particles coming from antiproton annihilations at different stages of the setup. To protect the MCP from burning when detecting the whole antiproton beam, the data were recorded with a decreased voltage on the detector. That is why it is expected to obtain much more distinct signals in the future. This is only a qualitative result, which shows what can be expected during the next antiproton run. Also, even at much lower antiproton beam intensity, we did not manage to reconstruct an antiproton annihilation vertex with MCP and MicroMegas detectors.

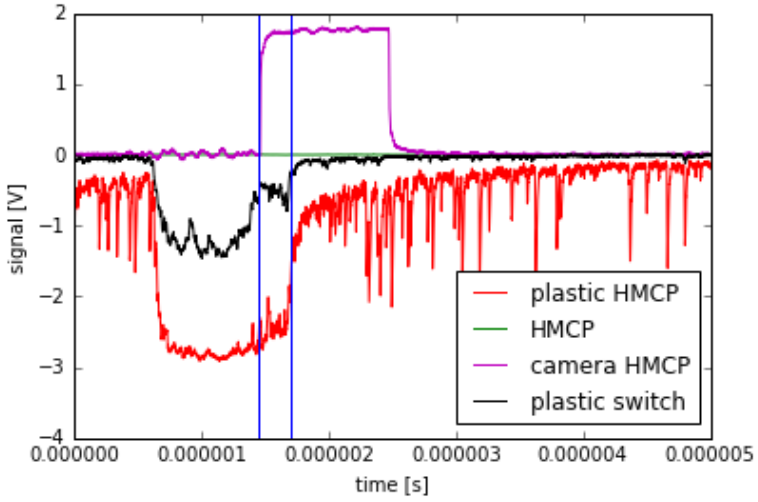

Figure 8.15: Signals from two plastic scintillators and MCP detector. The signal between two blue lines corresponds to the 10 keV antiproton beam. The signal before the first blue line comes from the 100 keV antiproton beam.

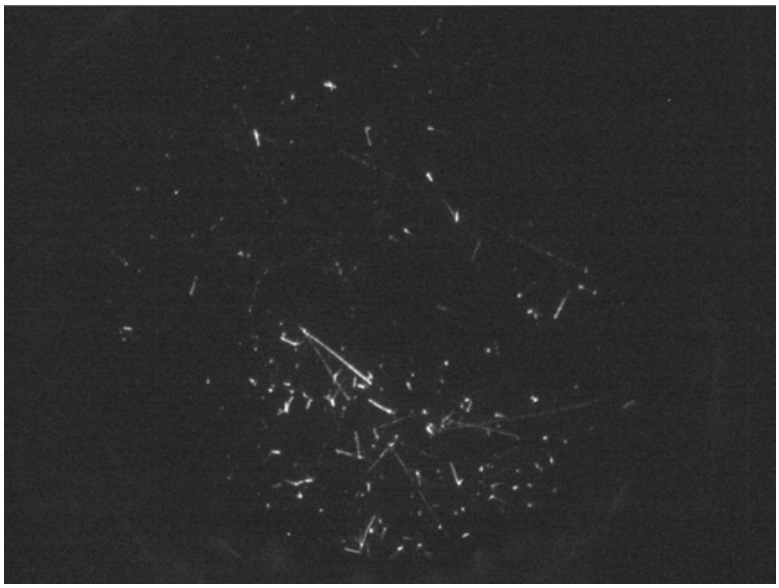

Figure 8.16: An exemplary image of 10 keV antiproton annihilation on the MCP surface. On the image also secondary particles produced in antiproton annihilations at different stages of the setup are visible.

8.6 Summary

The detection system for the antihydrogen atoms and ions was developed. The first tests show promising results. However, more experimental studies are required.

The systematic errors of the detection were studied. The primary source of the error comes from the unknown detection efficiency of the MCP detector for the antihydrogen atoms and ions. It has to be thoroughly studied, and for that, three measurements were proposed. The

second correction is related to the background estimation. According to performed Geant4 simulations, the antihydrogen atom detection is almost background free for all measurements with the reaction cavity (Case A.1. and A.2.) and the flat target experiments (Case B.) for the whole energy range. The antihydrogen ion signal is almost as small as the background, which is produced from the antiproton annihilations in the dump. However, it should be possible to discriminate the remaining background produced by neutrons and photons by a simple cut on the amplitude of the signal.

Chapter 9

Summary

9.1 Conclusion

The main topic of this thesis is the study of the cross-section measurement for the formation of antihydrogen atoms and ions. During the duration of the Ph.D., the whole cross-section measurement system including the proton or antiproton source, positron source, positron trapping, the reaction cavity with the positronium converter and the detection system were built at CERN. Parts of the system were successfully tested, also with the first GBAR antiproton beam. With the designed system it is expected to reach even 20 % precision on the measurement of the cross-sections for antihydrogen formation.

This thesis focuses on the production of antiprotons, antihydrogen atoms and ions and detection problems, together with the estimation of backgrounds. The design of the system was optimised to minimise all possible backgrounds.

It is expected to produce up to 3000 antihydrogen atoms with 5×10^{10} positrons and 5×10^{6} antiprotons participating in the reaction. This measurement is almost background free. In the second considered case when only 5×10^{8} positrons are injected into the reaction chamber the measurements are a bit more challenging. It is expected to produce between 3 and 30 antihydrogen atoms in the scheme with the reaction cavity and between 0.4 and 4 antihydrogen atoms in the scheme with the flat target. The main background for these tests comes from the antiproton annihilation in the reaction chamber. The expected signal to background ratio is between 0.1 % to 2 % in the cavity scheme and between 2 % and 11 % in the flat target scheme. This ratio can be improved only by decreasing the antiproton beam size and its annihilation on the collimator in front of the reaction region.

The most challenging is the antihydrogen ion detection due to the low signal to background ratio. The expected number of detected antihydrogen ions for 10 keV antiproton beam energy is about 0.2 and for 6 keV antiproton energy is between 0.4 and 0.8. The corresponding background is 0.01 - 0.05 (10 keV) and 0.01 - 0.03 (6 keV) detected events. The signal to background ratio in the worst case is about 26 %. However, the detection should be still possible due to the difference in the amplitude of the antihydrogen atoms, gammas, and neutrons signals. The first very general tests of that method look promising. The other possibility is to swap the locations of the detection system of antiprotons with that of the antihydrogen ions. This would delay the antiproton annihilation, and the antihydrogen ion measurement would be background free.

An additional opportunity was to study the GBAR slow positron source, which is essential to obtain the high flux positron beam for the formation of positronium. The achieved positron

flux is $N_{e^+/1s} = 4.94 \pm 0.001(stat) \pm 0.030(sys) \times 10^7$ e^+/s at 300 Hz linac repetition frequency. It is at least 5 times higher with respect to the maximum flux available with Na^{22} source.

Currently, the system is being tested with protons to perform the formation of hydrogen atoms and ions. It is believed, that the designed system can allow producing hydrogen atoms within a few months.

Appendices

Appendix A

Calibration of the NaI detectors for a positron annihilation

A.1 Slow positron beam diagnostics

The positron beam diagnostic station is placed downstream the transport line, just in front of the buffer gas trap. It consists of an energy analyser and two gamma radiation detectors.

The energy analyser is presented in Figure A.1. It is made of a stainless steel target with 3 molybdenum grid layers in front (transparency $\approx$ 96.5%), which allows to stop particles. The first grid is grounded and the other two are biased. Such architecture allows to minimise the microlensing effect, in which local inhomogeneities of the electric field focus a part of the beam in an uncontrolled way. When positrons hit the target, they annihilate into two 511 keV photons, $e^- + e^+ \rightarrow \gamma + \gamma$, which are later registered by the NaI and plastic scintillator detectors. The negative voltage on the target (currently used: -30 V) helps to collect all positrons. The presented setup allows to estimate its size, using the fact that the internal diameter of the grid is equal to 1" (2.54 mm). The side length of the grid and the target is 40 mm.

The goal of Appendix A is to describe the method used to calibrate the NaI and plastic scintillator detectors for 511 keV gammas originating from positron annihilation on the stainless steel target. The calibration allows to measure the number of positrons in the beam at the level of the energy analyser. The NaI detector was chosen as the main detector for the positron flux measurement because it has a good energy resolution which allows to distinguish the 511 keV peak from the Compton background. The beam from the linac consists of positrons and electrons. In order to measure the flux of positrons directly via the charge deposited on the target, the electrons must be repelled until their flux is smaller than that of the slow positrons.

A.1.1 Detectors

Two types of detectors are used to estimate the intensity of the slow positron beam. One is a NaI crystal which is very sensitive to photons, and the other is a fast plastic scintillator. Each of them is equipped with a photomultiplier. They are presented together with the target cross in Figure A.2.

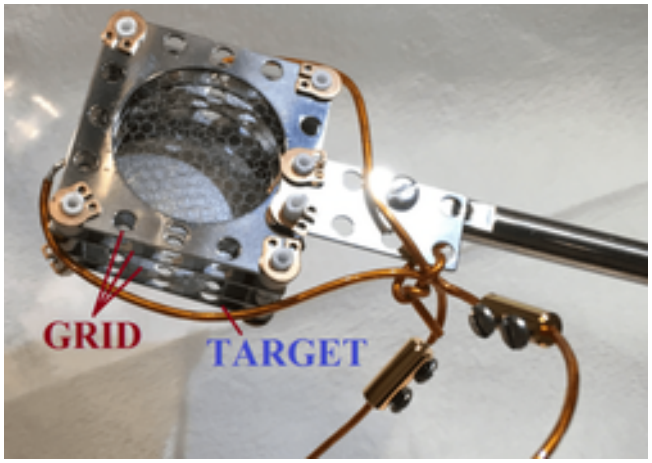

Figure A.1: The energy analyser made from three grids and a target.

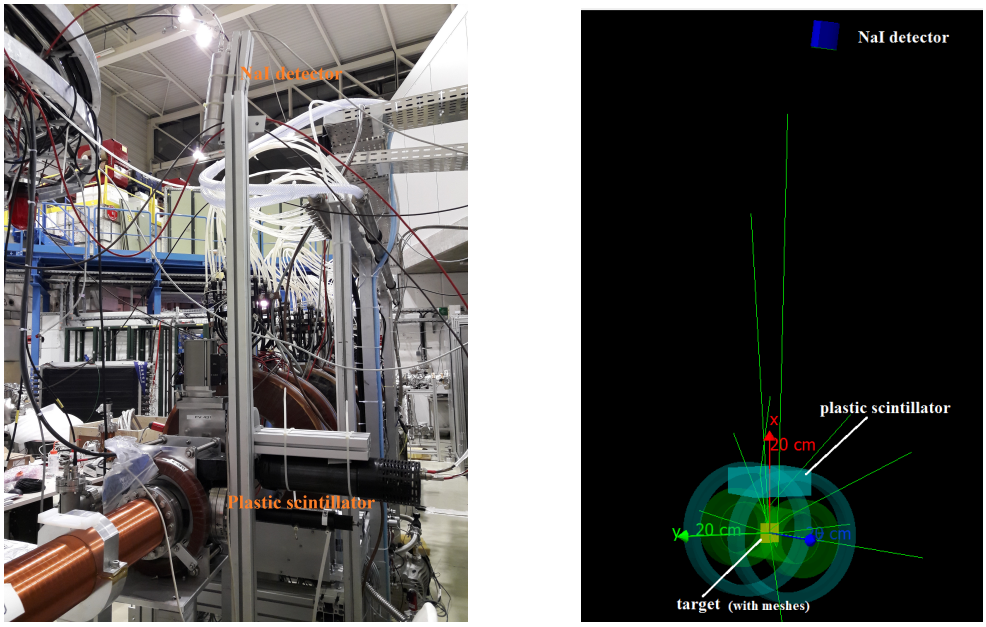

Figure A.2: NaI and plastic scintillator detectors with the target cross. Left: picture of the actual setup. Right: Geant4 scheme.

NaI(Ti) detector

The main device used to estimate the number of positrons in the beam is a 2" diameter, cylindrical NaI(Ti) detector. It is equipped with a CANBERRA Model 2007 photomultiplier with an internal magnetic and light shield and an preamplifier. It is placed 940 mm from the centre of the target with its axis pointing towards the annihilation point. The usual working voltage of the detector's photomultiplier is $V_{NaI} = 700$ V ($V_{NaI} = 800$ V was used for one measurement), which is in the linear response range of the detector, see Subsection A.3.2.

Plastic scintillator

The second device used for positron beam diagnostics is a 50 mm thick plastic scintillator with a lightguide and an XP2020 photomultiplier tube on the side. The centre of the detector is placed 100 mm from the centre of the target. The working voltage of the detector's photomultiplier is $V_{plastic\_scint} = -1400$ V.

Principle of detection

Both detectors are examples of scintillation detectors. When a gamma ray of energy smaller than 1022 keV is penetrating through the crystal it may interact with the material and emit a visible photon. One gamma may cause the emission of many particles. The produced light is collected by a photomultiplier and changed into an electric signal. The signal distribution for which the primary particle lost all its energy in the detector is called the photopeak. However, very often a gamma ray goes through the edge of the detector and thus causes the emission of less photons than in the photopeak. Additionally, electrons from Compton scattering also leave a signal in the detector. Thus the response of the detector for particles of a given energy is not always a single value, but a distribution. The goal of the calibration is to estimate this distribution.

The main difference between the plastic scintillator and the NaI(Ti) detector is that in the second case the energy resolution of the detector has a higher density and it is possible to distinguish the photopeak corresponding to the nominal energy of the incoming particles. A schematic response of the NaI(Ti) detector for monoenergetic gammas is shown in Figure A.3. The continuous background is mainly the result of Compton scattering.

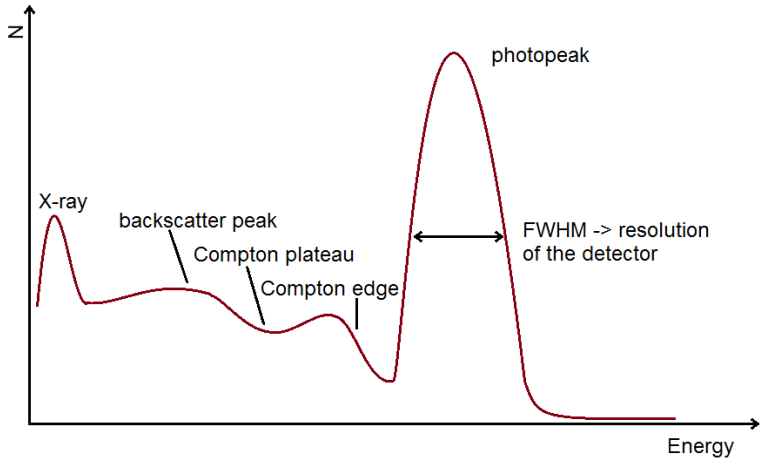

Figure A.3: A schematic response of the NaI(Ti) detector (*energy spectrum*) for monoenergetic gammas.

A.1.2 Measurement

The main task for the two detectors is to measure the positron bunch intensity and length. The integrated signal from the slow, but very sensitive NaI detector is used to measure the total beam intensity. If the detector is in the linear response range, the total number of particles can be estimated using the average response of the detector for one particle. In the present

case the calibration would require information about the average response of the NaI detector for 511 keV photons originating from the annihilation target. It is important to include in the calibration the surrounding environment, as photons with that energy may produce a lot of Compton radiation during the propagation in the direction of the detector, which may bias the measurement.

The fast signal from the plastic scintillator may also be used to estimate the total number of positrons. However, as it is situated much closer to the target, the measurement is very sensitive to the beam size and position. This detector, being very fast, is rather used to measure the beam shape and fast changes in the beam flux. In that case also the integral of the signal is used.

Examples of signals obtained from the NaI and plastic scintillator detectors during the measurement of the positron beam flux are shown in Figure A.4. This is a screen shot from the oscilloscope which is used to collect data.

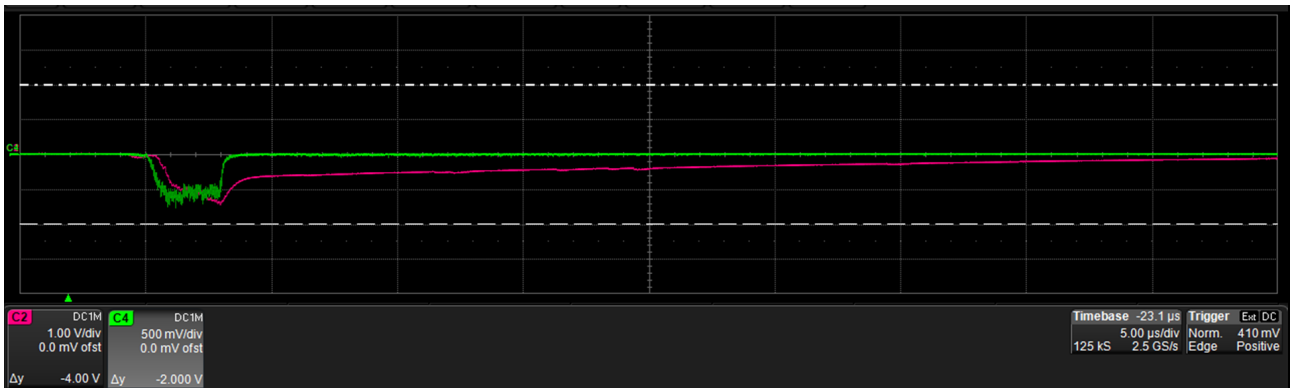

Figure A.4: Screen shot from the oscilloscope of the positron beam flux measurement. The green curve is the signal from the plastic scintillator detector. The magenta curve is the signal from the NaI detector. The scale is 5 μs per division.

A.1.3 Calibration

The number of positrons in a pulse is equal to:

$$N_{e^+} = \frac{S_{NaI}}{C_{e^+}} = S_{NaI} / \left(C_\gamma \cdot P_{1\gamma}\right) = S_{NaI} / \left(E_{1\_\gamma} \cdot C_{511\_keV\gamma} \cdot P_{1\gamma}\right) \tag{A.1}$$

where

S_{NaI} - integral of the signal measured by the NaI detector;

C_{e^+} -estimated signal corresponding to one positron in the NaI detector;

C_γ - average signal left in the detector by one photon reaching the detector;

$P_{1\gamma}$ - probability that a photon produced in positron annihilation reaches the detector;

$E_{1\gamma}$ - mean detector response for 511 keV photons coming from positron annihilation on the target normalised to the 511 keV photopeak position (simulation);

$C_{511\_keV\gamma}$ - mean signal of the 511 keV photopeak measured experimentally.

Parameter S_{NaI} is equal to $S_{NaI} = S_{NaI\_meas} - S_{NaI\_zero}$, where S_{NaI_meas} is the direct integral of the signal and $S_{NaI\_zero} = (4.2285 \pm 0.0022) \times 10^{-8}$ Vs is the baseline response of the detector.

The goal of the calibration is to estimate C_{e^+}:

$$C_{e^+} = E_{1\gamma} \cdot C_{511\_keV\gamma} \cdot P_{1\gamma}. \tag{A.2}$$

$C_{511\_keV\gamma}$ can be measured experimentally using a Na^{22} source. Parameters $E_{1\gamma}$ and $P_{1\gamma}$ have to be extracted from simulation, because there is no source of single 511 keV photons.

A.2 NaI detector simulation and simulation tests

In order to estimate parameters E_{1_γ} and P_{1_γ} for a 511 keV gamma ray a Geant4 simulation is performed. It calculates the energy deposited in the crystal by each photon, which is proportional to the final detector response. The simulation takes into account not only the position of the detector, but also other parts of the setup - the structure of the surrounding coil, the stainless steel tube and the CF100 flanges. The target has three grids in front with 96.5 % transmission. It is assumed that the effect of the concrete walls and the floor is negligible. In Figure A.2 the simulated setup is presented.

The accuracy of the simulation for this case can not be checked experimentally, because there is no source of single 511 keV photons. The quality of the simulation is tested by comparing the simulation and the measurement of the detector response for a Na^{22} sodium source. The Na^{22} spectrum is the result of β^+ decay to stable Ne^{22}. The positron annihilation produces 511.0 keV gammas (179.8% abundance/annihilation). Neon is mostly generated in an excited state, which decays into the ground state emitting a 1275 keV gamma (99.9%).

A.2.1 Tests of the simulation with the Na^{22} source

In order to test the accuracy of the simulation, comparisons tests with Na^{22} were performed. The results show only energies up to the 511 keV photopeak because this is the region of interest with the linac beam that has no 1275 keV photons.

Measurement conditions

In the current setup it is impossible to place the source at the location of the annihilation target, this is why three other configurations were chosen, see Figure A.5:

A on the plastic scintillator;

B under the plastic scintillator;

C under the target chamber.

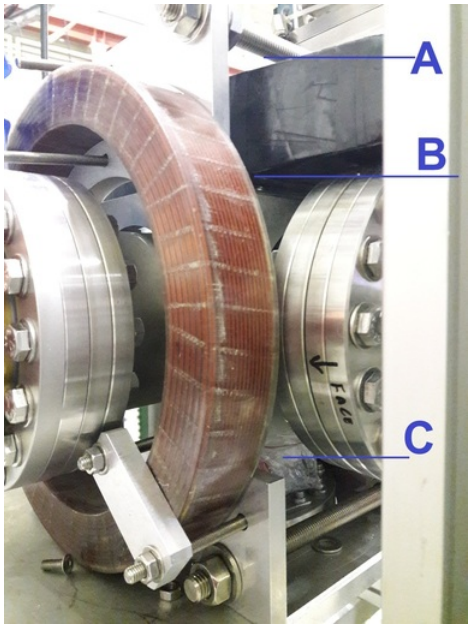

(a) Three positions of the Na^{22} source.

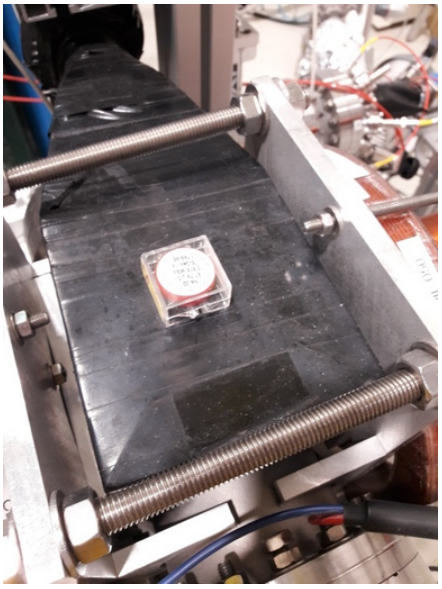

(b) Position of the source on the plastic scintillator.

Figure A.5: Location of the Na^{22} source during measurements.

In order to increase the detection resolution, the electric signal was collected through a preamplifier built in the base of the photomultiplier and an external spectroscopic amplifier. The source activity was 2.03 MBq measured on the 15th of February 2017. The duration of each measurement is 30 minutes.

Results - 511 keV photopeak position

The first goal of the measurement is to check if the position of the 511 keV photopeak changes for different positions of the source. It is important, as in the configuration with the peak coming from the linac, the source of gamma rays is located between positions B and C.

The result of the measurement of the signal amplitude after background subtraction is shown in Figure A.6. The position of the photopeak is determined through a gaussian fit:

A $\mu_{511\ keV} = 0.3041$ V, $\sigma_{511\_keV} = 0.0084$ V;

B $\mu_{511\ keV} = 0.3030$ V, $\sigma_{511\_keV} = 0.0091$ V;

C $\mu_{511\ keV} = 0.3024$ V, $\sigma_{511\_keV} = 0.0092$ V;

The position of the photopeak and its dispersion is the same for all cases, thus it can be assumed that it is identical for the measurement in the final configuration.

Results - simulation accuracy

The measurement results were cross-checked with a simulation for position B, i.e. with the source localised under the plastic scintillator. The original simulated energy deposited in the NaI detector by 511 keV gammas is shown in Figure A.7a. The 511 keV peak is clearly visible around $x_{simu} = 0.51$ MeV. The peak position in the measurement is at $x_{meas} = 0.303$ V. In

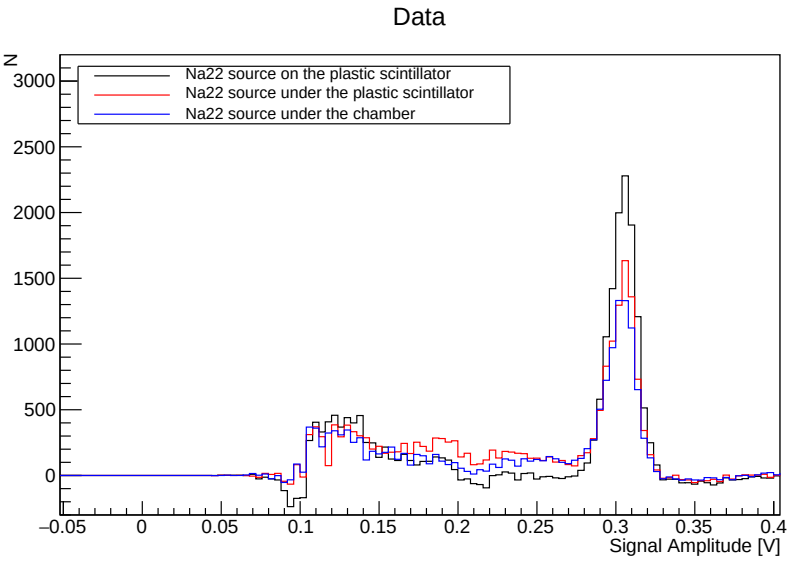

Figure A.6: Measurement of the energy spectrum of gammas from Na22 source for the NaI(Ti) detector ($V_{NaI} = 800$ V). Data after the background subtraction. The total number of events are 16702 ± 320 - on the plastic scintillator, 17646 ± 321 - under the plastic scintillator, and 15357 ± 318 - under the chamber.

order to compare the simulation with the measurement all data have to be scaled by a factor $a = x_{meas}/x_{simu}$ and convoluted with the normalised gaussian distribution with σ corresponding to the detector resolution, $\sigma_{511\ keV} = 0.0091$ V.

The results of the simulation and of the measurement for position B are shown in Figure A.7b. In the data, the threshold to trigger acquisition is set at 100 mV, which is not reproduced in the simulation. For voltages above this value, data and simulation are in good agreement. Under the assumption that for smaller signals the simulation is also correct, it is possible to rely on the simulation in later calculations.

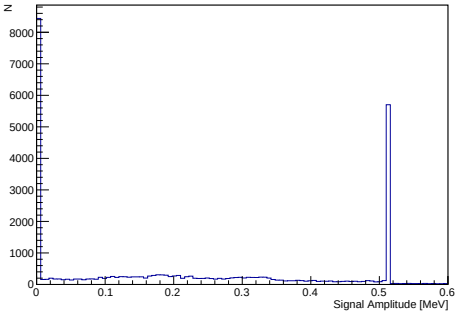

(a) Simulation of the energy deposited in the NaI detector.

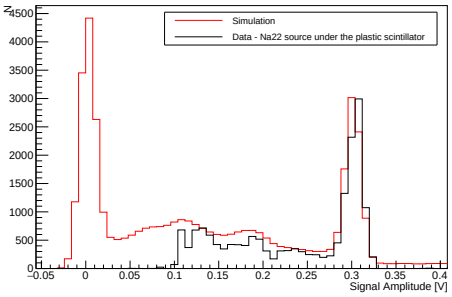

(b) Comparison of the data and simulation result.

Figure A.7: Measurement and simulation results for Na^{22} source, case B ($V_{NaI} = 800$ V).

A.2.2 Simulation for the detector calibration

In the positron flux measurement the NaI detector has to measure a flux of about 10^6 monoenergetic gammas per pulse. In order to calibrate the detector for that purpose, the simulation of the detector response for 511 keV gammas originating from the annihilation target is needed.

Positron beam parameters in the simulation:

- the spatial distribution in the plane perpendicular to the positron beam is flat over a disk of radius 5 mm;
- number of e^+: 5×10^9 (corresponding to 10^{10} gammas).

Geant4 electromagnetic model:

- Penelope - this library is based on special low-energy electromagnetic models. It is recommended for applications with low energy electrons, positrons and gammas.

According to the simulation, from 5×10^9 positrons hitting the target, 1147980 ± 1071 (*stat*) (0.1%) gammas reach the detector, i.e. $P_{1\gamma} = 2.296 \pm 0.002 \times 10^{-4}$. The histogram of the energy deposited in the NaI detector by isotropically distributed 511 keV gammas is presented in Figure A.8. The mean energy deposited by one γ is 0.2501 ± 0.0003 (*stat*) MeV, which is $E_{1\gamma} = 48.90 \pm 0.05\%$ of the energy corresponding to the 511 keV gamma photopeak. These values are later used for the detector calibration.

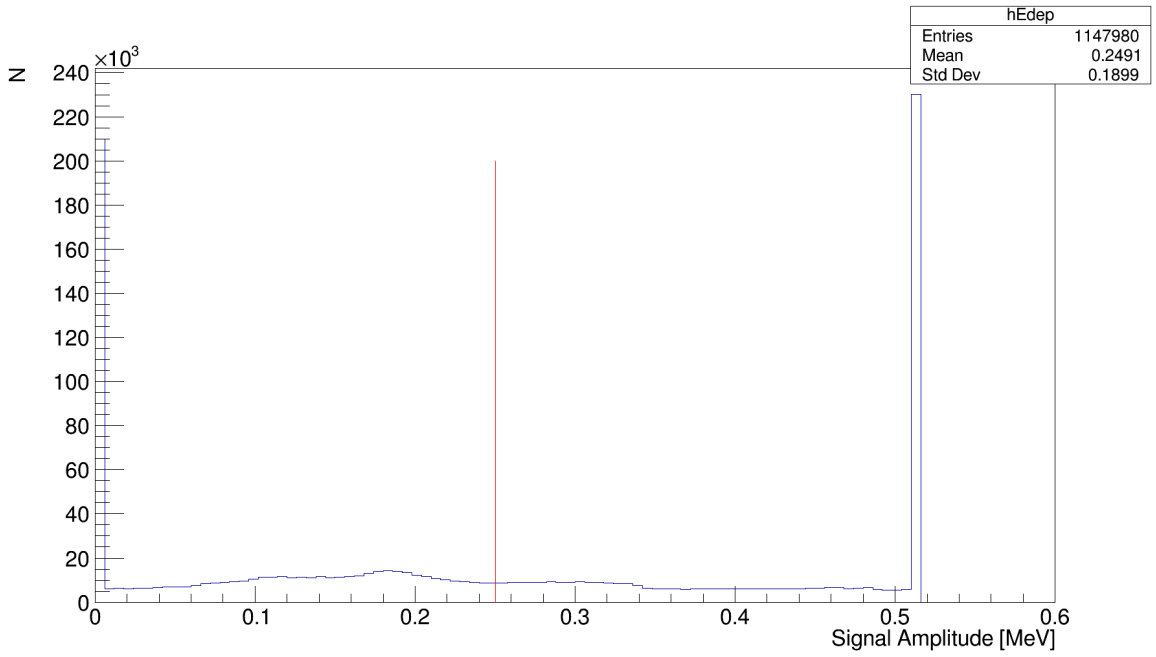

Figure A.8: The histogram of the energy deposited in the NaI detector by isotropically distributed 511 keV gammas (Geant4 simulation). The red line indicates the average signal deposited in the detector by one particle.

A.2.3 Systematic errors $\Delta P_{1\gamma}$ and $\Delta E_{1\gamma}$

The estimation of $P_{1\gamma}$ and $E_{1\gamma}$ from the simulation is dependent on a few parameters. This results in a systematic error due to the following reasons:

- the model of the electromagnetic interaction;
- the beam size on the target;
- the target plane inclination with respect to the beam direction;
- the NaI detector position with respect to the beam position.

Estimation of the systematic error due to the model of the electromagnetic interaction

The comparison between different electromagnetic models is presented in paper [177]. For electron energies greater than 10 keV the models give the same results within 1% accuracy. In the energy range smaller than 10 keV, the largest difference is between Geant4 models: Standard Option 4 and Penelope library. The results are presented in Table A.1. The error is a difference between two simulation results. The systematic error $\Delta P_{1\gamma}$ it is equal to 0.13 % and $\Delta E_{1\gamma}$ is equal to 0.41 %.

	Penelope	Standard Option 4	max Δ	Δ%
$P_{1\gamma}$	$(2.296 \pm 0.002) \times 10^{-4}$	$(2.293 \pm 0.002) \times 10^{-4}$	$(0.003 + 0.003) \times 10^{-4}$	$(0.13 + 0.13)$%
$E_{1\gamma}$	48.90 ± 0.05	48.70 ± 0.05	$0.2 + 0.07$	(0.41+0.14) %

Table A.1: Comparison of $P_{1\gamma}$ and $E_{1\gamma}$ values for two different electromagnetic models from Geant4.

Estimation of the systematic error due to the target plane inclination

The detection target is inclined into the beam direction with an angle equal to 2.6 degrees. The systematic errors due to the target plane inclination with respect to the beam direction are presented in Table A.2. The maximum systematic error for $P_{1\gamma}$ is equal to 9.1 %. The error on $E_{1\gamma}$ is equal to 4.07 %. The large systematic error is caused by the fact that the detector is placed above the annihilation target. In this case, some of the gammas reaching the detector are going through the annihilation target, which increases their stopping probability. The smaller is the target plane inclination, the larger part of the detector is placed within the target shadow.

	2.6 deg	1.7 deg	3.4 deg
$P_{1\gamma}$	$(2.296 \pm 0.002) \times 10^{-4}$	$(2.087 \pm 0.002) \times 10^{-4}$	$(2.472 \pm 0.002) \times 10^{-4}$
$E_{1\gamma}$	48.90 ± 0.05	46.91 ± 0.05	49.37 ± 0.05
	max Δ	Δ%	
$P_{1\gamma}$	$(0.209 + 0.003) \times 10^{-4}$	$(9.10 + 0.13)$ %	
$E_{1\gamma}$	1.99 ± 0.07	$(4.07 + 0.14)$ %	

Table A.2: Comparison of $P_{1\gamma}$ and $E_{1\gamma}$ values for three different target angles.

Estimation of the systematic error due to the beam size on the target

It is expected that the spatial distribution of the positron beam in the plane perpendicular to its average direction is flat over a disk of radius 5 mm. It is an approximation, since it is presently difficult to estimate the correct beam spatial distribution. The systematic errors due to the change of the positron beam size are presented in Table A.3. The systematic error $\Delta P_{1\gamma}$ it is equal to 0.35 % and $\Delta E_{1\gamma}$ is equal to 0.27 %.

	5 mm	10 mm	max Δ	Δ%
$P_{1\gamma}$	$(2.296 \pm 0.002) \times 10^{-4}$	$(2.304 \pm 0.002) \times 10^{-4}$	$(0.008 + 0.003) \times 10^{-4}$	$(0.35 + 0.13)$ %
$E_{1\gamma}$	48.90 ± 0.05	48.77 ± 0.05	0.13 ± 0.07	$(0.27 + 0.14)$ %

Table A.3: Comparison of $P_{1\gamma}$ and $E_{1\gamma}$ for two different values of the beam radius.

Estimation of the systematic error due to the NaI detector position with respect to the beam position

In principle, the beam should hit the centre of the target. However, it was observed that the beam moves together with a change of the magnetic field of the Antiproton Decelerator. Also, there may be other unexpected changes in the magnetic field in the experimental area. The observed effects can not be easily suppressed, thus a systematic error due to the change of the beam position is introduced. Additionally, there is a certain uncertainty due to the NaI detector position. Both sources of errors are correlated, thus it is enough to study the change of the position of the NaI detector.

The centre of the NaI detector is positioned at $x = 965$ mm, $z = -5$ mm and $y = -120$ mm with respect to the centre of the cross in which the target is placed. The simulation results obtained for different NaI detector positions are presented in Table A.4, Table A.5 and Table A.6. The displacements with respect to the nominal position correspond to the achievable precision in the positioning of the detector with respect to the target centre.

	$x = 965$ mm	$x = 963$ mm	$x = 967$ mm
$P_{1\gamma}$	$(2.296 \pm 0.002) \times 10^{-4}$	$(2.302 \pm 0.002) \times 10^{-4}$	$(2.269 \pm 0.002) \times 10^{-4}$
$E_{1\gamma}$	48.90 ± 0.05	48.47 ± 0.06	48.83 ± 0.05
	max Δ	Δ%	
$P_{1\gamma}$	$(0.027 + 0.003) \times 10^{-4}$	$(1.18 + 0.13)$ %	
$E_{1\gamma}$	$0.43 + 0.08$	$(0.88 + 0.16)$ %	

Table A.4: Comparison of $P_{1\gamma}$ and $E_{1\gamma}$ values for three different NaI detector positions $x \in \{965, 963, 967\}$ mm, $y = -120$ mm and $z = -5$ mm.

	$y = -120$ mm	$y = -121$ mm	$y = -119$ mm
$P_{1\gamma}$	$(2.296 \pm 0.002) \times 10^{-4}$	$(2.291 \pm 0.003) \times 10^{-4}$	$(2.269 \pm 0.002) \times 10^{-4}$
$E_{1\gamma}$	48.90 ± 0.05	48.16 ± 0.06	48.90 ± 0.05
	max Δ	Δ%	
$P_{1\gamma}$	$(0.027 + 0.003) \times 10^{-4}$	$(1.18 + 0.13)$ %	
$E_{1\gamma}$	$0.74 + 0.08$	$(1.51 + 0.17)$ %	

Table A.5: Comparison of $P_{1\gamma}$ and $E_{1\gamma}$ values for three different NaI detector positions $y \in \{-120, -121, -119\}$ mm, $x = 965$ mm, $z = -5$ mm.

	$z = -5$ mm	$z = -7$ mm	$z = -3$ mm
$P_{1\gamma}$	$(2.296 \pm 0.002) \times 10^{-4}$	$(2.317 \pm 0.002) \times 10^{-4}$	$(2.245 \pm 0.002) \times 10^{-4}$
$E_{1\gamma}$	48.90 ± 0.05	48.24 ± 0.05%	47.97 ± 0.05%
	max Δ	Δ%	
$P_{1\gamma}$	$(0.051 + 0.003) \times 10^{-4}$	$(2.22 + 0.13)$ %	
$E_{1\gamma}$	$0.93 + 0.07$	$(1.90 + 0.14)$ %	

Table A.6: Comparison of $P_{1\gamma}$ and $E_{1\gamma}$ values for three different NaI detector positions $z \in \{-5, -7, -3\}$ mm, $x = 965$ mm, $y = -120$ mm.

Summary

The total systematic error consists of two components, systematic and statistical, added quadratically. The statistical error is related to the statistics of performed simulations and is a quadratic sum of all statistical errors from described simulations. The same procedure was used to obtain the systematic part of the error.

The sum of all the systematic errors:

- $\Delta P_{1\gamma} = [(0.219(sys) + 0.007(stat)) \times 10^{-4}] = 0.219 \times 10^{-4}$ (9.5 %);
- $\Delta E_{1\gamma} = [(2.37(sys) + 0.18(stat))\%] = 2.38$ % (4.9 %).

The most significant error comes from the target plane inclination and the displacement of the detector in z-coordinate with respect to the target position. Both errors are caused by the fact that a significant part of detected gammas is going through the annihilation target. That error can be decreased in the future by moving the detector from above the target.

A.3 Calibration - summary

A.3.1 Measurement of $C_{511\_keV\gamma}$ parameter

In the final experiment, the positron flux is measured directly by an oscilloscope through a 10 kΩ resistor.The integral of the signal is measured. In order to calibrate correctly the detector, the position of the 511 keV photopeak measured with the same electronics as during

the final experiment is needed. The energy spectrum of the Na^{22} source is shown in Figure A.9. The peak corresponding to 511.0 keV is clearly visible. It is fitted with a gaussian distribution $f(x) = p_0 \cdot exp(-0.5 \cdot ((x - mean)/\sigma)^2)$ plus an exponential function for background $g(x) = g_0 \cdot exp(-x/\tau)$. The mean value of the Gaussian distribution is equal to the parameter $C_{meas\_511\_keV\gamma} = -1.69627 \pm 0.000054 \times 10^{-7}$ Vs. After subtracting the baseline value it is $C_{511\_keV\gamma} = -2.11912 \pm 0.00027 \times 10^{-7}$ Vs.

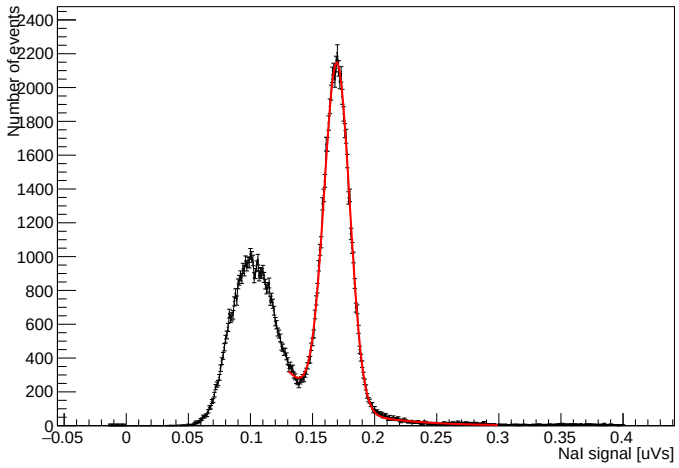

Figure A.9: Gamma spectrum - the histogram of the NaI detector response for single gammas. The low energy gammas are cut due to the trigger threshold. The integral of the signal is measured.

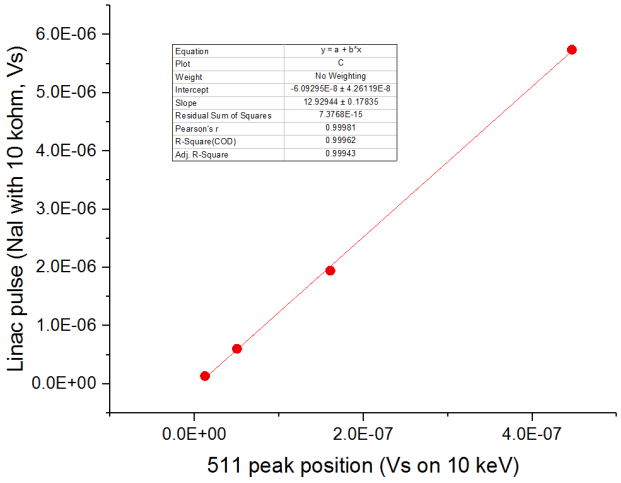

Figure A.10: The NaI signal as a function of the position of the 511 keV photopeak for different voltage on the phototube $V_{NaI} \in [500\ V, 800\ V]$.

A.3.2 Linear response of the detector

The linearity of the NaI response was verified by measuring the integrated response of the detector for a linac pulse as a function of the position of the 511 keV photopeak for different voltages on the phototube, $V_{NaI} \in [500\ V, 800\ V]$. The result is presented in Figure A.10. The slope of the fitted curve is 12.9 ± 0.2.

A.3.3 Summary

According to equations A.2:

$$C_{e^+} = E_{1\gamma} \cdot C_{511\_keV\gamma} \cdot P_{1\gamma} = -2.379 \times 10^{-11}\ \text{Vs}$$

and

$$\Delta C_{e^+} = \sqrt{(C_{511\_keV\gamma} \cdot P_{1\gamma})^2 \cdot \Delta E_{1\gamma}^2 + (E_{1\gamma} \cdot P_{1\gamma})^2 \cdot \Delta C_{511\_keV\gamma}^2 + (E_{1\gamma} \cdot C_{511\_keV\gamma}) \cdot \Delta P_{1\gamma}^2}.$$

$$\Delta C_{e^+} = 0.254(sys) \times 10^{-11}\ \text{Vs}\ (11\ \%).$$

The statistical error is smaller than 0.02 %. It is negligible in comparison to the systematic error, so it is neglected.

Appendix B

Study of the MCP detector

B.1 Working principle of the MCP detector

The MicroChannel Plate (MCP) detector [178] is a plate made from resistive material with many empty channels of 10 μm typical diameter, see Figure B.1. The front and the backside of the plate are coated with metal, so the plate can be biased. In that configuration, every channel works like an individual particle multiplier, which turns a single particle into an avalanche of secondary electrons. The multiplied electron charge is collected from the MCP using a spatially sensitive anode or a phosphor screen. The channels of the MCP detector are slightly rotated with an angle between 2° and 8° in order to increase the probability that the particle will hit the wall of the channel. A single MCP has a spatial resolution equal to the spacing between two channels and a time resolution smaller than 200 ps [178]. Its gain is between 10^3 and 10^4 with the exponential pulse height distribution. Typically, the channels cover between 50 to 70 % of the surface of the detector.

The MCP detector can be used to detect a wide variety of particles, both neutral and charged. The secondary electrons can be released from a depth up to 20 nm.

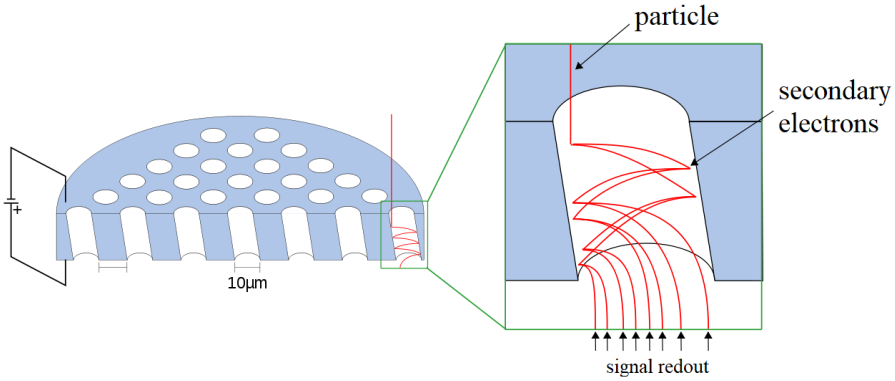

Figure B.1: Scheme of the MCP detector.

The most commonly used is the MCP detector in the Chevron configuration. It is made from two MCP plates with angled channels rotated by 180°. The electrons from the first plate are multiplied in the second plate to increase the gain of the detector up to 10^7 while keeping the spatial resolution. The rotation of an angle in the second plate prevents the ion feedback.

B.2 MCP detector - more details

First tests of a MCP based detection system were performed with a MCP detector made from two Microchannel Plates in Chevron configuration and a fiberoptic phosphor screen with P46 phosphor. All three plates are mounted in stainless steel hardware. In front of the MCP there are two circular electrodes. The detector is presented in Figure B.2. This detector model has a gap between two MCPs with a metal coating which allows to switch on/off the detector very fast. This feature was considered to be used in order to minimise the unwanted background.

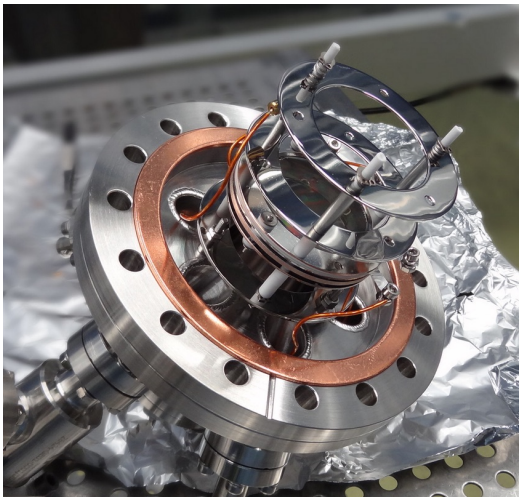

Figure B.2: MCP/phosphor screen detector for the antihydrogen detection.

The most important producer's information about used MCP are:

- thickness: 0.5 mm;
- diameter: 40 mm (minimum);
- center-to-center spacing: 12 μm nominal;
- pore size: 10 μm nominal;
- bias angle: $8° \pm 1°$;
- open area ratio: 55% minimum;
- electron Gain at 2400 Volts: 1×10^7;
- dark count and gain volts: 0.4 (cts/sec/cm^2) maximum.

For more information please refer to the data sheet [179].

MCP has 6 high voltage outputs. For each connection, the following value of voltage was used:

- MCP in $-2kV$
- MCP middle up - for gamma efficiency measurement it was disconnected;

- MCP middle down - for gamma eficiency measurement it was disconnected;
- MCP out GND
- phosphor screen $+2kV$
- grid $+2kV$

B.2.1 CCD sensor properties

After the phosphor screen the CCD camera was used (pco.pixelfly usb). For the measurement of the gamma detection efficiency, the distance between the first MCP plate and the metal frame of the focusing lens of the camera is equal to 216 mm. The MCP covers 36 % of the CCD sensor. Later, for other measurements like detection of protons, the upgraded setup was used (distance 157 mm, 60% of the CCD sensor).

CCD camera detect the light produced by the phosphor screen, so thus its internal properties have a huge influence on received data. The most important producer's information about used CCD sensor are:

- sensor type: ICX285AL
- resolution: 1392 x 1040 pixel
- it is not cooled down
- trigger input signals: TTL level
- trigger output signals: 3.3 V LVTTL level.

For more information please refer to the data sheet [180].

Detailed analysis of the CCD properties showed large deviations for mean and standard deviation values between different pixels. Mean and standard deviation maps, calculated using 200 images, $t_{ex} = 10\mu$s, are presented in Figure B.3. Clearly visible spacial effects are related to the readout system and inner properties of the CCD sensor. In order to minimize influence of CCD fluctuations to the number of detected events, presented maps are used as a constant background in the later analysis.

Significance of the correction for the CCD sensor properties fluctuations is clearly visible in the following example. In Figure B.4 the results of basic analysis (described later) of 200 dark CCD images are presented. Histograms show position distributions of detected peaks. On the left/right histogram results of the analysis without/with correction for CCD inequalities are presented (watch out for different colour scale). The difference between two results is clearly visible, therefore described correction is essential.

Due to a low speed of the camera, it is possible to save maximum one picture every $\approx$ 160ms.

B.2.2 MCP detector system - not used for efficiency of gamma detection measurement

In the proces of the study of MCP detector two improvements were developed.

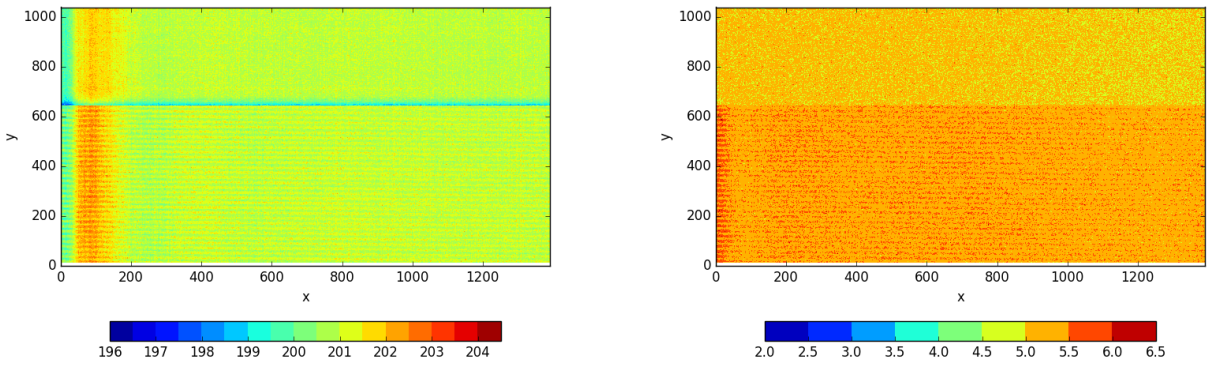

Figure B.3: Mean $mean(x, y)$ (left) and standard deviation $mean\_std(x, y)$ (right) distributions for every pixel of the CCD sensor.

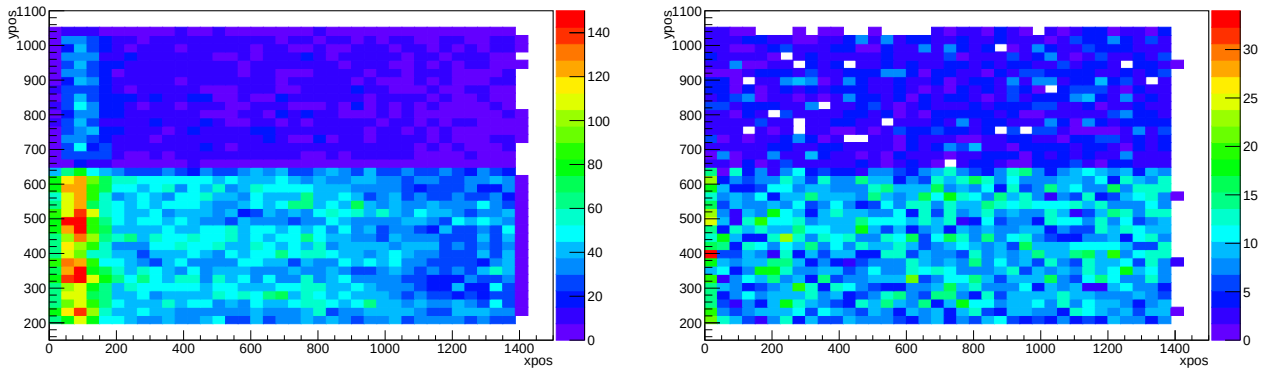

Figure B.4: Peaks' position distribution obtained using basic analysis algorithm (described in section B.3.4) for 200 dark CCD images. On the left/right histogram results of the analysis without/with correction for CCD inequalities are presented (watch out for different colour scale). White squares indicate that no peaks were found.

New focusing system In order to increase the spatial resolution of the detector, the new focusing system was developed. The goal was to focus the phosphor screen picture at the whole CCD sensor (in smaller parameter y - 1040 pixels), and thus cover 60% of the CCD sensor (before it was 36%).

This idea was realised by adding an extra metal ring between the camera and the lens. It allowed to decrease the distance between the edge of the camera lens and the MCP detector to 157 mm. An image of the edge of the detector structure is presented in Figure B.5. The MCP is a little bit smaller than the bright, gray circle.

The metal ring is 1 mm thick and its internal diameter is equal to 25.5 mm (external is 30 mm, but can be larger), see Figure B.6.

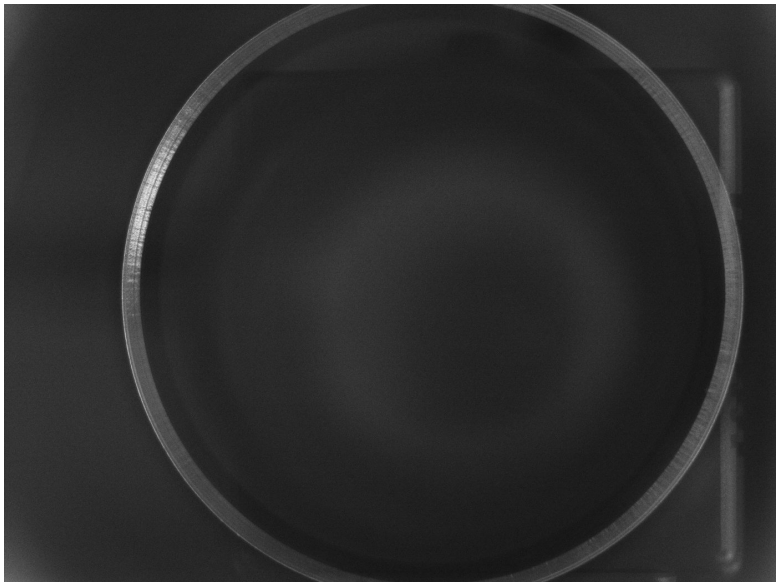

Figure B.5: An image of the edge of the detector structure. The MCP is a little bit smaller than the bright, grey circle.)

Figure B.6: Metal ring used to increase the MCP/CCD detector resolution.

Better electrical connections The MCP setup which was proposed for the experiment is made from two MCPs separated by a gap in the order of 0.1 mm. In principle, it allows to fastly turn off the second MCP wafer and thus protect the phosphor screen and MCP from burning. However, in that situation, in order to prevent from electrons' dissipation between wafers, it is important to put around $100 - 150$V between two MCPs [181]. In our primary setup two walls of that gap were connected. This created the region with zero electrical filed and thus a blurred image.

In the new setup the MCP was supplied with the high voltage through the resistance box presented in Figure B.7. During test measurements, a large improvement in the image quality has been observed.

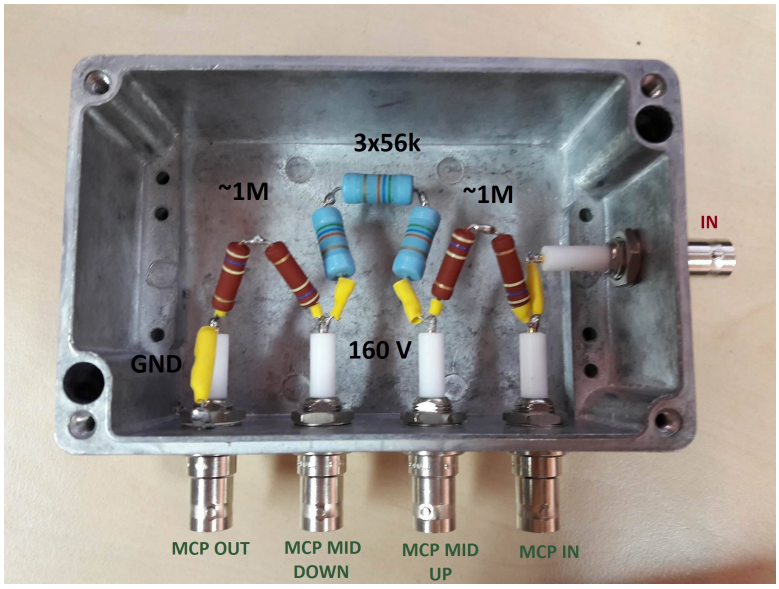

Figure B.7: The resistance box used to supply voltage to the MCP detector.

B.3 An examplary scheme for future data analysis based on gamma detection efficiency and dark counts tests

B.3.1 MCP gamma detection efficiency test

The absolute detection efficiency of the gamma radiation ϵ can be estimated by dividing a detected number of particles N_d by an incident number of particles N_a, $\epsilon = N_d/N_a$. In this section, a part of a procedure required to obtain N_d and N_a is described.

The whole experimental setup is presented in Figure B.8, B.9. In order to provide the same measurement conditions for N_d and N_a, two detectors, MCP and CsI, have been used simultaneously. The positron beam annihilating on the stainless steel target was used as a source of gamma particles. The annihilation process took place in the center of the cross (right part of Figure, hidden behind brown, round coil) after the last stage of buffer gas trap. It is assumed, that the uniform distribution of gammas was produced.

According to that assumption acceptances of two detectors are:

- MCP: $A_{MCP} = (5.12 \pm 0.07) \times 10^{-4}$;
- CsI: $A_{CsI} = (7.12 \pm 0.84) \times 10^{-4}$.

A number of detected particles is estimated using the analysis software described later. Incident number of particles hitting the MCP is equal to $N_a = N_{CsI} \cdot A_{MCP}/A_{CsI}$, where N_{CsI} is a number of photons detected by the CsI detector. A method which was used in order to obtain that number is described in the subsection B.3.2.

MCP acceptance calculations

MCP is a round, flat detector with a radius $r_{MCP} = 20$ mm (taken from the data sheet). The distance between the MCP surface and the middle of the gamma source is $r = 442 \pm 3$ mm. According to those information MCP acceptance is:

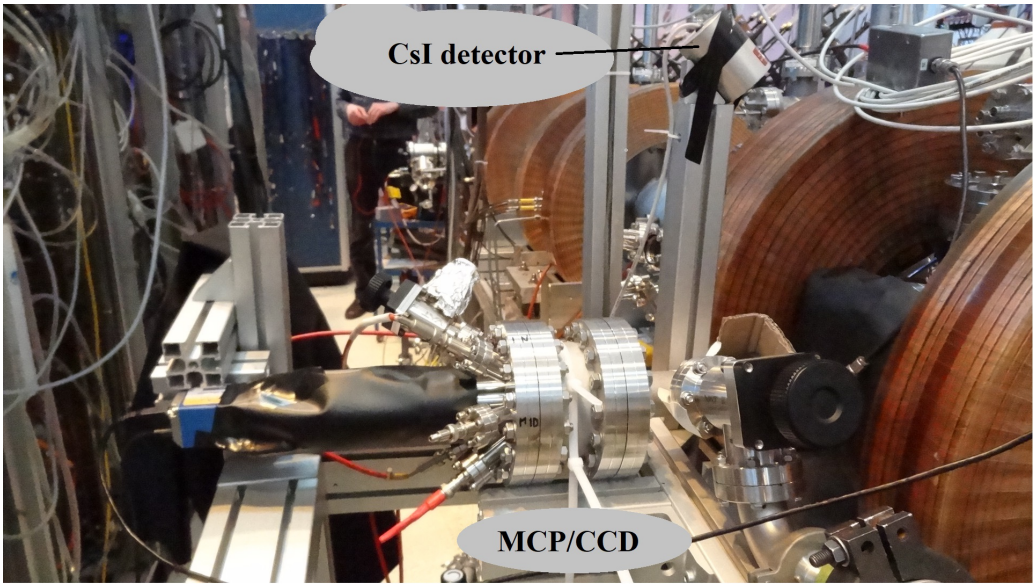

Figure B.8: The experimental setup made to measure gamma detection efficiency. In the top-right corner the CsI detector is visible.

$$A_{MCP} = \frac{\pi r_{MCP}^2}{4\pi r^2} = (5,12 \pm 0,07) \times 10^{-4}. \tag{B.1}$$

Error was estimated using exact differential method.

CsI acceptance calculations

CsI detector has a cylindrical (bottom) plus conical (top) shape, see Figure B.10. During the experiment, the part with larger round cross-secion was facing the target, which means, that the main contribution to the acceptance came from that part of the crystal. The radius of a cylindrical part of a crystal is equal to$r_{CsI} = 25.5$ mm, while its height is equal to $h_{CsI} = 51$ mm. The distance between the front of the detector and a center of the target is equal to $r = 453 \pm 3$ mm.

In that case acceptance is an average of maximum (max) and minimum (min) acceptances for which errors where estimated using exact differential method:

$$A_{CsI\_max} = \frac{\pi r_{CsI}^2}{4\pi r^2} = (7.92 \pm 0.11) \times 10^{-4},$$

$$A_{CsI\_min} = \frac{\pi r_{CsI}^2}{4\pi (r + h_{CsI})^2} = (6.40 \pm 0.08) \times 10^{-4},$$

$$A_{CsI} = \frac{A_{CsI\_max} + A_{CsI\_min}}{2} = (7.16 \pm 0.14) \times 10^{-4}.$$

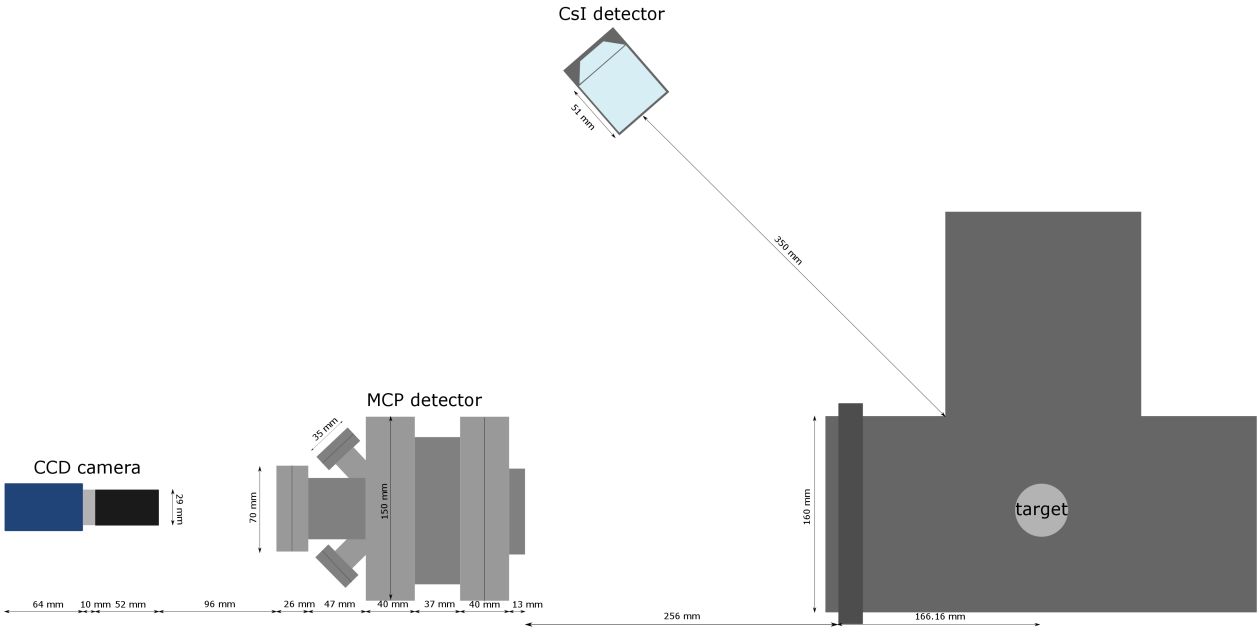

Figure B.9: Scheme of the experimental setup made to measure gamma detection efficiency.

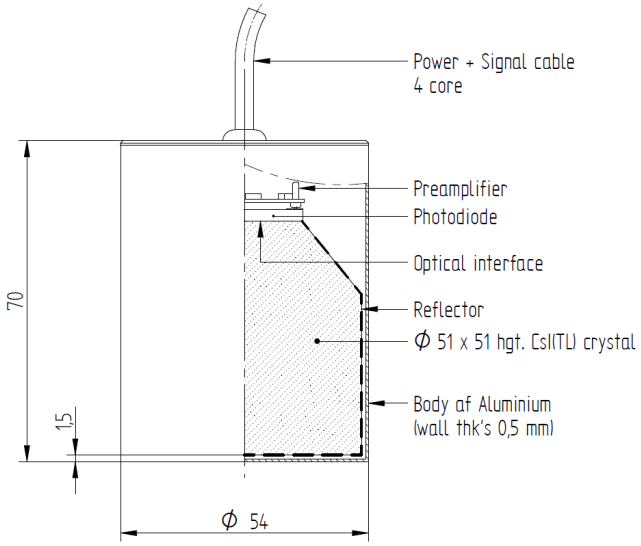

Figure B.10: CsI detector

B.3.2 CsI calibration

The signal from the CsI was collected through amplifier (integrator) using LeCroy oscilloscope (HDO 6054) and trigger adjusted to detect a rising edge. In order to estimate the number of particles hitting the detector, the maximum height of a triggered signal was measured.

Calibration of the CsI detector (author Laszlo Liszkay) gives $V_{max} = 1.512$ mV/gamma for gamma of energy 511 keV.

Measured mean value of a peak height for one bunch of annihilating positrons is 28.9 mV. Assuming that CsI detector has 100% efficiency for gamma detection, there were 28.9/1.512 mV/mV= 19.11 gamma/pulse. That number should have about 20 % of an error coming from the calibration method. As this error was not studied in details, the final errors are just an approximation.

B.3.3 Dark events measurements

A first systematic error for the measurement comes from constant natural radiation background. Additionally, the MCP itself produces some fake events by electron emission. Later in the text "dark event" is going to refer to either cosmic radiation or random MCP event. According to the MCP data sheet [179] the number of dark counts should be equal to the 0.4 cts/sec/cm^2.

In order to estimate that number the same experimental setup were used as described before, but without a positron source. Data set description:

- date of the measurement: 15-02-2017 and 20-02-2017;
- camera exposure time: $t_{ex} = 10\mu$s;
- number of saved images: 31818.

Those data were later analysed using the same analysis procedure as for the data with gammas, thus results are presented later.

B.3.4 Basic analysis algorithm, general description

Data analysis is performed using software developed in python and ROOT/C++ programming languages. The most important libraries that have been used are astropy/photutils: v0.3 [182] and ROOT version 5.34/34 [183]. New version of phototuils, released in November 2016, provides professional tools for detecting and performing photometry of astronomical sources. CCD/MCP images are similar to picutres of a night sky, that is why a chosen library meets the software requirements.

Basis analysis algorithm:

- Save files using LabView program in 16 bit *.tif* files.
- Load one picture, convert it to an array and divide it by 4. Pictures saved as *.tif* files have 16bits (U16), while the camera is 14bits. That is why pixels values are multiplied by 4.
- Open previously prepared background $back(x, y) \pm std(x, y)$. Procedure how to made a background is described in the following subsection.
- Find all pixels above a given threshold and then assign them to different peak candidates. If two pixels share an edge or a corner, tag them as the same peak.
- Measure properties of found peaks.
- Save list of peaks in the .root file.

In this analysis, the basic threshold was equal to $t(x,y) = back(x,y) + 2 \cdot std(x,y)$. It cuts off most of the CCD noise excitations and still allow to detect a part of low intensity signal. Generally, that analysis gives a primary set of peaks candidates, which later can by studied in more details and in much less time.

Variables calculated for each peak:

- *area* - number of pixels taged as a peak;
- max_value - maximum pixel's intensity I for a peak;
- *xpos*, *ypos* - position of the center of the peak, in units of pixel, pixel;
- $covar\_sigx2 = \frac{\sum_{i \in P} I_i x_i^2}{\sum_{i \in P} I_i} - \bar{x}^2$, in units of pixel^2;
- $covar\_sigy2 = \frac{\sum_{i \in P} I_i y_i^2}{\sum_{i \in P} I_i} - \bar{y}^2$, in units of pixel^2;
- $int\_16 = \sum_{\{x_i : |x_{max} - x_i| \leq 8\}} \sum_{\{y_i : |y_{max} - y_i| \leq 8\}} I(x_i, y_i)$;
- $int40 = \sum_{\{x_i : |x_{max} - x_i| \leq 20\}} \sum_{\{y_i : |y_{max} - y_i| \leq 20\}} I(x_i, y_i)$.

Background preparations $back(x,y) \pm std(x,y)$

According to the fact that CCD sensor does not have the same mean value for all pixels, one should use two dimensional distribution as a background $back(x,y)$. Also, external sources of light can bias the basic threshold value. In order to estimate a CCD background for a given setup, about 200 images should be taken just before the measurement and used as a basic camera calibration. Then the average camera response for each pixel should be calculated. If there is no external light in the setup, the $back(x,y)$ should be equal to mean pixel values measured with a closed camera opening $mean(x,y)$.

B.3.5 Data analysis

In the following section, the steps of a more detailed analysis are going to be presented together with their explanations. The same analysis was later performed for dark images.

Data set description:

- date of the measurement: 23-01-2017 ;
- camera exposure time: $t_{ex} = 10\mu$s;
- number of saved images: 51200 (two sets A and B, where $N_A = 26724$ and $N_B = 24476$).

First correction In Figure B.11 peak position (x,y) distribution for first 26 724 pictures is presented. There are higher background fluctuations for $xpos < 50$ [pixel] and for $600 < ypos < 700$ [pixel]. In presented picture, the center of the MCP is $(x,y) = (700, 500)$ [pixel,pixel] and radius $r = 400$ [pixel], that is why only contribution form $600 < ypos < 700$ pixels (14% of the whole picture) may produce additional errors. At that stage, that part of the picture was not taken into account in the analysis.

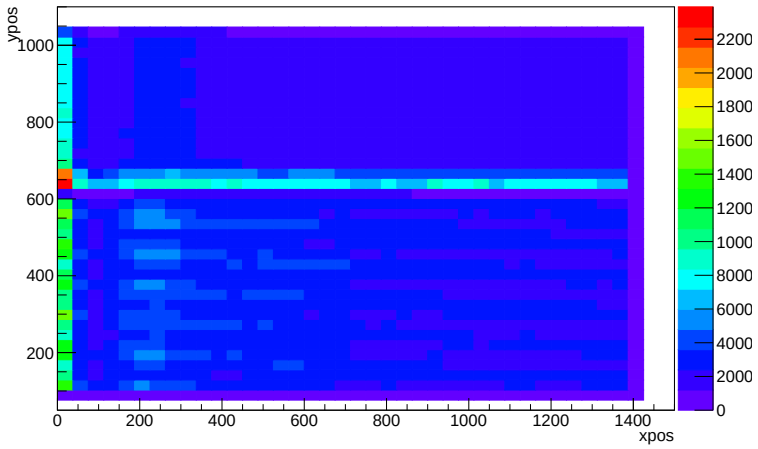

Figure B.11: Peak position distribution for 26724 images after basic analysis.

Second correction

- Select peaks with the highest max_value inside a square 59 by 59 pixels (at least) and center in a chosen peak position.

- Motivation: for low intensity signal background fluctuations may completely change the shape of the signal. For example, instead of one large peak, there may be 2 or 3 smaller ones. It is important to exclude all those artifacts, which is done by choosing the peak with the largest max_value inside a defined region. In order to find it, algorithm choose one peak and then compare its max_value with max_values of all peaks founded in the square 59 by 59 pixels around him. If it does not find any better candidate, it saves peak on a special list. If a higher peak is found, then algorithm do not save the old peak and check the new peak. Size of a side of a square should be chosen according to expected number of detected events.

Third correction

- $max\_value > back(x,y) + 3 \cdot std(x,y)$ $(mean(x,y) + 3 \cdot std(x,y))$.

- Basic cut for max_value still allows to pass to a lot of background fluctuations. That is a problem, which can be only solved by additional intensity cut. However, to make it not too strong, it is required that only one pixel in a peak has higher intensity than $3 \cdot std(x,y)$.

In Figure B.12 peak position (x,y) distribution after third correction (for all data) is presented.

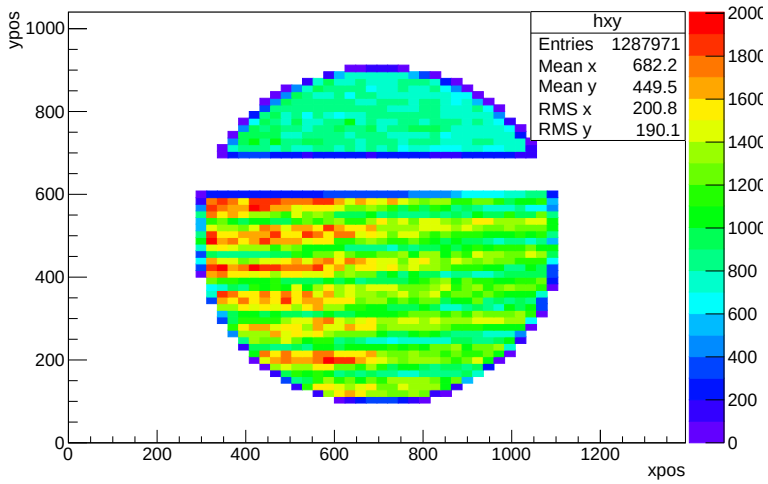

Figure B.12: Peak position distribution for all collected data after third correction.

Fourth correction

- $int\_40 > 3000 \vee int\_16 > 2000$.

- Comparison of the results between data with and without gamma particles showed, that fake events usually have $int\_40 < 3000 \wedge int\_16 < 2000$, compare Figures B.13 and B.14. Also all events in that region have $covar\_sigx2/covar\_sigy2 < 3$, which means that these are very narrow peaks. For gamma signal it is expected to have rather wide peak, however it is possible that some low intensity peaks are deleted with that cut.

In Figure B.15 peak position $(xpos, ypos)$ distribution after third correction (for all data) is presented.

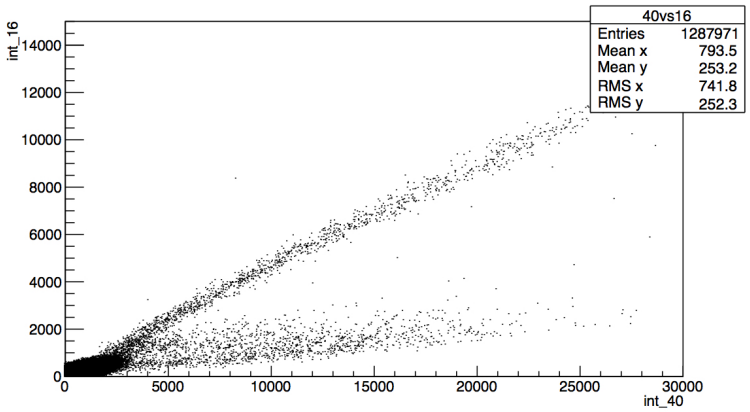

Figure B.13: $Int\_16(Int\_40)$ distribution for all collected data after third correction. Distribution for the MCP region.

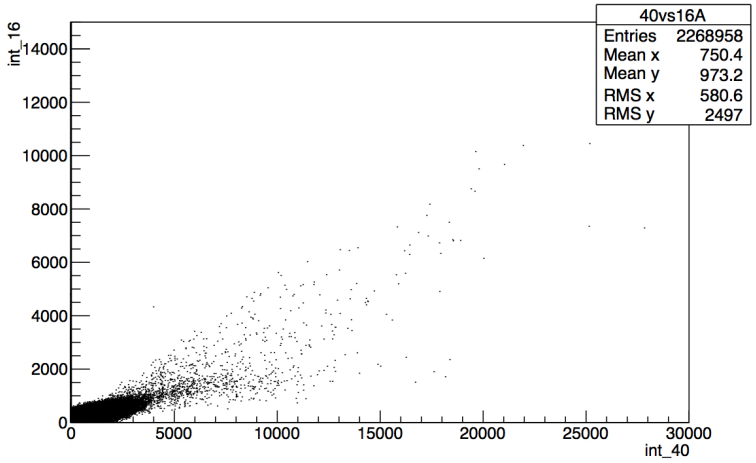

Figure B.14: $Int\_16(Int\_40)$ distribution for all collected data after third correction. Distribution for the region outside the MCP. It is important to remember that in that histogram also some reflections are visible, not only background fluctuations.

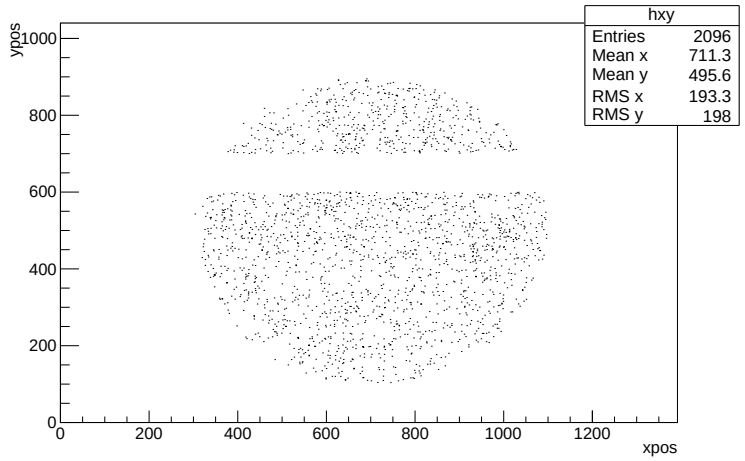

Figure B.15: Peak position distribution for all collected data after fourth correction, excluding $600 < ypos < 700$ [pixel] due to large background fluctuations.

Fifth correction

- $covar\_sigx2 > 2 \wedge covar\_sigy2 > 2$.
- Analysis of the region outside the MCP at that stage (after all previous cuts) still finds a number of events which can not be explained by light reflections (not automatic analysis showed that around 20 % from 20 found events would have any reflections). It means that cuts are not efficient enough. As can be seen in Figure B.16, most of found events have $covar\_sigx2 < 2 \vee covar\_sigy2 < 2$. Additionally, the similar histogram made for data inside the MCP region has an unnatural peak for small $covar\_sig$, see Figure B.17.

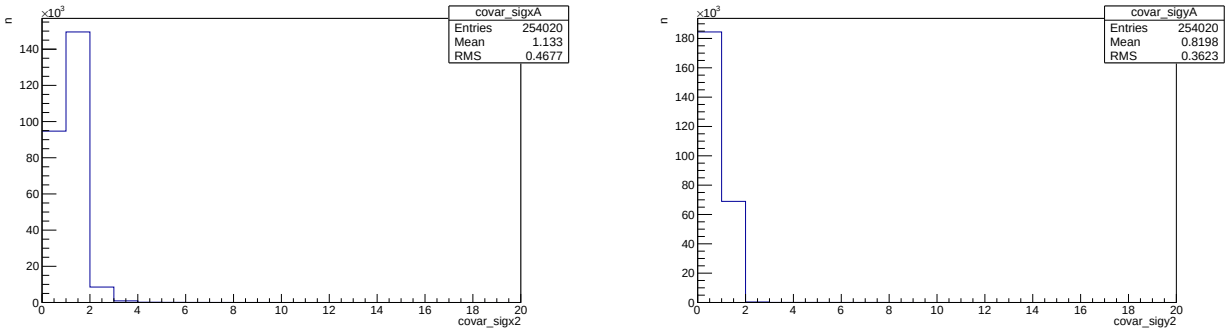

Figure B.16: $Covar\_sigx2$ and $covar\_sigy2$ distributions for data after fourth correction, region outside the MCP. It is important to remember, that some events with high $covar\_sigx2$ or $covar\_sigy2$ are caused by light reflections inside the metal tube.

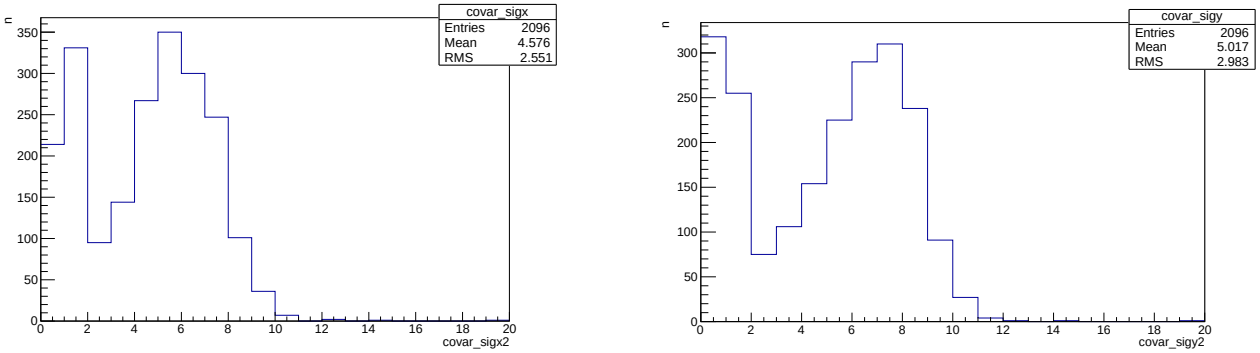

Figure B.17: $Covar\_sigx2$ and $covar\_sigy2$ distributions for data after fourth correction, MCP region.

Analysis results and discussion

- Detection probability (per one image) of a dark event: $p_D = 2.2 \pm 0.83 \times 10^{-4}$ (7 events were found).
- Probability (per one image) of finding any event for gammas' measurement: $p_{all} = 3.55 \pm 0.022 \times 10^{-2}$ (corrected for the fact that only 86% of the MCP surface was analyzed).
- Number of incident particles: 13.7.
- Gamma detection efficiency for the MCP: $\epsilon_\gamma = 2.57 \times 10^{-3}$ (an error is omitter due to unknown positron flux error).

Obtained gamma detection efficiency is in agreement with other publications [184, 185, 186, 187]. Closer analysis of obtained events shows some important properties.

Firstly, it can be stated that in the first approximation, gamma detection for the MCP is not position dependent. In Figure B.18 the peak position distribution for all collected data and full analysis is presented. There are no visible irregularities between different regions.

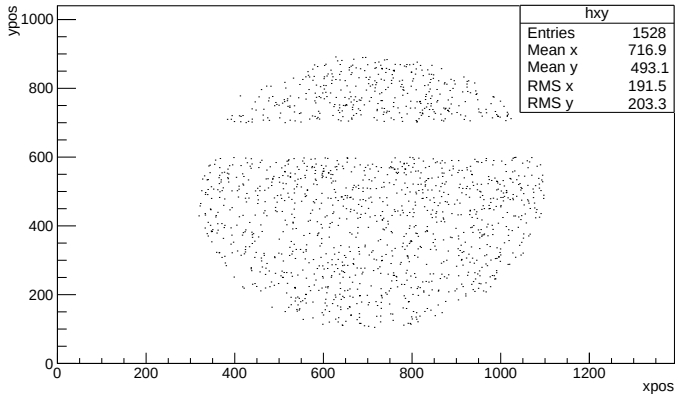

Figure B.18: Peak position distribution for all collected data and full analysis.

Secondly, there is a problem of the non uniform signal detection efficiency of the CCD camera. In previous paragraph it was mentioned that part of the image is excluded from the analysis, due to large background. In Figure B.19 peak position distribution for full analysis and whole MCP region is presented. Apparently there is no visible difference between region for $600 < ypos < 700$ [pixel] and other parts of the MCP. Using data set obtained for truncated MCP region, it is expected to find 1819 events, while the analysis for the whole MCP finds 1841 peaks. Both numbers are in agreement within error bars. Due to that argument, it is not possible to decide whether $600 < ypos < 700$ [pixel] region should be excluded or not, however it is sure, that in the future, it is important to remember about that property of the CCD sensor. Presented data also support the hypothesis that ϵ_γ of the MCP is not position dependent.

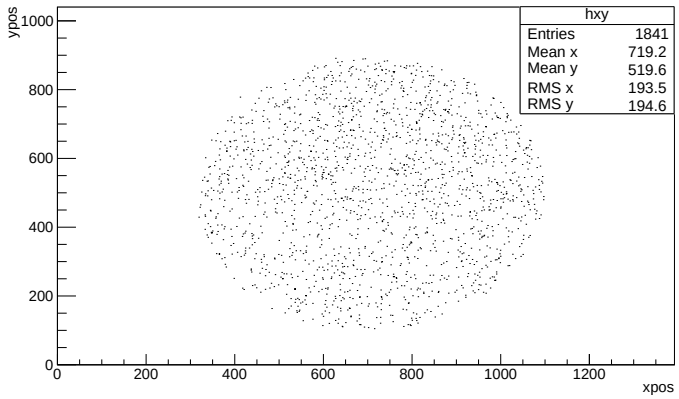

Figure B.19: Peak position distribution for all collected data and full analysis but for the whole MCP region (without excluding $600 < ypos < 700$ [pixel]).

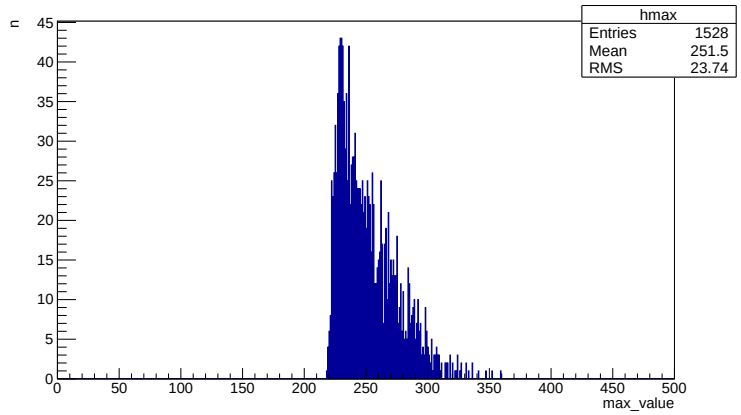

Figure B.20: Max_value distribution for all collected data and full analysis (excluding $600 < ypos < 700$ [pixel]).

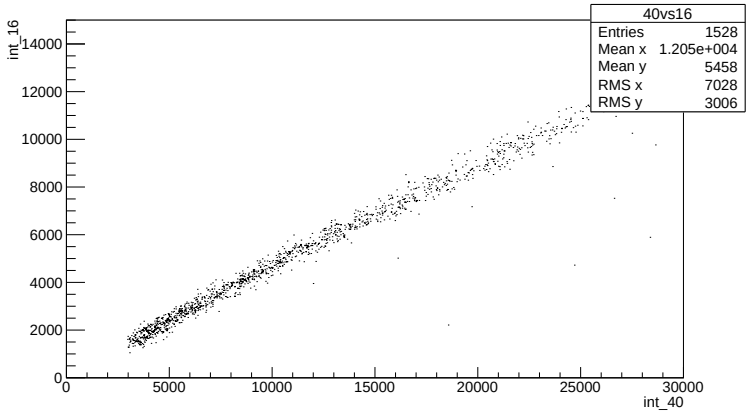

Figure B.21: $Int\_16(Int\_40)$ distribution for all collected data and full analysis (excluding $600 < ypos < 700$ [pixel]).

In Figure B.20 the max_value distribution for all collected data and full analysis is presented. It is a rapidly decreasing distribution which is similar to the exponential one. However, the formula of the distribution is not known, because of the possibility of many small internal interactions between MCP channels and gamma particles. Due to that it is not possible to fully estimate the analysis efficiency.

The $int\_16(Int\_40)$ distribution is presented in Figure B.21. As it is expected, int_16 value increases together with int_40. This means, that found events are correctly detected gamma particles or cosmic radiation.

B.4 Summary and consequences for antihydrogen/hydrogen detection

The detection efficiency of 511 keV gammas is about 0.26 %. This is because 511 keV gammas penetrate deeply into the MCP structure, from where the probability of the emission of the secondary electron is very small. For the same reason, the distribution of the signal height of the gammas is almost exponential.

In the case of heavily ionising particles like protons or antiprotons, the expected signal height distribution is more similar to the one presented in Figure B.22. This distribution has a clear peak, which allows distinguishing protons from the gamma signals. It is a crucial observation for antihydrogen atom detection. Additionally, due to the secondary electron emission process [173], the (anti)hydrogen atoms and ions with energy higher than 1 keV have the maximum possible detection efficiency.

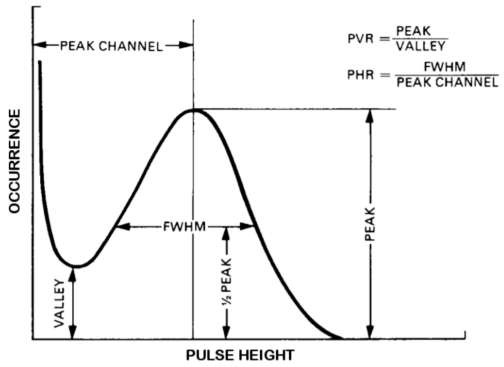

Figure B.22: Example of the signal height distribution for the MCP in the Chevron configuration. Image taken from Hamamatsu.

The 511 keV gamma detection efficiency should be repeated with the positron annihilation in the centre of the reaction chamber. It would allow to measure directly 511 keV gammas without any material in between. Also, the large distance between the centre of the reaction chamber and the detector would allow to eliminate a significant part of the Compton scattered photons.

Appendix C

First proton beam tests in CEA Saclay

First tests of the proton beam source and focusing system for the GBAR experiment were performed in CEA Saclay. The proton source was supposed to be used for the formation of hydrogen in the charge exchange reaction with positronium. This appendix describes the first tests of the MCP detector with the a intensity proton beam.

C.1 Experimental setup

An experimental setup for the proton beam preparation was developed in CEA Saclay, see Figure C.1. A Penning-type proton source is used, supplied by a bottle filled with hydrogen gas with a manual system to control the pressure. The optimum discharge voltage is 3.5 kV, however, even at that value the source is not stable and the beam flux strongly varies in time. After the chamber, particles are electrostatically accelerated to an energy between 1 keV and 10 keV. Later, the beam is focused and steered by the electrostatic quadrupoles. A restriction allows for differential pumping between the discharge chamber and the rest of the system. It is followed by a cylindrical Einzel lens and steering plates in between which a Faraday cup is placed. The reaction chamber is located at the end of the proton line, followed by the MCP/CCD detector.

C.1.1 Measurements with the phosphor screen

In order to check the beam profile before shooting it into the MCP it was decided to insert a phosphor screen into the reaction chamber. The phosphor screen is shown in Figure C.2. The screen is biased to reject all particles with negative charge.

Initially, the results obtained with the phosphor screen were very optimistic. The beam spot was clearly visible. Unfortunately, with time, the results became worse. After taking the detector out it turned out that the surface of the screen is metalised. Most probably, the beam takes metal molecules during its transition through the pumping restriction. Unfortunately, the setup does not allow for better beam focusing before the restriction.

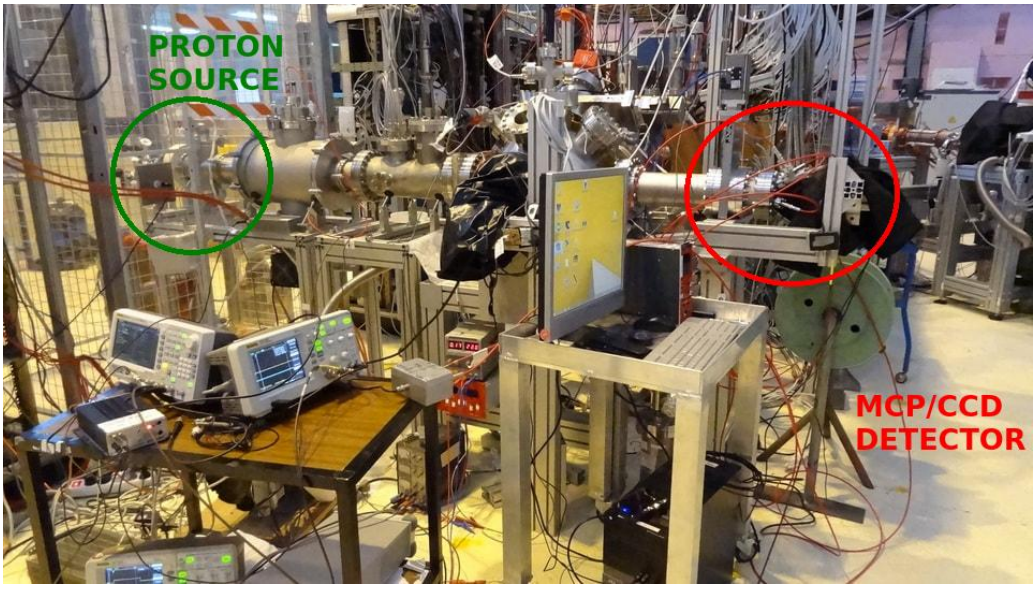

Figure C.1: Photograph of the proton line together with the reaction chamber and the MCP/CCD detector.

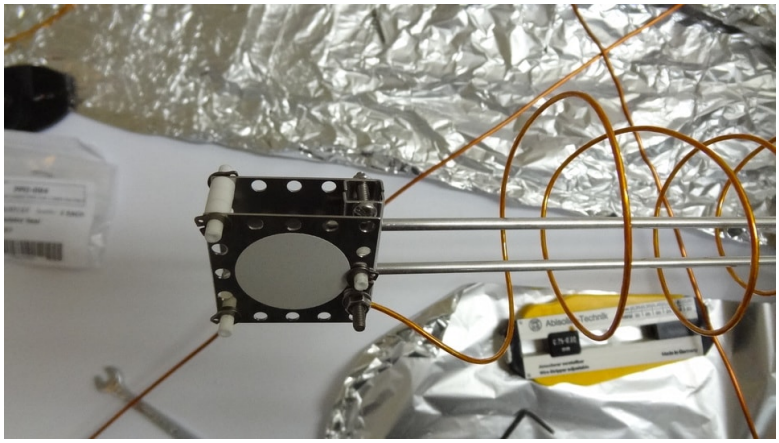

Figure C.2: Phosphor screen used for the proton beam tests.

C.1.2 Time of flight measurements

The standard method to check the quality of the beam is to perform a time of flight measurement. To this aim, the beam was chopped by turning on one of the quadrupole electrodes for less than one microsecond using a fast switch. The signal was measured on the Faraday Cup through the preamplifier, placed between the Einzel lens and the steering plates before the reaction chamber. The signal amplitude is in the order of tens to hundreds of nA. An example result is shown in Figure C.3, where the screen from the oscilloscope is presented.

The time of flight measurement shows that the 'proton' beam is made from many components, as expected. The main ingredients are protons, H_2^+ and N_2^+ (not visible in the Figure). The times of flight of the detected particles correspond to calculations.

The percentage of protons in the beam depends on the pressure p in the discharge chamber ($V_{acc} = 1\text{kV}$). The measured values are

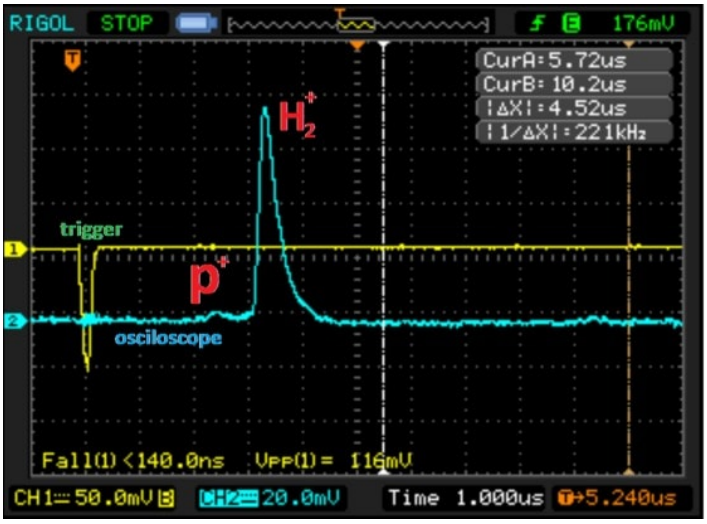

Figure C.3: Time of flight measurement of the 'proton' beam for 1 keV energy and a distance between the source and the Faraday Cup of 0.9 m. One division corresponds to 1 μs. The blue curve represents the signal from the Faraday Cup and the yellow line is the trigger signal.

- $p = 3 \times 10^{-6}$ mbar – $I_{H_2} = 80$ mV, $I_p = 4$ mV, 5% of protons;
- $p = 2 \times 10^{-6}$ mbar – $I_{H_2} = 96$ mV, $I_p = 5$ mV, 5,2% of protons ($\approx$ 8000 protons in one pulse);
- $p = 1 \times 10^{-6}$ mbar – $I_{H_2} = 37$ mV, $I_p = 4$ mV, 11% of protons;
- $p = 6 \times 10^{-7}$ mbar – $I_{H_2} = 12$ mV, $I_p = 3$ mV, 20% of protons.

In the best case for $p = 2 \times 10^{-6}$ mbar pressure, it is possible to produce about 8000 protons per pulse. Such number of protons in the beam is too low to produce hydrogen, which requires at least 10^6 p/pulse. Therefore, a decision was made to buy a new ECR proton source in order to perform the final measurements.

C.1.3 Detection of protons with the MCP

A systematic measurement of hydrogen or antihydrogen production requires information about the MCP detection efficiency for hydrogen or antihydrogen atoms. Many of such experiments were made in the past and show consistent results. However, as every detector is different, it is necessary to check the efficiency for a given MCP.

Taking advantage of the low intensity proton beam, the detection of protons on the MCP was briefly tested. In order to lower the intensity of the unwanted H_2^+, which in that amount could burn the phosphor screen of the MCP, a pressure of 10^{-7} mbar in the discharge chamber was used ($V_{acc} = 1$ kV, $V_{dis} = 3.5$ kV). In such conditions 20% of the beam is made of protons. In order to protect the detector it was necessary to use lower values of voltages on the MCP $V_{IN} = -1650$ V and $V_{PH} = 800$ V.

Both the charge on the MCP and the image from the CCD camera were measured. The exposure time was 1μs. The trigger of the camera can be delayed in order to separate the detection of protons and molecular hydrogen ions. This is possible because the 90% - 10%

decay time of a signal is about 100 to 300 ns. Example results are shown in Figure C.4. For 2.5 μs delay time the protons are visible. Then they disappear for 4 μs, and for 4.5 μs we see a much brighter spot of hydrogen atoms. The beam has the same circular shape on every picture, smaller than the surface of the MCP. This shape is a reminder of the pumping restriction. Another artifact is the empty line in the upper part of some pictures. It is the shadow of the wire which causes the discharge in the hydrogen gas.

Even though the results looked promising, due to the fact that it was dangerous for the detector to increase voltages on the MCP to the nominal working parameters ($V_{IN} = -2$ kV, $V_{PH} = 2$ kV), a proper proton detection efficiency measurement could not be achieved. In addition, the fact that the beam was polluted by metal ions also encouraged us to stop the tests.

C.1.4 Grid properties

In front of the MCP two circular electrodes are assembled. They are supposed to eject charged particles from the background, for example ions from the ions pump. In Figure C.5 the effect of different grid voltages on the proton part of the beam is presented. The electrostatic field induces a triangular symmetry, pushing particles into the middle. This is the result of the charging of three dielectric legs that support the electrodes.

C.1.5 Summary

We have shown that the old proton source developed for experiments at CEA had to be replaced with a new one. The MCP detector is able to detect protons. The developed system with a fast phosphor screen allows separating different signals in time. It is a very important feature which is used to disriminate background in the final measurement.

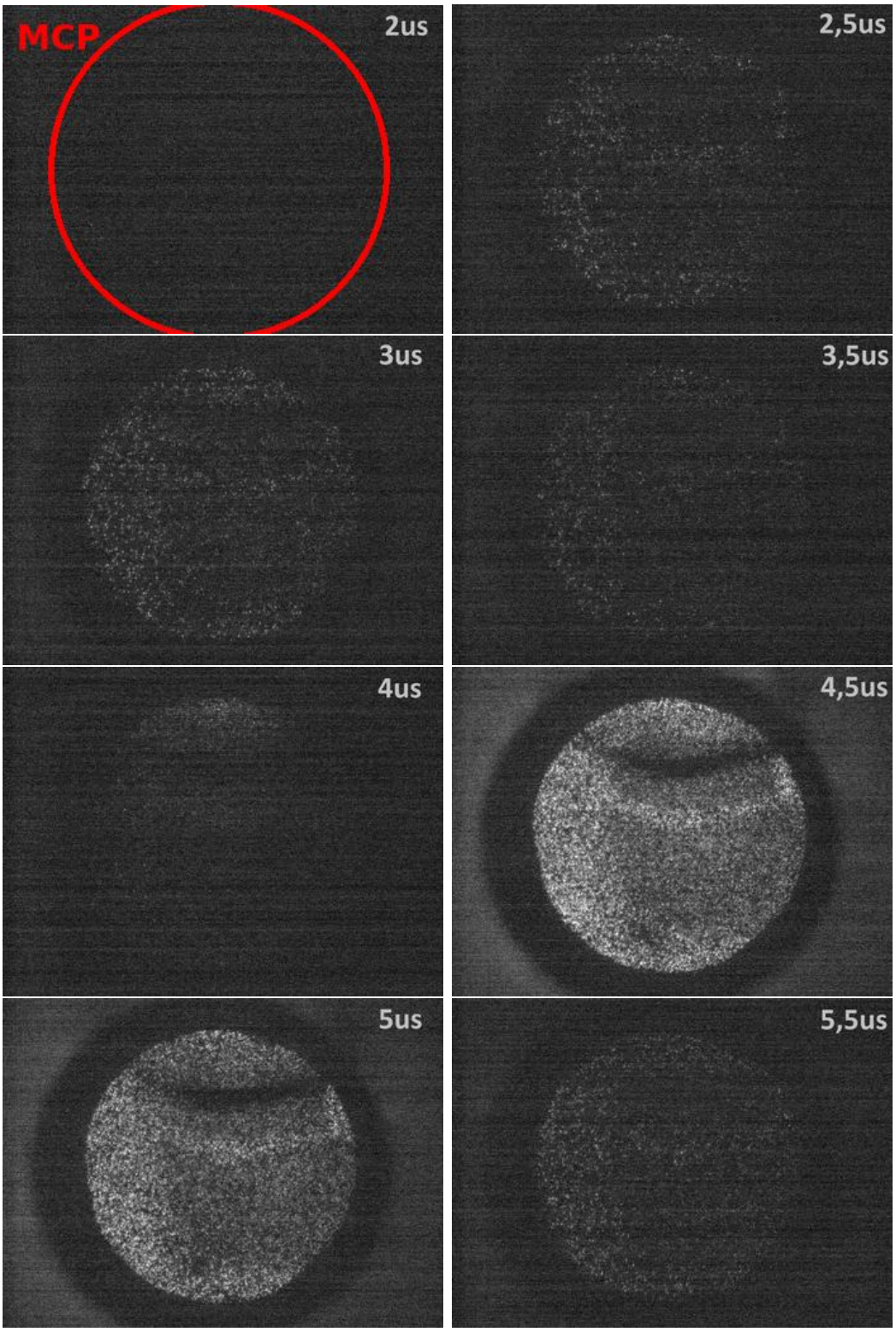

Figure C.4: CCD images of the 'proton' beam for a different delay of the camera trigger (delay time values are in the right-top corner of each picture). For 2.5 μs delay time the protons are visible and for 4.5 μs and 5 μs we see hydrogen atoms.

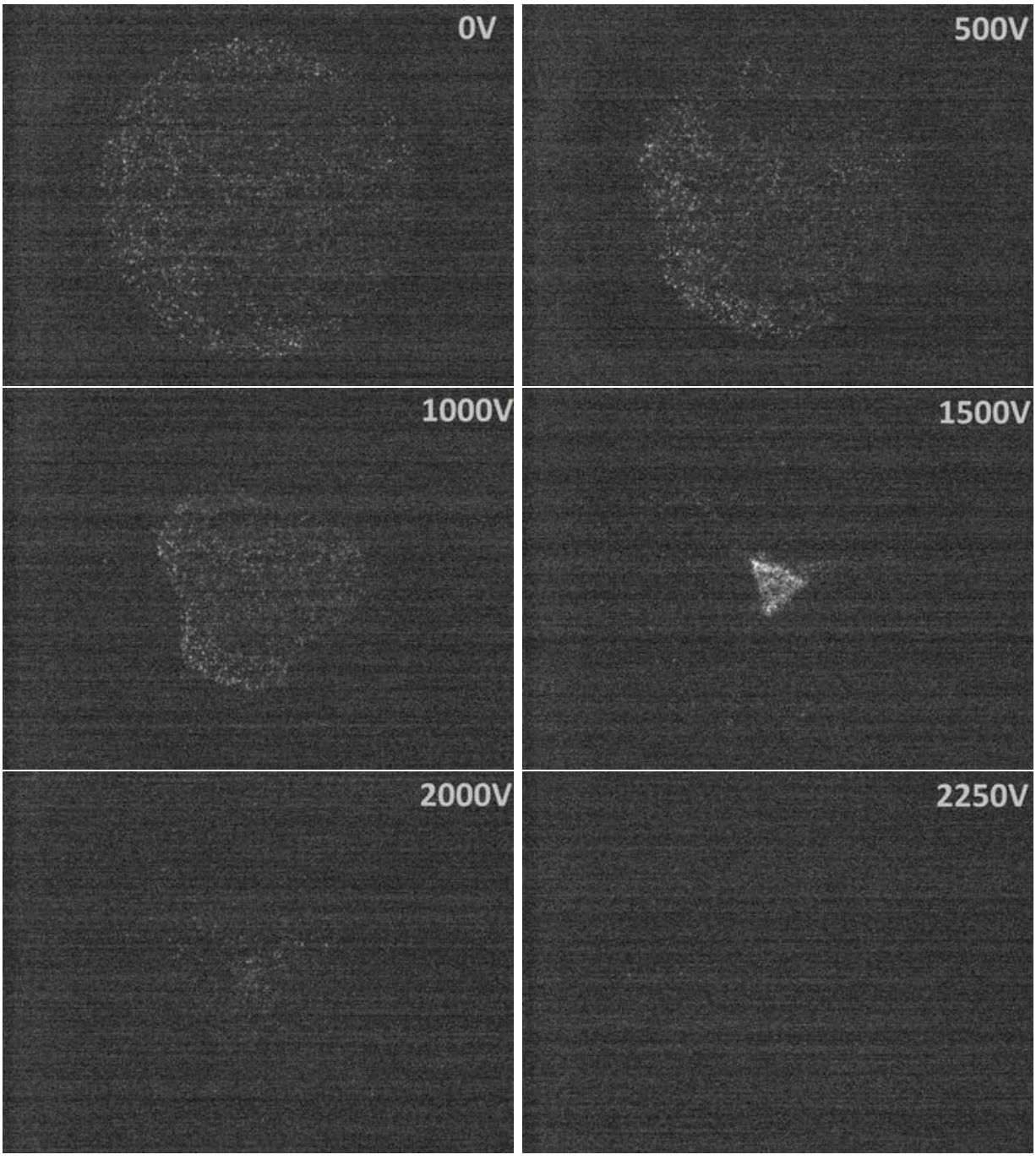

Figure C.5: Shape of the proton beam for different voltage values on the electrodes in front of the MCP detector.

Appendix D

Control system

The GBAR experiment is placed in the AD hall at CERN. Due to safety reasons it is impossible to enter the zone during the main experiment. Thus a remote control system is required.

The main experiment is based on many smaller subexperiments. One of them is the antihydrogen ion production project, which, together with the traps and the proton or antiproton source is responsible for the antihydrogen production. As these are strongly correlated, they require the same control system. The appendix describes a control system which could be used for hydrogen production.

D.1 General design

The control software for antihydrogen production can be divided into two main parts: traps control and "others". The control of the traps was developed by Dirk Van der Werf with LabView2015. It contains two parts, a slow control system which controls the values of pressures, magnetic fields etc. and a control of the trapping, which allows for online changes of the trap parameters. The system for all other devices is much more diffused. It contains one main program which can control everything and other smaller pieces of software – each for every device. The main idea is that every device has its own independent program, which can function either on its own, or together with the others. The scheme of the system is presented in Figure D.1. It is developed with LabView2017, compatible with LabView2015.

D.1.1 Main control variable

The control over the experiment is done using "enum constant" named **control** (see LabView programing tutorial) shared as a network variable. It has 5 options, presented in Figure D.2, which are controlling different phases of the experiment:

0 - Default The so-called "idle" state, when there is no measurement and it is still possible to read values from the devices. It can be used to manually change values of parameters.

1 - Initialise In this state the main program sends parameters to the programs running for single devices.

2 - Load Load parameters into the devices.

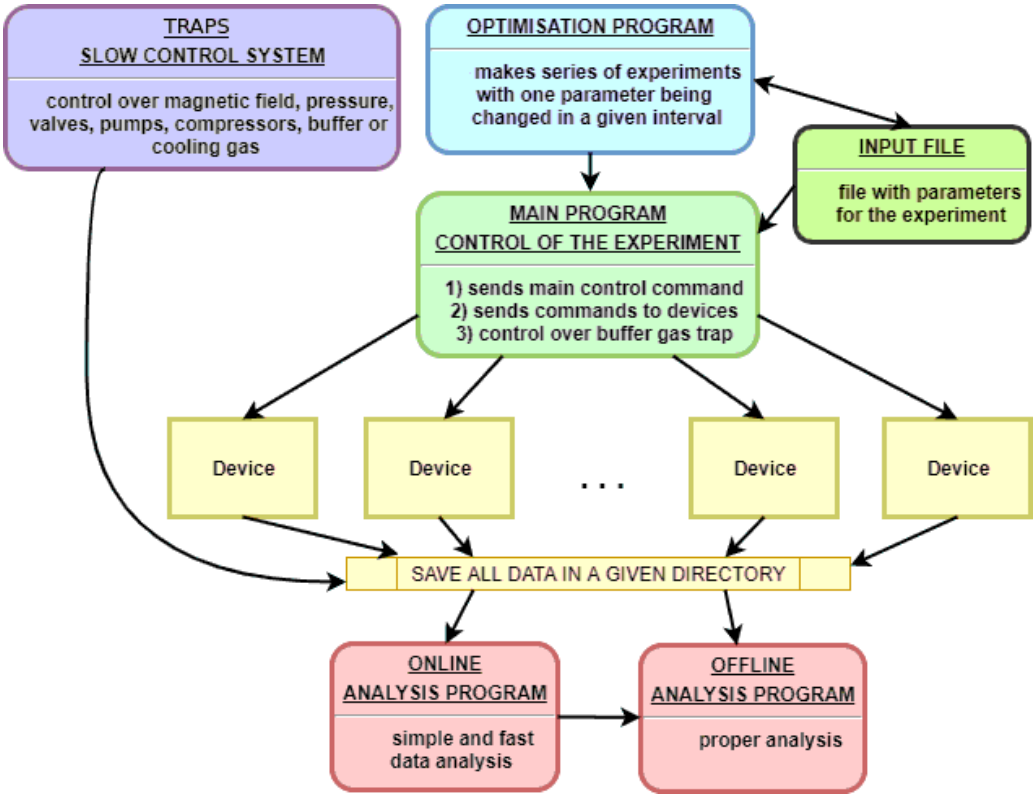

Figure D.1: Scheme of the control system.

3 - Run Runs the experiment. In most cases, devices are waiting for a trigger, which is sent during this phase.

4 - Abort Stops the program.

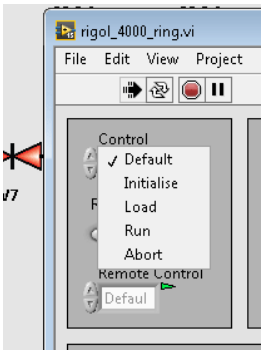

Figure D.2: Main control variable.

The main feature of the *control* variable is that its value can be changed only from the Main Program. In order for make devices subservient to that variable, a "Remote Control" button has to be pushed in each of them.

D.1.2 Input File

To save time and prevent unexpected mistakes, the parameters used to run the whole experiment can be saved in the *Input File*. The file consists of series of commands described in the sections for individual devices.

The main rules for writing the Input File are as follows:

- a command indicating a new device starts with a hash-tag character # and ends with a colon **:** ;
- if a device is not mentioned in the Input File, default values saved for the device are used;
- after the acronym of a device, it is expected to write specific commands (like *OCH1* which means *turn on channel 1*), however, it is not needed to mention all of them;
- a command always has its value separated from its name by the space character;
- it is obligatory to end different commands with a semicolon **;** character;
- due to the large number of devices it is recommended to always start commands for a new device from a new line.

An example:
#Acronym_of_a_device: Command1 VALUE; Command2 VALUE; Command3 VALUE;
#Acronym_of_a_device2: Command1 VALUE; Command2 VALUE;

The main advantages of using the Input File system are the possibility of an efficient and automatic change of any parameter during the optimisation run (described in Section D.3) and the easy access to the parameters of all devices without the need of opening individual programs.

D.2 Main Program

The Main Program is responsible for managing the full experiment. This is why it is merged with the control of the positron traps. It can work in both local and remote modes. The local mode allows to run the experiment defined by an Input File or by filling all non-grey controls by hand (Array, base path, Run No, Input Filename).

The communication between the Main Program and the Devices is done using network variables. Usually one variable corresponds to one device. An exception is the buffer gas trap which requires at least 4 variables. The names of the related variables are written in the devices' subsections.

The front panel of the Main Program is presented in Figure D.3. In the top-left corner the control of the system is placed. Then, there are numerous indicators showing the variables sent to the devices. For instance, there is a *Camera_Antion* indicator, which is related to the camera used for the antihydrogen ion MCP detector. The *Array* represents the traps control with the different sequences in the defined order. The saving parameters are visible in the top-right corner. It is possible to define the directory where to save all the files (*base path*), the run number (*Run No*) and the base for all filenames (*Input Filename*). The program automatically

adds a time stamp and creates a folder for the data with the current date. In order to save the data it is necessary to press the *SAVE or NOT* button.

These simple instructions show how to run the experiment:

- Start from the *Default* state and check if you opened the programs for all the requested devices. Remember that all of them have to be in the Remote control state.
- Change to *Initialise* state – it should read all parameters from the Input File to string controllers corresponding to the appropriate devices. You may check briefly if everything is correct and you did not forget something.
- Move to the *Load* state – it will load all the parameters to the devices.
- Run the experiment.
- To stop the experiment change to *Abort*. Should you prefer to stop the experiment just for a moment, without changing any parameter, you may switch to the *Default* mode and then go back to *Run*.

D.3 Optimisation Program

Sometimes it is necessary to perform the optimisation of the experiment for a given parameter. For such scenario, an optimisation program was created, see Figure D.4. Its main feature is based on the ability to read and change the Input File according to the programmed scheme, and later, to control the Main Program to perform a set of measurements.

It is possible to change only one parameter during the optimisation. The user has to define:

- **Device** – the code of the device which is being optimised;
- **Command** – the code of the command;
- **Starting/Finishing value** boundaries for the optimisation;
- **Number of points** – the number of measurement points.

Important tips:

- To start the program change a **NON STANDARD CONTROL** to **RUN** mode.
- In order to run the optimisation, the Main Program has to be in the remote control state.

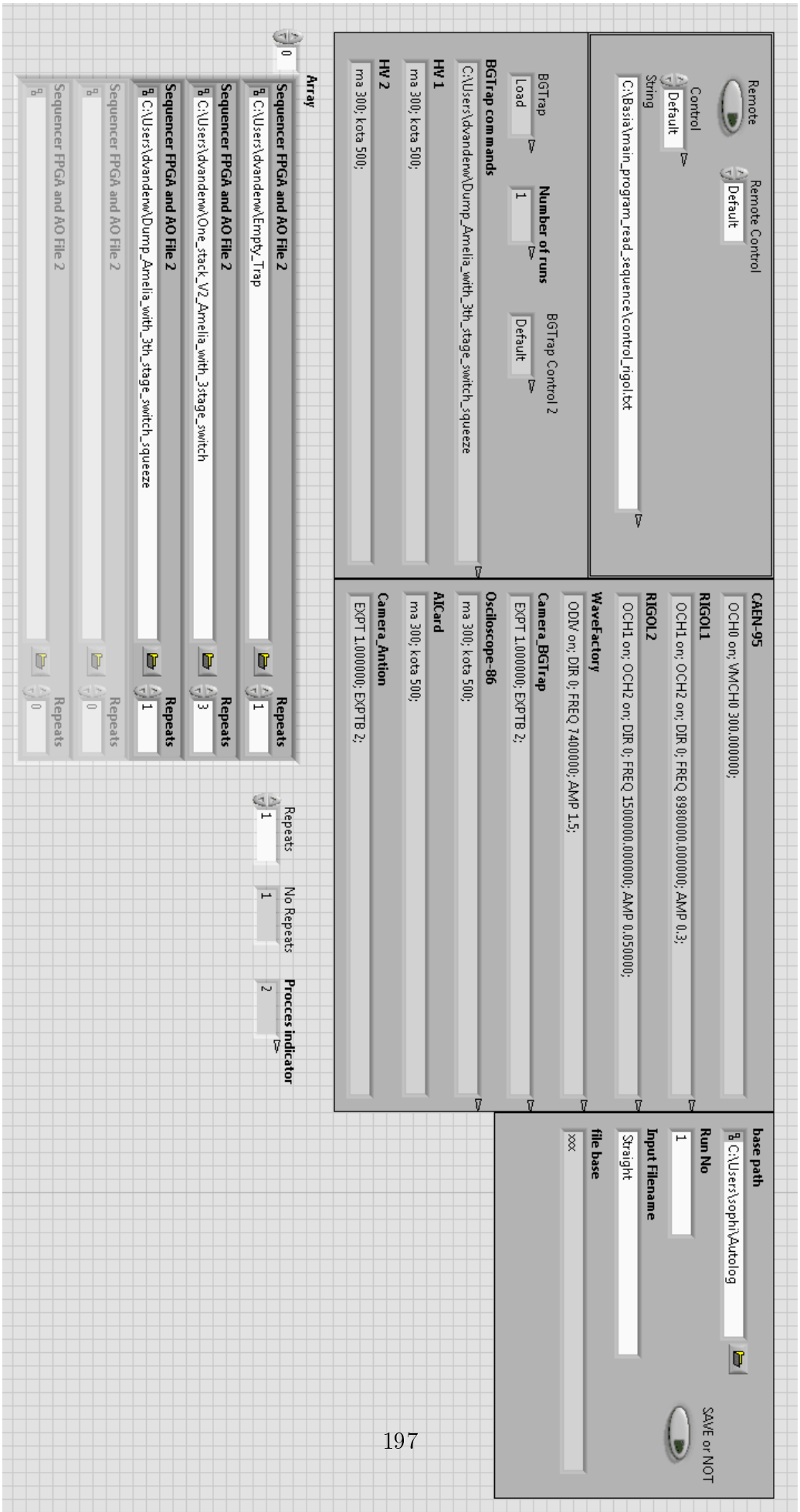

Figure D.3: GUI (graphical user interface) of the main program.

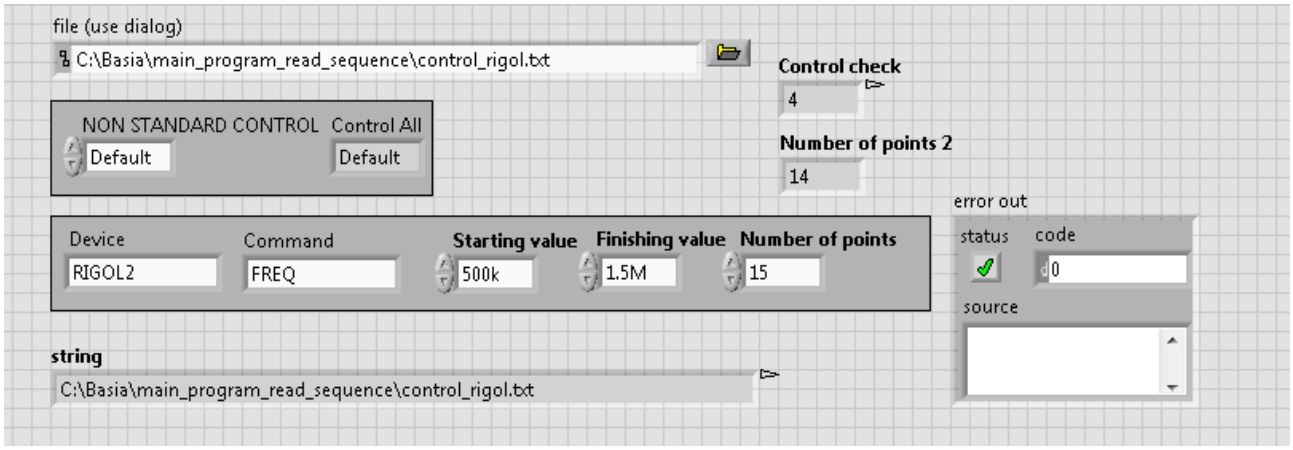

Figure D.4: Gui for the optimisation program.

D.4 Positron traps control

Dirk van der Werf designed and developed a program for the control of the positron traps. Its two main parts are the slow control system, presented in Figure D.6, and the sequencer, see Figure D.5. The second one, based on an FPGA system, is able to control voltages on the buffer gas trap electrodes and send triggers to all devices via a file containing the required voltage values; the first is responsible for all devices that have to be permanently controlled but do not have to be changed during the measurement (e.g. valves, pumps etc.). The traps program sends a trigger to other devices (NI PXIe-7820R card). However, this process is controlled from the Main Program to maintain the order in which commands are executed.

Commands:

- Network variable/ code of a device: BGTrap;
- DFile0 – string – absolute path to the positron traps sequence file;
- RFile0 – integer – number of repeats of the sequence in the file defined in the DFile0 command; it is obligatory to set RFile if the DFile was defined!
- DFileX and RFileX – it is possible to have an access to as many files as needed. Please remember about the correct order of files (the commands are executed starting from number 0).

Figure D.5: Sequencer – the program to control positron traps and all trigger outputs.

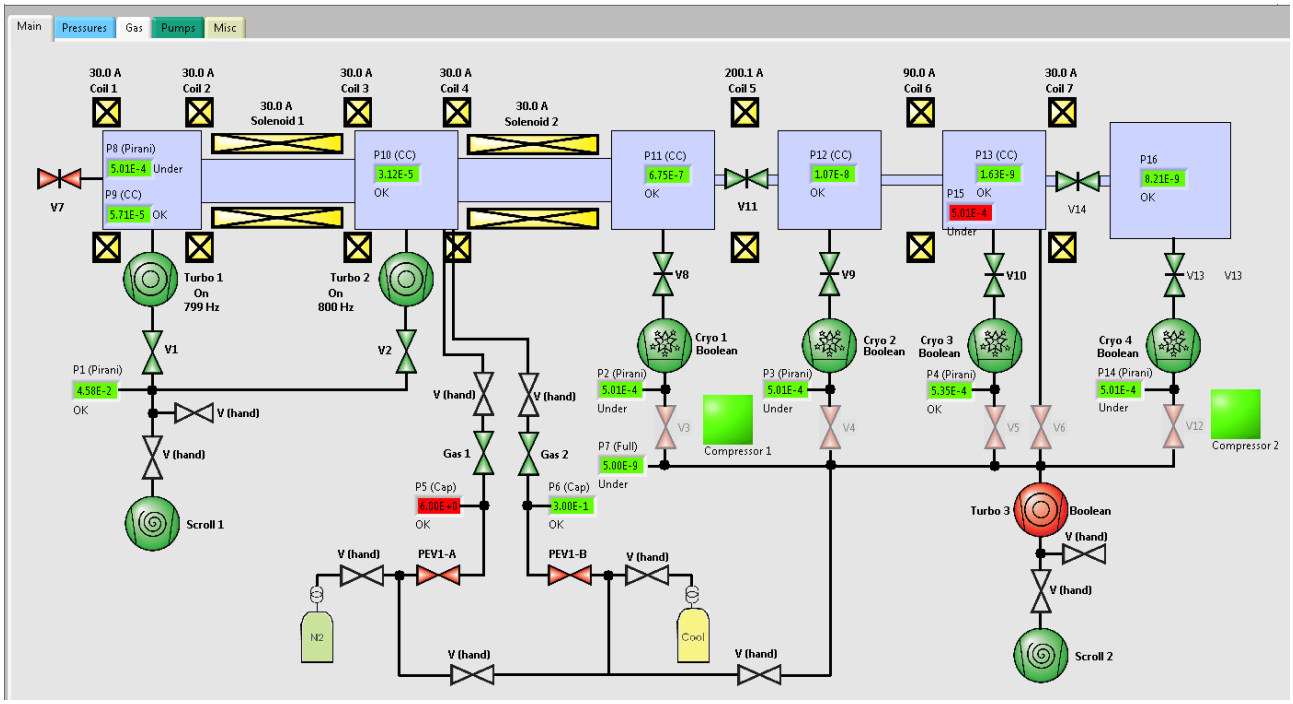

Figure D.6: Buffer Gas Trap – the slow control system.

D.5 Programs for single devices

Every device used during the experiment has to be controlled in **remote**, **standard** or **offline** modes. The last one represents the situation when the operator uses the device directly without the interface of the main program. This case is not described here, as all required information can be found in the data sheets. The *standard* mode should be used when the operator would like to directly control the device from a computer. The *remote* mode is very similar to the *standard* mode, however, the control is taken over by the Main or Optimisation program. In order to turn on that mode the **Remote Control** button has to be pressed.

Example of single device program are described in the following sections. More programs are available fro other devices.

D.5.1 Rotating walls

The program for the rotating walls of the positron traps consists of three parts managing three wave generator. Each can be used independently, however, for aesthetic reasons they are in the same LabView routine. The front panel of the program is presented in Figure D.7.

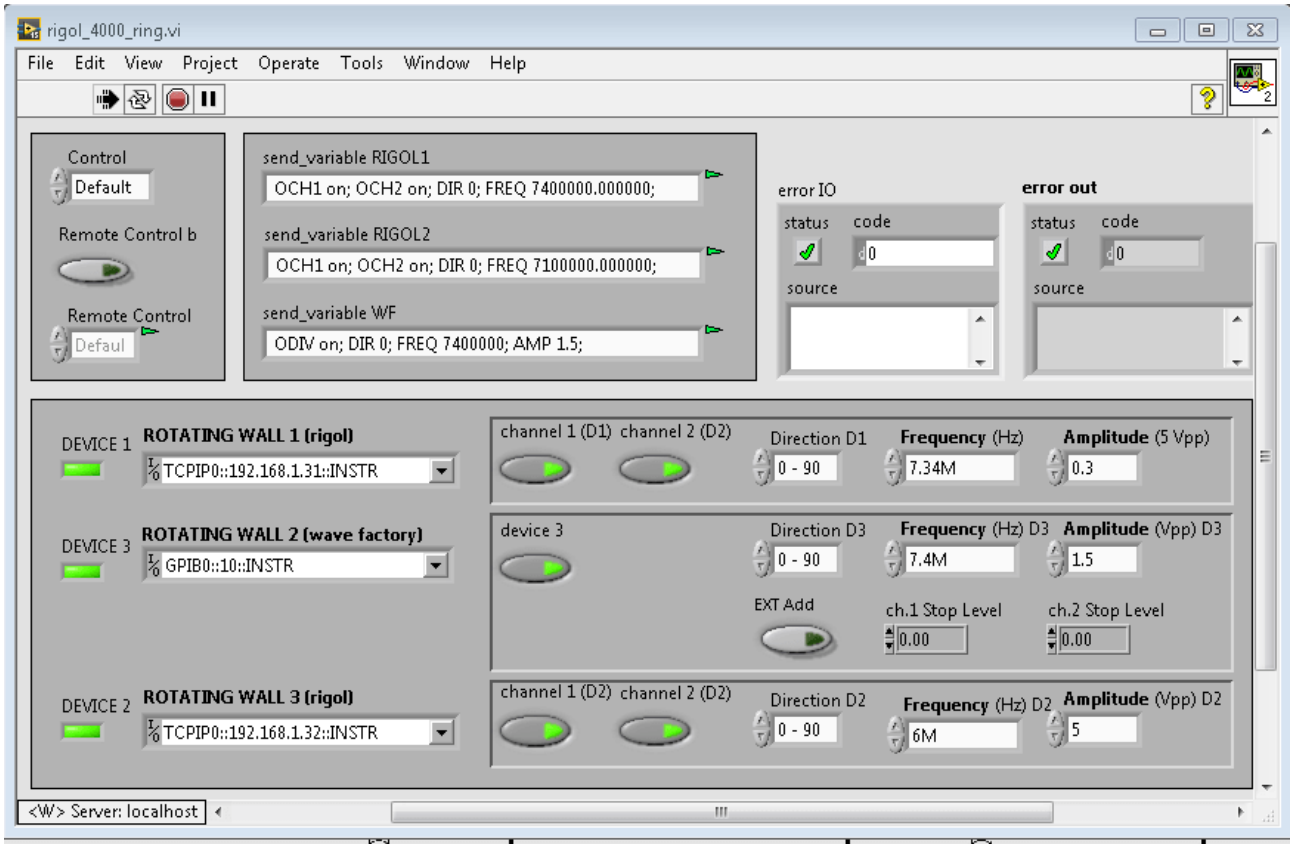

Figure D.7: Rotating walls devices.

RIGOL waveform generator

This program should work for all RIGOL waveform generators from series DG4000 connected to the computer through the USB. It requires RIGOL DG4000 Series LabView library.

Commands for the input file:

- Network variable or a code of a device: RIGOL1 / RIGOL2;
- OCH1 - on/off - turn on/turn off channel 1;
- OCH2 - on/off - turn on/turn off channel 2;
- DIR - 0 / 1 is enum constant, 0 is $0° - 90°$, 1 is $270° - 0°$;
- FREQ - double [Hz] - frequency of the sine wave;
- AMP - double [Vpp] - amplitude of the signal.

Wave Factory waveform generator

Model of the device: WF1946-A and WF1948. It requires a proper LabView library.
Commands for the input file:

- Network variable or a code of a device: WaveFactory;
- ODIV – on/off – turn on/turn off a device;
- DIR – 0 / 1 is enum constant, 0 is $0° - 90°$, 1 is $270° - 0°$;
- FREQ – double [Hz] – frequency of the sine wave;
- AMP – double [Vpp] – amplitude of the signal;
- EXTA – TRUE/FALSE
- CH1S – double – channel 1 stop level;
- CH2S – double – channel 2 stop level.

D.5.2 CAEN high voltage power supply

Model of the device: NDT1470 This program works for all CAEN high voltage power supplies from a series N14XX connected both through Ethernet of USB. It requires CAEN N14XX LabView library.
Commands:

- Network variable or a code of a device: CAEN-95;
- RATE – double [V] – input voltage on the first channel;
- TRIGM – double [V] – input voltage on the second channel;
- EXPT – integer – exposure time;
- EXPTB – integer – exposure time base.

D.5.3 Oscilloscope

Model of the device: LeCroy HDO6054 It requires a proper LabView library.

Commands:

- Network variable or a code of a device: Oscilloscope-86;
- OCH1/OCH2/OCH3/OCH4 – on/off – turn on/ turn of first/second/third/fourth channel;
- VC1/VC2/VC3/VC4 – integer – vertical coupling; 0 - A1M, 1 - D1M, 2 - D50, 3 - Ground, 4 - DC, 5 - AC;
- VR1/VR2/VR3/VR4 – double [V] – vertical range (max 10.0 V);
- VO1/VO2/VO3/VO4 – double [V] – vertical offset;
- TOUT – integer [ms] – timeout (default 10 000 ms);
- TBASE – double [s] – timebase (default 0.0005 s);
- TRIGS – 0/1 - trigger slope; 0 - rising, 1 - falling;
- TRIGC – integer $\in \{0, 1, 2, 3, 4, 5, 6, 7\}$ - trigger source; 0 - Channel 1, 1 - Channel 2, 2 - Channel 3, 3 - Channel 4, 4 - External, 5 - Line, 6 - Ext, 7 - Ext10.

D.5.4 CCD Cameras

This program is universal for most types of PCO cameras. The only requirement is the special PCO LabView library.

Commands:

- Network variable or a code of a device: Camera_BGTrap / Camera_ANTION;
- RATE – double [V] – input voltage on the first channel;
- TRIGM – double [V] – input voltage on the second channel;
- EXPT – integer – exposure time;
- EXPTB – microsecond/milisecond/second – unit of the exposure time.

D.5.5 Analog Input Card

The analog input card, NI PXIe-6366 digitizer card with 2 Mega samples per second per channel and 16-bit resolution.

Commands:

- Network variable/ code of a device: AICard;
- SAVE – yes/no – turn on/off saving the data files;
- TOUT – double [s] – timeout;

- RATE – double – sampling rate;
- NSAMP – integer – number of samples.

D.6 Saving the data and analysis

The main goal of the control system is to collect the data from all devices during the experiment. When the button "SAVE or NOT" in the Main Program is pushed, all data are saved in the same directory using the same file name base. The name of every file consists of:

- Common name base which is sent through the network variable **file base**:

  base path - a catalog where a folder with proper date will be created; can be changed in the Main Program;

  Run No - run number; can be changed in the Main Program;

  Input Filename - a command word which characterises data from a given run, like e.x. gamma, antihydrogen; can be changed in the Main Program;

  Time Stamp - a time stamp is generated automatically with microsecond precision;

- **Part_Characteristic_for_every_device** - can be changed only in the control programs for each device.

A file name is updated and sent for every trigger signal. The speed of the system is limited by the slowest device. As a result of using a Time Stamp it is possible to reliably distinguish matching data sets.

D.7 Summary

A prototype of the control system for the antihydrogen ion production experiment was developed. Many programs for single devices were written, some of them not mentioned in this summary.

The presented control system was successfully tested by performing the optimisation of the rotating wall frequencies of the buffer gas trap. It can be easily extended for all devices used for the experiment. Many programs for single devices were developed, some of them not mentioned in this summary.

Chapter 10

Bibliography

[1] R. Descartes, (1824-1826), V. Cousin. Les principes de la philosophie (1644). Oeuvres de Descartes, Paris: F.-G. Levrault, 3.

[2] R. Descartes, 1644; Zehe, 1980, pp. 65-70; Van Lunteren, p. 47.

[3] H. Kragh. *Quantum generations: A history of physics in the twentieth century.* Princeton University Press, 2002.

[4] A. Schuster. Potential Matter – A Holiday Dream. *Nature*, 58(1503):367, 1898.

[5] P. A. M. Dirac. The quantum theory of the electron. *Proceedings of the Royal Society of London, Series A, Containing Papers of a Mathematical and Physical Character*, 117(778):610–624, 1928.

[6] C. D. Anderson. The positive electron. *Physical Review*, 43(6):491, 1933.

[7] S. L. Glashow. Partial-symmetries of weak interactions. *Nuclear Physics*, 22(4):579–588, 1961.

[8] S. Weinberg. A model of leptons. *Physical Review Letters*, 19(21):1264, 1967.

[9] A. Salam (1968) and N. Svartholm. Elementary Particle Physics: Relativistic Groups and Analyticity. Eighth Nobel Symposium. Stockholm: Almquvist and Wiksell. p. 367.

[10] F. Englert and R. Brout. Broken symmetry and the mass of gauge vector mesons. *Physical Review Letters*, 13(9):321, 1964.

[11] P. W. Higgs. Broken symmetries and the masses of gauge bosons. *Physical Review Letters*, 13(16):508, 1964.

[12] G. S. Guralnik, C. R. Hagen, and T. W. B. Kibble. Global conservation laws and massless particles. *Physical Review Letters*, 13(20):585, 1964.

[13] C.-S. Wu, E. Ambler, R. W. Hayward, D. D. Hoppes, and R. P. Hudson. Experimental test of parity conservation in beta decay. *Physical Review*, 105(4):1413, 1957.

[14] M. Goldhaber, L. Grodzins, and A. W. Sunyar. Helicity of neutrinos. *Physical Review*, 109(3):1015, 1958.

[15] J. H. Christenson, J. W. Cronin, V. L. Fitch, and R. Turlay. Evidence for the 2π decay of the K_2^0 meson. *Physical Review Letters*, 13(4):138, 1964.

[16] K. Abe et al. Observation of large CP violation in the neutral B meson system. *Physical Review Letters*, 87(9):091802, 2001.

[17] R. Aaij et al. Observation of CP violation in charm decays. *Physical Review Letters*, 122(21):211803, 2019.

[18] V. A. Kosteleckỳ and N. Russell. Data tables for Lorentz and CPT violation. *Reviews of Modern Physics*, 83(1):11, 2011.

[19] R. Bluhm, V. A. Kosteleckỳ, and N. Russell. CPT and Lorentz tests in hydrogen and antihydrogen. *Physical Review Letters*, 82(11):2254, 1999.

[20] P. A. R. Ade et al. Planck 2013 results. I. Overview of products and scientific results. *Astronomy & Astrophysics*, 571:A1, 2014.

[21] A. D. Sakharov. Violation of CP invariance, C asymmetry, and baryon asymmetry of the universe. *Letters to Jounal of Experimental and Theoretical Physics*, 5:24–27, 1967.

[22] L. Canetti, M. Drewes, and M. Shaposhnikov. Matter and Antimatter in the Universe. *New Journal of Physics*, 14(9):095012, 2012.

[23] V. A. Rubakov and M. E. Shaposhnikov. Electroweak baryon number non-conservation in the early universe and in high energy collisions. In *AIP Conference Proceedings*, volume 419, pages 347–412. AIP, 1998.

[24] M. Quirós. Field theory at finite temperature and phase transition. *Helvetica Physica Acta*, 67:451–583, 1994.

[25] V. A. Rubakov and M. E. Shaposhnikov, Uspekhi Fizicheskikh Nauk 166 (1996) 493-537.

[26] A. Riotto and M. Trodden. Recent progress in baryogenesis. *Annual Review of Nuclear and Particle Science*, 49(1):35–75, 1999.

[27] M. Quirós and M. Seco. Electroweak baryogenesis in the minimal supersymmetric standard model. *Nuclear Physics B - Proceedings Supplements*, 81:63–70, 2000.

[28] G. Hinshaw et al. Nine-year wilkinson microwave anisotropy probe (wmap) observations: cosmological parameter results. *The Astrophysical Journal Supplement Series*, 208(2):19, 2013.

[29] G. R. Farrar and M. E. Shaposhnikov. Baryon asymmetry of the universe in the standard model. *Physical Review D*, 50(2):774, 1994.

[30] M. Kowitt. Gravitational repulsion and Dirac antimatter. *International Journal of Theoretical Physics*, 35(3):605–631, 1996.

[31] R. M. Santilli. A classical isodual theory of antimatter and its prediction of antigravity. *International Journal of Modern Physics A*, 14(14):2205–2238, 1999.

[32] M. Villata. CPT symmetry and antimatter gravity in general relativity. *Europhysics Letters*, 94(2):20001, 2011.

[33] P. Perez et al. Proposal to measure the Gravitational Behaviour of Antihydrogen at Rest GBAR. CERN-SPSC-2011-029; SPSC-P-342, 2011.

[34] G. Yu. Drobychev et al. Proposal for the AEGIS experiment at the CERN antiproton decelerator (Antimatter Experiment: Gravity, Interferometry, Spectroscopy). CERN-SPSC-2007-017; SPSC-P-334, (2007).

[35] J. S. Hangst, Addendum to the ALPHA Proposal. The ALPHA-g Apparatus. CERN-SPSC-2016-031; SPSC-P-325-ADD-1, 2016.

[36] A. Antognini, D. Kaplan, K. Kirch, A. Knecht, D. Mancini, J. Phillips, T. Phillips, R. Reasenberg, T. Roberts, and A. Soter. Studying antimatter gravity with muonium. *Atoms*, 6(2):17, 2018.

[37] D. B. Cassidy and S. D. Hogan. Atom control and gravity measurements using Rydberg positronium. In *International Journal of Modern Physics: Conference Series*, volume 30, page 1460259. World Scientific, 2014.

[38] Ch. Smorra et al. Base – the baryon antibaryon symmetry experiment. *The European Physical Journal Special Topics*, 224(16):3055–3108, 2015.

[39] S. Ulmer et al. High-precision comparison of the antiproton-to-proton charge-to-mass ratio. *Nature*, 524(7564):196, 2015.

[40] G. Gabrielse, A. Khabbaz, D. S. Hall, C. Heimann, H. Kalinowsky, and W. Jhe. Precision mass spectroscopy of the antiproton and proton using simultaneously trapped particles. *Physical Review Letters*, 82(16):3198, 1999.

[41] S. Ulmer, A. Mooser, H. Nagahama, S. Sellner, and C. Smorra. Challenging the standard model by high-precision comparisons of the fundamental properties of protons and antiprotons. *Philosophical Transactions of the Royal Society A: Mathematical, Physical and Engineering Sciences*, 376(2116):20170275, 2018.

[42] M. Deutsch. Three-quantum decay of positronium. *Physical Review*, 83(4):866, 1951.

[43] V. W. Hughes, D. W. McColm, K. Ziock, and R. Prepost. Formation of muonium and observation of its Larmor precession. In *A Festschrift In Honor Of Vernon W Hughes*, pages 208–210. World Scientific, 1992.

[44] M. Iwasaki et al. Discovery of antiproton trapping by long-lived metastable states in liquid helium. *Physical Review Letters*, 67(10):1246, 1991.

[45] G. Baur et al. Production of antihydrogen. *Physics Letters B*, 368(3):251–258, 1996.

[46] Ch. G. Parthey et al. Improved measurement of the hydrogen 1s–2s transition frequency. *Physical Review Letters*, 107(20):203001, 2011.

[47] M. Ahmadi et al. Characterization of the 1S–2S transition in antihydrogen. *Nature*, 557(7703):71, 2018.

[48] G. Baur et al. Production of antihydrogen. *Physics Letters B*, 368(3):251–258, 1996.

[49] G. Blanford, D. C. Christian, K. Gollwitzer, M. Mandelkern, C. T. Munger, J. Schultz, and G. Zioulas. Observation of atomic antihydrogen. *Physical Review Letters*, 80(14):3037, 1998.

[50] G. Gabrielse et al.. Proposal presented to the SPSLC: The production and study of cold antihydrogen. CERN-SPSC-97-8; SPSC-P-306, 1997.

[51] T. Azuma et al. Atomic spectroscopy and collisions using slow antiprotons. CERN-SPSC-2000-004; SPSC-M-642, 2000.

[52] J. S. Hangst et al. ALPHA Proposal. CERN-SPSC-2005-006; SPSC-P-325, 2005.

[53] S. Maury. The antiproton decelerator (ad). *Hyperfine Interactions*, 109, 1997.

[54] ELENA website, https://espace.cern.ch/elena-project/SitePages/Home.aspx, accessed 27.07.2019.

[55] W. Oelert. The ELENA project at CERN. *Acta Physica Polonica B. 46 (1): 181*, 2015.

[56] H. H. Gutbrod, I. Augustin, H. Eickhoff, K. D. Groß, W. F. Henning, D. Krämer, and G. Walter. FAIR – Baseline technical report. Executive summary. 2006.

[57] J. Walz and T. W. Hänsch. A proposal to measure antimatter gravity using ultracold antihydrogen atoms. *General Relativity and Gravitation*, 36(3):561–570, 2004.

[58] P. Perez, A. Mohri, H. A. Torii, L. Liszkay, N. Kuroda, B. Mansoulié, J. M. Rey, and Y. Yamazaki. A new path to measure antimatter free fall. Technical report, 2007.

[59] A. Y. Voronin, P. Froelich, and V. V. Nesvizhevsky. Gravitational quantum states of Antihydrogen. *Physical Review A*, 83(3):032903, 2011.

[60] V. V. Nesvizhevsky, A. Y. Voronin, P.-P. Crépin, and S. Reynaud. Interference of several gravitational quantum states of antihydrogen in GBAR experiment. *Hyperfine Interactions*, 240(1):32, 2019.

[61] V. V. Nesvizhevsky et al. Quantum states of neutrons in the Earth's gravitational field. *Nature*, 415(6869):297, 2002.

[62] J. W. Humberston, M. Charlton, F. M. Jacobson, and B. I. Deutch. On antihydrogen formation in collisions of antiprotons with positronium. *Journal of Physics B: Atomic and Molecular Physics*, 20(1):L25, 1987.

[63] J. P. Merrison, H. Bluhme, J. Chevallier, B. I. Deutch, P. Hvelplund, L. V. Jørgensen, H. Knudsen, M. R. Poulsen, and M. Charlton. Hydrogen formation by proton impact on positronium. *Physical Review Letters*, 78(14):2728, 1997.

[64] F. Herfurth et al. A linear radiofrequency ion trap for accumulation, bunching, and emittance improvement of radioactive ion beams. *Nuclear Instruments and Methods in Physics Research Section A: Accelerators, Spectrometers, Detectors and Associated Equipment*, 469(2):254–275, 2001.

[65] A. Husson. Deceleration of antiprotons from CERN's ELENA synchrotron and transport of antimatter beams through the GBAR experiment (Doctoral dissertation). Thesis: 2018SACLS255, 2018.

[66] A. Leite. Development of a buffer gas trap for the confinement of positrons and study of positronium production in the GBAR experiment (Doctoral dissertation). CERN-THESIS-2017-251 27/10/2017, 2017.

[67] S. J. Gilbert, C. Kurz, R. G. Greaves, and C. M. Surko. Creation of a monoenergetic pulsed positron beam. *Applied Physics Letters*, 70(15):1944–1946, 1997.

[68] C. Kurz, S. J. Gilbert, R. G. Greaves, and C. M. Surko. New source of ultra-cold positron and electron beams. *Nuclear Instruments and Methods in Physics Research Section B: Beam Interactions with Materials and Atoms*, 143(1-2):188–194, 1998.

[69] J. H. Malmberg and J. S. DeGrassie. Properties of nonneutral plasma. *Physical Review Letters*, 35(9):577, 1975.

[70] M. R. Natisin, J. R. Danielson, and C. M. Surko. Formation of buffer-gas-trap based positron beams. *Physics of Plasmas*, 22(3):033501, 2015.

[71] P. Dupré. Piégeage de positons dans un piège de Penning Malmberg, en vue de leur accumulation avec un faisceau pulsé (Doctoral dissertation). URI: https://www.theses.fr/165611588, 2011.

[72] P. Grandemange. Piégeage et accumulation de positons issus d'un faisceau pulsé produit par un accélérateur pour l'étude de l'interaction gravitationnelle de l'antimatière (Doctoral dissertation). URI: https://www.theses.fr/175714673, 2013.

[73] N. Oshima, T. M. Kojima, M. Niigaki, A. Mohri, K. Komaki, and Y. Yamazaki. New scheme for positron accumulation in ultrahigh vacuum. *Physical Review Letters*, 93(19):195001, 2004.

[74] D. W. Gidley, W. E. Frieze, T. L. Dull, A. F. Yee, E. T. Ryan, and H.-M. Ho. Positronium annihilation in mesoporous thin films. *Physical Review B*, 60(8):R5157, 1999.

[75] L. Liszkay et al. Positronium reemission yield from mesostructured silica films. *Applied Physics Letters*, 92(6):063114, 2008.

[76] L. Liszkay et al. Mesoporous silica films with varying porous volume fraction: direct correlation between ortho-positronium annihilation decay and escape yield into vacuum. *Applied Physics Letters*, 95(12):124103, 2009.

[77] L. Liszkay. Positronium for antihydrogen production page 297 in: Physics With many Positrons. *Proceedings of the International School of Physics "Enrico Fermi"Sisyphus cooling, course CLXXIV, edited by A. Dupasquier, AP Mills, Jr., RS Brusa, IOS Press, Amsterdam, Oxford, Tokyo, Washington DC*, 2010.

[78] P. Comini and P.-A. Hervieux. $\bar{\mathrm{H}}^{+}$ ion production from collisions between antiprotons and excited positronium: cross sections calculations in the framework of the GBAR experiment. *New Journal of Physics*, 15(9):095022, 2013.

[79] O. Halpern. Magnetic quenching of the positronium decay. *Physical Review*, 94(4):904, 1954.

[80] K. Abe et al. Solar neutrino measurements in Super-Kamiokande-IV. *Physical Review D*, 94:052010, 2016.

[81] L. Hilico, J.-P. Karr, A. Douillet, P. Indelicato, S. Wolf, and F. S. Kaler. Preparing single ultra-cold antihydrogen atoms for free-fall in GBAR. In *International Journal of Modern Physics: Conference Series*, volume 30, page 1460269. World Scientific, 2014.

[82] N. Sillitoe, J.-P. Karr, J. Heinrich, T. Louvradoux, A. Douillet, and L. Hilico. Sympathetic Cooling Simulations with a Variable Time Step. In *Proceedings of the 12th International Conference on Low Energy Antiproton Physics (LEAP2016)*, page 011014, 2017.

[83] D. Leibfried, R. Blatt, C. Monroe, and D. Wineland. Quantum dynamics of single trapped ions. *Reviews of Modern Physics*, 75:281–324, 2003.

[84] D. Banerjee. Resistive Multiplexed Micromegas Detectors to Search for Dark Sector Physics and Test the Weak Equivalence Principle for Anti-Matter at CERN (Doctoral dissertation). DOI: 10.3929/ethz-b-000231250, 2017.

[85] P. Hamilton, A. Zhmoginov, F. Robicheaux, J. Fajans, J. S. Wurtele, and H. Müller. Antimatter Interferometry for Gravity Measurements. *Physical Review Letters*, 112:121102, 2014.

[86] G. L. Brownell, D. Marcum, B. Hoop and D. E. Bohning. Quantitative dynamic studies using short-lived radioisotopes and positron detection. Proceedings of the Symposium on Dynamic Studies with Radioisotopes in Medicine. Rotterdam. August 31-September 4, 1945. IAEA. Vienna. 194824. pp. 161-172.

[87] S. Golge, B. Vlahovic, et al. Review of low-energy positron beam facilities. *Proc. of IPAC*, 12:1464–1466, 2012.

[88] Ch. Hugenschmidt, H. Ceeh, T. Gigl, F. Lippert, C. Piochacz, M. Reiner, K. Schreckenbach, S. Vohburger, J. Weber, and S. Zimnik. Positron beam characteristics at NEPOMUC upgrade. In *Journal of Physics: Conference Series*, volume 505, page 012029. IOP Publishing, 2014.

[89] P. Perez and A. Rosowsky. Intense source of slow positrons. *Nuclear Instruments and Methods in Physics Research Section A: Accelerators, Spectrometers, Detectors and Associated Equipment*, 532(3):523–532, 2004.

[90] A. P. Mills Jr and E. M. Gullikson. Solid neon moderator for producing slow positrons. *Applied Physics Letters*, 49(17):1121–1123, 1986.

[91] Ch. Hugenschmidt. Positrons in surface physics. *Surface Science Reports*, 71(4):547–594, 2016.

[92] P. G. Coleman. *Positron beams and their applications*. World Scientific, 2000.

[93] A. I. Williams, D. J. Murtagh, S. E. Fayer, S. L. Andersen, J. Chevallier, Á. Kövér, P. Van Reeth, J. W. Humberston, and G. Laricchia. Moderation and diffusion of positrons in tungsten meshes and foils. *Journal of Applied Physics*, 118(10):105302, 2015.

[94] J. M. Rey et al. Status of the Linac based positron source at Saclay. In *Journal of Physics: Conference Series*, volume 443, page 012077. IOP Publishing, 2013.

[95] A. Vehanen and J. Mäkinen. Thin films for slow positron generation. *Applied Physics A*, 36(2):97–101, 1985.

[96] A. Vehanen, K. G. Lynn, P. J. Schultz, and M. Eldrup. Improved slow-positron yield using a single crystal tungsten moderator. *Applied Physics A*, 32(3):163–167, 1983.

[97] I. Y. Al-Qaradawi and P. G. Coleman. Re-emission of slow positrons from tungsten at elevated temperatures. *Applied surface science*, 194(1-4):20–23, 2002.

[98] T. S. Pedersen. The guiding center approximation. In *Trapped Charged Particles: A Graduate Textbook with Problems and Solutions*, pages 55–80. World Scientific, 2016.

[99] M. Muramatsu, T. Ohdaira, and R. Suzuki. Reemission of positrons from mesh and powder moderators. *Japanese journal of applied physics*, 44(8R):6283, 2005.

[100] A. P. Mills Jr and E. M. Gullikson. Solid neon moderator for producing slow positrons. *Applied Physics Letters*, 49(17):1121–1123, 1986.

[101] Y. C. Wu, Y. Q. Chen, S. L. Wu, Z. Q. Chen, S. J. Wang, and R. G. Greaves. High moderation efficiency positron beamline. *Physica status solidi C*, 4(10):4032–4035, 2007.

[102] P. Comini. Study of the antihydrogen atom and ion formation in the collisions antiproton-positronium (Doctoral dissertation). DOI: 10.13140/2.1.4519.7605, 2014.

[103] M. Valdes. Calcul de sections efficaces du système à trois corps $(e^+, e^-, \bar{p})$ avec les équations de Faddeev-Merkuriev (Doctoral dissertation). URI: http://www.theses.fr/2017STRAE031, 2017.

[104] I. Abdurakhmanov. Convergent close-coupling approach to positron-helium collisions (Doctoral dissertation). URI: http://hdl.handle.net/20.500.11937/1603, 2011.

[105] P. Froelich, T. Yamashita, Y. Kino, S. Jonsell, E. Hiyama, and K. Piszczatowski. Four-body treatment of the antihydrogen-positronium system: binding, structure, resonant states and collisions. *Hyperfine Interactions*, 240(1):46, 2019.

[106] L. D. Faddeev. ZhETF (USSR) 39 (1960) 1459. *Journal of Experimental and Theoretical Physics (Sov. Phys.)*, 12(1014):216, 1961.

[107] S. P. Merkuriev. Three-body Coulomb scattering. In *New Developments in Mathematical Physics*, pages 65–110. Springer, 1981.

[108] M. Valdes, M. Dufour, R. Lazauskas, and P.-A. Hervieux. Ab initio calculations of scattering cross sections of the three-body system $(\overline{p}, e^+, e^-)$ between the $e^- + \overline{\mathrm{H}}(n = 2)$ and $e^- + \overline{\mathrm{H}}(n = 3)$ thresholds. *Physical Review A*, 97:012709, 2018.

[109] A. S. Kadyrov, C. M. Rawlins, A. T. Stelbovics, I. Bray, and M. Charlton. Antihydrogen formation via antiproton scattering with excited positronium. *Physical Review Letters*, 114(18):183201, 2015.

[110] C. M. Rawlins, A. S. Kadyrov, A. T. Stelbovics, I. Bray, and M. Charlton. Calculation of antihydrogen formation via antiproton scattering with excited positronium. *Physical Review A*, 93(1):012709, 2016.

[111] P. Comini and P.-A. Hervieux. Ion production from collisions between antiprotons and excited positronium: cross sections calculations in the framework of the GBAR experiment. *New Journal of Physics*, 15(9):095022, 2013.

[112] P. Comini, P.-A. Hervieux, and F. Biraben. $\bar{\mathrm{H}}^+$ production from collisions between positronium and keV antiprotons for GBAR. *Hyperfine Interactions*, 228(1-3):159–165, 2014.

[113] M. Weber, A. Hofmann, W. Raith, W. Sperber, F. Jacobsen, and K. G. Lynn. Results of the bielefeld-brookhaven e^+−H experiment. *Hyperfine Interactions*, 89(1):221–242, 1994.

[114] S. Zhou, H. Li, W. E. Kauppila, C. K. Kwan, and T. S. Stein. Measurements of total and positronium formation cross sections for positrons and electrons scattered by hydrogen atoms and molecules. *Physical Review A*, 55:361–368, 1997.

[115] H. Bethe, Zeitschrift für Physik November 1929, Volume 57, Issue 11-12, pp 815-821.

[116] J. C. Straton and R. J. Drachman. Formation of positronium in e^++H^- collisions. *Physical Review A*, 44:7335–7342, 1991.

[117] P. K. Biswas. Effect of H^- ion formation on positronium-hydrogen elastic scattering. *Journal of Physics B: Atomic, Molecular and Optical Physics*, 34(23):4831, 2001.

[118] J. E. Blackwood, M. T. McAlinden, and H. R. J. Walters. Importance of the H^- channel in Ps-H scattering. *Physical Review A*, 65(3):030502, 2002.

[119] M. T. McAlinden, J. E. Blackwood, and H. R. J. Walters. Positron scattering by the negative hydrogen ion. *Physical Review A*, 65:032715, 2002.

[120] S. Roy and C. Sinha. Formation of negative hydrogen ion in positronium-hydrogen collisions. *The European Physical Journal D*, 47(3):327–334, 2008.

[121] P. Comini, private communication.

[122] G. B. Andresen et al. Antiproton, positron, and electron imaging with a microchannel plate/phosphor detector. *Review of Scientific Instruments*, 80(12):123701, 2009.

[123] P. Crivelli, D. Cooke, and M.W. Heiss. Antiproton charge radius. *Physical Review D*, 94:052008, 2016.

[124] P. Crivelli, U. Gendotti, A. Rubbia, L. Liszkay, P. Perez, and C. Corbel. Measurement of the orthopositronium confinement energy in mesoporous thin films. *Physical Review A*, 81(5):052703, 2010.

[125] A. Deller, B. S. Cooper, T. E. Wall, and D. B. Cassidy. Positronium emission from mesoporous silica studied by laser-enhanced time-of-flight spectroscopy. *New Journal of Physics*, 17(4):043059, 2015.

[126] H.-P. Dürr and E. Teller. Interaction of antiprotons with nuclear fields. *Physical Review*, 101(1):494, 1956.

[127] K. Nordlund, D. Sundholm, P. Pyykkö, D. M. Zambrano, and F. Djurabekova. Nuclear stopping power of antiprotons. *Physical Review A*, 96(4):042717, 2017.

[128] E. Fermi and E. Teller. The capture of negative mesotrons in matter. *Physical Review*, 72(5):399, 1947.

[129] F. Balestra et al. Determination of the ratio $\sigma(\bar{p}n)/\sigma(\bar{p}p)$ from $\bar{p}^4$He reaction data. *Nuclear Physics A*, 465(4):714–732, 1987.

[130] M. Hori. Recent progress of laser spectroscopy experiments on antiprotonic helium. *Philosophical Transactions of the Royal Society A: Mathematical, Physical and Engineering Sciences*, 376(2116):20170270, 2018.

[131] L. Venturelli, M. Amoretti, C. Amsler, G. Bonomi, C. Carraro, C. L. Cesar, M. Charlton, M. Doser, A. Fontana, R. Funakoshi, et al. Protonium production in athena. *Nuclear Instruments and Methods in Physics Research Section B: Beam Interactions with Materials and Atoms*, 261(1-2):40–43, 2007.

[132] S. J. Orfanidis and V. Rittenberg. Nucleon-antinucleon annihilation into pions. *Nuclear Physics B*, 59(2):570–582, 1973.

[133] M. Hori, K. Yamashita, R. S. Hayano, and T. Yamazaki. Analog Cherenkov detectors used in laser spectroscopy experiments on antiprotonic helium. *Nuclear Instruments and Methods in Physics Research Section A: Accelerators, Spectrometers, Detectors and Associated Equipment*, 496(1):102–122, 2003.

[134] C. Amsler et al. Antiproton-proton annihilation at rest into two-body final states. *Zeitschrift für Physik C Particles and Fields*, 58(2):175–189, 1993.

[135] C. Ghesquiere, CERN Yellow Report 74-18 p. 436, CERN, Geneva, 1974.

[136] S. Ahmad et al. Search for monochromatic pion emission in pp annihilation from atomic P states. *Physics Letters B*, 152(1-2):135–139, 1985.

[137] J. Sedlák and V. Simak. Antinucleon–nucleon annihilation at rest and in flight. *Soviet Journal of Particles and Nuclei (English Translation)*, 19(3):191–227, 1988.

[138] A. Abele et al. ρ-ω interference in pp-annihilation at rest into $\pi^+\pi^-\eta$. *Physics Letters B*, 411(3-4):354–360, 1997.

[139] N. Semprini Cesari and Obelix Collaboration. Coupled-channel analysis of $\pi\pi\pi$ and $KK\pi$ final states from pp annihilation at rest in hydrogen targets at three densities. *Nuclear Physics A*, 655(1-2):c82–c88, 1999.

[140] A. Abele et al. Antiproton-proton annihilation at rest into $K^+K^-\pi^0$. *Physics Letters B*, 468(1-2):178–188, 1999.

[141] A. Bettini et al. Annihilation into pions of the $\bar{p}n$ system from antiprotons at rest in deuterium. *Il Nuovo Cimento A (1971-1996)*, 47(3):642–661, 1967.

[142] J. Hrtánková and J. Mareš. Interaction of antiprotons with nuclei. *Nuclear Physics A*, 945:197–215, 2016.

[143] K. Todoroki et al. Instrumentation for measurement of in-flight annihilations of 130 keV antiprotons on thin target foils. *Nuclear Instruments and Methods in Physics Research Section A: Accelerators, Spectrometers, Detectors and Associated Equipment*, 835:110–118, 2016.

[144] H. Aghai-Khozani et al. First experimental detection of antiproton in-flight annihilation on nuclei at 130 keV. *The European Physical Journal Plus*, 127(10):125, 2012.

[145] A. Galoyan, A. Ribon, and V. Uzhinsky. Production of strange particles in hadronic interactions. *arXiv preprint arXiv:1810.09973*, 2018.

[146] S. Aghion et al. Measurement of antiproton annihilation on Cu, Ag and Au with emulsion films. *Journal of instrumentation*, 12(04):P04021, 2017.

[147] O. D. Dalkarov and V. A. Karmanov. Scattering of low-energy antiprotons from nuclei. *Nuclear Physics A*, 445(4):579–604, 1985.

[148] V. Uzhinsky, J. Apostolakis, A. Galoyan, G. Folger, V. M. Grichine, V. N. Ivanchenko, and D. H. Wright. Antinucleus–nucleus cross sections implemented in geant4. *Physics Letters B*, 705(3):235–239, 2011.

[149] A. S. Iljinov, V. I. Nazaruk, and S. E. Chigrinov. Nuclear absorption of stopped antiprotons: Multipion-nucleus interactions. *Nuclear Physics A*, 382(3):378–400, 1982.

[150] W. Markiel et al. Emission of helium ions after antiproton annihilation in nuclei. *Nuclear Physics A*, 485(3-4):445–460, 1988.

[151] D. Polster et al. Light particle emission induced by stopped antiprotons in nuclei: energy dissipation and neutron-to-proton ratio. *Physical Review C*, 51(3):1167, 1995.

[152] T. Von Egidy et al. Neutrons produced by 1.22 GeV antiproton interactions with nuclei. *The European Physical Journal A*, 8(2):197–204, 2000.

[153] L. E. Agnew Jr, T. Elioff, W. B. Fowler, R. L. Lander, W. M. Powell, E. Segrè, H. M. Steiner, H. S. White, C. Wiegand, and T. Ypsilantis. Antiproton interactions in hydrogen and carbon below 200 MeV. *Physical Review*, 118(5):1371, 1960.

[154] M. Cahay, J. Cugnon, and J. Vandermeulen. Low-energy antiproton annihilation in nuclei. *Nuclear Physics A*, 393(3):237–251, 1983.

[155] R. Engfer et al. Nuclear pion capture at rest. In *AIP Conference Proceedings*, volume 54, pages 176–177. AIP, 1979.

[156] M. Tulej, S. Meyer, M. Lüthi, D. Lasi, A. Galli, L. Desorgher, W. Hajdas, S. Karlsson, L. Kalla, and P. Wurz. Detection efficiency of microchannel plates for e^- and π^- in the momentum range from 17.5 to 345 MeV/c. *Review of Scientific Instruments*, 86(8):083310, 2015.

[157] MCP Hamamatsu. MCP assembly selection guide. *Hamamatsu Photonics KK*.

[158] Y. T. Tanaka, I. Yoshikawa, K. Yoshioka, T. Terasawa, Y. Saito, and T. Mukai. Gamma-ray detection efficiency of the microchannel plate installed as an ion detector in the low energy particle instrument onboard the GEOTAIL satellite. *Review of Scientific Instruments*, 78(3):034501, 2007.

[159] R. C. Blase, R. R. Benke, K. S. Pickens, and J. H. Waite. Microchannel plate detection efficiency to monoenergetic photons between 0.66 and 20 MeV. *IEEE Transactions on Nuclear Science*, 65(4):980–988, 2018.

[160] A. V. Sy. Advanced Penning-type ion source development and passive beam focusing techniques for an associated particle imaging neutron generator with enhanced spatial resolution (Doctoral dissertation). ISBN: 9781303375033, 2013.

[161] L. Valyi. Atom and ion sources. Wiley-Interscience Publications, Wiley, 1977.

[162] H. Tawara, Y. Itikawa, H. Nishimura, and M. Yoshino. Cross sections and related data for electron collisions with hydrogen molecules and molecular ions. *Journal of Physical and Chemical Reference Data*, 19(3):617–636, 1990.

[163] R. Scrivens. Classification of Ion Sources. arXiv:1411.2445, CERN-2013-007.

[164] W. Wien. Untersuchungen über die electrische Entladung in verdünnten Gasen. *Annalen der Physik*, 301(6):440–452, 1898.

[165] B. L. Peko and T. M. Stephen. Absolute detection efficiencies of low energy H, H^-, H^+, H_2^+ and H_3^+ incident on a multichannel plate detector. *Nuclear Instruments and Methods in Physics Research Section B: Beam Interactions with Materials and Atoms*, 171(4):597–604, 2000.

[166] N. Takahashi, Y. Adachi, M. Saito, and Y. Haruyama. Absolute detection efficiencies for keV energy atoms incident on a microchannel plate detector. *Nuclear Instruments and Methods in Physics Research Section B: Beam Interactions with Materials and Atoms*, 315:51–54, 2013.

[167] S. Hosokawa, N. Takahashi, M. Saito, and Y. Haruyama. Absolute detection efficiencies of a microchannel plate detector for 0.5–5 keV neutrals. *Review of Scientific Instruments*, 81(6):063301, 2010.

[168] T. Kirchner and H. Knudsen. Current status of antiproton impact ionization of atoms and molecules: theoretical and experimental perspectives. *Journal of Physics B: Atomic, Molecular and Optical Physics*, 44(12):122001, 2011.

[169] M. McGovern, D. Assafrão, J. R. Mohallem, C. T. Whelan, and H. R. J. Walters. Differential and total cross sections for antiproton-impact ionization of atomic hydrogen and helium. *Physical Review A*, 79(4):042707, 2009.

[170] P. Hvelplund, H. Knudsen, U. Mikkelsen, E. Morenzoni, S. P. Moller, E. Uggerhoj, and T. Worm. Ionization of helium and molecular hydrogen by slow antiprotons. *Journal of Physics B: Atomic, Molecular and Optical Physics*, 27(5):925, 1994.

[171] J. S. Cohen. Reactive collisions of atomic antihydrogen with the H_2 and H_2^+ molecules. *Journal of Physics B: Atomic, Molecular and Optical Physics*, 39(17):3561, 2006.

[172] J.S. Cohen. Reactive collisions of atomic antihydrogen with H, He^+ and He. *Journal of Physics B: Atomic, Molecular and Optical Physics*, 39(6):1517, 2006.

[173] P. Mahadevan, J. K. Layton, and D. B. Medved. Secondary electron emission from clean surface of molybdenum due to low-energy noble gas ions. *Physical Review*, 129(1):79, 1963.

[174] Pfeiffer introduction to ion pumps, https://www.pfeiffer-vacuum.com/en/know-how/introduction-to-vacuum-technology/influences-in-real-vacuum-systems/residual-gas-composition/, accessed 27.07.2019.

[175] G. W. McClure. Electron Transfer in Proton-Hydrogen-Atom Collisions: 2-117 keV. *Physical Review*, 148:47–54, 1966.

[176] V. S. Nikolaev. Calculation of the effective cross sections for proton charge exchange in collisions with multi-electron atoms. *Soviet Journal of Experimental and Theoretical Physics*, 24:847, 1967.

[177] J. Allison et al. Recent developments in Geant4. *Nuclear Instruments and Methods in Physics Research Section A: Accelerators, Spectrometers, Detectors and Associated Equipment*, 835:186 – 225, 2016.

[178] J. L. Wiza et al. Microchannel plate detectors. *Nuclear Instruments and Methods in Physics Research*, 162(1-3):587–601, 1979.

[179] MCP detector manual, Photonis, available on request.

[180] PCO pixelfly data sheet, https://www.pco.de/fileadmin/user_upload/pco-product_sheets/pco.pixelfly_usb_data_sheet.pdf, accessed 27.07.2019.

[181] D. Rogers and R. F. Malina. Optimization of the performance of a tandem microchannel plate detector as a function of interplate spacing and voltage. *Review of Scientific Instruments*, 53(9):1438–1441, 1982.

[182] L. Bradley et al. Library astropy/photutils: v0.3, https://doi.org/10.5281/zenodo.164986, accessed 27.07.2019.

[183] R. Brun and F. Rademakers. Root – an object oriented data analysis framework. *Nuclear Instruments and Methods in Physics Research Section A: Accelerators, Spectrometers, Detectors and Associated Equipment*, 389(1-2):81–86, 1997.

[184] J. E. Bateman. The detection of hard X-rays (10–140 keV) by channel plate electron multipliers. *Nuclear Instruments and Methods*, 144(3):537–545, 1977.

[185] J. G. Timothy and R. L. Bybee. Effects of 1-MeV gamma radiation on a multi-anode microchannel array detector tube. *Review of Scientific Instruments*, 50(6):743–746, 1979.

[186] K. W. Dolan and J. Chang. Microchannel plate response to hard X-rays. In *X-ray imaging*, volume 106, pages 178–188. International Society for Optics and Photonics, 1977.

[187] J. Adams. X-ray detection by channel electron multipliers. In *Advances in Electronics and Electron Physics*, volume 22, pages 139–153. Elsevier, 1966.